

Assisting Self-Assembly
of 3d/4f Coordination Clusters

Zur Erlangung des akademischen Grades eines
DOKTORS DER NATURWISSENSCHAFTEN

(Dr. rer. nat.)

von der KIT-Fakultät für Chemie und Biowissenschaften

des Karlsruher Instituts für Technologie (KIT)

angenommene

DISSERTATION

von

Dipl. Chem. Hagen Kämmerer

Dekan: Prof. Dr. Hans-Achim Wagenknecht

Referentin: Prof. Dr. Annie K. Powell

Korreferent: Prof. Dr. Peter W. Roesky

Tag der mündlichen Prüfung: 26.04.2022

Note

The ions shown in the illustrations are not to scale. Organic hydrogen atoms are often omitted for better visualisation. Atoms and ions are shown in the following colours in all illustrations:

Grey: Carbon; blue: nitrogen; red: oxygen; bright green: chloride; yellow: gadolinium; lavender/dark purple: dysprosium; flesh pink: praeodymium; pale pink: manganese(II), pink: manganese(III); dark green: iron; dark teal: chromium;

Numerical quantities such as bond lengths and angles are given with their standard uncertainties in round brackets after the respective values and refer to last digits. The lengths are given in Angstrom, where $1 \text{ \AA} = 1 \cdot 10^{-10} \text{ m}$.

This thesis was prepared from 1st of June 2018 to 16th of March 2022 at the Institute of Inorganic Chemistry, Faculty of Chemistry and Biosciences of the Karlsruhe Institute of Technology (KIT) under the supervision of Prof. Dr. Annie K. Powell.

Eidesstattliche Erklärung

Bei der eingereichten Dissertation zu dem Thema

Assisting self-assembly of 3d/4f Coordination Clusters

handelt es sich um meine eigenständig erbrachte Leistung.

Ich habe nur die angegebenen Quellen und Hilfsmittel benutzt und mich keiner unzulässigen Hilfe Dritter bedient. Insbesondere habe ich wörtlich oder sinngemäß aus anderen Werken übernommene Inhalte als solche kenntlich gemacht.

Die Arbeit oder Teile davon habe ich bislang nicht an einer Hochschule des In- oder Auslands als Bestandteil einer Prüfungs- oder Qualifikationsleistung vorgelegt.

Die Richtigkeit der vorstehenden Erklärungen bestätige ich.

Die Bedeutung der eidesstattlichen Versicherung und die strafrechtlichen Folgen einer unrichtigen oder unvollständigen eidesstattlichen Versicherung sind mir bekannt.

Ich versichere an Eides statt, dass ich nach bestem Wissen die reine Wahrheit erklärt und nichts verschwiegen habe.

Karlsruhe, 16.03.2022

.....

Ort und Datum

Kurzzusammenfassung

Diese Dissertation befasst sich mit dem Konzept der unterstützten Selbstorganisation, mit dem Ziel neuartige 3d/4f Koordinationscluster zu synthetisieren. Bei diesem Ansatz werden vorgeformte Übergangsmetallbausteine als Vektor verwendet um diverse Übergangsmetalle, Liganden und Co-Liganden in die Reaktion einzubringen.

Die strukturelle Untersuchung der Verbindungen erfolgt mittels Einkristallstrukturanalyse, Infrarotspektroskopie sowie in einigen Fällen Massenspektrometrie. Magnetische Analysen werden mittels SQUID-Magnetometrie und in einigen Fällen in Kollaboration mit anderen Forschungsgruppen durch microSQUID- und ^{57}Fe -Mößbauer-Techniken durchgeführt. Theoretische Methoden wie MAGELLAN und ALPS/QMC ergänzen die physikalischen Messungen.

Wichtige Konzepte wie das allgemeine Konzept der unterstützten Selbstorganisation sowie die Verwendung des M_2Ln_2 Schmetterlings Motivs als standardisierte Testumgebung um die Auswirkung der Verwendung unterschiedlicher Metalle und Liganden auf die magnetischen Eigenschaften der zu untersuchenden Verbindungen werden in Kapitel 1 eingeführt.

Darüber hinaus wird die Variabilität der verwendeten Bausteine durch die Untersuchung ausgewählter dreikerniger Übergangsmetallcluster hervorgehoben. Ein systematischer Syntheseansatz wird vorgestellt, der den gezielten Austausch des Übergangsmetalls in diesen Verbindungen ermöglicht. Einige dreikernige Verbindungen wurden mittels SQUID-Magnetometrie, ^{57}Fe Mößbauer sowie Massenspektrometrie untersucht.

In Kapitel 4 wird die Synthese von Mangan basierten Koordinationsclustern beschrieben, die einen Mn_6 Cluster als Startmaterial verwendet. Mangan spielt durch die besondere historische und biochemische Bedeutsamkeit eine spezielle Rolle in dem Fachgebiet des molekularen Magnetismus.

In Kapitel 5 wurden unter Verwendung von dreikernigen Übergangsmetallclustern zwei verschiedene Strukturtypen erhalten: (I) neuartige Schmetterlings-Systeme mit verschiedenen Liganden, sowie ein riesiger zyklischer Koordinationscluster, der faszinierende magnetische Eigenschaften aufweist.

Abstract

This thesis highlights the use of an assisted self-assembly approach to target new 3d/4f coordination clusters. In this approach, preformed transition metal building blocks are used as a vector to introduce various transition metal, ligands and co-ligands into the reaction.

The compounds are analysed structurally via single-crystal X-Ray crystallography, infrared spectroscopy and in some cases mass spectrometry, as well as magnetically using SQUID magnetometry, and in some cases microSQUID and Mößbauer techniques in collaboration with other working groups. Theoretical methods like MAGELLAN and ALPS/QMC complement the physical measurements.

Important concepts are introduced in Chapter 1, such as the general concept of assisted self-assembly and the use of the well-known M_2Ln_2 butterfly as a “test-bed” to investigate changes of the metals and ligands used on the overall magnetic properties of the compound.

Furthermore, the variability of the building blocks used is highlighted by investigations of different trinuclear transition metal carboxylates in Chapter 3. A systematic synthetic approach is introduced to allow targeted replacement of the transition metal within these compounds. Selected trinuclear compounds have been investigated using SQUID magnetometry, ^{57}Fe Mößbauer and mass spectrometry.

In Chapter 4, manganese-based coordination clusters are described, using a Mn_6 building block as the starting material. Manganese has a special role in molecular magnetism, seeing as the first molecule to show magnetic bistability was $Mn_{12}O_{12}(\text{CH}_3\text{CO}_2)_{12}$. Additionally, the role of Mn in the oxygen-evolving centre of PSII makes Mn-based materials of further importance to biochemical processes.

Chapter 5 explores the use of trinuclear starting material using tripodal ligands. In this chapter, two types of compounds were obtained: (I) new examples of Type I butterfly systems for two different ligand systems and (II) a giant cyclic coordination cluster, showing fascinating magnetic properties.

Table of contents

1	Introduction and theory	1
1.1	General magnetism.....	2
1.2	Exotic magnetic properties.....	4
1.2.1	Single-Molecule Magnetism.....	5
1.2.2	Spin Frustration.....	7
1.2.3	Toroidicity.....	8
1.2.4	Mößbauer Spectroscopy.....	10
1.3	Assisted Self-Assembly.....	11
1.3.1	Assisted self-assembly in literature.....	12
1.3.2	Cluster-assisted self-assembly.....	15
1.4	The M_2Ln_2 Butterfly.....	16
2	Motivation	18
3	Building Blocks	20
3.1	Trinuclear transition metal carboxylates.....	20
3.1.1	Introduction.....	20
3.1.2	Variations of the basic iron carboxylate $[Fe_3O(O_2C-R)_6L_3]X$	22
3.1.3	Variations for the basic carboxylates $[M_3O(O_2C-R)_6L_3]X$ ($M = Cr, Mn, Fe, Co, Ni$).....	43
3.1.4	Summary.....	56
3.2	Hexanuclear mixed valence Manganese Oxide complexes with a $[Mn_6O_2]^{10+}$ core.....	57
3.2.1	Introduction.....	57
3.2.2	History of $[Mn^{II}_4Mn^{III}_2O_2(\mu_3-O_2C-R)_4(\mu_2-O_2C-R)_6(L)_4]$	58
3.2.3	$[Mn_6O_2(piv)_{10}(pivH)_2(4-Me-py)_2]$	63
3.2.4	Summary of Hexanuclear mixed valence $[Mn_6O_2]^{10+}$ core complexes...	68
4	Mn-based coordination clusters	69
4.1	Introduction.....	69
4.2	Decanuclear Mn_7Ln_3 complexes.....	70
4.3	Nonanuclear Mn_5Ln_4 complexes.....	77
4.4	Tetranuclear Mn_2Ln_2 complexes.....	85
4.5	Summary of Mn-based coordination clusters.....	87
5	Fe-based coordination clusters	89
5.1	Tetranuclear M_2Ln_2 complexes.....	89
5.1.1	Introduction.....	89

5.1.2	[M ₂ Ln ₂ (ampd) ₄ (O ₂ C-Ph) ₆] synthesised with 2-amino-2-methyl-1,3-propanediol	91
5.1.3	[Fe ₂ Dy ₂ (μ ₃ -OH) ₂ (Me-teaH) ₂ (O ₂ C-Ph) ₆] synthesised with the chiral Me-teaH ₃ ligand.....	98
5.1.4	Summary of tetranuclear M ₂ Ln ₂ complexes	111
5.2	Giant cyclic coordination clusters synthesised with 2-amino-2-methyl-1,3-propanediol	112
5.2.1	[Fe ₁₈ Ln ₆ (μ-OH) ₆ (ampd) ₁₂ (Hampd) ₁₂ (O ₂ C-Ph) ₂₄](NO ₃) ₆ ·38MeCN	112
5.2.2	Summary of giant cyclic coordination clusters	124
6	Overall summary and conclusion.....	126
7	Experimental section.....	129
7.1	General procedures	129
7.2	Synthesis	130
8	Crystallographic data	137
9	Literature	154
10	Acknowledgements	160
11	Appendix	162
11.1	List of abbreviations	162
11.2	List of tables.....	163
11.3	List of figures	164

1 Introduction and theory

The compound class of single-molecule magnets (SMMs) was established at the end of the last millennium, when the Gateschi group determined the magnetic bistability in the $\text{Mn}_{12}\text{O}_{12}(\text{CH}_3\text{CO}_2)_{12}$ coordination cluster.^[1-3] Since then researchers have tried to synthesise new SMMs in a quest to find an answer to the problems arising from the abundance of information the modern society consumes and processes daily.

In 1965 the co-founder of Intel Gordon Moore formulated the now (in)famous Moore's law, according to which the number of microchips on electronic components and in turn their performance double every two years. Moore's law is officially at an end in many experts' opinions. Microchips are reaching physical limits to how small they can get, this is why researchers try to develop single-molecule magnets with potential use in data-storage and processing. If it is possible to have one molecule act as one bit it would be possible to overcome the physical limitations and revitalise the race for processing components.

The magnetic bistability is so far only observed at very low temperatures, the highest temperature at which magnetic hysteresis was observed is close to 80K, just above liquid nitrogen temperature. However, such molecules are very air-sensitive and their ability for application is questionable, although they provide fundamental understanding of relaxation processes.

In the presented thesis new strategies for the synthesis of single-molecule magnets incorporating transition metal and lanthanide ions are investigated. The approach described uses preformed clusters as a vector to introduce various transition metals, ligands and co-ligands into the reaction.

The compounds presented in this thesis have been analysed structurally via single-crystal X-Ray crystallography, infrared spectroscopy and in some cases mass spectrometry, as well as magnetically using SQUID magnetometry, and in some cases microSQUID and ^{57}Fe Mößbauer techniques in collaboration with other working groups. Theoretical methods like magnetostructural correlations,^[4] MAGELLAN^[5] and ALPS/QMC^[6-7] complement the physical measurements.

1.1 General magnetism

The magnetic properties of materials around us are of huge importance to everyday life. There is a lot of literature explaining magnetic phenomena and the interested reader is encouraged to find detailed explanations in there.^[8-13] In the scope of this chapter a summary of the aspects essential to the results presented in the thesis is given.

Macroscopic magnetic properties are based on the electronic structure of a substance, arising from paired and unpaired electrons. Every moving electronic charge, which the electrons can be described as, causes a magnetic moment.

$$m = \frac{Q}{2M} \cdot L = \gamma \cdot L$$

The charge Q and mass M combine to give the gyromagnetic ratio γ , L refers to the angular momentum. The resulting magnetic moment is defined as:

$$\hat{\mu} = -\mu_B \cdot (\hat{L} + g_e \cdot \hat{S})$$

with the Bohr magneton μ_B defined as the quantized magnetic moment of a free electron:

$$\mu_B = \frac{e}{2m_e} \cdot \hbar$$

In this formula, e represents the electronic charge, m_e is the corresponding mass of the electron and \hbar the reduced Planck constant. According to the Heisenberg uncertainty principle only one spatial direction can be described exactly, this allows the simplification of the equation to

$$\vec{\mu}_l = \sqrt{l \cdot (l + 1)} \cdot \mu_B \quad \text{and} \quad \vec{\mu}_s = g_e \cdot \sqrt{s \cdot (s + 1)} \cdot \mu_B$$

for the angular and spin magnetic moment with the angular momentum quantum number l and spin quantum number s, respectively. The factor g_e is called the Landé-factor.

In conclusion, the total magnetic moment is the simple addition of the two magnetic contributions:

$$\mu_J = \mu_s + \mu_l$$

For systems incorporating 3d and 4f metal ions, the Landé-factor cannot always be obtained easily, due to the spin-orbit-coupling and has to be derived from the Russell-Saunders-coupling scheme:

$$g = 1 + \frac{J \cdot (J + 1) + S \cdot (S + 1) - L \cdot (L + 1)}{2J(J + 1)}$$

Conversely, for pure 3d systems the orbital moment is often quenched by the ligand field and the magnetic moment can be described by the spin-only formula:

$$\mu_{spin-only} = g_e \sqrt{S \cdot (S + 1)} \cdot \mu_B$$

The magnetic susceptibility quantifies how susceptible a substance is to an applied external field H with the magnetisation M:

$$\chi = \frac{\partial M}{\partial H}$$

Magnetic systems are classified as either diamagnetic ($\chi < 0$) or paramagnetic ($\chi > 0$). For diamagnetic substances, the net magnetic moment is zero, due to antiparallel pairing of electrons. It is worth noting that due to the atomic structure, every substance possesses a diamagnetic component.

Furthermore, the Curie-Weiss law highlights the temperature dependence for paramagnetic substances:

$$\chi_{mol} = \frac{C}{T - \Theta}$$

The Curie-constant C is a substance specific constant defined as:

$$C = \frac{N_A \cdot \mu_B^2}{3 \cdot k_B}$$

By introducing the Weiss-constant paramagnetic substances can be further distinguished into ferromagnetic ($\Theta > 0$), antiferromagnetic ($\Theta < 0$) and ferrimagnetic substances.

For quantum systems the macroscopic description of magnetic properties is often not sufficient, therefore van-Vleck proposed the following formula based on a weighted summation of microscopic magnetisation moments of a molecule:

$$M = \frac{N_A \sum_n \left(-\frac{\partial E_n}{\partial H} \right) \cdot \exp\left(-\frac{E_n}{k_B T}\right)}{\sum_n e^{-\frac{E_n}{k_B T}}}$$

with the Zeeman-coefficients of the first and second order:

$$E_n = E_n^{(0)} + H E_n^{(1)} + H^2 E_n^{(2)}$$

There are multiple approximations that simplify the van-Vleck equation, namely that no long-range ferro- or ferrimagnetic ordering takes place and only weak magnetic fields or high temperatures are discussed, in these cases the van-Vleck equation can be simplified to obtain the molar susceptibility as:

$$\chi_M = N_A \frac{g^2 \mu_B^2}{3kT} S(S + 1)$$

allowing the determination of the room temperature χT product of a system as:

$$\chi T = \frac{g^2}{8} \cdot S(S + 1)$$

1.2 Exotic magnetic properties

Some phenomena that can be observed in molecular magnetism are not easily explained by the classical processes explained above and some of these more exotic magnetic properties are discussed in the following sections.

1.2.1 Single-Molecule Magnetism

Single-molecule magnets are compounds that exhibit magnetic bistability. The first example of this compound class was $\text{Mn}_{12}\text{O}_{12}(\text{CH}_3\text{CO}_2)_{12}$ investigated by the Gateschi group in 1993.^[2-3]

The phenomenon can be explained by the splitting of the m_s states of the molecule. If an external magnetic field is applied the $+m_s$ and $-m_s$ states lose their degeneracy, leading to the population of only one type of state. Upon removing the external field, the system relaxes and the spins return to the degenerate state. In order to do so the electronic spins have to cross an energy barrier for the reversal of magnetisation U_{eff} . A schematic overview of the process is shown in **Figure 1.2-1**.

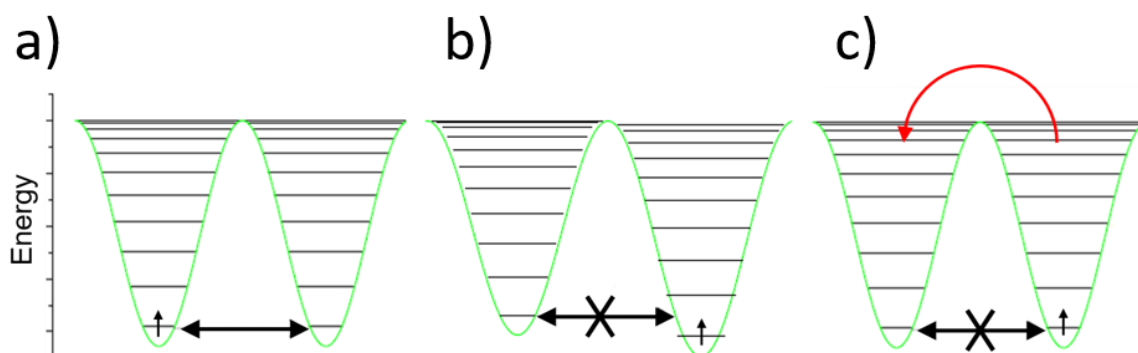


Figure 1.2-1 Schematic representation of the double-well potential in $\text{Mn}_{12}\text{O}_{12}(\text{CH}_3\text{CO}_2)_{12}$, reimagined from reference ^[2]. Degenerate m_s states (a) removing degeneracy through application of an external field (b) and relaxation over the energy barrier after removal of the external field (c)

The energy barrier U_{eff} is defined as

$$U_{\text{eff}} = S^2 |D| \quad \text{for systems with integer spins and}$$

$$U_{\text{eff}} = \left(S^2 - \frac{1}{4}\right) |D| \quad \text{for half-integer spins respectively,}$$

with the overall spin S and the absolute value for the zero-field splitting parameter D . The system does not necessarily have to follow the path over the energy barrier. Many different relaxation processes have been identified. The various relaxation processes are linked to the relaxation time via the following equation:

$$\tau^{-1} = \underbrace{AH^{n_1}T}_{\text{Direct}} + \underbrace{CT^{n_2}}_{\text{Raman}} + \underbrace{\tau_0^{-1} \exp\left(-\frac{U_{eff}}{k_B T}\right)}_{\text{Orbach}} + \underbrace{\frac{B_1}{1 + B_2 H^2}}_{\text{QTM}}$$

A schematic representation of the processes is shown in **Figure 1.2-2**.

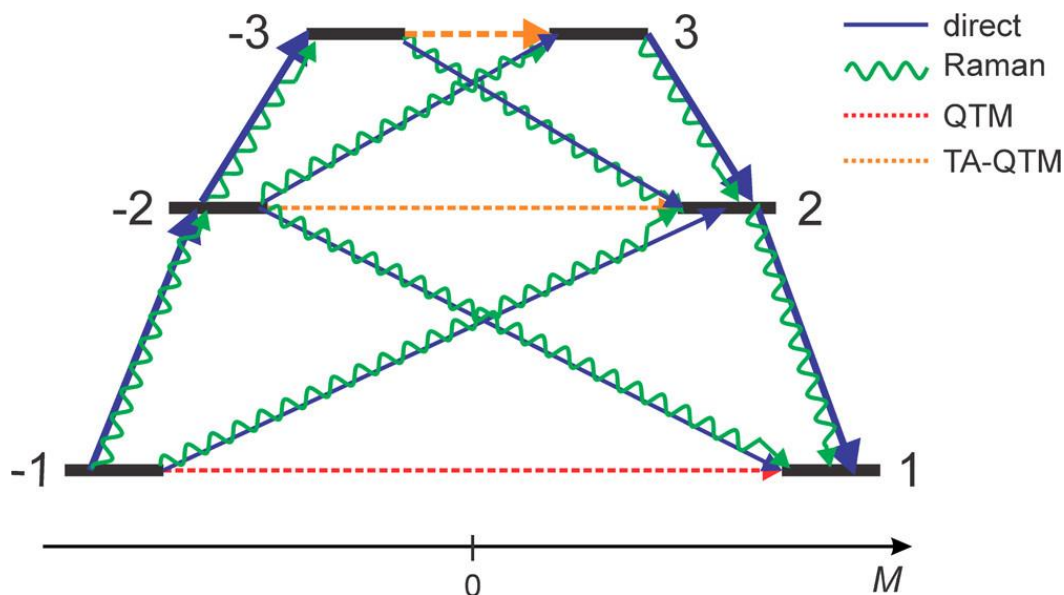


Figure 1.2-2 Schematic representation of the different relaxation processes, reprinted from reference ^[14] with permission from the American Chemical Society.

Another important parameter is the pre-exponential factor τ_0 which can be calculated from the Arrhenius law for the Orbach process:

$$\tau = \tau_0 \cdot \exp\left(\frac{U_{eff}}{kT}\right)$$

Lastly, when investigating single-molecule magnets incorporating lanthanide ions the shape of the anisotropy ellipsoids of the lanthanides has to be considered. It has been established that for oblate anisotropy ellipsoids an axial ligand field leads to favourable SMM properties. An overview of the trends for the anisotropy ellipsoids in the lanthanide series in combination with their Russell-Saunders term is shown in **Figure 1.2-3**.

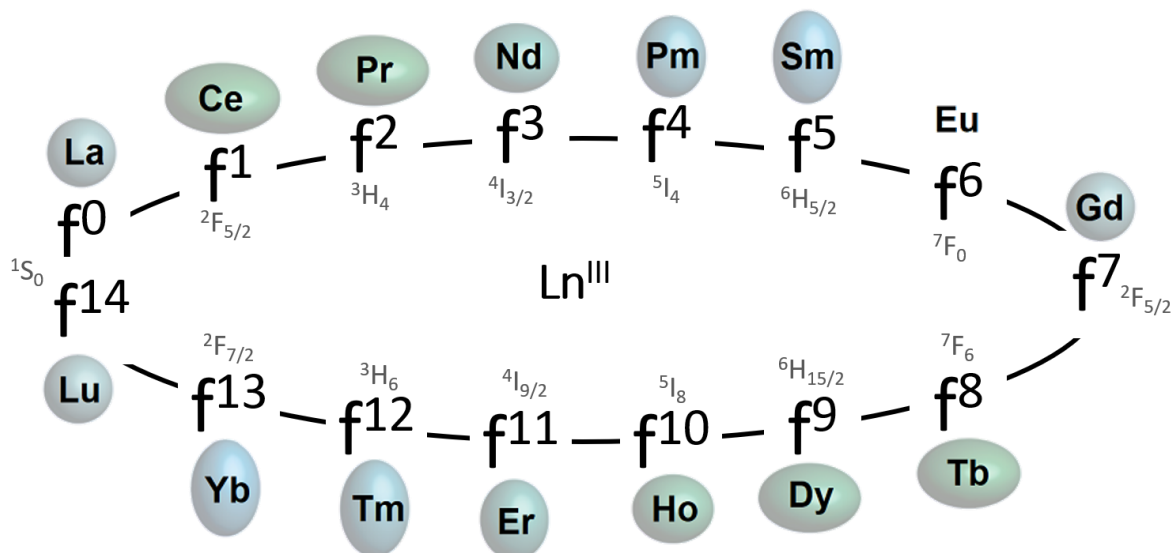


Figure 1.2-3 Illustration highlighting the inverse relationship of the anisotropy ellipsoids for the lanthanide series, reimagined from reference ^[15] Ln^{III} = Ce-Sm show the opposite shape of the ellipsoids compared to Ln^{III} = Dy-Yb, Tb does not have a counterpart as Eu is expected to be diamagnetic at low temperatures.

1.2.2 Spin Frustration

Spin frustration is an effect that occurs when competing interactions in the ground state cannot be satisfied for all spin carriers at the same time.^[16]

An example that can be easily visualised (see **Figure 1.2-4**) is the geometric frustration of localised spins which want to adopt an antiparallel arrangement. For example, in a triangular or butterfly arrangement it is not possible for all spins to couple antiferromagnetically to each other.

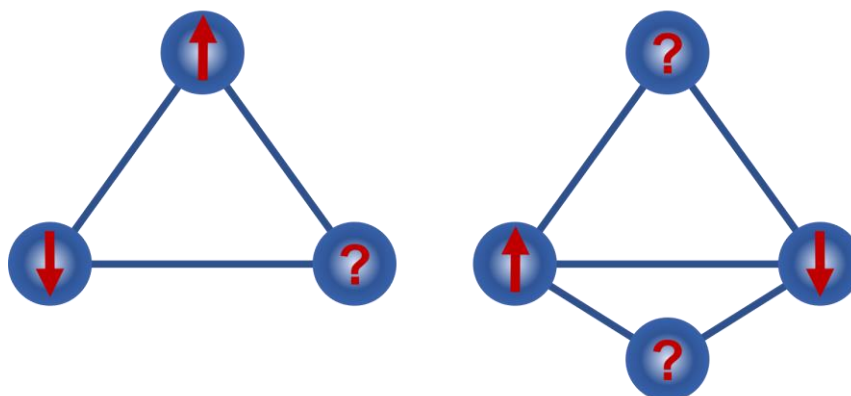


Figure 1.2-4 Rationalisation of possible spin arrangements leading to spin frustration, arising from competing antiferromagnetic interactions that cannot be satisfied.

The classical model of spin frustration was first described on spinel type minerals which can be described as a Kagomé lattice, a system of interwoven triangular arrangements.^[17]

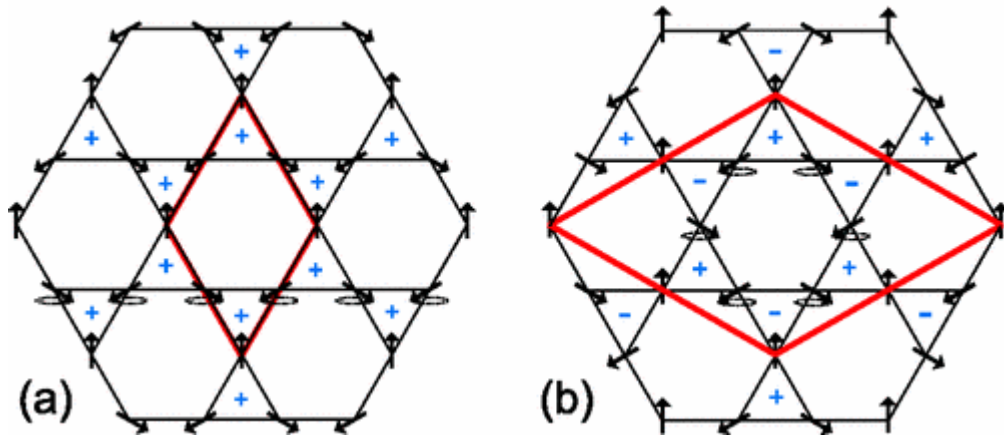


Figure 1.2-5 Arrangement of frustrated spins in a Kagomé lattice, reproduced from reference ^[18]

Possible results of spin frustration are a higher level of degeneracy of lower energy states or the formation of a spin glass.

1.2.3 Toroidicity

A special kind of spin arrangement within the aforementioned Kagomé lattices is a toroidal arrangement. The vortex like arrangement of spin moments can be rationalised as a way for the system to overcome the spin frustration arising from the inability to attain antiferromagnetic coupling for all spin carriers.

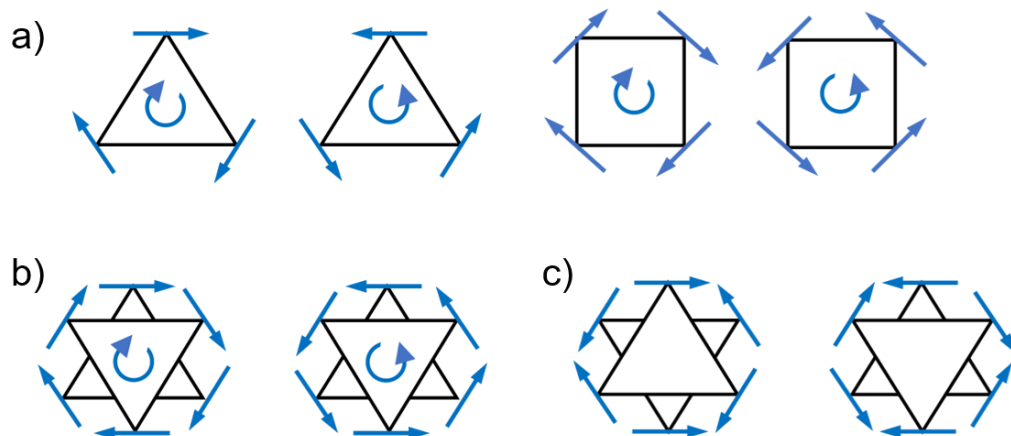


Figure 1.2-6 Possible arrangement of non-collinear spins in vortex like orientations resulting in a toroidal (a), ferrotoroidal (b) and antiferrotoroidal (c) system.

The first molecular toroidal arrangement was identified for a compound published by our working group in 2006.^[19] In 2008 it could be shown experimentally and using theory methods that it possesses a single molecule toroidal moment.^[20] Since then the field of single molecule toroids as a subset of single-molecule magnetism provided additional examples of these spin arrangements.^[21-27]

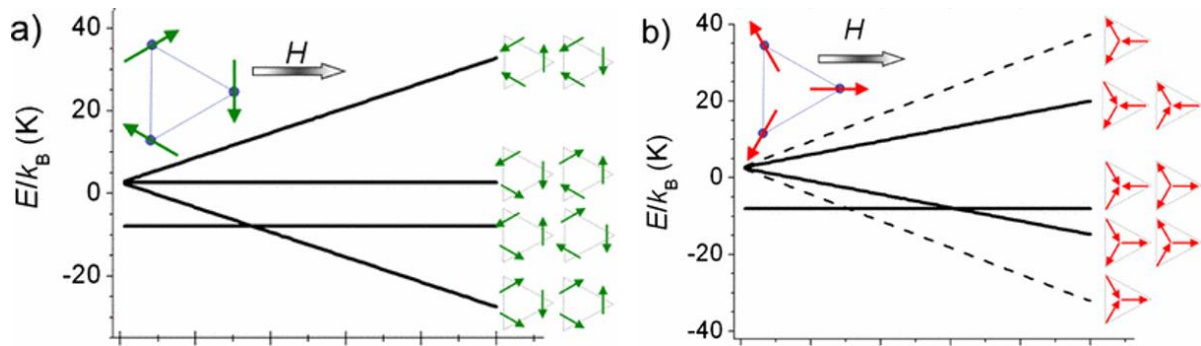


Figure 1.2-7 Possible spin ground states for the archetypical Dy₃ toroidal moment, reprinted from reference ^[20] with permission from the American Physical Society.

The toroidal moment can be described as the result of head-to-tail arrangement of spins as shown in **Figure 1.2-8** (bottom right) it is therefore the cross product of spins s_i on the site i with the radius r_i from the origin of the molecule.

$$T = \sum_{i=1}^N r_i \times s_i$$

		Space	
		Invariant	Change
Time	Invariant	Ferroelastic 	Ferroelectric
	Change	Ferromagnetic 	Ferrotoroidic

Figure 1.2-8 Alternative description of the toroidal moment as the fourth ferroic order arising from a tail-to-head arrangement of spins. Reprinted from reference ^[28] with permission from Springer Nature Limited.

1.2.4 Mößbauer Spectroscopy

The Mößbauer effect was first observed by Rudolf L. Mößbauer during his dissertation in 1958, only three years later he was awarded the Nobel prize for this achievement at only 32 years old.^[29-31]

The Mößbauer effect relies on the recoilless nuclear resonance absorption of γ -rays. (Figure 1.2-9)

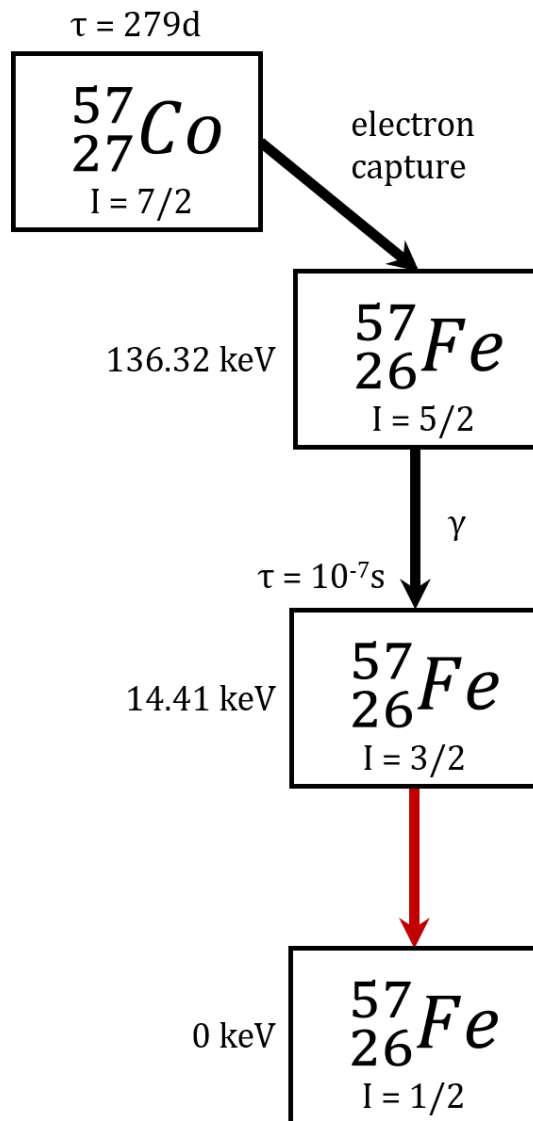


Figure 1.2-9 Decay of the radioactive Mößbauer source ^{57}Co via the $I=5/2$ excited state to the $I=3/2$, 14.41keV state of ^{57}Fe , the resonance of the excited 14.41keV energy level with the sample leads to the detection of the Mößbauer effect.

The radioactive ^{57}Co source with a half-life of 279 days decays by electron capture to ^{57}Fe populating the $I = 5/2$ nuclear spin state, this excited state decays after 10^{-7}s to the $I = 3/2$ state of ^{57}Fe corresponding to 14.41keV.

Mössbauer spectroscopy is a technique that can provide valuable information concerning the local environment of the Fe nucleus.

The measured observables are:

- (I) The isomer shift δ caused by the electric monopole interaction between protons, providing information on the oxidation state, spin state and binding states.
- (II) The quadrupole splitting ΔE_Q caused by the electric quadrupole interaction provides further information on the oxidation state, spin state and site symmetry.
- (III) The magnetic splitting ΔE_M caused by the magnetic dipole interaction, provides information regarding the magnetic properties of the sample.

Classic Mössbauer spectroscopy is limited by the availability of suitable Mössbauer active isotopes with reasonable half-lives. However, recently synchrotron studies allowed the observation of the Mössbauer effect, for example, by generating the corresponding energies for ^{161}Dy , to give insights into the properties of Dy-based SMMs.^[32-33]

1.3 Assisted Self-Assembly

As chemists, we try to predict the outcome of a given chemical reaction making reasonable assumptions based on the properties of the reagents used. The vast landscape of chemical literature provides data that helps chemists make reasonable decisions on reagents and reaction conditions used to get the desired result. The synthesis of coordination complexes is usually the result of “serendipitous” assembly of the components added to the reaction mixture.^[34]

This process is also widely referred to as “self-assembly”, a concept that is well-known in biological processes, where biomolecules self-organise into higher structures due to their molecular properties. These properties can be specific local interactions among the molecules themselves, without external direction.^[35]

Naturally, researchers have tried to find ways to manipulate reactions by external means to overcome the limitations of self-assembly processes. The following sections describe some examples from the literature, as well as establishing what we understand as assisted self-assembly in coordination chemistry.

1.3.1 Assisted self-assembly in literature

The articles highlighted here are only a few examples of assisted self-assembly processes and do not represent an exhaustive list.

A 2014 publication by Hung et al.^[36] describes the synthesis of a thin graphene oxide membrane for efficient filtering of isopropanol from water. Water and isopropanol form an azeotrope mixture with a composition of around 88% isopropanol and 12% water, which leads to the problem that environmentally friendly disposal of isopropanol used in the semiconductor industry is very cost inefficient. Usually the recycling is done via very energy-consuming techniques or the isopropanol is simply diluted with large quantities of water and subsequently disposed of along with waste water.

The authors show how the use of very thin layered graphene membranes could solve this problem. A schematic view of the synthetic procedure is shown in **Figure 1.3-1**. The membranes synthesised by this method show a spacing of the membrane layers of just 3.6Å, compared to current commercial membranes with 8.5Å.

This technique is referred to as pressure-assisted self-assembly, where the synthetic procedure aims to overcome the serendipitous nature of the self-assembly process by adding external factors, in this case applied pressure, leading to a much-improved result (i.e. smaller layer spacing) compared to the serendipitous self-assembly.

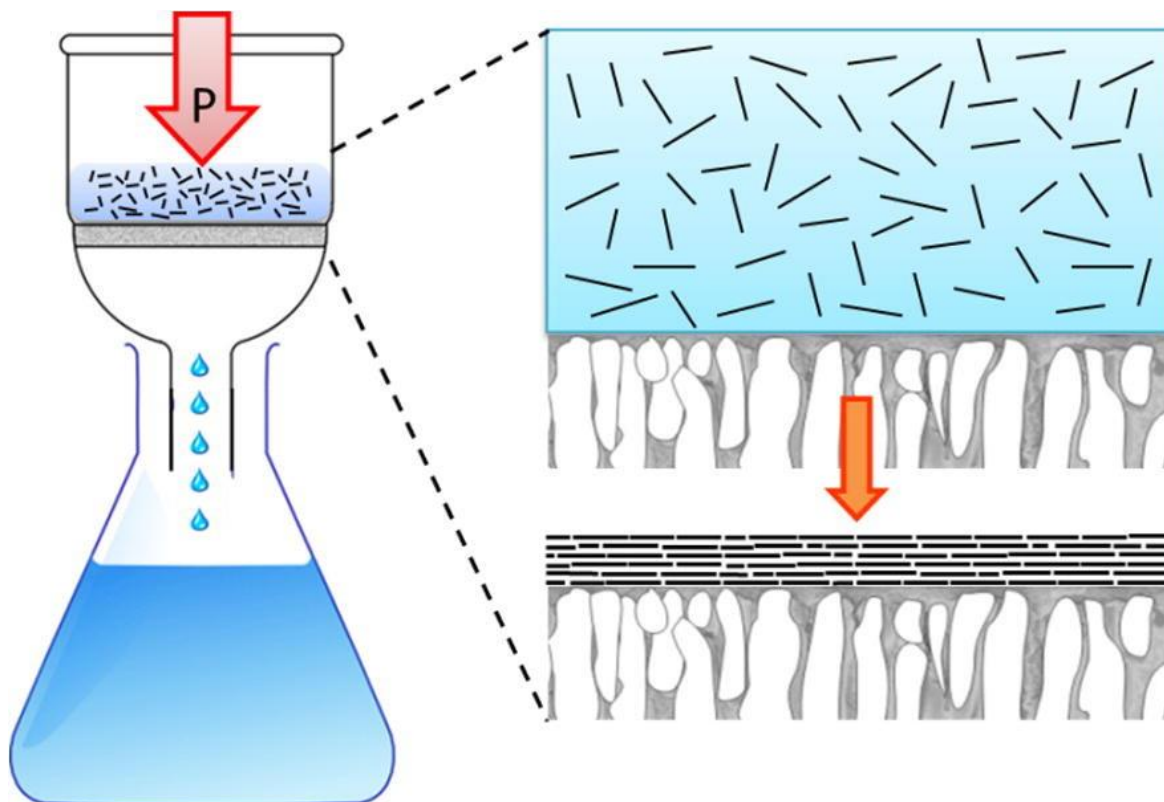


Figure 1.3-1 Scheme of the synthetic procedure to form thin graphene membranes via the pressure-assisted self-assembly described in the text. Reprinted from reference ^[36] with the permission of Elsevier.

Another example of manipulating the self-assembly process is the synthesis of uniaxial organic single-crystalline micro ribbon arrays reported by Zhang et al.^[37]

The authors report the synthesis of organic semiconductors as an ink by application on to a substrate that has a temperature gradient applied to it. A drop of the ink was put on the substrate and monitored via thermal imaging. The ink automatically moves from the high-temperature to the low-temperature region of the substrate, effectively “printing” the organic semiconductor on the surface.

A schematic overview of the experimental setup is shown in **Figure 1.3-2**.

The formation of single-crystal arrays in this way is then referred to as temperature-assisted self-assembly, representing another example of an external factor, in this case temperature, to manipulate the self-assembly process.

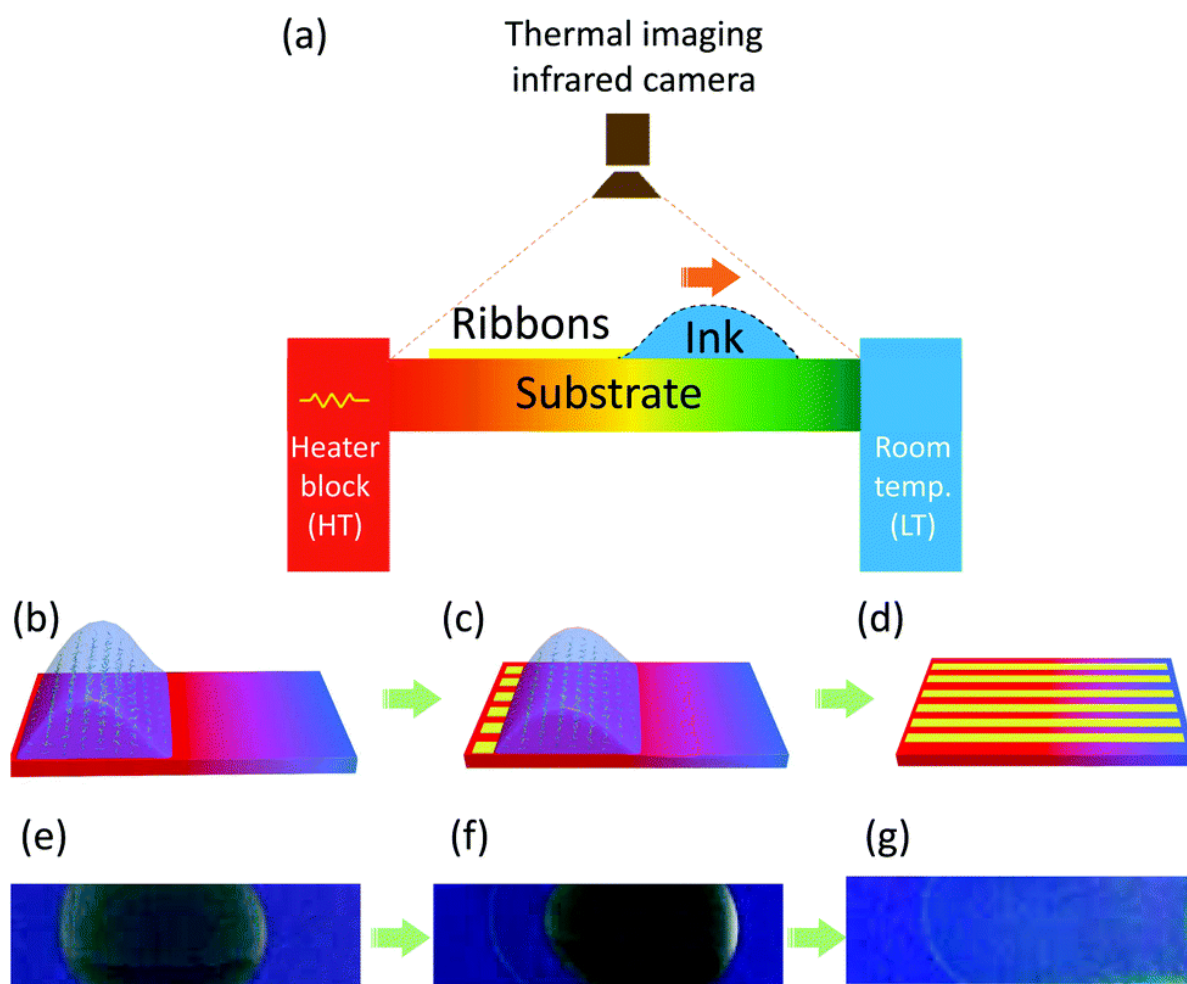


Figure 1.3-2 Schematic overview of the temperature-assisted self-assembly process discussed in the text, reprinted from reference ^[37] with permission from the Royal Society of Chemistry.

Lastly, in a recent publication by Hanske et al.^[38] another method of assisting self-assembly processes is presented. The authors describe the combination of using a template to form arrays of gold nanoparticles with the effect that different solvent mixtures have on the composition of the resulting arrays. A schematic representation of the process is shown in **Figure 1.3-3**.

This method combines two forms of assistance, first the template used to deposit the gold nanoparticles on the surface is usually referred to as template-assisted self-assembly, while the addition of different solvent mixtures is described as solvent-assisted self-assembly by the authors.

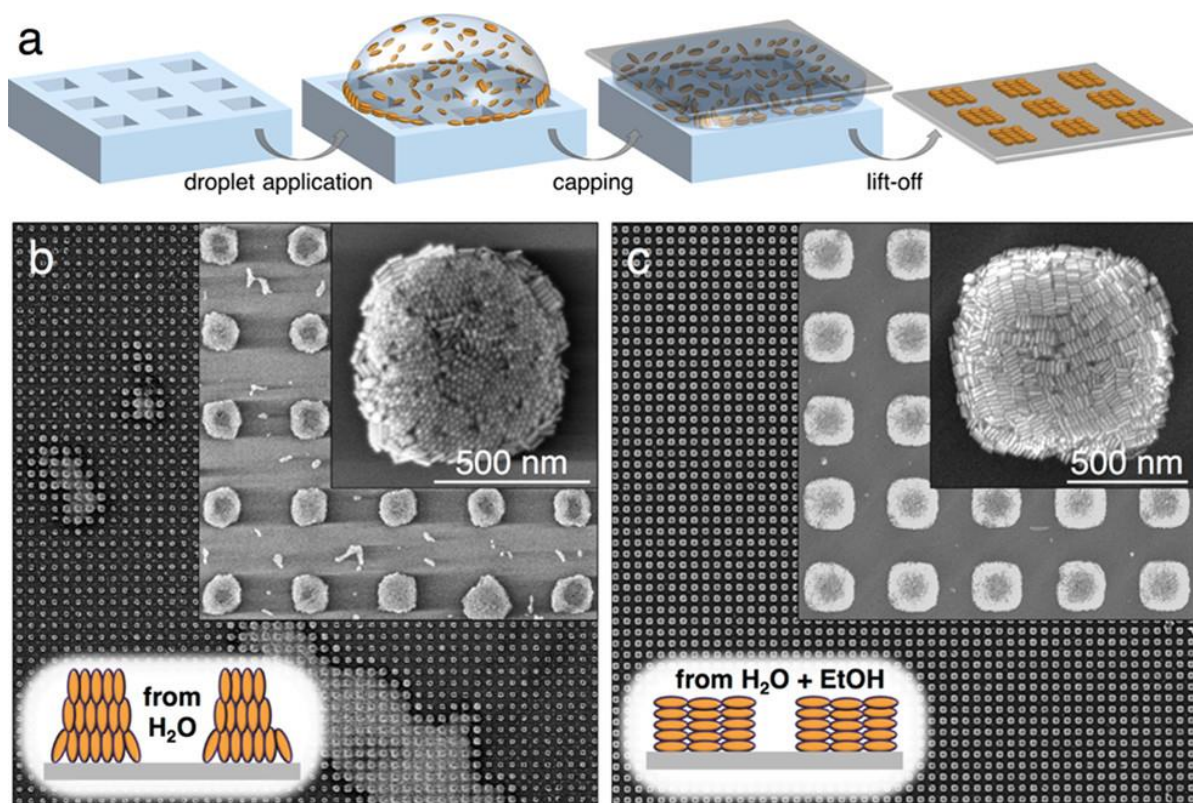


Figure 1.3-3 Schematic representation of the synthetic procedure to produce arrays of gold nanorods (a), SEM images of the formation of gold nanorod arrays from H₂O (b) and a H₂O/EtOH mixture (c), reprinted from reference [38] with permission by the American Chemical Society.

1.3.2 Cluster-assisted self-assembly

The previous section described processes reported in the literature that are classified as assisted self-assembly.

This thesis utilises a procedure where preformed building blocks are used as starting materials in syntheses to obtain 3d/4f coordination clusters. This process can be described as cluster assisted self-assembly.

In the molecular magnetism community, the use of preformed clusters like the well-known $\{M^{III}_3O\}^+$ carboxylates or the mixed-valence $\{Mn^{II}_2Mn^{III}_4O_2\}$ cluster is a common synthetic method to achieve high nuclearity 3d/4f clusters.^[39-43]

The assisted self-assembly approach enables various ligands and co-ligands to be introduced into the final product. The tuning possibilities of the trinuclear M_3O complexes will be highlighted in detail in section 3.1.

One example of utilising the variability of the M_3O includes an investigation of the effect that differently substituted benzoate ligands have on the SMM behaviour of Fe_2Dy_2 SMMs. In this method the Fe_3O triangles are used as a vector to introduce the different benzoate ligands into the system.^[44]

Furthermore, Fe_3O triangles are used in the synthesis of high nuclearity Fe/4f clusters.^[27, 42] It is thought that using these preformed clusters as starting material affects the kinetics of the synthesis by limiting the availability of the Fe to the reaction. This results from the need to break up the cluster, leading to higher nuclearity clusters than could be achieved using a mononuclear transition metal source.

1.4 The M_2Ln_2 Butterfly

In a recent review published by Peng and Powell^[45] the importance of the 3d/4f butterfly structural type to the molecular magnetism community is highlighted. Some key aspects that are of importance to the results presented in this thesis are explained here.

There is a wide variety of structural types for 3d/4f coordination clusters in the literature with a plethora of different synthetic strategies.^[46] The scope of different structural types and nuclearities makes it difficult to gain fundamental insights into the magnetic interactions between 3d and 4f ions. Additionally, the ability to target specifically a given nuclearity of cluster is very challenging.^[47-48] Due to the different electronic nature of 3d and 4f ions, the preferred coordination environments vary largely, posing a synthetic challenge to accommodate both types of ions.

The M_2Ln_2 butterfly arrangement is adopted by a relatively large number of 3d/4f coordination clusters, enabling systematic study of their magnetic properties.

The different butterfly complexes reported in the literature can be divided into two structural types:

(I) For a Type I butterfly the Ln^{III} ions are situated in the wingtip positions of the butterfly, while the 3d ions occupy the body positions. The 3d ions are bridged to the Ln^{III} via a μ_3 -OR group, connecting the two body positions with one wingtip ion. This leads to interesting possibilities for the magnetic properties of the overall molecule. If

the 3d ions are diamagnetic or not coupling to the Ln^{III} for any other reason, the single ion properties of the Ln^{III} dominate the systems. If there is coupling between 3d and 4f ions that means that the whole system has to be viewed as a cooperative entity that is influenced by the magnetic properties of all incorporated ions.

(II) A Type II butterfly represents the case where the body and wingtip positions have been swapped, the Ln^{III} are now occupying the body positions, while the 3d ions are situated at the wingtip positions. In this case, any possible 3d-3d coupling is completely eliminated and only the single 4f ion properties and 3d-4f coupling is relevant to the overall magnetic behaviour.

A definition of the positions the metal ions can occupy and a schematic overview of the different butterfly types is shown in **Figure 1.4-1**.

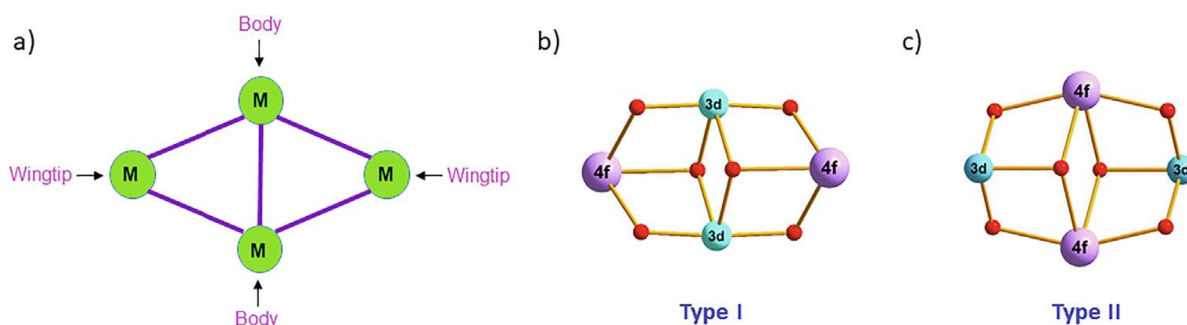


Figure 1.4-1 The definition of the possible positions the metal ions can occupy (a) and the ball-and-stick representations of a Type I (b) or Type II (c) butterfly structure. Reprinted from reference ^[45] with permission from Elsevier.

In conclusion, the M_2Ln_2 butterfly motif represents a very rigid structural type with a huge variety of different 3d and 4f ions adopting the same core structure. Therefore, the butterfly structure can be used as a test bed system to conduct systematic studies investigating the interactions between 3d and 4f ions.

Furthermore, the rigid core structure allows the investigation of effects caused by subtle changes to the ligand system.

2 Motivation

In our modern world there is an abundance of data being processed every day. One reason why the field of molecular magnetism is an ever-evolving research area has been the prospect of producing new data storage devices and advance technology via the use of magnetically interesting materials in quantum computing.

Although significant advances have been made in the field within the last years, such as the observation of magnetic hysteresis at liquid nitrogen temperatures in a dysprosium metallocene single-molecule magnet,^[49] these new type of mononuclear dysprosium compounds are highly air-sensitive. Therefore, they might “break through the nitrogen ceiling” as the authors say, but they will not find their place in every day devices just yet. Of course, although they might be very difficult to handle this does not diminish their fundamental value to the field of molecular magnetism.

This thesis aims to investigate synthetic methods that provide a benefit to the synthesis of new single-molecule magnets by combining the strengths of lanthanide-based materials with the fundamental knowledge that was gathered for transition metal compounds. The synthetic methods investigated follow an assisted self-assembly approach, using preformed transition metal clusters and combining them with lanthanides in synthetic procedures in aerobic conditions.

In addition to introducing transition metals to the synthesis these preformed clusters can also function as vectors to introduce co-ligands into the final compounds, allowing for subtle changes that might have significant impact on the magnetic properties.

Furthermore, the composition of the transition metal complexes used, mostly oxo-centred triangular complexes suggests that their magnetic properties could be interesting in their own right. The starting materials used in this thesis are mostly Fe-based compounds. Due to its natural abundance in earths’ crust and important role in our day-to-day life iron is a natural choice when considering magnetic compounds.

The iron based trinuclear compounds are used in different synthetic approaches with very different products, highlighting the flexibility of the trinuclear starting materials.

Besides Iron, the second transition metal that plays a very important role in molecular magnetism, both historically and as far as the quality of the results is concerned is

manganese. $\text{Mn}_{12}\text{O}_{12}(\text{CH}_3\text{CO}_2)_{12}$ was the first molecule to be identified as showing slow relaxation of magnetisation and is still the most investigated single-molecule magnet to date. Naturally that makes it interesting to use in 3d/4f synthesis as well.

The results shown in this thesis highlight the benefit of the assisted self-assembly approach.

Chapter 4 shows the expansion of a known synthetic method over the whole lanthanide series. It was possible to establish that different structure types that were thought to be based on the nature of the lanthanide were indeed available over the expanded lanthanide series.

Chapter 5 highlights the use of triangular Fe complexes with two different ligand types to access two vastly different products. A chiral ligand system allows the investigation of symmetry breaking effects on the magnetic behaviour of single-molecule magnets while the second ligand system provides a giant cyclic coordination cluster that shows very exotic magnetic behaviour.

In both chapters the M_2Ln_2 butterfly structural type can be observed, suggesting that this molecular composition could in fact represent a sort of very stable thermodynamic sink in many synthetic reaction schemes.

3 Building Blocks

3.1 Trinuclear transition metal carboxylates

3.1.1 Introduction

As was already discussed in chapter 1.3 the concept of assisted self-assembly used in the scope of this thesis utilizes preformed coordination clusters as starting materials for the reactions as a means to manipulate the kinetics and thermodynamics. The rationale is that the system is supplied with limited amounts of metal ions for incorporation into large cluster systems. Additionally, these preformed clusters can be used as a vector to introduce structural elements, co-ligands and metal ions into the given reaction. Here triangular building blocks have been used as the preformed clusters.

The synthesis of these triangular starting materials allows for the use of a plethora of carboxylic acids and metal ions. Historically these compounds go back to one of the founding fathers of modern coordination chemistry, Alfred Werner, who described them in an article published in *Berichte der deutschen chemischen Gesellschaft* in 1908 as so-called organic metal salts.^[50] This specific publication discusses the chromium analogues of formate and acetate salts and was confirmed and expanded in the following years by Weinland.^[51-53] Due to the lack of modern structure determination techniques Werner, Weinland and their peers relied on observing the macroscopic properties such as colour and crystal shape as well as the reactivity of the compounds they were analysing. This led to the proposal for the general sum formula of these salts as $[\text{Cr}_3(\text{OH})_2\text{Ac}_6]\text{X}$ (see **Figure 3.1-1**) with varying carboxylic acid ligands (Ac) (usually Ac stands for acetate) and anions (X).

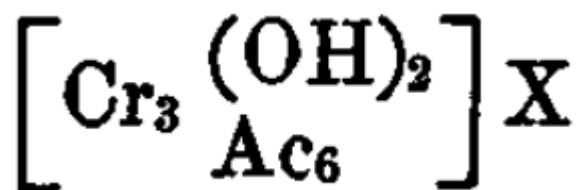


Figure 3.1-1 The original sum formula for the basic carboxylates published by Werner.^[50]

The presence of two hydroxyl groups in the sum formula is based on the observation of these salts generally leading to a basic reaction with water, hence the reason for calling them basic carboxylates in subsequent publications. However, the correct triangular arrangement was first postulated by Welo^[54-55] on the basis of magnetic data and supported in a speculative communication by Orgel in 1960.^[56] Ultimately in 1965 modern single-crystal X-Ray diffraction confirmed the core structure of these compounds consisting of three ions bridged by a μ_3 -oxygen ion.^[57]

As far as the building blocks used in this work are concerned there is an emphasis on iron containing compounds.

In this chapter many variants of these basic carboxylates are discussed and in order to present the data in a structured and analytical way a generic characterization scheme is given below, highlighting the various tweaking possibilities for this structure type. (see **Figure 3.1-2**)

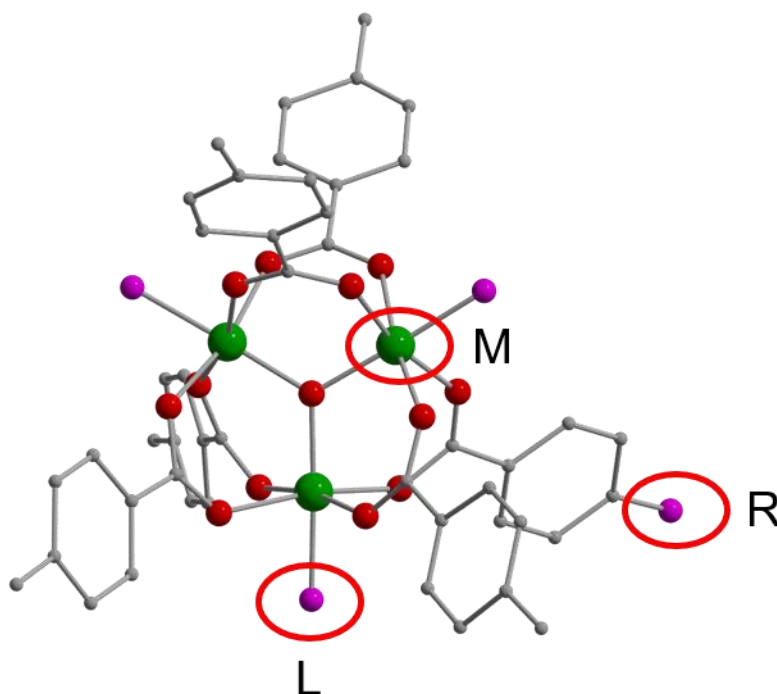


Figure 3.1-2 Generic scheme of the basic carboxylates used in this work, highlighting the various tweaking possibilities of M (transition metals), R (aromatic substituents) and L (terminal ligand). The core of the three transition metals bridged by a μ_3 -oxide ion remains the same for all variations.

Within this scheme M represents the metals used. We can identify four tuning handles for the properties of such triangular compounds: the metal, bridging carboxylate, terminal ligand and counteranion.

(I) The majority of the triangular compounds discussed in this chapter are made with Fe^{3+} ^[58-59] but many other trivalent metals can yield the same core structure. There are examples of Cr^{3+} ,^[60] Mn^{3+} ,^[61-62] Co^{3+} ^[63-64] and Al^{3+} ^[65] carboxylates. Additionally, there are the possibilities of synthesizing mixed-metal carboxylates with different trivalent transition metals^[66], mixed-valent compounds using the same metals^[67-69] as well as mixed-metal, mixed-valent triangles^[70-74] utilizing different oxidation states of varying transition metals within the same compound. This first tuning handle already introduces vastly different chemical and electronic properties.

(II) The second tuning handle is the use of different carboxylic acids. In the literature there are various examples of carboxylic acids used in triangular compounds, including acetate^[75], pivalate^[76] and benzoate^[58] variants. The latter ones are of further interest because the reactivity of differently substituted benzoates is relatively similar, but the resulting electronic and magnetic properties can be markedly different.^[77]

(III) Thirdly the nature of the terminal ligand L is mostly determined by the solvent in which the given crystallization takes place, which in turn changes the solubility of the product in said solvents.

(IV) It is important to note that for the basic carboxylates of trivalent metals the core structure $[\text{M}_3\text{O}(\text{O}_2\text{C-R})_6\text{L}_3]^+$ retains a positive charge and this opens up the possibility of using a fourth tuning mechanism by introducing different counteranions and subsequently manipulate the crystallization of the compounds.

3.1.2 Variations of the basic iron carboxylate $[\text{Fe}_3\text{O}(\text{O}_2\text{C-R})_6\text{L}_3]\text{X}$

$[\text{Fe}_3\text{O}(\text{O}_2\text{C-Ph})_6(\text{py})_3]\text{ClO}_4$ was first reported and investigated using incoherent inelastic neutron scattering (IINS) by Sowrey et al.^[58] These studies made it possible to deduce a set of coupling constants revealing the frustrated nature of the system. The seemingly simple nature of three coupled magnetic centres arranged as an equilateral triangle appears to be confirmed by the trigonal site symmetry in the crystal structure, but this in fact results from disorder of a lower-symmetry molecular structure. The compound was reproduced in this work as part of a systematic survey on the influence of the different tuning handles discussed above.

$\text{FeCl}_3 \cdot 6\text{H}_2\text{O}$ and sodium benzoate are mixed in water, the resulting precipitate is washed and dried at room temperature. Suspending the precipitate in ethanol and adding perchloric acid leads to a clear solution. The resulting product is precipitated by adding water and subsequently recrystallised in pyridine to form $[\text{Fe}_3\text{O}(\text{O}_2\text{C-Ph})_6(\text{py}_3)]\text{ClO}_4$. Due to the potentially explosive nature of perchlorate compounds this compound was not recrystallized or used further after the initial characterisation.

The synthesised crystallised compound $[\text{Fe}_3\text{O}(\text{O}_2\text{C-Ph})_6(\text{EtOH})_2(\text{H}_2\text{O})]\text{ClO}_4$ (**1**) represents the intermediate product of the first step of the synthesis of $[\text{Fe}_3\text{O}(\text{O}_2\text{C-Ph})_6(\text{py}_3)]\text{ClO}_4$ before recrystallisation from pyridine. The reduction of symmetry by having two ethanol and one water molecule within compound (**1**) instead of three pyridine leads to the crystallisation in a different space group, (**1**) crystallises in the monoclinic space group $P2_1/c$ in contrast to the compound reported by Sowrey et al., which crystallises in $P6_3/m$.

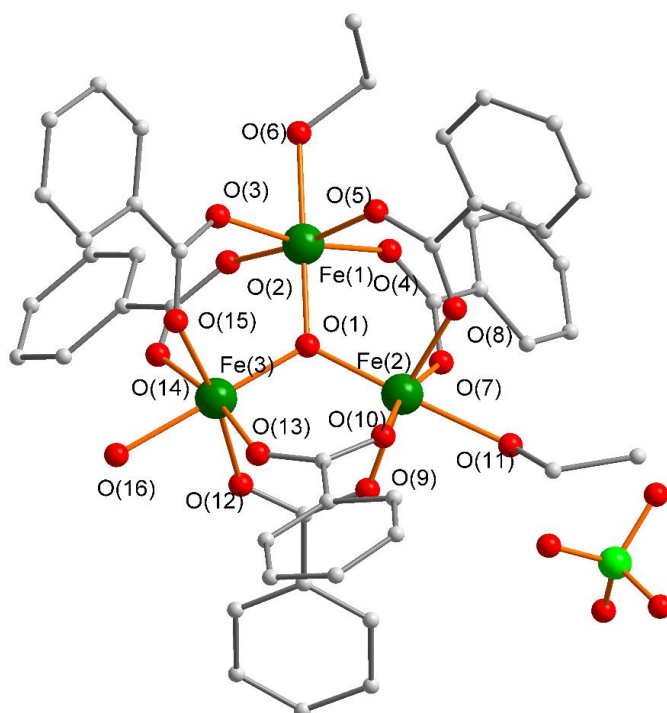


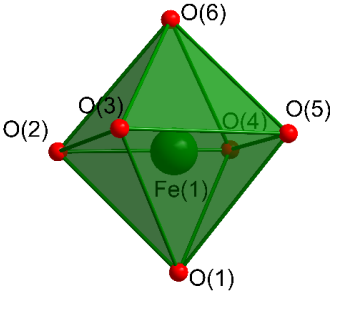
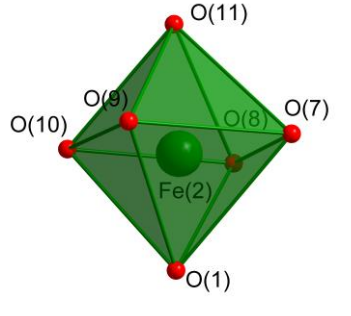
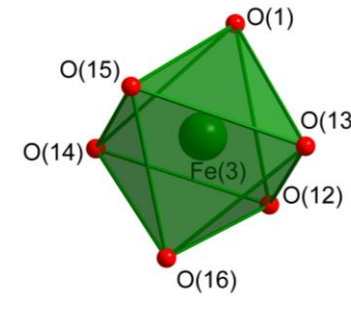
Figure 3.1-3 Molecular structure of $[\text{Fe}_3\text{O}(\text{O}_2\text{C-Ph})_6(\text{EtOH})_2(\text{H}_2\text{O})]\text{ClO}_4$ (**1**), H-atoms are omitted for clarity.

The core of (1) has three Fe^{III} ions bridged by a μ_3 -O²⁻ ion. Pairs of Fe ions forming the edges of the triangle are bridged by two benzoates. The coordination spheres of both Fe(1) and Fe(2) is completed by one terminal ethanol ligand, whereas the coordination sphere of Fe(3) is completed by a terminal water ligand. (see **Figure 3.1-3**) The bond lengths within the core vary slightly with (Fe(1)-O(1) = 1.901(4)Å, Fe(2)-O(1) = 1.890(4)Å, Fe(3)-O(1) = 1.905(5)Å) but are noticeably shorter than those to the terminal ligand oxygens (Fe(1)-O(6) = 2.072(4)Å, Fe(2)-O(11) = 2.111(5)Å, Fe(3)-O(16) = 2.064(5)Å). The Fe-O bond lengths to the bridging carboxylates fall in the range 2.004(4)Å to 2.022(5)Å. Due to the shorter Fe-O(1) bonds the octahedral coordination polyhedron is slightly distorted and this is seen from the distorted octahedral angles between the bridging μ_3 -O and the equatorial oxygen atoms (\angle O(1)-Fe(1)-Oeq = 94.7(2)°, \angle O(6)-Fe(1)-Oeq = 85.3(2)°, \angle O(1)-Fe(2)-Oeq = 95.5(1)°, \angle O(11)-Fe(2)-Oeq = 84.6(1)°, \angle O(1)-Fe(3)-Oeq = 94.9(2)°, \angle O(16)-Fe(3)-Oeq = 85.2(2)°) and can be further validated by a SHAPE^[78] analysis as well as the analysis of the deviation from a perfect 90° for the 12 cis angles of the octahedron. The analysis of the cis angles according to **Equation 3.1-1** is a commonly used procedure in spin-crossover compounds.^[79] (see **Table 3-1**)

$$\Sigma = \sum_i |90 - \angle O - Fe - O|_i$$

Equation 3.1-1 Formula used to calculate the sum of the deviation from a 90° octahedral cis angles.

Table 3-1 SHAPE analysis of the Fe^{III} coordination environment in (1), polyhedra drawn as they are oriented in the crystal structure, deviation factor from optimal octahedral coordination geometry (OC-6) and sum of the absolute values of the deviation from the 90° octahedral cis angles (Σ).

		
OC-6	OC-6	OC-6
0.126	0.219	0.139
Σ	Σ	Σ
51.1	41.4	45.9

The Fe^{III} ions are positioned in a nearly perfect equilateral triangle arrangement. (Fe(1)-Fe(2) = 3.285(1)Å, Fe(2)-Fe(3) = 3.298(1)Å, Fe(1)-Fe(3) = 3.281(1)Å, ∠Fe(2)-Fe(1)-Fe(3) = 60.29(3)°, ∠Fe(1)-Fe(2)-Fe(3) = 59.80(3)°, ∠Fe(2)-Fe(3)-Fe(1) = 59.92(3)°) Similar to the compound reported by Sowrey et al. the unit cell of (1) can be described in terms of the Fe₃O triangles alternating with the perchlorate anions. Interestingly the Fe₃O-triangles still show some π-π interactions between the benzoate rings, although the distance is just outside the generally accepted^[80-81] distance for traditional π-π stacking (3.707Å). (see **Figure 3.1-4**) For the compound reported in the literature the presence of solvent pyridine molecules enhances the interactions between the triangles.

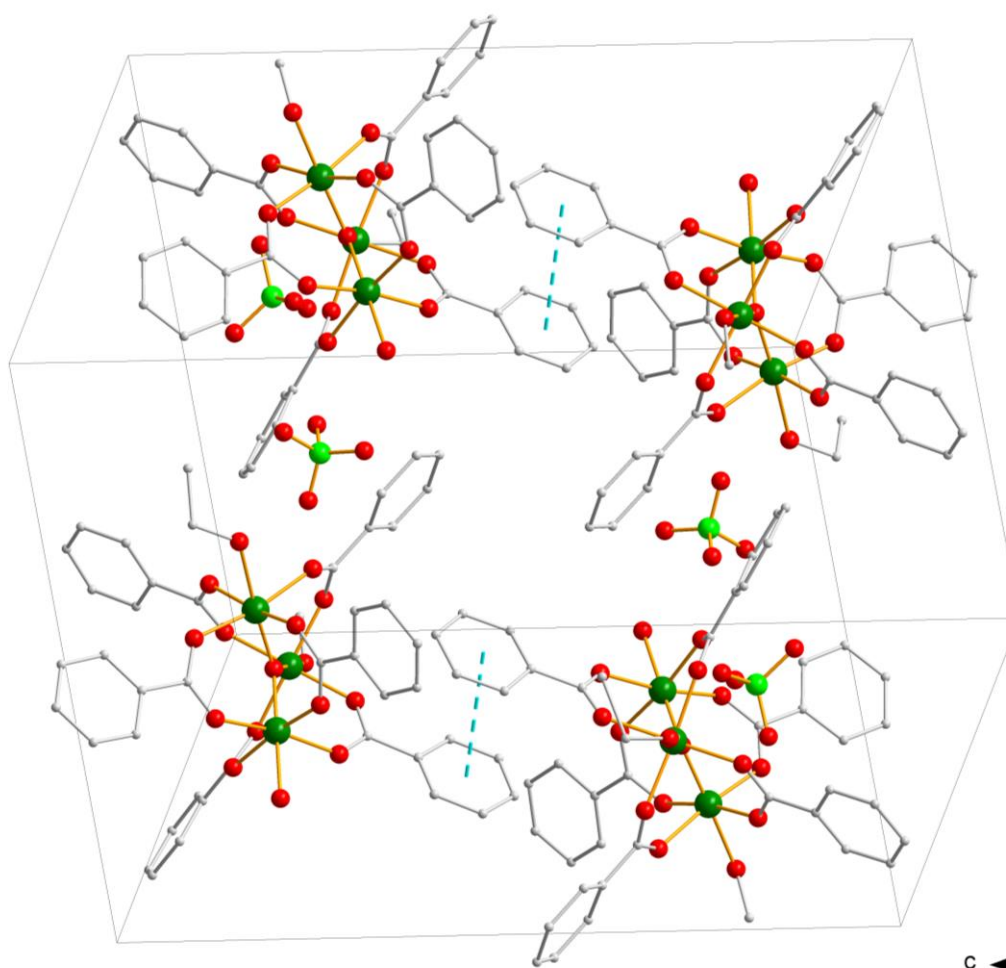


Figure 3.1-4 Unit cell of $[\text{Fe}_3\text{O}(\text{O}_2\text{C-Ph})_6(\text{EtOH})_2(\text{H}_2\text{O})]\text{ClO}_4$ (1), highlighted in turquoise is the distance between two benzoates (3.707Å) interacting via π-π stacking. H-atoms omitted for clarity.

As already mentioned, perchlorate salts can be highly explosive, therefore compound (1) was not investigated or used any further. In fact, the synthesis was adapted in attempts to obtain less dangerous products. Given the size of the core compound $[\text{Fe}_3\text{O}(\text{C}_2\text{O-Ph})_6(\text{L}_3)]^+$ the tetraphenylborate anion was chosen in an initial attempt. Unfortunately, the crystal data are of rather poor quality, so any bond lengths and angles should be treated with caution. Nonetheless, the use of a counteranion of similar size to the core compound in fact leads to a significantly bigger unit cell for compound (2) (7240.7 \AA^3) compared to compound (1) (5957.3 \AA^3). (see **Table 3-2**)

Table 3-2 Space groups and unit cell volume of compounds (1)-(4).

	space group	$V[\text{\AA}^3]$
(1) $[\text{Fe}_3\text{O}(\text{O}_2\text{C-Ph})_6(\text{EtOH})_2(\text{H}_2\text{O})]\text{ClO}_4$	$P2_1/c$	5957.3
(2) $[\text{Fe}_3\text{O}(\text{O}_2\text{C-Ph})_6(\text{EtOH})_2(\text{H}_2\text{O})]\text{BPh}_4$	$P2_1/c$	7240.7
(3) $[\text{Fe}_3\text{O}(\text{O}_2\text{C-}^t\text{But-Ph})_6(\text{py})_2\text{Cl}]$	$P4_1$	8461.8
(4) $\text{Fe}_3\text{O}(\text{O}_2\text{C-Ph})_5(\text{EtOH})_3\text{SO}_4$	$P2_1/c$	4850.2

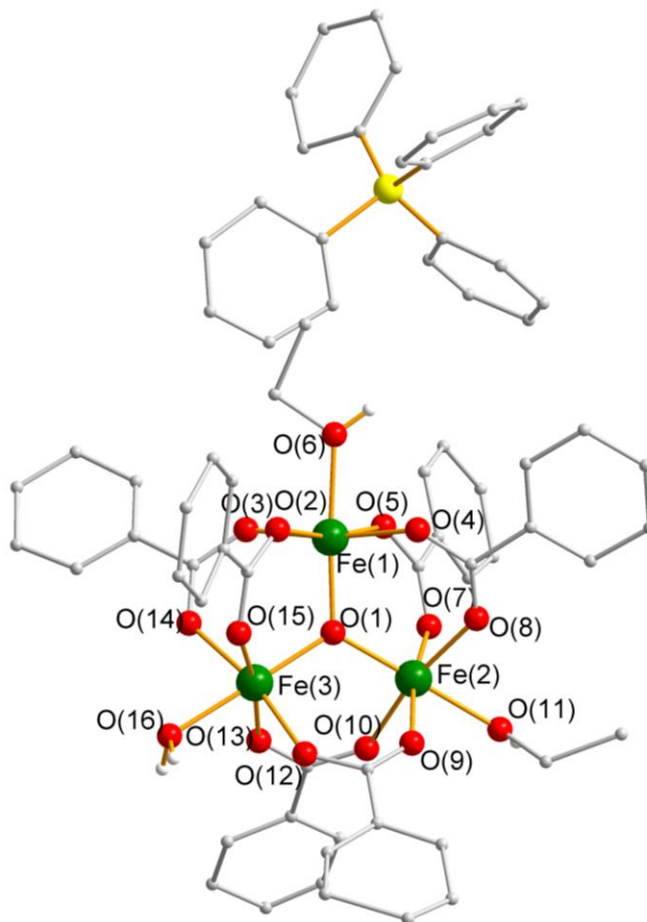
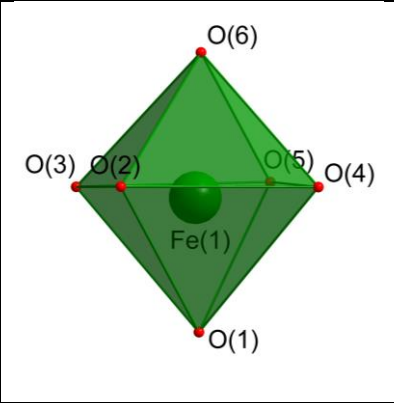
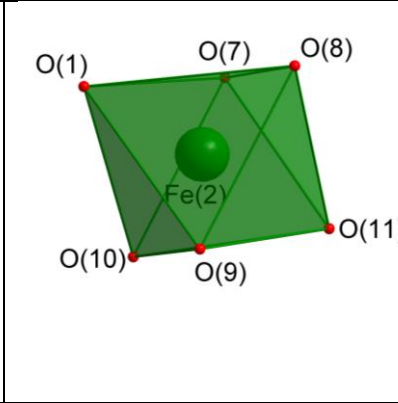
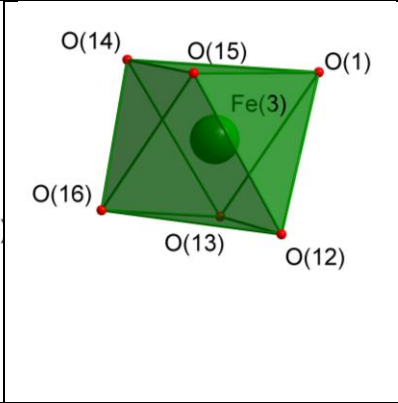


Figure 3.1-5 Molecular structure of $[\text{Fe}_3\text{O}(\text{O}_2\text{C-Ph})_6(\text{EtOH})_2(\text{H}_2\text{O})]\text{BPh}_4$ (2), organic H-atoms are omitted for clarity.

[Fe₃O(O₂C-Ph)₆(EtOH)₂(H₂O)]BPh₄ (**2**) crystallises in the monoclinic space group *P2₁/c* with the same basic core structure as (**1**) (see **Figure 3.1-5**). The bond lengths are comparable to (**1**) with Fe(1)-O(1) = 1.903(9)Å, Fe(2)-O(1) = 1.904(7)Å and Fe(3)-O(1) = 1.916(7)Å. The bond lengths between the metal ions of the core and the bridging carboxylate oxygens range from 1.933(11)Å-2.023(12)Å with the bond lengths to the terminal oxygens of the terminal ligands being elongated (2.046(9)-2.066(10)Å) similar to (**1**) The octahedral coordination geometry is distorted as expected, evidenced by the bonding angles (\angle O(1)-Fe(1)-Oeq = 94.3(4)°, \angle O(6)-Fe(1)-Oeq = 85.7(4)°, \angle O(1)-Fe(2)-Oeq = 95.9(4)°, \angle O(11)-Fe(2)-Oeq = 84.0(5)°, \angle O(1)-Fe(3)-Oeq = 95.1(4)°, \angle O(16)-Fe(3)-Oeq = 84.9(4)°), SHAPE analysis and the analysis of the 12 octahedral cis angles. (see **Figure 3.1-5**)

The shape of the triangle built up by the Fe^{III} ions is nearly identical to that of (**1**) showing a nearly perfect equilateral triangle. (Fe(1)-Fe(2) = 3.307(3)Å, Fe(2)-Fe(3) = 3.308(3)Å, Fe(1)-Fe(3) = 3.299(3)Å, \angle Fe(2)-Fe(1)-Fe(3) = 60.10(7)°, \angle Fe(1)-Fe(2)-Fe(3) = 59.84(6)°, \angle Fe(2)-Fe(3)-Fe(1) = 60.06(7)°)

Table 3-3 SHAPE analysis of the Fe^{III} coordination environment in (**2**), polyhedra are drawn as they are oriented in the crystal structure, deviation factor from optimal octahedral coordination geometry (OC-6) and sum of the absolute values of the deviation from the 90° octahedral cis angles (Σ).

		
OC-6	OC-6	OC-6
0.173	0.186	0.154
Σ	Σ	Σ
38.5	54.1	43.8

The incorporation of a counterion that is of a more similar size to the [Fe₃O(O₂C-Ph)₆(EtOH)₂(H₂O)]⁺ core leads to a more homogeneous packing pattern, although the

overall sequence of alternating core and anions is still present. Interestingly, in compound **(2)** there are also some π - π interactions present, albeit they are significantly longer (4.173Å) than the ones in **(1)**.

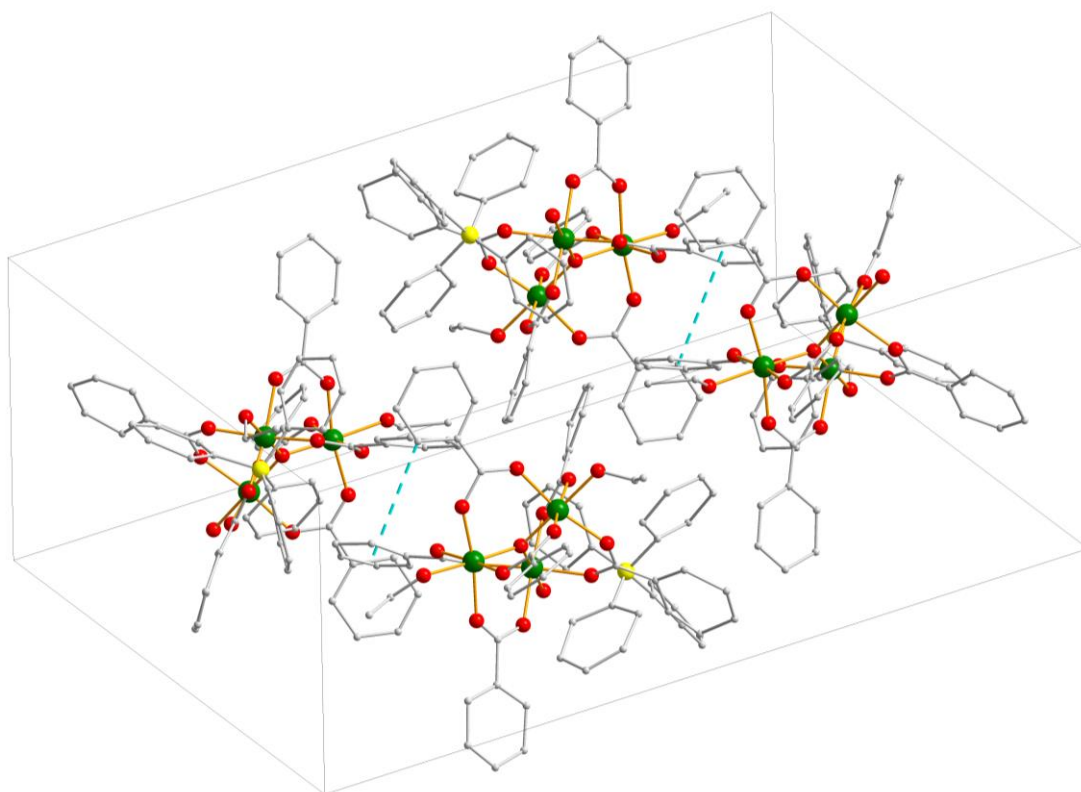


Figure 3.1-6 Unit cell of $[\text{Fe}_3\text{O}(\text{O}_2\text{C-Ph})_6(\text{EtOH})_2(\text{H}_2\text{O})]\text{BPh}_4$ (**2**), highlighted in turquoise is the distance between two benzoates (4.173Å) interacting via π - π stacking. H-atoms omitted for clarity.

The next approach concerning the variation of the counterion was to choose a different kind of counteranion. Thus, whereas for **(2)** the idea is to use a counteranion of roughly the same size as the triangular core, compound **(3)** uses a single chloride ion as a counterion. As is often the case for chemical synthesis the outcome of any given reaction does not always go as predicted. Compound **(3)** shows the same core structure of three Fe^{III} ions bridged by benzoic acid derivatives. The terminal ligands L in this compound are two pyridine molecules and the chloride ion, which thus does not act as a traditional counterion but rather as a ligand. This leads to a neutral complex for **(3)** without any need for a counterion. (see **Figure 3.1-7**)

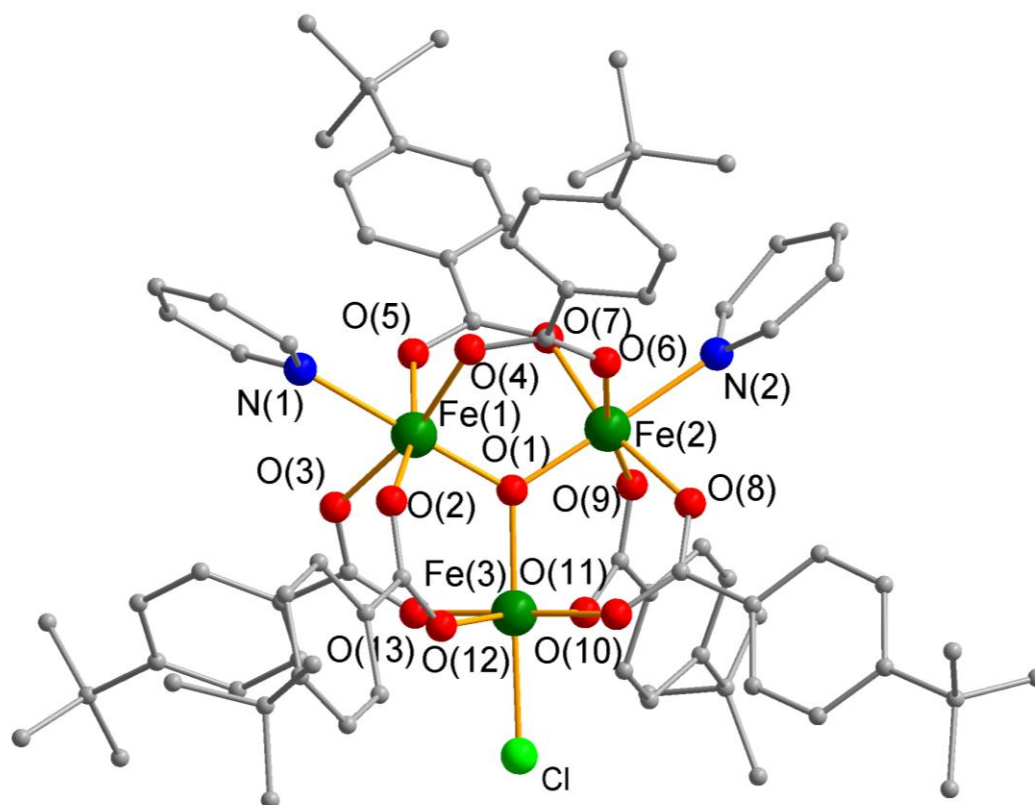
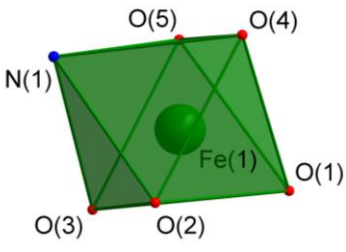
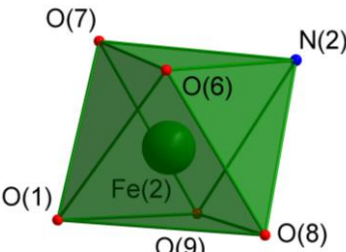
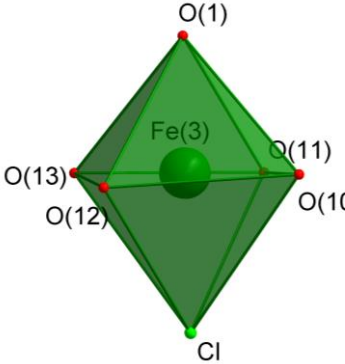


Figure 3.1-7 Molecular structure of $[\text{Fe}_3\text{O}(\text{O}_2\text{C-tBut-Ph})_6(\text{py})_2\text{Cl}]$ (**3**), organic H-atoms are omitted for clarity.

$[\text{Fe}_3\text{O}(\text{O}_2\text{C-tBut-Ph})_6(\text{py})_2\text{Cl}]$ (**3**) crystallises in the tetragonal space group $P4_1$ with the four triangles in the unit cell being more tightly packed compared to both (**1**) and (**2**). The unit cell volume is larger than for the previous examples (8461.8\AA^3) (see **Table 3-2**). The core triangular motif is significantly impacted by the coordination of the chloride ion, as seen in the for the iron coordinated by where the Fe(3)-O(1) bond length is significantly longer than those for Fe(1)-O(1) and Fe(2)-O(1). Here (Fe(1)-O(1) = $1.887(4)\text{\AA}$, Fe(2)-O(1) = $1.877(4)\text{\AA}$, whereas Fe(3)-O(1) = $1.978(4)\text{\AA}$. The bond lengths between the core Fe^{III} and bridging carboxylates are consistent with the previous compounds, ranging from $1.985(4)\text{\AA}$ - $2.043(4)\text{\AA}$. As expected the bond lengths of the terminal pyridine ligands are elongated (Fe(1)-N(1) = $2.199(5)\text{\AA}$, Fe(2)-N(2) = $2.176(5)\text{\AA}$). The bond length of the coordinated terminal chloride is the longest (Fe(3)-Cl = $2.303(3)$), which is slightly longer than a usual Fe^{III} -Cl bond found for example in FeCl_3 (2.27\AA). As expected, the octahedral coordination geometry is once again distorted as seen in the bond angles ($\angle\text{O}(1)\text{-Fe}(1)\text{-Oeq} = 96.4(2)^\circ$, $\angle\text{N}(1)\text{-Fe}(1)\text{-Oeq} = 83.6(2)^\circ$, $\angle\text{O}(1)\text{-Fe}(2)\text{-Oeq} = 96.1(2)^\circ$, $\angle\text{N}(2)\text{-Fe}(2)\text{-Oeq} = 83.9(2)^\circ$,

$\angle O(1)-Fe(3)-O_{eq} = 91.6(2)^\circ$, $\angle Cl-Fe(3)-O_{eq} = 88.4(2)^\circ$) and can be further validated by a SHAPE^[78] analysis, as well as the analysis of the octahedral cis angles. Interestingly, the elongated Fe-Cl bond leads to a less distorted octahedral angle at Fe(3), but the overall geometry is still a less ideal octahedron compared to (1) and (2) (see **Table 3-4**). The coordination of the chloride ion is also reflected in the shape of the triangle built up by the three Fe^{III} ions, the adjacent distances of Fe(3) are slightly elongated (Fe(1)-(Fe(2) = 3.259(1)Å, Fe(2)-Fe(3) = 3.351(1)Å, Fe(1)-Fe(3) = 3.336(1)Å) and the interior triangle angle at Fe(3) is more acute than those at Fe(1) and Fe(2). ($\angle Fe(2)-Fe(1)-Fe(3) = 61.06(3)^\circ$, $\angle Fe(1)-Fe(2)-Fe(3) = 60.60(2)^\circ$, $\angle Fe(2)-Fe(3)-Fe(1) = 58.34(2)^\circ$)

Table 3-4 SHAPE analysis of the Fe^{III} coordination environment in (3), polyhedra are drawn as they are oriented in the crystal structure, deviation factor from optimal octahedral coordination geometry (OC-6) and sum of the absolute values of the deviation from the 90° octahedral cis angles (Σ).

		
OC-6	OC-6	OC-6
0.200	0.212	0.242
Σ	Σ	Σ
57.5	57.5	19.6

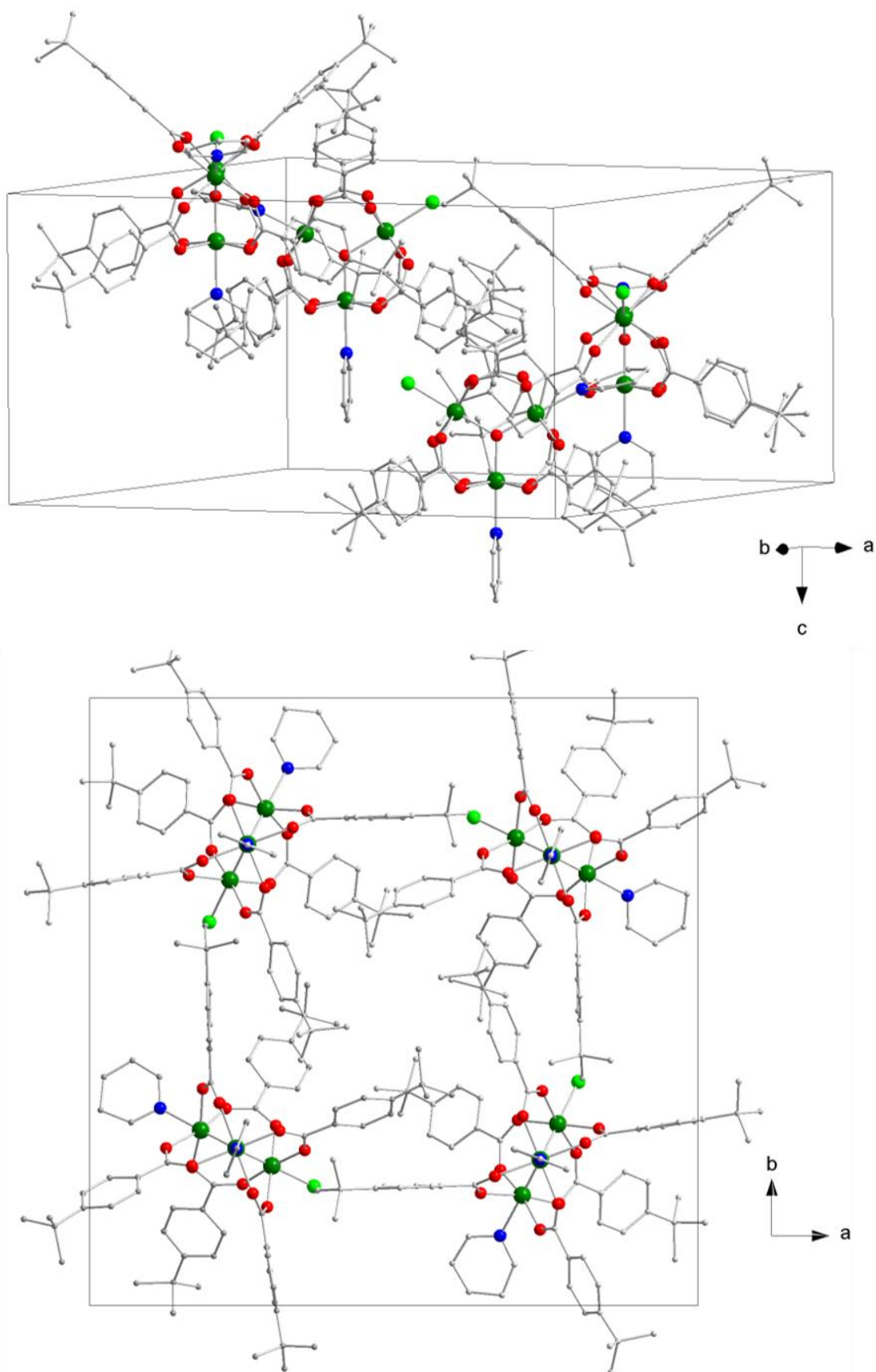


Figure 3.1-8 Unit cell of [Fe₃O(O₂C-*t*-But-Ph)₆(Py)₂Cl] (**3**) (visual representation and view along the c-axis highlighting the 4₁ symmetry). H-atoms omitted for clarity.

It seems that despite the fact that no space is required to accommodate a counterion, the combination of pyridine terminal ligands and the bulkier *p*-^tbutyl benzoic acid used leads to the core triangles being further apart in **(3)** compared to the previous examples. Also, there are no π - π interactions falling within the commonly accepted limits to be observed. It is interesting to note that the question concerning the origin of this particular structural element remains, as it is unclear if the interactions between phenyl groups leads to the 4_1 screw axis or if the presence of the screw axis in the crystal packing aligns the phenyl groups to be stacked that way. However, the unit cell of **(3)** nicely shows the 4-fold screw axis present in the $P4_1$ space group visible by the triangles being rotated by 90° relative to each other and located along the *c*-axis. (as can be seen in **Figure 3.1-8**)

Due to the different coordination environments for the Fe^{III} centres, this compound represents an interesting candidate for further investigation of its electronic properties. The magnetic coupling between the Fe^{III} centres is probably affected by the coordination of a chloride ion. Unfortunately, it was not possible to conduct magnetic characterisation on **(3)** because of instrumental restrictions.

After the success with coordinating a much smaller anion to the triangular core a different approach was investigated. This time instead of changing the size of the anion the idea was to change the charge by using a sulfate anion and see if it would be possible to co-crystallise two clusters with one anion. Surprisingly, the resulting compound was yet another structural type. This time one of the bridging benzoates was replaced by the sulfate ion, yet again resulting in a neutral complex. (see **Figure 3.1-9**) The possibility of other bidentate ligands coordinating to this triangular arrangement has been reported by Giacobazzo et al. describing Maus' salt $\text{K}_5[\text{Fe}_3\text{O}(\text{SO}_4)_6(\text{H}_2\text{O})_3]$ which can be crystallised from partially basified iron sulfate solutions^[82] as well as the naturally occurring mineral metavoltine investigated by Scordari et al.^[83]

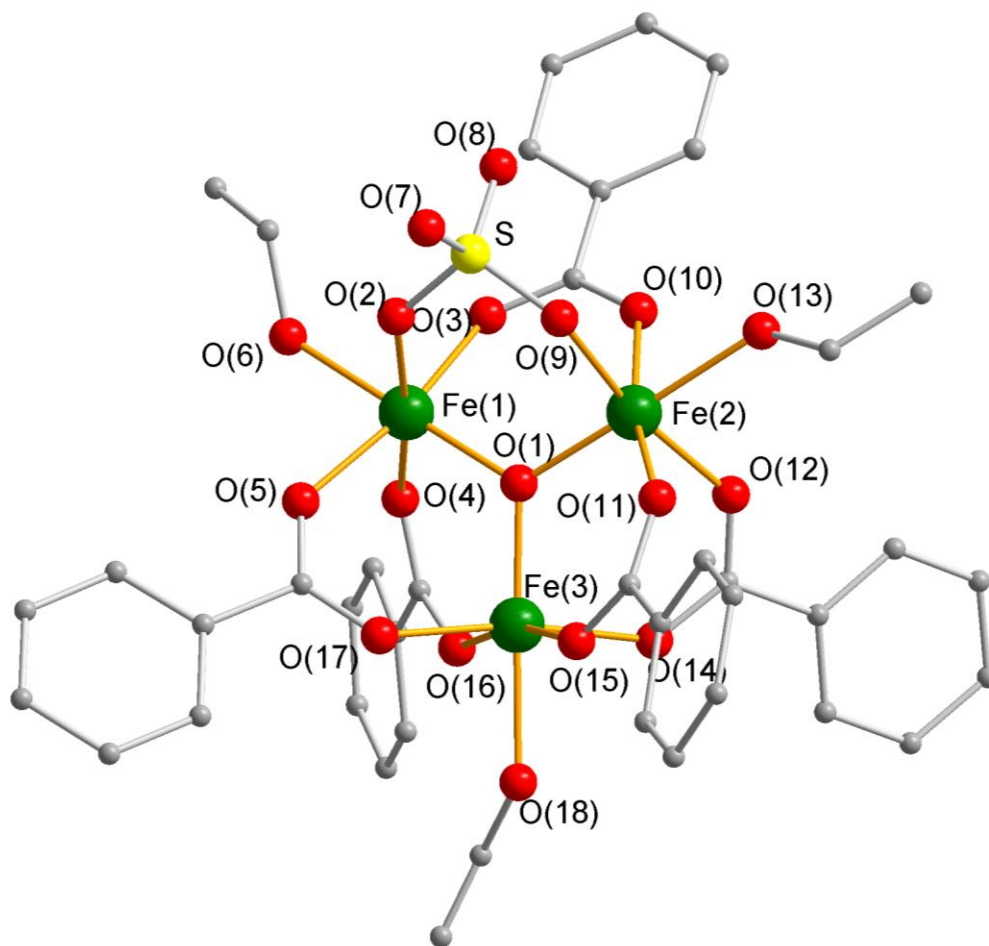
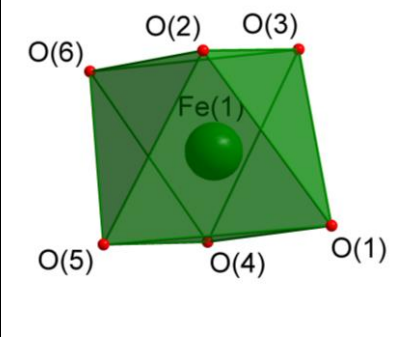
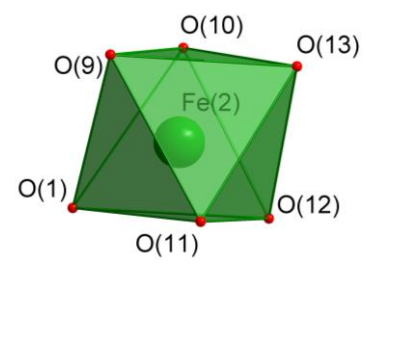
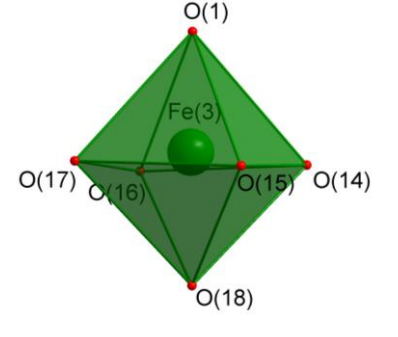


Figure 3.1-9 The molecular structure of $[\text{Fe}_3\text{O}(\text{O}_2\text{C-Ph})_5(\text{EtOH})_3\text{SO}_4]$ (**4**), organic H-atoms are omitted for clarity.

$[\text{Fe}_3\text{O}(\text{O}_2\text{C-Ph})_5(\text{EtOH})_3\text{SO}_4]$ (**4**) crystallises in the monoclinic space group $P2_1/c$ showing the same basic core structure as the triangles presented so far. One of the bridging benzoates between Fe(1) and Fe(2) is replaced by a sulfate ion, resulting in a neutral complex because in addition to the usual negative charge of the benzoate the doubly negatively charged sulfate compensates the charge of the bridging carboxylate plus counteranion charge. The terminal ligands L are provided by three ethanols giving the complex the expected trimeric look. The bond lengths between the Fe^{III} and the central μ_3 -oxygen are very similar to those in (**1**) although it is notable that the Fe(1)-O(1) and Fe(2)-O(1) bonds are both longer than the Fe(3)-O(1) bond, resulting from the coordination of the sulfate ion (Fe(1)-O(1) = 1.924(2)Å, Fe(2)-O(1) = 1.913(2)Å and Fe(3)-O(1) = 1.899(2)Å). Surprisingly, the different Fe-O(1) bond lengths are not reflected in the Fe-O_L bond lengths of the terminal ethanol ligands

(Fe(1)-O(6) = 2.057(2)Å, Fe(2)-O(13) = 2.113(3)Å, Fe(3)-O(18) = 2.104(2)Å). The bond lengths of the bridging carboxylates (Fe-O_{Ph}) are in line with previous measurements and the sulfate bridged bond lengths are within the same order as well (Fe-O_{Ph} = 1.983(2)Å-2.037(2)Å, Fe(1)-O(2) = 2.007(2)Å, Fe(2)-O(9) = 1.996(2)Å). The only noticeable effect of the coordination of the sulfate ion is reflected in the Fe-Fe distances. The distance between the two irons linked by the sulfate, Fe(1) and Fe(2), is significantly longer (Fe(1)-Fe(2) = 3.336(6)Å) than those for Fe(3) and Fe(1) (Fe(3)-Fe(1) = 3.303(6)Å) and Fe(3) and Fe(2) (Fe(3)-Fe(2) = 3.295(6)Å), respectively. The octahedral coordination geometry of the Fe's and in fact the bond angles are very similar to those found within (1) and (2) ($\angle O(1)-Fe(1)-O_{eq} = 95.0^\circ$, $\angle O(6)-Fe(1)-O_{eq} = 85.0^\circ$, $\angle O(1)-Fe(2)-O_{eq} = 95.9^\circ$, $\angle O(13)-Fe(2)-O_{eq} = 84.1^\circ$, $\angle O(1)-Fe(3)-O_{eq} = 96.1^\circ$, $\angle O(18)-Fe(3)-O_{eq} = 83.9^\circ$). This observation is confirmed by the SHAPE analysis and investigation of the octahedral cis angles, highlighting a stronger deviation from the ideal coordination geometry for Fe(2) and Fe(3) that can be rationalised as arising from the disorder of the terminal ethanol ligand. The Fe₃ triangle is slightly more isosceles shaped because of the elongated Fe(1)-Fe(2) distance of 3.336(06)Å (Fe(1)-Fe(3) = 3.303(06)Å, Fe(2)-Fe(3) = 3.295(06)Å) and this is also reflected in the interior triangle angles. ($\angle Fe(2)-Fe(1)-Fe(3) = 59.51(1)^\circ$, $\angle Fe(1)-Fe(2)-Fe(3) = 59.74(1)^\circ$, $\angle Fe(2)-Fe(3)-Fe(1) = 60.75(1)^\circ$)

Table 3-5 SHAPE analysis of the Fe^{III} coordination environment in (4), polyhedra are drawn as they are oriented in the crystal structure, deviation factor from optimal octahedral coordination geometry (OC-6) and sum of the absolute values of the deviation from the 90° octahedral cis angles (Σ).

		
OC-6	OC-6	OC-6
0.181	0.223	0.245
Σ	Σ	Σ
48.3	52.9	52.7

In this case the packing diagram nicely illustrates the effect having incorporated the charge-balancing sulfate ion into the core structure as had been originally expected for (3). Compared to the complexes discussed earlier, compound (4) shows a drastically reduced volume of the unit cell of 4850.2\AA^3 compared to 5957.3\AA^3 for (1), 7240.7\AA^3 for (2) and 8461.8\AA^3 for (3) respectively (see **Table 3-2**). Despite this there are no obvious π - π interactions present, although the closest C-C contact in the unit cell is just above 4\AA .

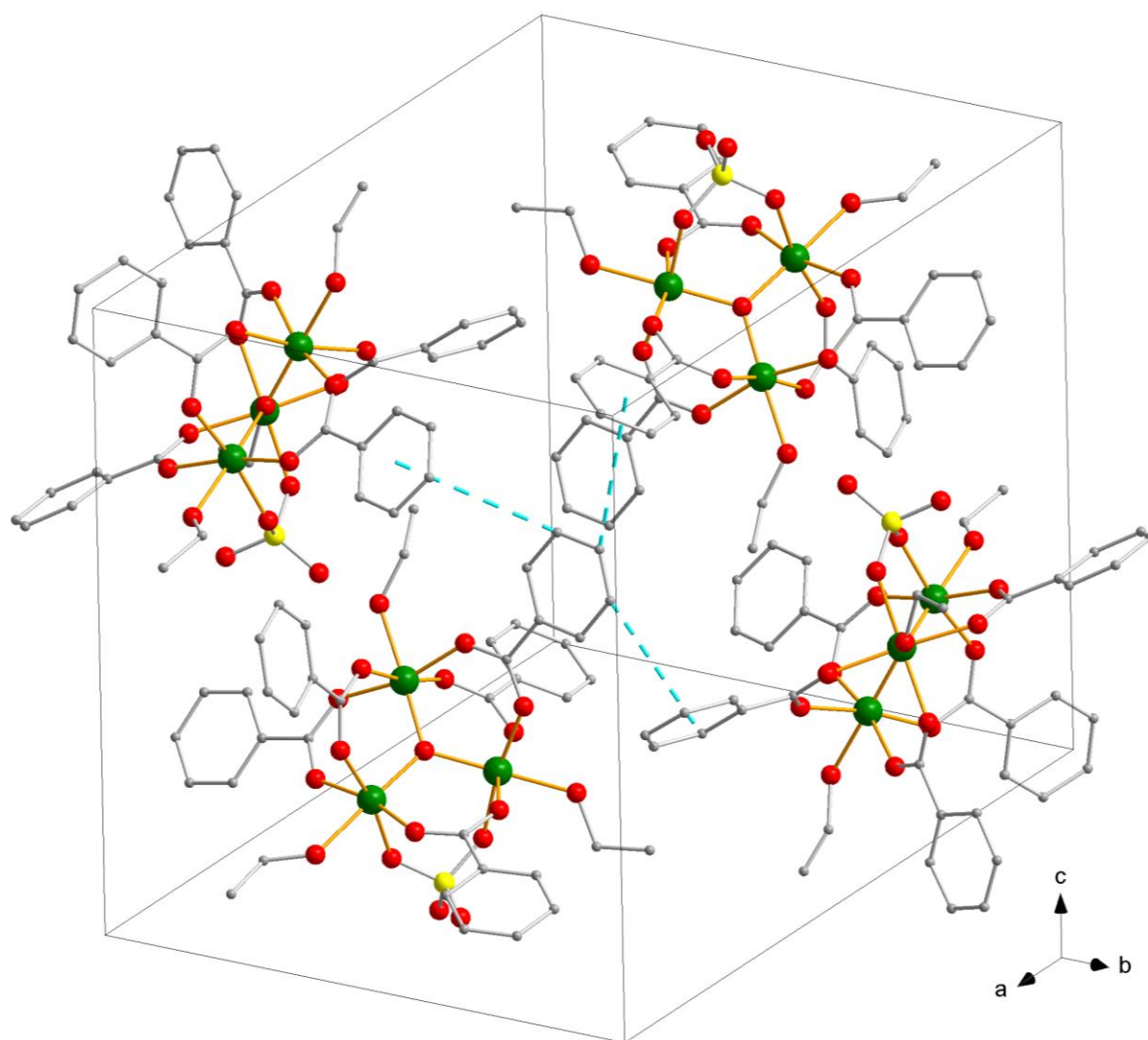


Figure 3.1-10 The unit cell of $[\text{Fe}_3\text{O}(\text{O}_2\text{C-Ph})_5(\text{EtOH})_3\text{SO}_4]$ (4), shown in turquoise are the closest C-C distances between the complexes (4.116\AA - 4.490\AA) H-atoms omitted for clarity.

This unique coordination paired with the densely packed complexes and good quality of the crystalline material makes this compound a rather intriguing candidate for investigations of its magnetic properties.

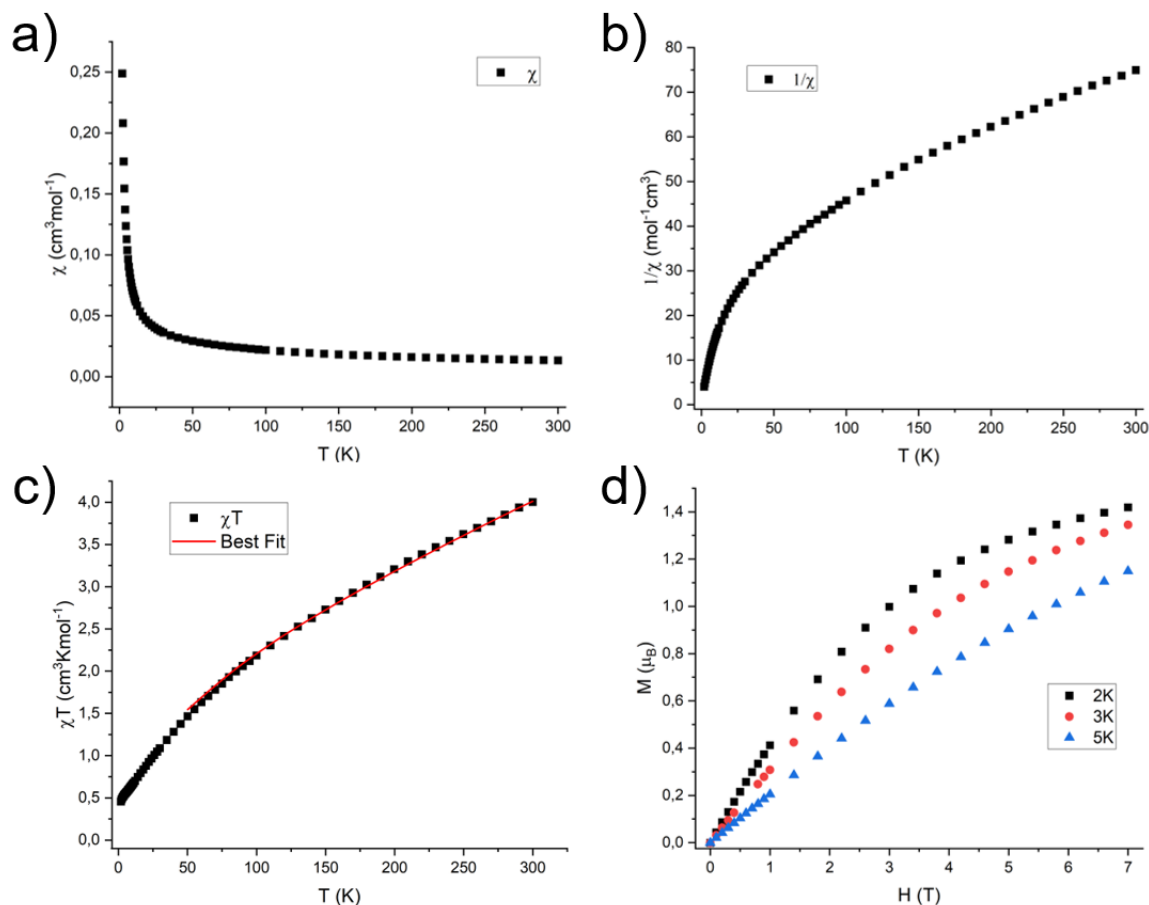


Figure 3.1-11 Magnetic data of $[\text{Fe}_3\text{O}(\text{O}_2\text{C-Ph})_5(\text{EtOH})_3\text{SO}_4]$ (**4**): χ vs T plot (a), χ^{-1} vs T plot (b), χT vs T (c) measured at 1000Oe with the best fit for χT discussed in the text shown as a red line and M vs H measured at 2, 3 and 5K (d).

The variable temperature dependence of the molar susceptibility for $[\text{Fe}_3\text{O}(\text{O}_2\text{C-Ph})_5(\text{EtOH})_3\text{SO}_4]$ (**4**) was measured at 1000Oe in the range from 1.8-300K. The steady decrease of the χT product of (**4**) from 300K down to 2K indicates dominant antiferromagnet interactions (**Figure 3.1-11 c**). The χT product at 300K is 4.00 $\text{cm}^3\text{K/mol}$ which is a lot lower than the theoretical value for three non-interacting $S=5/2$ Fe (12.73 $\text{cm}^3\text{K/mol}$) but only slightly below the theoretical value for an overall spin equal to one $S=5/2$ high-spin Fe^{III} (4.25 $\text{cm}^3\text{K/mol}$, $g=1.97$). Upon lowering the temperature, the χT value decreases to 0.46 $\text{cm}^3\text{K/mol}$ at 1.8K which is slightly higher than the minimum expected value for one low-spin Fe^{III} (0.36 $\text{cm}^3\text{K/mol}$) suggesting a rather complex magnetic behaviour of the compound. The removal of symmetry due to the replacement of one benzoate by a sulfate was thought to remove some of the degeneracy of energy levels and in turn simplify the magnetic behaviour. Comparing the χT values of (**4**) to that reported for

[Fe₃O(O₂C-Ph)₆(py)₃]ClO₄·py by Georgopoulou et al.^[59] reveals that they are indeed different. The reported data show a much steeper decline over the 2-300K temperature range from 4.97 cm³K/mol at 300K to 0.26 cm³K/mol at 2K, 0.2 cm³K/mol lower than the experimental value for (4). The authors suggest that this is due to possible antisymmetric exchange interactions, this is supported by EPR data that suggests multiple highly axial anisotropic S=1/2 species.

Fits based on the Hamiltonian for the exchange interactions given in

Equation 3.1-2 were carried out in the 50-300K temperature range using the PHI software.^[84] Below 50K the fit diverges noticeably, indicating a much more complex situation.

Using two coupling constants is usually the case for these basic carboxylates, even when a symmetrical substitution is present. This approach makes even more sense for compound (4), as the exchange coupling between the two Fe^{III} bridged by the sulfate is going to be heavily changed, given the different coordination environments.

$$\hat{H}_{EX} = -2 \cdot J_1 \cdot (S_1 S_2 + S_1 S_3) - 2 \cdot J_2 \cdot (S_2 S_3)$$

Equation 3.1-2 The Hamiltonian used to calculate the exchange coupling in (4).

The fitting yielded two vastly different coupling constants ($J_1 = 26.2\text{cm}^{-1}$, $J_2 = 43.9\text{cm}^{-1}$), one of the calculated coupling constants is fairly similar to those reported by Georgopoulou et al.^[59] ($J_1 = -22.9\text{cm}^{-1}$, $J_2 = 19.1\text{cm}^{-1}$) while the second one is nearly twice as big. The stronger exchange coupling constant is attributed to the interaction between Fe(1) and Fe(2).

Further EPR studies on (4) would provide valuable information of the electronic properties. If it is possible to further reduce the degeneracy of the ground state this type of compound could be very interesting for quantum computing. The DiVincenzo criteria^[85] represent some of the properties a quantum bit should possess, for example a well-defined ground state and scalability of the system. If [Fe₃O(O₂C-Ph)₅(EtOH)₃SO₄] can check more of the boxes, for example showing satisfactory coherence times, then it would be a fascinating candidate for further investigations.

This is especially true because of the magnetic relaxation that is described for $[\text{Fe}_3\text{O}(\text{O}_2\text{C-Ph})_6(\text{py})_3]\text{ClO}_4\cdot\text{py}$ by Georgopoulou et al.^[59]

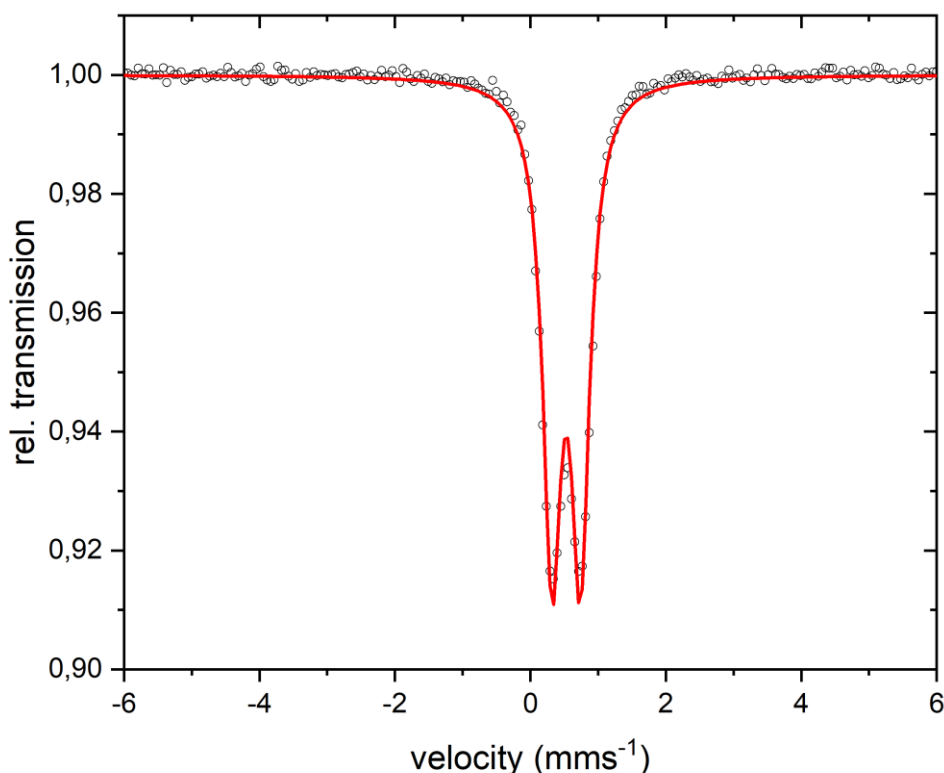


Figure 3.1-12 Mössbauer spectrum of $[\text{Fe}_3\text{O}(\text{O}_2\text{C-Ph})_5(\text{EtOH})_3\text{SO}_4]$ (**4**) measured at 77 K. The solid line is the result of a least square analysis with parameters isomer shift $\delta = 0.53 \text{ mms}^{-1}$, quadrupole splitting $\Delta E_Q = 0.42 \text{ mms}^{-1}$ and a line width of $\Gamma = 0.33 \text{ mms}^{-1}$. The experimental error of δ , ΔE_Q and Γ is $\pm 0.02 \text{ mms}^{-1}$.

Figure 3.1-12 shows the ^{57}Fe Mössbauer spectrum of (**4**) measured at 77K. The isomer shift directly determines the energy density at the Fe nucleus and therefore directly shows the bonding properties. The measured value of $\delta = 0.53 \text{ mms}^{-1}$ is very typical for a high-spin Fe^{III} .^[29, 86]

According to a 2010 study of the Mössbauer spectra of various Fe_3O carboxylates by Georgopoulou et al.^[87] the quadrupole splitting strongly depends on the nature of the bridging carboxylate in the complex, the value found for (**4**) ($\Delta E_Q = 0.42 \text{ mms}^{-1}$) is very close to that found for a purely benzoate bridged compound ($\Delta E_Q = 0.40 \text{ mms}^{-1}$)

These results seem to suggest that there is barely any measurable impact of replacing a benzoate by the dianionic sulfate at the measured temperature of 77K. Additional measurements, most interestingly below 50K could give greater insight into

the electronic structure, especially since the magnetic susceptibility measurements suggest a more complex behaviour below 50K.

Given that we can put an anion in the neutral terminal position L (**3**), use a bridging dianion ligand in place of the monoanionic carboxylate (**4**) to produce a neutral cluster, rather than needing a counteranionic species and that naphthalimides could provide either of these functions we explored N-(p-aminobenzenesulfonate)-1,8-naphthalimide (naph) in this system. Since changing the counterion seems to be a legitimate strategy to change the packing of the complexes and therefore potentially manipulating their magnetic properties a more exotic approach was chosen. As could be seen for compounds (**1**) and (**2**) the core complexes tend to exhibit π - π interactions. Therefore, the natural next step is to incorporate structure-directing counterions, as has been investigated by Carter et al.^[88] In this approach N-substituted 1,8-naphthalimide based counterions are used since they are known for their ability to form strong π - π stacking structures.

The poor solubility of the counterions means that the synthesis had to be adapted significantly, but this unfortunately led to the decomposition of the triangular core structure.

The preformed trinuclear $[\text{Fe}_3\text{O}(\text{O}_2\text{C-Ph})_6(\text{H}_2\text{O})_3]\text{NO}_3$ and N-(p-aminobenzenesulfonate)-1,8-naphthalimide are dissolved in a mixture of 20ml MeOH and 5ml DMF, afterwards the reaction mixture is stirred at 90°C for 2h. After cooling down the solution is filtered and left for crystallisation.

Due to the poor quality of the structural data the evaluation of bond lengths and angles is inherently flawed, for this reason any bond lengths and angles are reported with one decimal place since the reported errors are also within this order of magnitude. For the sake of consistency, a discussion of the structural data is attempted nonetheless.

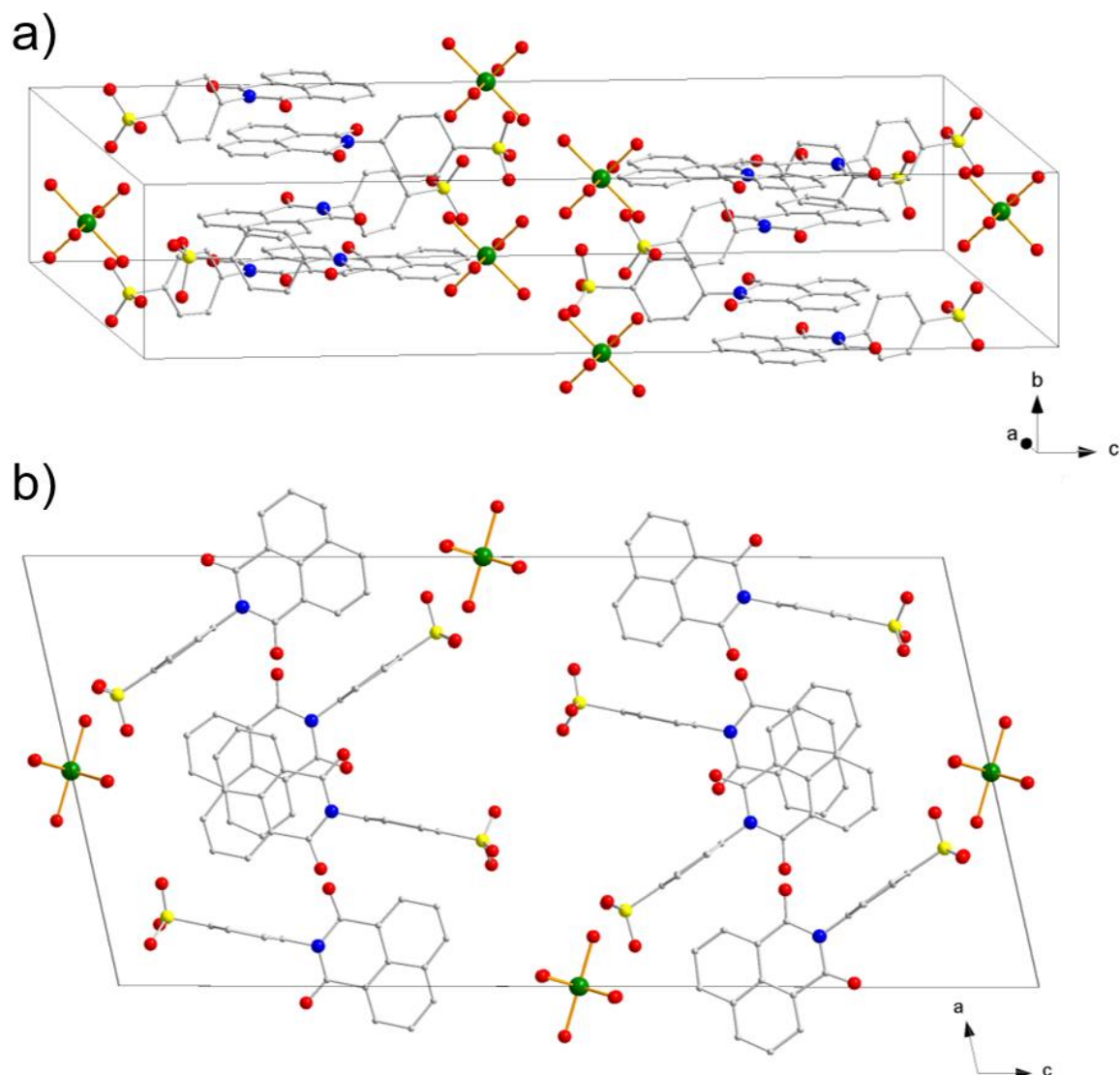


Figure 3.1-13 Visual representation (a) of the unit cell of $[\text{Fe}(\text{H}_2\text{O})_6](\text{naph})_3$ (**5**) and view along the b-axis (b) highlighting the π -stacking effect of the N-(p-aminobenzenesulfonate)-1,8-naphthalimide anions, organic H-atoms omitted for clarity.

$[\text{Fe}(\text{H}_2\text{O})_6](\text{naph})_3$ (**5**) crystallises in the monoclinic space group $P2_1/n$. The crystal structure consists of octahedrally coordinated $[\text{Fe}(\text{H}_2\text{O})_6]^{3+}$ units, interlaced by π - π -stacking N-(p-aminobenzenesulfonate)-1,8-naphthalimide anions. Each $[\text{Fe}(\text{H}_2\text{O})_6]^{3+}$ moiety has the charge balanced by three naph^- anions, which are stacked with a 47.2° angle between them (see **Figure 3.1-14**). This gives the compound a nicely layered structure. The π - π distances between two naph^- anions are well within the usual π - π stacking range (3.5 - 3.6\AA). (see **Figure 3.1-15**)

The $[\text{Fe}(\text{H}_2\text{O})_6]^{3+}$ complexes are rather symmetric as a result of the simple hexa-aqua coordination environment and the fact that the complex lies on a mirror plane on the

unit cell edge with half the molecule inside. This symmetry naturally leads to only three unique Fe-O bond lengths ($\text{Fe}(1)\text{-O}(1) = 2.0(1)\text{\AA}$, $\text{Fe}(1)\text{-O}(2) = 2.1(2)\text{\AA}$, $\text{Fe}(1)\text{-O}(3) = 2.1(2)\text{\AA}$) with a near perfect octahedral coordination geometry due to the symmetry generation, as is highlighted by the SHAPE analysis and investigation of the twelve cis angles generated from the Fe-O angles. ($\angle\text{O}(1)\text{-Fe}(1)\text{-O}(2) = 90.6(6)^\circ$, $\angle\text{O}(1)\text{-Fe}(1)\text{-O}(3) = 88.6(6)^\circ$, $\angle\text{O}(2)\text{-Fe}(2)\text{-O}(3) = 89.7(7)^\circ$ (see **Table 3-6**)

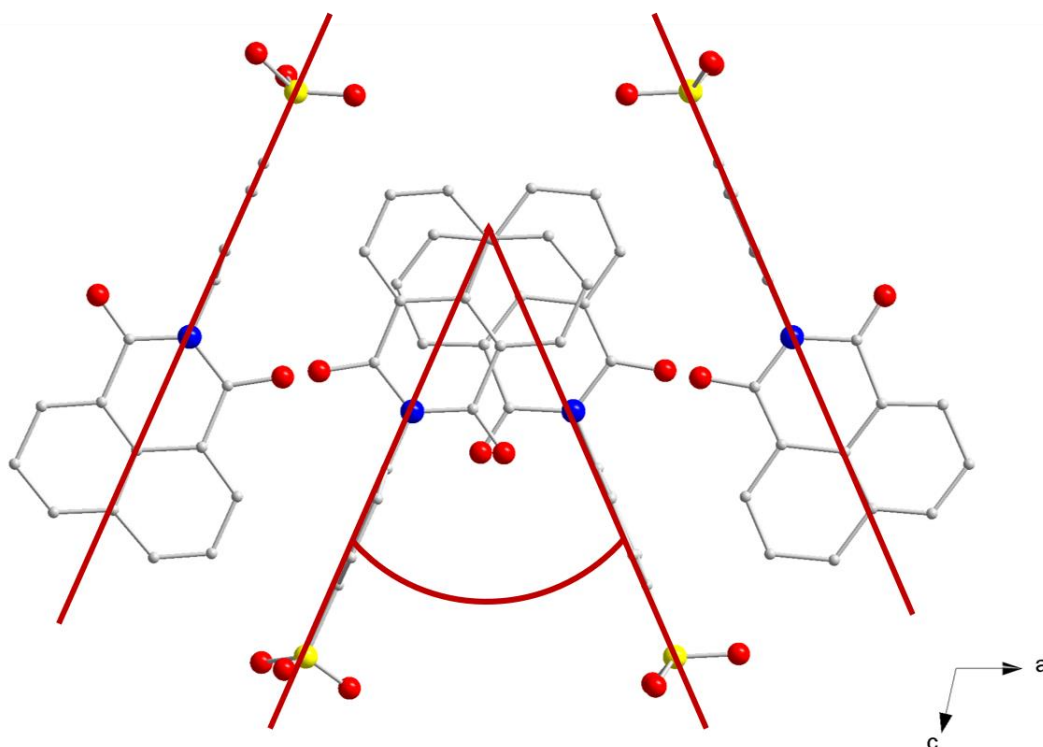


Figure 3.1-14 Cutout of the structure of **(5)** highlighted in red is the angle between the stacked N-(p-aminobenzenesulfonate)-1,8-naphthalimide anions.

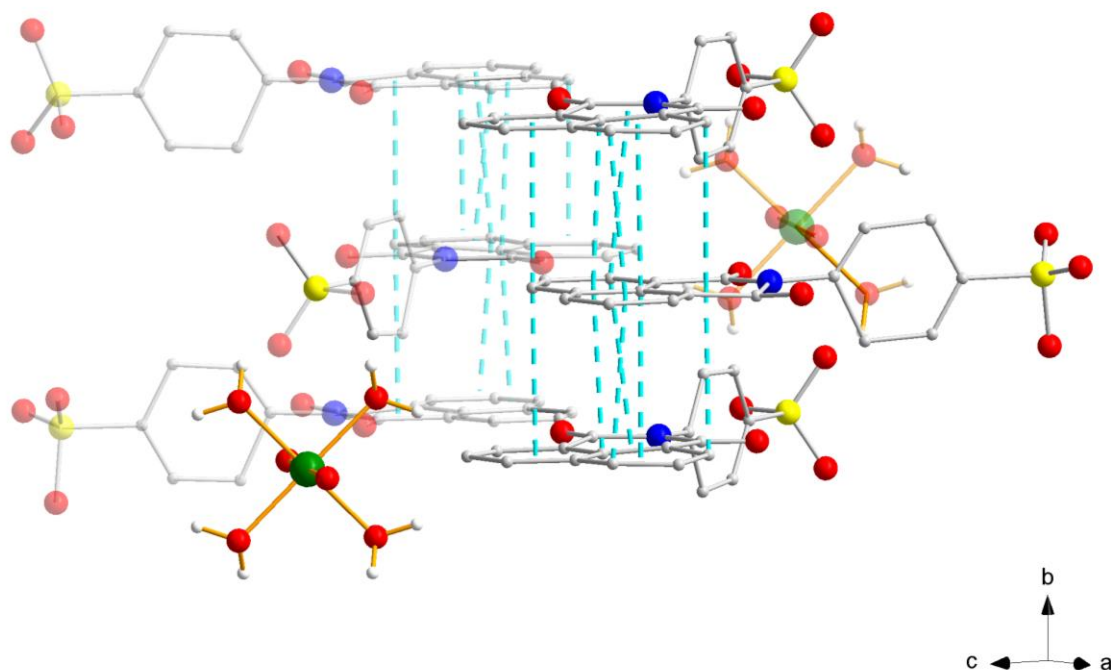


Figure 3.1-15 Cutout of one $[\text{Fe}(\text{H}_2\text{O})_6](\text{naph})_3$ moiety, π - π stacking highlighted in turquoise, the distances between π systems is well within the commonly accepted values (3.5 - 3.6\AA), organic H atoms omitted for clarity.

Table 3-6 SHAPE analysis of the Fe^{III} coordination environment in (5), polyhedra are drawn as they are oriented in the crystal structure, deviation factor from optimal octahedral coordination geometry (OC-6) and sum of the absolute values of the deviation from the 90° octahedral cis angles (Σ).

OC-6
0.039
Σ
8.7

The fact that compound (5) shows the desired structure-directing properties of the naphthalimide anions proves that this is indeed a valuable approach, even though the triangular core complex dissociated in the process of the synthesis. This prompts further investigations into this synthesis method with potential applications to put magnetically relevant molecules onto surfaces using the strong π - π stacking properties of the anions.

Although the resulting compound was not the desired result it is of great fundamental value to investigate the magnetic properties of single Fe^{III} complexes. This is due to the fact that although Fe^{III} adopts a high-spin configuration in most compounds it shows strong zero-field splitting effects and potentially strong axial anisotropy as was discussed for compound (4). This helps make iron an ideal candidate for use in the synthesis of single molecule magnets, making it the second most important 3d metal ion after Mn^{3+} when taking into consideration the number of publications and variety of compounds reported.

Furthermore, the fact that iron is the most abundant transition metal in earth's crust^[89] makes it very accessible and a clearly more eco-friendly option for use in magnetic and electronic devices compared to lithium, manganese and rare earths.

Finally, the possibility to carry out ^{57}Fe Mößbauer studies to investigate oxidation states, electronic and magnetic behaviour under applied fields on a very fast time scale gives a useful method gain valuable insights into relaxation processes.

3.1.3 Variations for the basic carboxylates $[\text{M}_3\text{O}(\text{O}_2\text{C-R})_6\text{L}_3]\text{X}$ (M = Cr, Mn, Fe, Co, Ni)

Since the literature suggests that these triangular complexes can be synthesised with a variable assortment of different transition metals this was an obvious avenue to pursue. The prospect of being able to use synthesised triangles as a vector to introduce varying transition metals into bigger clusters is very intriguing. A systematic synthetic approach was chosen: Most trivalent transition metals react in a similar way as iron when subjecting them to the same reaction procedure as was chosen for compound (1), but isolating the intermediate product formed in the synthesis of the triangle described by Sowrey et al.^[58] This approach rarely produces single crystals

suitable for X-ray diffraction, but the microcrystalline powders obtained can be used as starting materials for further reactions.

$MCl_3 \cdot xH_2O$ (M= Cr, Fe), $M(NO_3)_3 \cdot xH_2O$ (M= Cr, Fe), $MCl_2 \cdot xH_2O$ (M= Mn, Co, Ni), $M(NO_3)_2 \cdot xH_2O$ (M= Mn, Co, Ni) and sodium benzoate are mixed in water, the resulting precipitate is washed and dried at room temperature. These generic “ M_3O ” samples were subsequently reacted in pyridine in a stoichiometric ratio to access mixed-metal complexes, mixed-valent complexes as well as mixed-metal complexes showing mixed-valency. This strategy yielded a variety of results, but due to the similarity of the transition metals used in the synthesis in terms of their electronic structure as well as the varying crystallographic space group it can be very difficult to distinguish between them. Some selected examples are presented here.

The reaction of two equivalents of microcrystalline orange coloured “ Fe_3O ” with one equivalent green coloured “ Ni_3O ” in pyridine yields dark black crystals of $[Fe^{III}_2M^{II}(O_2C-Ph)_6(py)_3]$ (**6**). Compound (**6**) crystallises in the triclinic space group $P\bar{1}$ with two $[Fe^{III}_2Fe^{II}(O_2C-Ph)_6(py)_3]$ molecules in the asymmetric unit. As is the case for compounds (**3**) and (**4**) the triangular core structure is neutral, here as a result of the presence of the M^{II} ion, but, unlike in the previous examples, all the ions have equivalent coordination environments. The core of (**6**) thus consists of the three transition metal ions connected via a μ_3 -oxygen ion. As before, two benzoate ions bridge between pairs of ions defining the edges of the triangles and a coordinated terminal pyridine ligand completes the octahedral coordination environment for each of the ions. Three lattice pyridine molecules are part of the asymmetric unit. It is unclear where the divalent transition metal is situated within the complex, but the dark colour of the compound suggests that this compound is a mixed-valent $\{Fe^{III}_2Fe^{II}\}$ system rather than an $\{Fe^{III}_2Ni^{II}\}$ mixed-metal triangle.

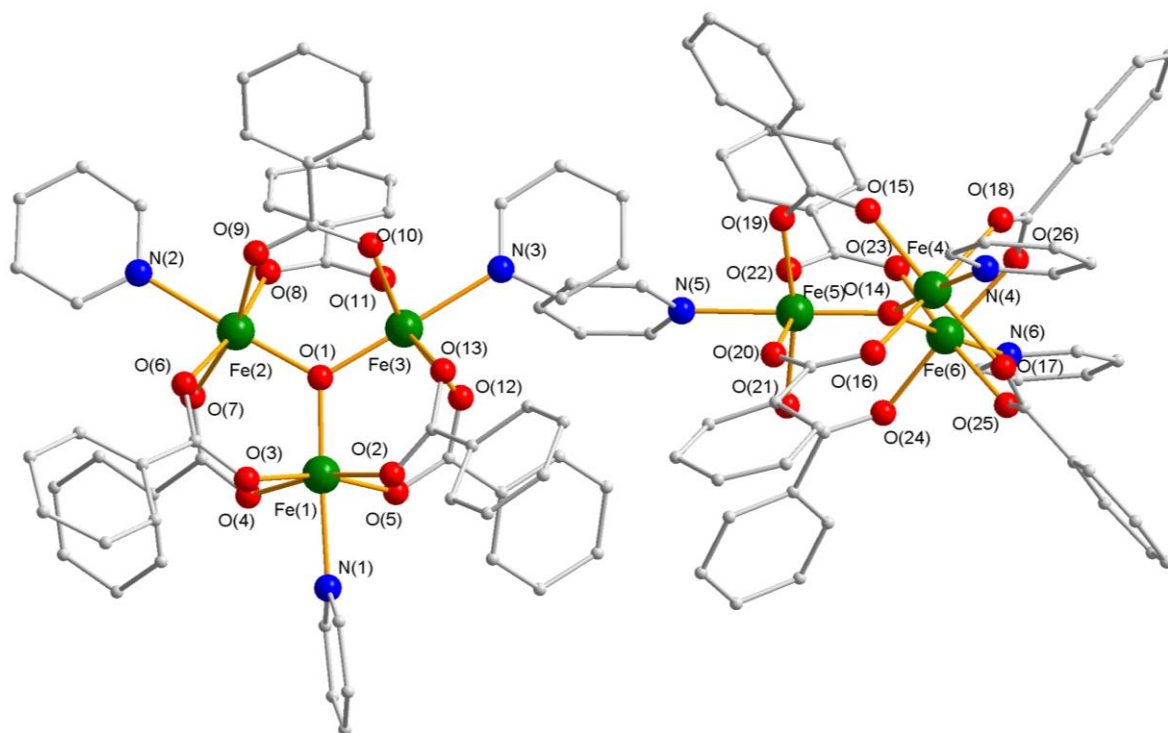


Figure 3.1-16 The molecular structure of $[\text{Fe}_3\text{O}(\text{O}_2\text{C-Ph})_6(\text{py})_3]_2$ (**6**), organic H-atoms and solvent pyridine molecules are omitted for clarity.

Table 3-7 Selected bond lengths and angles for the triangles in (**6**) discussed in the text.

Fe(1)-Fe(2)-Fe(3)		Fe(4)-Fe(5)-Fe(6)	
Fe(1)-O(1)	1.897(2)Å	Fe(4)-O(14)	1.892(2)Å
Fe(2)-O(1)	1.886(2)Å	Fe(5)-O(14)	1.863(2)Å
Fe(3)-O(1)	1.888(2)Å	Fe(6)-O(14)	1.903(2)Å
Fe(1)-N(1)	2.206(2)Å	Fe(4)-N(4)	2.184(2)Å
Fe(2)-N(2)	2.219(2)Å	Fe(5)-N(5)	2.211(2)Å
Fe(3)-N(3)	2.210(2)Å	Fe(6)-N(6)	2.193(2)Å
Fe-O _{Ph}	2.019(2)Å-2.054(2)Å	Fe-O _{Ph}	2.009(2)Å-2.055(2)Å
∠O(1)-Fe(1)-O _{eq}	95.9(07)°	∠O(14)-Fe(4)-O _{eq}	95.8(08)°
∠N(1)-Fe(1)-O _{eq}	84.2(07)°	∠N(4)-Fe(4)-O _{eq}	84.2(09)°
∠O(1)-Fe(2)-O _{eq}	96.4(07)°	∠O(14)-Fe(5)-O _{eq}	96.7(08)
∠N(2)-Fe(2)-O _{eq}	83.6(08)°	∠N(5)-Fe(5)-O _{eq}	83.3(08)°
∠O(1)-Fe(3)-O _{eq}	96.4(07)°	∠O(14)-Fe(6)-O _{eq}	95.9(07)°
∠N(3)-Fe(3)-O _{eq}	83.7(07)°	∠N(6)-Fe(6)-O _{eq}	84.0(09)°

Overall the two triangular complexes within the asymmetric unit appear to be nearly identical, the bond lengths and angles discussed are listed in **Table 3-7** for ease of comparison. However, an analysis of bond lengths and angles for both of them is carried out separately. For the first triangle the bond lengths between the Fe^{III} and the central μ_3 -oxygen are very similar to those in previously reported triangles with terminal pyridine ligands such as compound (3) (Fe(1)-O(1) = 1.897(2)Å, Fe(2)-O(1) = 1.886(2)Å and Fe(3)-O(1) = 1.888(2)Å) with the bonds to the terminal pyridine ligands significantly elongated (Fe(1)-N(1) = 2.206(2)Å, Fe(2)-N(2) = 2.219(2)Å, Fe(3)-N(3) = 2.210(2)Å). The variance within the bond lengths of the bridging carboxylates (Fe-O_{Ph}) are in line with previous measurements, although it has to be noted that all of them are above 2Å (Fe-O_{Ph} = 2.019(2)Å-2.054(2)Å). The octahedral coordination geometry is distorted due to the rather strong elongation of the bond lengths to the terminal pyridine ligands, as evidenced by the bond angles. (\angle O(1)-Fe(1)-O_{eq} = 95.9(07)°, \angle N(1)-Fe(1)-O_{eq} = 84.2(07)°, \angle O(1)-Fe(2)-O_{eq} = 96.4(07)°, \angle N(2)-Fe(2)-O_{eq} = 83.6(08)°, \angle O(1)-Fe(3)-O_{eq} = 96.4(07)°, \angle N(3)-Fe(3)-O_{eq} = 83.7(07)°)

For the second triangle the corresponding measurements are consistent, although it has to be noted that all Fe-O bond lengths measured at Fe(5) are slightly shorter than those for Fe(4) and Fe(6) (Fe(4)-O(14) = 1.892(2)Å, Fe(5)-O(14) = 1.863(2)Å and Fe(6)-O(14) = 1.903(2)Å) with the bonds to the terminal pyridine ligands significantly elongated (Fe(4)-N(4) = 2.184(2)Å, Fe(5)-N(5) = 2.211(2)Å, Fe(6)-N(6) = 2.193(2)Å). The bond lengths of the bridging carboxylates (Fe-O_{Ph}) are also consistent with previous ones (Fe-O_{Ph} = 2.009(2)Å-2.055(2)Å). The distortion of the octahedral coordination is confirmed by the bond angles. (\angle O(14)-Fe(4)-O_{eq} = 95.8(08)°, \angle N(4)-Fe(4)-O_{eq} = 84.2(09)°, \angle O(14)-Fe(5)-O_{eq} = 96.7(08)°, \angle N(5)-Fe(5)-O_{eq} = 83.3(08)°, \angle O(14)-Fe(6)-O_{eq} = 95.9(07)°, \angle N(6)-Fe(6)-O_{eq} = 84.0(09)°)

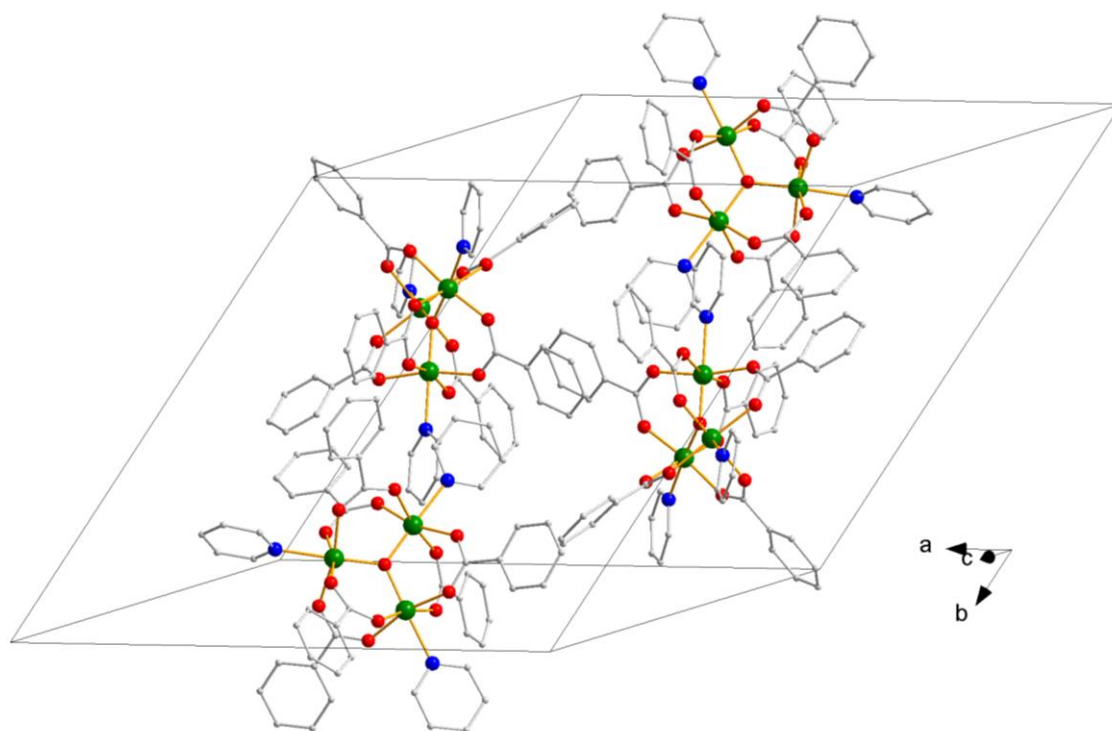
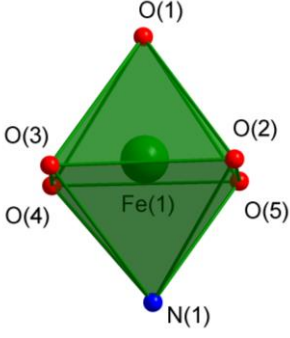
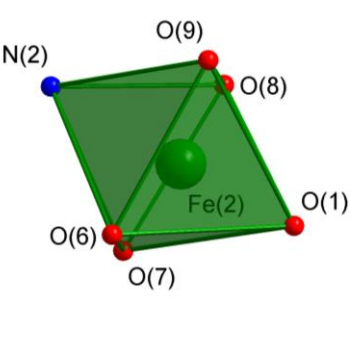
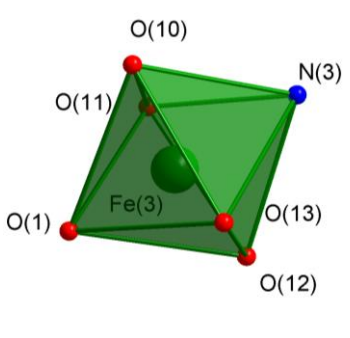
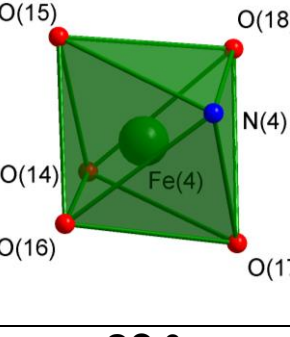
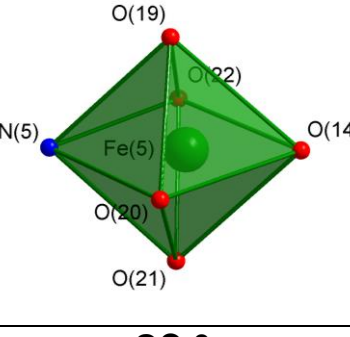
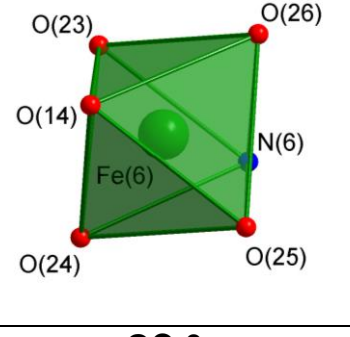


Figure 3.1-17 The unit cell of $[\text{Fe}^{\text{III}}_2\text{Fe}^{\text{II}}\text{O}(\text{O}_2\text{C-Ph})_6(\text{py})_3]$ (6), organic H-atoms omitted for clarity.

The distortion of the octahedral coordination environment is further exemplified by the SHAPE analysis and investigation of the twelve octahedral cis angles. It is notable that the deviation of the octahedral cis angles is biggest for Fe(2) and Fe(5), although this is not obvious from the SHAPE analysis.

Both Fe_3 triangles diverge slightly from an equilateral arrangement, with one distance being slightly longer than the other two ($\text{Fe}(1)\text{-Fe}(2) = 3.271(05)\text{\AA}$, $\text{Fe}(2)\text{-Fe}(3) = 3.278(05)\text{\AA}$, ($\text{Fe}(1)\text{-Fe}(3) = 3.272(05)\text{\AA}$, $\text{Fe}(4)\text{-Fe}(5) = 3.247(06)\text{\AA}$, $\text{Fe}(5)\text{-Fe}(6) = 3.259(05)\text{\AA}$, ($\text{Fe}(4)\text{-Fe}(6) = 3.293(05)\text{\AA}$) and this is reflected in the interior triangle angles. ($\angle\text{Fe}(2)\text{-Fe}(1)\text{-Fe}(3) = 60.13(1)^\circ$, $\angle\text{Fe}(1)\text{-Fe}(2)\text{-Fe}(3) = 59.95(1)^\circ$, $\angle\text{Fe}(2)\text{-Fe}(3)\text{-Fe}(1) = 59.92(1)^\circ$, $\angle\text{Fe}(5)\text{-Fe}(4)\text{-Fe}(6) = 59.79(1)^\circ$, $\angle\text{Fe}(4)\text{-Fe}(5)\text{-Fe}(6) = 60.80(1)^\circ$, $\angle\text{Fe}(5)\text{-Fe}(6)\text{-Fe}(4) = 59.41(1)^\circ$)

Table 3-8 SHAPE analysis of the Fe coordination environment in (6), polyhedra are drawn as they are oriented in the crystal structure, deviation factor from optimal octahedral coordination geometry (OC-6) and sum of the absolute values of the deviation from the 90° octahedral cis angles (Σ).

		
OC-6	OC-6	OC-6
0.228	0.221	0.215
Σ	Σ	Σ
52.0	56.9	54.5
		
OC-6	OC-6	OC-6
0.193	0.209	0.172
Σ	Σ	Σ
52.7	57.5	53.15

There is no certainty about the metal composition of compound (6) the difference in mass between Fe and Ni is only about 3 amu (58.6934 – 55.845) making it very hard to prove the incorporation of Ni into the compound via single-crystal X-Ray structure determination alone. An elemental analysis capable of detecting metals would show a statistical distribution and allow to establish that the incorporation of Ni into the triangle was successful. At the same time, even a statistical distribution of Ni into the bulk material would not confirm the composition of each triangular complex. The colour of the crystals further suggests a mixed valence $\{\text{Fe}^{\text{III}}_2\text{Fe}^{\text{II}}\}$ complex suggesting at least partially reduction of the starting material used in the synthesis.

Lastly, the crystal structure data suggests slightly different bond lengths and angles for Fe(2) and Fe(5) described above. Further investigation, most importantly via ^{57}Fe Mößbauer spectroscopy would allow the confirmation of the suspected composition.

There are quite a few points that support the suggested $\text{Fe}^{\text{III}}_2\text{Fe}^{\text{II}}$ composition, firstly the dark colour of the crystals suggests that there is charge transfer happening between the metal ions, which implies that it is indeed a mixed valent triangle rather than a mixed $\text{Fe}^{\text{III}}_2\text{Ni}^{\text{II}}$ one. A mixed valent $\text{Ni}_2^{\text{III}}\text{Ni}^{\text{II}}$ compound is also highly unlikely since although octahedral Ni^{II} has an energetically stable d^8 electron configuration, Ni^{III} is much less stable as an octahedral d^7 ion in either a high or low spin configuration. This results from the small ionic radius and the obvious trend across the 3d metals that higher oxidation states become less stable to the right of Mn.

The fact that the bond lengths only vary slightly is consistent with the suggestion that this is a delocalised system, i.e. a mixed valence $\text{Fe}^{\text{III}}_2\text{Fe}^{\text{II}}$ compound. The best strategy to investigate this would be to use a very fast spectroscopic method such as ^{57}Fe Mößbauer in conjunction with high resolution mass spectrometry.

Another attempt at the synthesis of a mixed metal triangle resulted from the reaction of “ Cr_3O ” and “ Mn_3O ” and similarly to compound (6) the determination of the metal composition is rather difficult. Judging from the green-blue colour of the crystals it is strongly implied that compound (7) consists of mostly $[\text{Cr}_3\text{O}(\text{O}_2\text{C-Ph})_6(\text{py})_3]\text{NO}_3\cdot\text{py}$.

Compound (7) crystallises in the hexagonal space group $P6_3/m$, with a third of the molecule inside the asymmetric unit. This threefold symmetry further complicates the investigation of the metal composition. The nitrate counteranion is disordered.

The bond lengths are consistent with those found for $[\text{Cr}_3\text{O}(\text{O}_2\text{C-Ph})_6(\text{py})_3]\text{ClO}_4\cdot\text{py}$ reported by Sowrey et al.^[58] In line with previously described complexes incorporating pyridine as the terminal ligand the Cr-N bond is elongated compared to the Cr-O bond. ($\text{Cr}(1)\text{-O}(1) = 1.908(04)\text{Å}$, $\text{Cr}(1)\text{-N}(1) = 2.133(3)\text{Å}$). The bond lengths of the bridging carboxylates are $\text{Cr}(1)\text{-O}(2) = 1.969(2)\text{Å}$ and $\text{Cr}(1)\text{-O}(3) = 1.966(2)\text{Å}$.

The inherent symmetry aligns the three chromium ions in a perfect equilateral triangle. ($\text{Cr}(1)\text{-Cr}(1') = 3.305(06)\text{Å}$)

Due to the elongated Cr-N bond length and the resulting displacement of the chromium ion from the centre of the octahedron the coordination geometry is slightly

distorted slightly as evidenced by the SHAPE analysis and investigation of the twelve octahedral cis angles. (see **Table 3-9**)

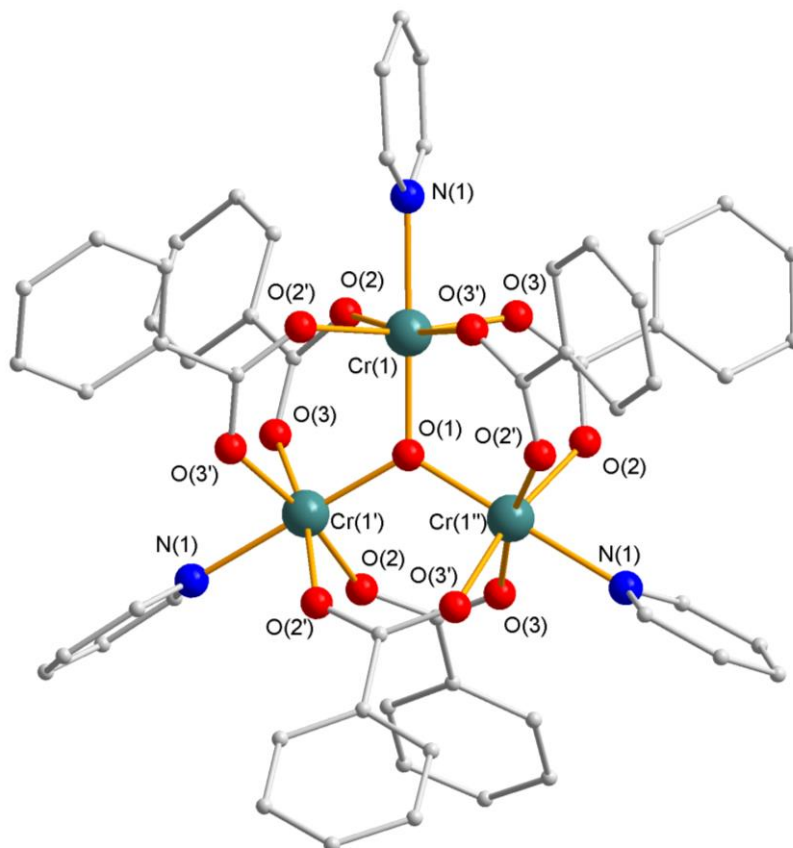


Figure 3.1-18 The molecular structure of $[\text{Cr}_3\text{O}(\text{O}_2\text{C-Ph})_6(\text{py})_3]_2$ (**7**), organic H-atoms, solvent pyridine molecule and nitrate counter ion omitted for clarity.

Table 3-9 SHAPE analysis of the Cr coordination environment in (**7**), deviation factor from optimal octahedral coordination geometry (OC-6) and sum of the absolute values of the deviation from the 90° octahedral cis angles (Σ).

OC-6
0.132
Σ
43.2

Given that this single crystal X-Ray structure determination on a highly symmetric complex does not necessarily give access to the desired information other techniques were pursued.

High resolution mass spectrometry comes to mind when analysing compounds that are very similar in mass. Although this would not necessarily give definitive answers to questions concerning the oxidation state of the metal used it should prove a viable strategy to analyse the core of the complexes. Furthermore, any difference in the counteranion used is irrelevant when using electro spray ionization (ESI) as only the charged complex and its fragments are investigated.

These measurements were made as part of a collaboration with the group of Prof. Niedner-Schatteburg at the TU Kaiserslautern (TUK) within the scope of the DFG SFB TRR88 "3MET". This group very recently published a study on the investigation of magnetic XMCD properties of $\text{Mn}_{12}\text{O}_{12}(\text{CH}_3\text{CO}_2)_{12}$ ^[90] in the gas phase. Investigating molecules in the gas phase eliminates the effects of the surface and crystal packing on the magnetic relaxation of single-molecule magnets.

The difficulty lies within the complexes used for these studies, as they have to meet certain criteria. First of all, they should preferably be magnetically interesting, hence the reason why the first molecule identified as showing slow relaxation of magnetisation was chosen for this study. Secondly, there is a limit to how large the molecular mass of any given molecule that is to be investigated can be, since it has to be ionised to be investigated in the gas phase.

As we are interested in the magnetic behaviour of the synthesised triangular complexes and they are rather light as far as transition metal complexes are concerned (around 1000 g/mol) this sparked interest in investigating the synthesised triangles. Since the Kaiserslautern group started to analyse the pure Fe_3O triangle in yet unpublished results, examples of the potentially mixed M_3O triangles were chosen first for analysis in Kaiserslautern using mass spectrometry to potentially expand the series.

A microcrystalline sample resulting from the combination of two equivalents of " Fe_3O " and one equivalent of " Co_3O " in a pyridine solution was prepared.

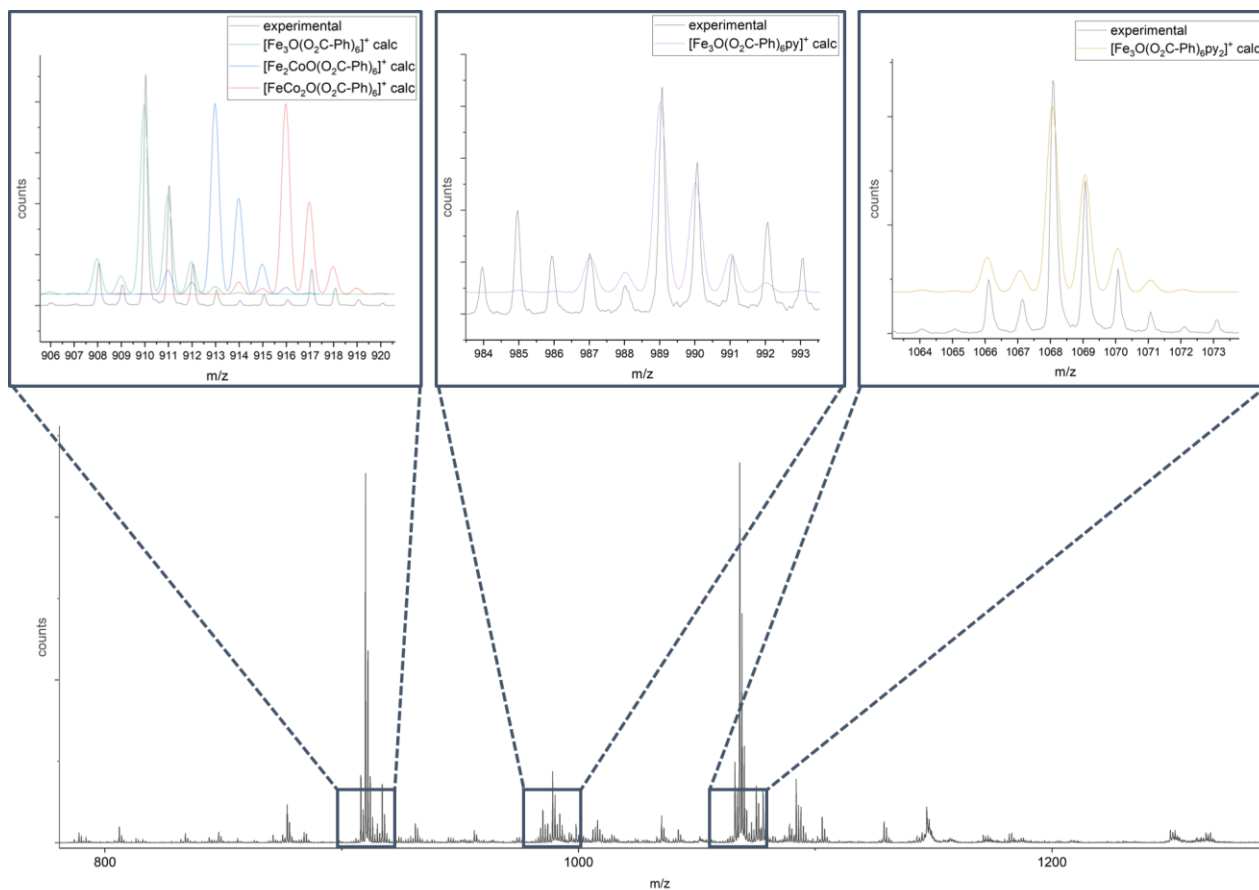


Figure 3.1-19 Mass spectrum of $[\text{Fe}_2\text{CoO}(\text{O}_2\text{C-Ph})_6(\text{py})_3]^+$ (**8**), zoomed in graphs show the comparison between calculated spectra and experimental data.

The mass spectrum of compound (**8**) is shown in **Figure 3.1-19**. From the calculated spectra for $[\text{Fe}_2\text{CoO}(\text{O}_2\text{C-Ph})_6(\text{py})_3]^+$ it is clearly visible that mostly $[\text{Fe}_3\text{O}(\text{O}_2\text{C-Ph})_6(\text{py})_3]^+$ resulted from this synthesis. The calculated mass spectra for $[\text{Fe}_2\text{Co}(\text{O}_2\text{C-Ph})_6(\text{py})_3]^+$ and $[\text{FeCo}_2\text{O}(\text{O}_2\text{C-Ph})_6(\text{py})_3]^+$ in the 906-920 m/z range show that trace amounts of these compounds might be present but a closer look at the signals in the 984-993 m/z and 1064-1073 m/z range confirms the presence of mostly $[\text{Fe}_3\text{O}(\text{O}_2\text{C-Ph})_6(\text{py})_3]^+$.

Next, a microcrystalline sample of the reaction of two equivalents “ Fe_3O ” and one equivalent “ Mn_3O ” isolated from the pyridine solution was investigated. The spectrum of compound (**9**) is shown in **Figure 3.1-21**. As found for compound (**8**) the mass spectrum shows mostly $[\text{Fe}_3\text{O}(\text{O}_2\text{C-Ph})_6(\text{py})_3]^+$. Interestingly, a closer look at the spectrum in the 906-913 m/z range (**Figure 3.1-20**) shows the difficulty of distinguishing Fe and Mn. The experimental data shows broad and shouldered peaks, suggesting the presence of both $[\text{Fe}_3\text{O}(\text{O}_2\text{C-Ph})_6(\text{py})_3]^+$ and

$[\text{Fe}_2\text{MnO}(\text{O}_2\text{C-Ph})_6(\text{py})_3]^+$. Given the mass difference of the elements in question (0.9amu) it is quite interesting to see these small differences reflected in the spectrum. The expected mass for the $[\text{Fe}_2\text{MnO}(\text{O}_2\text{C-Ph})_6]^+$ fragment is 909.3 amu, meaning that the difference between the mono metallic Fe cluster and the mixed metal compound is only about 0.1% and yet, these small differences are resolved in the mass spectrum of compound (**8**).

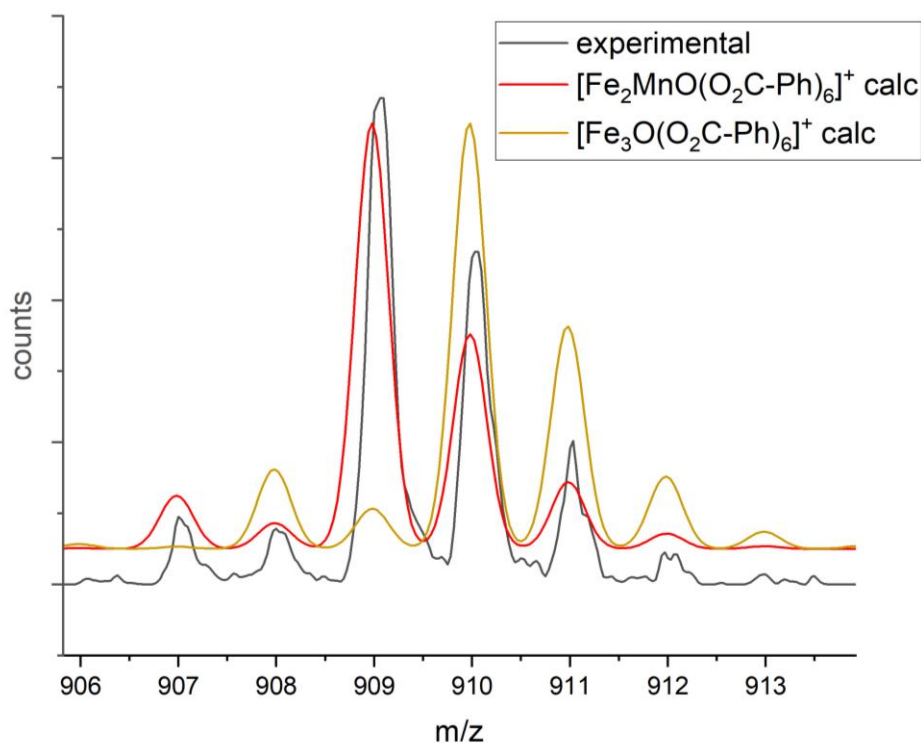


Figure 3.1-20 Cutout of the mass spectrum of (**9**) in the 906-913 m/z range, comparison between experimental data and calculated values for $[\text{Fe}_2\text{MnO}(\text{O}_2\text{C-Ph})_6(\text{py})_3]^+$ and $[\text{Fe}_3\text{O}(\text{O}_2\text{C-Ph})_6(\text{py})_3]^+$.

The calculated data for $[\text{Fe}_2\text{MnO}(\text{O}_2\text{C-Ph})_6(\text{py})_3]^+$ in the higher m/z ranges shows that either it is even harder to resolve the miniscule mass difference at higher masses, or else the fragmentation of the complex happens so effectively that barely any species with coordinated pyridine molecules can be detected.

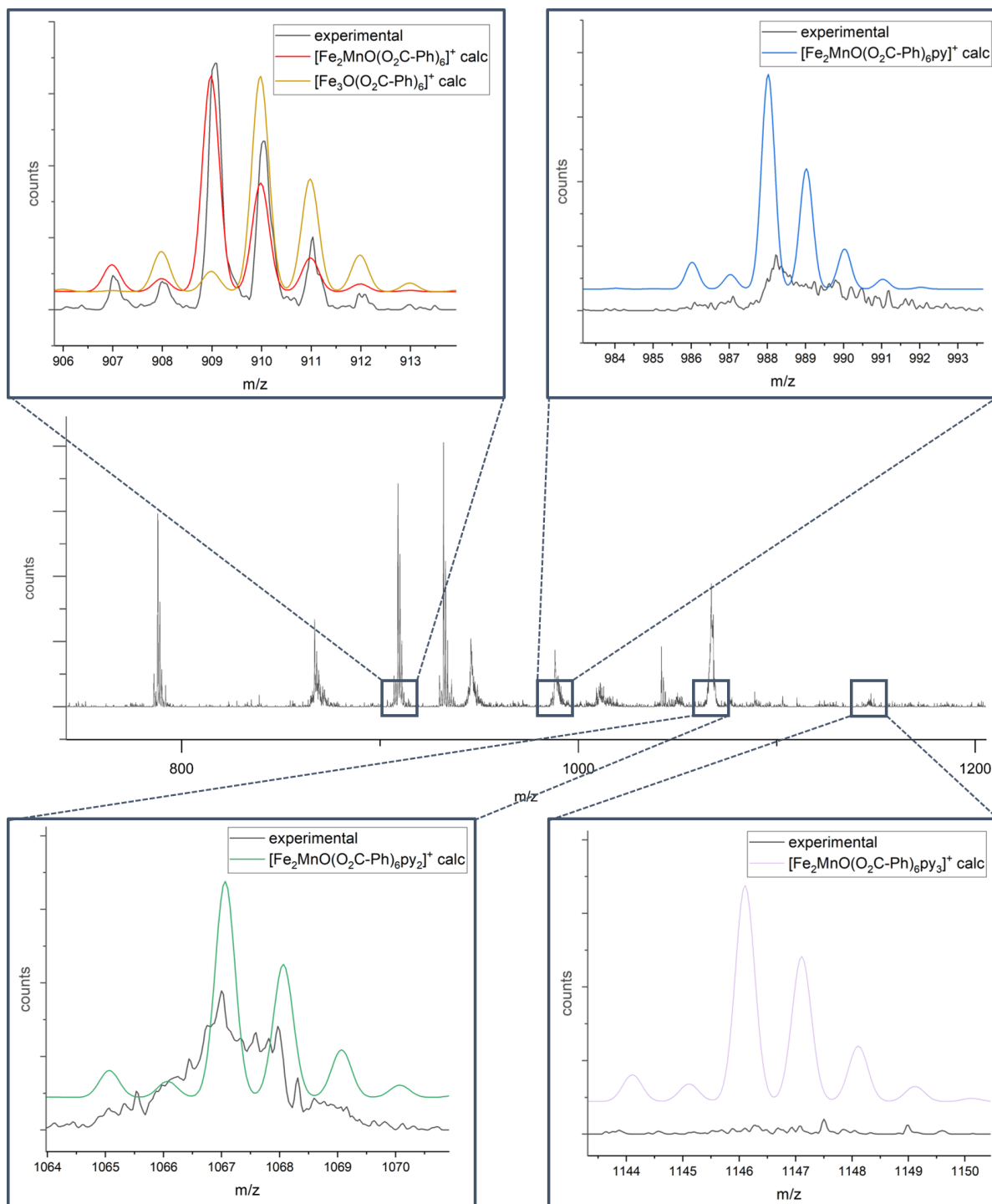


Figure 3.1-21 Mass spectrum of (9), zoomed in graphs show the comparison between calculated spectra and experimental data.

To avoid the problem of the mass difference between the metal ions being rather tiny compared to the overall mass of the complex another complex was investigated where the bridging benzoates were replaced by acetate ions.

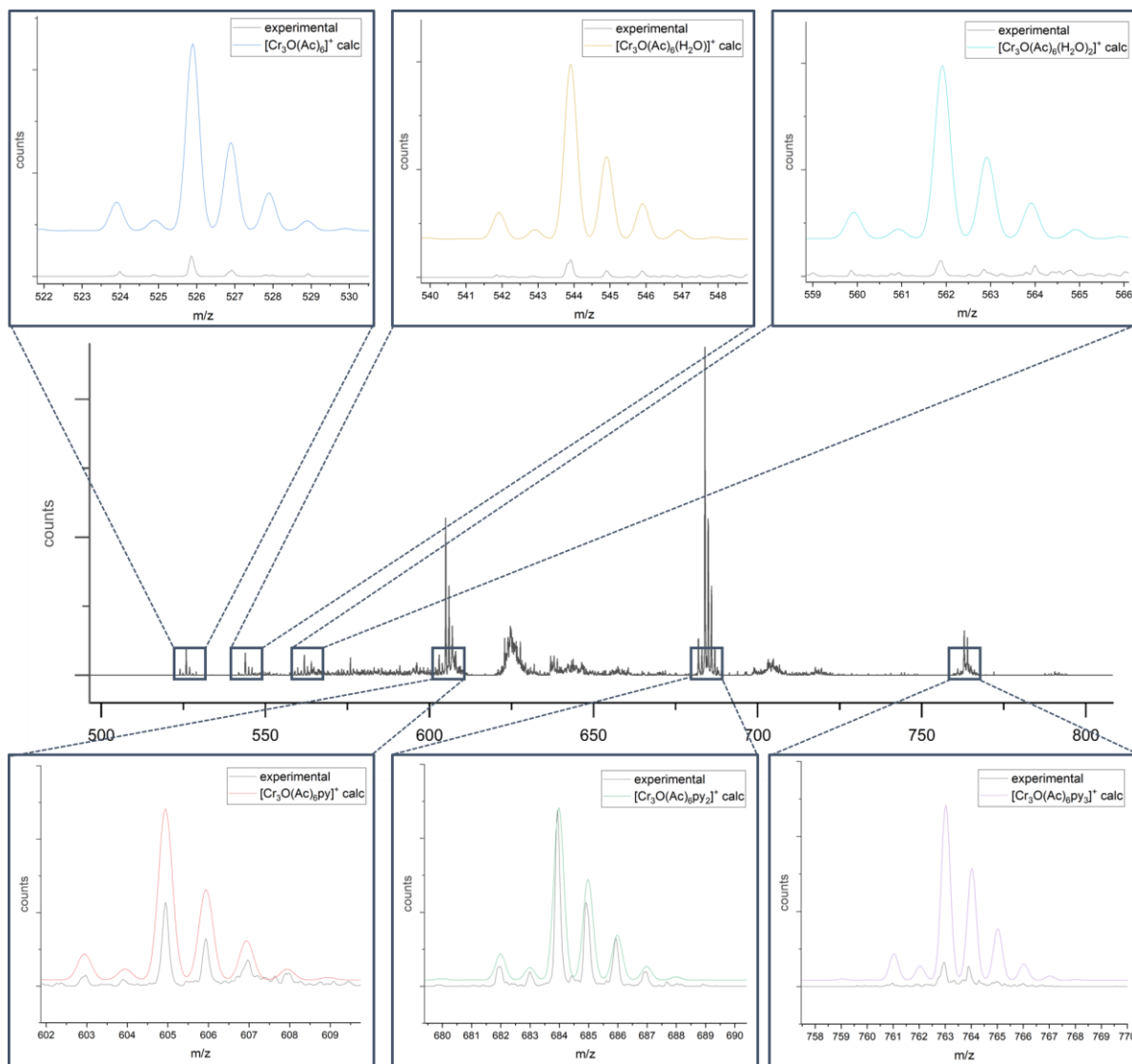


Figure 3.1-22 Mass spectrum of (10), zoomed in graphs show the comparison between calculated spectra and experimental data.

The microcrystalline powder of the generic “Cr₃O” was recrystallised from pyridine. A dried microcrystalline sample of [Cr₃O(O₂C-CH₃)₆(py)₃]⁺ (10) was then investigated by mass spectrometry. The analysis of the experimental data shows clear signals for [Cr₃O(O₂C-Ph)₆(py)₂]⁺ and [Cr₃O(O₂C-Ph)₆(py)]⁺ and [Cr₃O(O₂C-Ph)₆(py)₃]⁺ in agreement with the calculated values, confirming the strategy of a lighter complex leading to more complete ionisation. The signals between 532-566 m/z show trace amounts for the complex with the terminal pyridine ligands replaced by water.

So far, further attempts at isolating other variants were so far not successful. However, given that the synthesis could be shown to work for the benzoate systems this is clearly an avenue to pursue in further future investigations.

3.1.4 Summary

The previous section laid out the benefits of a simple recipe to access a multitude of different triangular compounds incorporating various transition metals, carboxylic acids, terminal ligands and counteranions. The possibility to access more exotic compounds such as the neutral compounds (3) and (4) shows that, in addition to their use as starting materials for further reactions, these seemingly simple molecules are potentially be very interesting in their own right.

The use of specific structure-directing anions such as N-(p-aminobenzenesulfonate)-1,8-naphthalimide presented for compound (5) opens the possibility for fundamental investigations on the electronic and magnetic properties of the cations used, as well as presenting the possibilities for attachment to various substrate surfaces.

The synthetic approach presented in this previous section furthermore gives access to trinuclear complexes incorporating different transition metal ions. In some cases, it was even possible to synthesise mixed metal triangles. Selected examples have been analysed via mass spectrometry.

In conclusion there are still further options regarding investigations of the vast possibilities to synthesise trinuclear compounds via the synthetic method presented. The characterisation of the iron-containing compounds can be further enhanced by ^{57}Fe Mößbauer spectroscopy, potentially adding measurements under an applied magnetic field as well. For complexes showing interesting magnetic properties it also possible to use advanced techniques such as magnetic measurements (XMCD) in the gas phase, especially those that are more readily ionisable due to a lower molecular mass.

3.2 Hexanuclear mixed valence Manganese Oxide complexes with a $[\text{Mn}_6\text{O}_2]^{10+}$ core

3.2.1 Introduction

In the field of molecular magnetism Mn-based materials are of great importance. The identification of slow relaxation of magnetisation in $[\text{Mn}_{12}\text{O}_{12}(\text{O}_2\text{CCH}_3)_{16}(\text{H}_2\text{O})_4]$, commonly abbreviated as Mn_{12}OAc , by Sessoli et al.^[2-3] in 1993 in a sense single-handedly sparked the whole field of single-molecule magnets (SMMs). To this day Mn_{12}OAc remains the most investigated SMM as noted by Bagai and Christou in a 2009 publication.^[91]

Arguably, when judging by the commonly used benchmarks concerning the quality of an SMM, Mn_{12}OAc can also be viewed as one of the best SMMs to date. Although it was possible to reach higher energy barriers for the reversal of magnetisation of over 1000K by using dysprosium,^[92] this benefit comes with the drawback of significantly increased amounts of quantum tunnelling of magnetisation (QTM), an effect that allows the system to relax back to its initial state without fully crossing the energy barrier.

Furthermore, although recent publications showed slow relaxation at even higher temperatures such as 80K in a dysprosium metallocene^[49] which allows the possibility of using liquid nitrogen cooling and making single-molecular magnetism a feasible technology, these new compounds are highly air sensitive and therefore show few potential applications but are important for gaining fundamental understanding regarding structural parameters for SMMs.

In addition to their role in molecular magnetism, Mn-based compounds are also of great interest for their biochemical properties. The oxygen evolving centre (OEC) of photosystem II (PSII) is a vital part of the biological mechanism for photosynthesis in plants and cyanobacteria.^[93] The ability of manganese to adopt varying oxidation states is at the core of this process.

Many model compounds have been investigated to mimic aspects of the water splitting within PSII which leads to the production of O_2 and 4H^+ plus four electrons.^[94-96] One can envisage applications in fuel cells and for H_2 production.

3.2.2 History of $[\text{Mn}^{\text{II}}_4\text{Mn}^{\text{III}}_2\text{O}_2(\mu_3\text{-O}_2\text{C-R})_4(\mu_2\text{-O}_2\text{C-R})_6(\text{L})_4]$

Introducing metal ions of different valences potentially provides an avenue to magnetically interesting complexes. One of the most commonly used mixed valence complexes in these syntheses is the hexanuclear manganese complex with the general formula $[\text{Mn}^{\text{II}}_4\text{Mn}^{\text{III}}_2\text{O}_2(\mu_3\text{-O}_2\text{C-R})_4(\mu_2\text{-O}_2\text{C-R})_6(\text{L})_4]$. In this complex the hexanuclear core is bridged via two $\mu_4\text{-O}$ ions, producing two types of manganese species: the four outer Mn^{II} ions are bridged by four $\mu_3\text{-}\eta^2\text{:}\eta^1$ -carboxylates bridging two outer Mn^{II} and one of the Mn^{III} inside the core. Two additional μ_2 -carboxylates bridge between the outer manganese, the octahedral coordination sphere is completed by one of the $\mu_4\text{-O}$ ions and a monodentate ligand L. The two Mn^{III} ions on the inside of the core are then coordinated by the two $\mu_4\text{-O}$ ions with the four $\mu_3\text{-}\eta^2\text{:}\eta^1$ -carboxylates completing the octahedral coordination sphere. The L ligands can be carboxylic acids or other monodentate ligands.

The first example of a structure of this type was reported by Baikie et al. in 1986^[97].

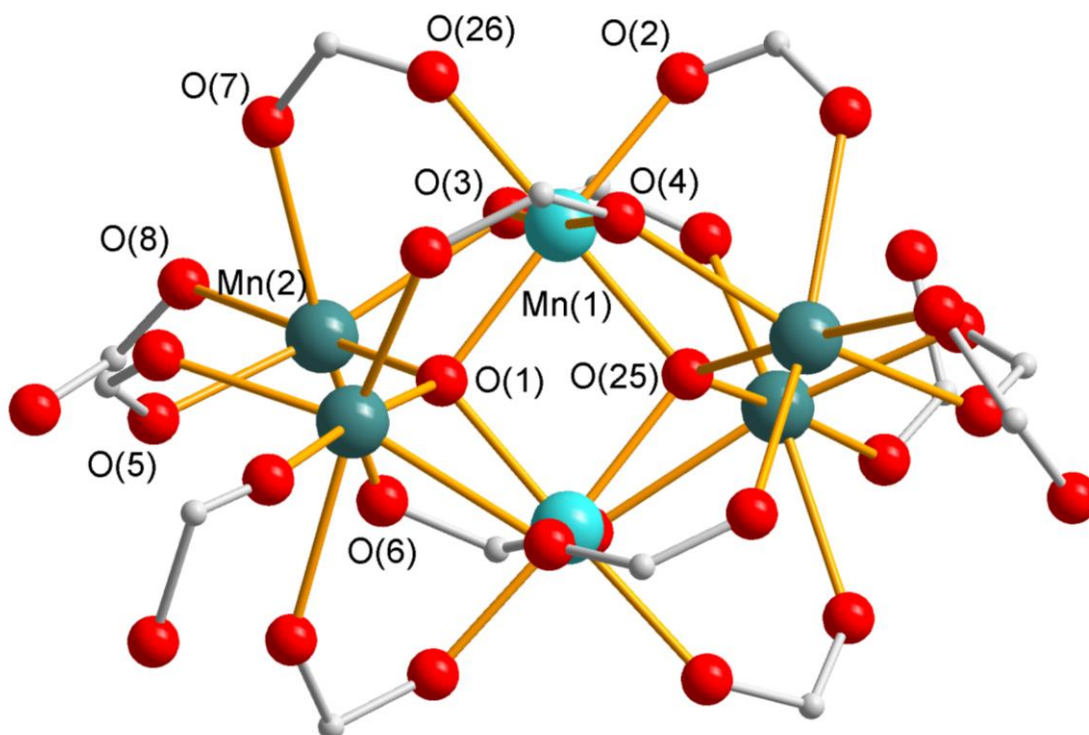


Figure 3.2-1 The core structure of $[\text{Mn}_6\text{O}_2(\text{piv})_{10}(\text{pivH})_4]$ published by Baikie et al.^[97] redrawn using the crystal data deposited with the cambridge crystallographic data centre (CCDC), the 'Butyl groups on the carboxylates and organic H-atoms have been omitted for clarity.

The reference compound $[\text{Mn}_6\text{O}_2(\text{piv})_{10}(\text{pivH})_4]$ crystallises in the orthorhombic space group $Pbca$ with a unit cell volume of 19613.8\AA^3 . The homogeneous aliphatic ligand shell of the complex leads to a nice separation of the clusters as evidenced by the packing which can be visualised by the view along the crystallographic axes. (**Figure 3.2-3**) The structure can be rationalised in terms of the three edge sharing coordination octahedral polyhedra of Mn(1) Mn(2) and Mn(3) being connected to those of Mn(4), Mn(5) and Mn(6) via edge sharing between Mn(1) and Mn(4). (see **Figure 3.2-2**)

The six Mn ions are all octahedrally coordinated and the two Mn^{III} ions (Mn(1) and Mn(4)) show clear Jahn-Teller elongation compared with the two longer Mn-O bond lengths (Mn(1)-O(3) = $2.31(3)\text{\AA}$, Mn(1)-O(4) = $2.31(3)\text{\AA}$, Mn(4)-O(15) = $2.28(2)\text{\AA}$, Mn(4)-O(16) = $2.27(3)\text{\AA}$) to that in the central plane of the octahedron (Mn(1)-O_{eq} = $1.89(3)\text{\AA}$ - $1.93(2)\text{\AA}$, Mn(4)-O_{eq} = $1.89(3)\text{\AA}$ - $1.94(3)\text{\AA}$). The octahedral coordination of the Mn^{II} is distorted as also reflected in the octahedral angles. (see **Table 3-10**)

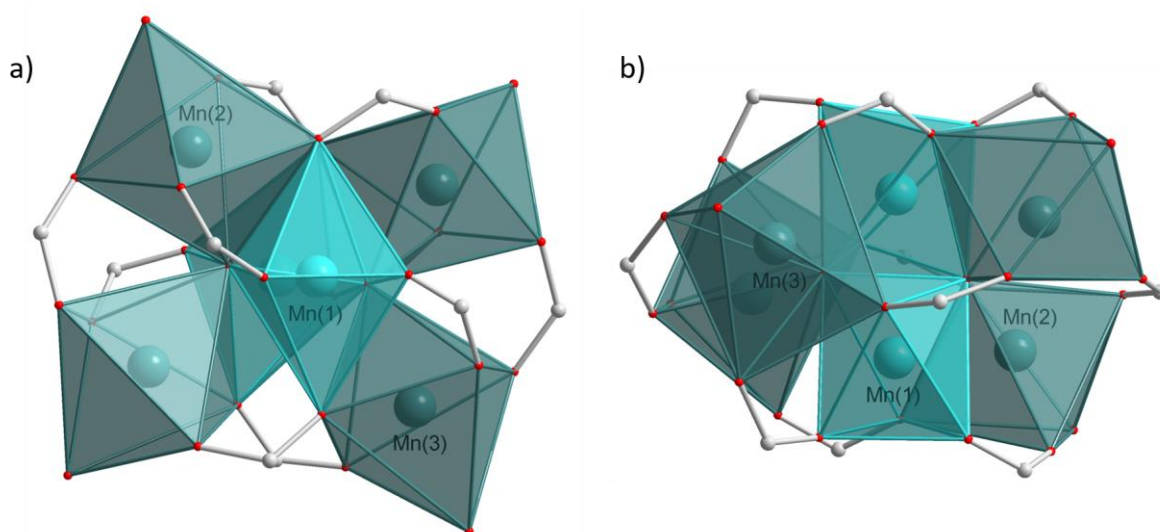


Figure 3.2-2 Visualisation of the edge sharing connection between the six Mn ions in $[\text{Mn}_6\text{O}_2(\text{piv})_{10}(\text{pivH})_4]$, front view (a) and top down view (b), 'Butyl groups and H-atoms omitted for clarity.

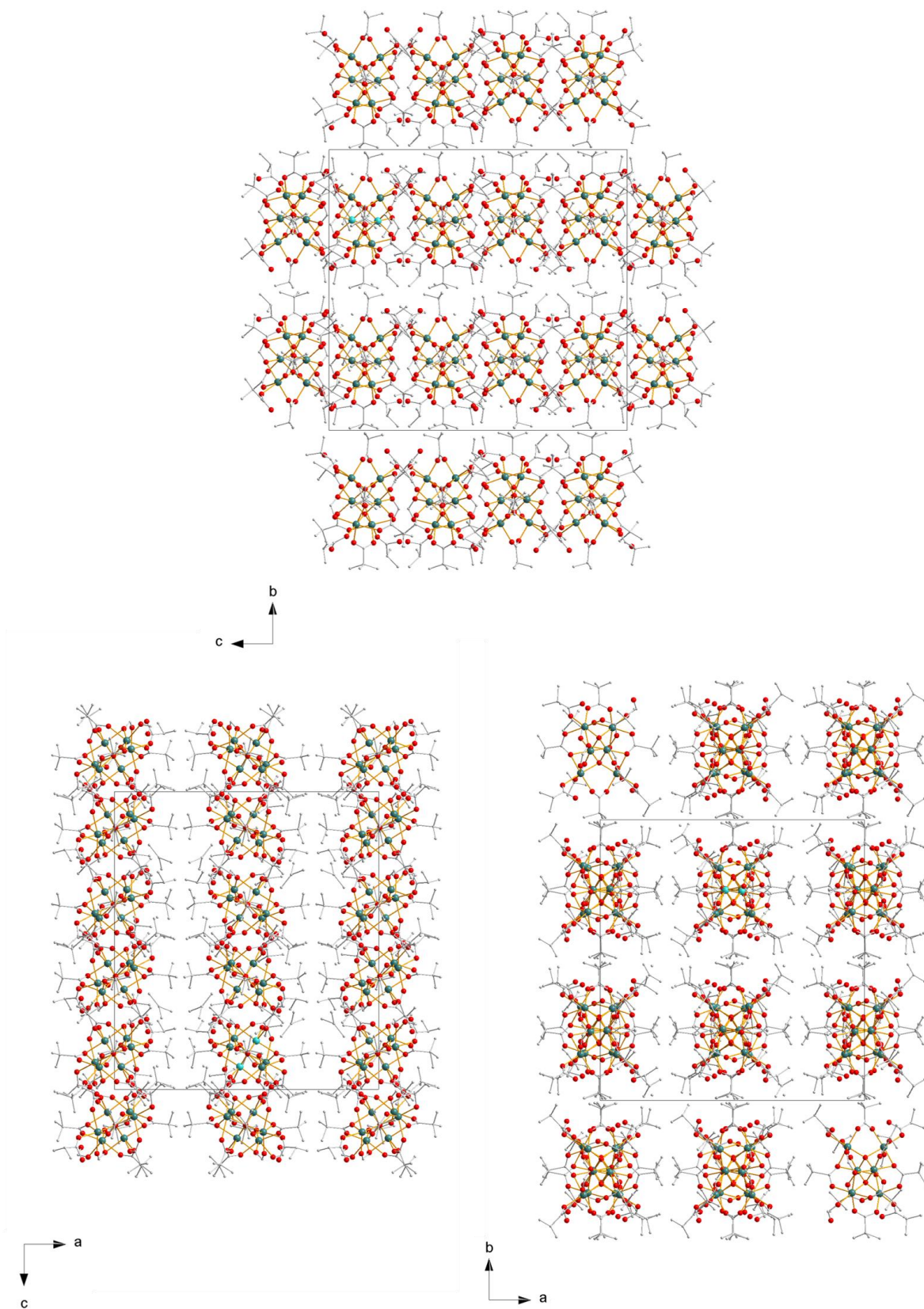


Figure 3.2-3 The unit cell of $[\text{Mn}_6\text{O}_2(\text{piv})_{10}(\text{pivH})_4]$ viewed along the crystallographic *a*-, *b*- and *c*-axis, highlighting the nice separation of the clusters by the aliphatic ligand shell.

Table 3-10 Selected bond lengths and angles for $[\text{Mn}_6\text{O}_2(\text{piv})_{10}(\text{pivH})_4]$

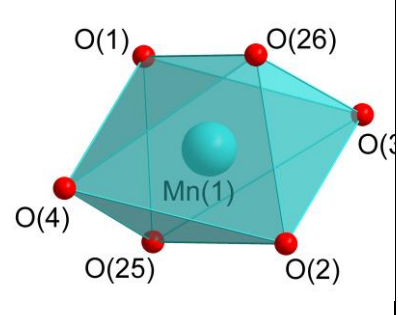
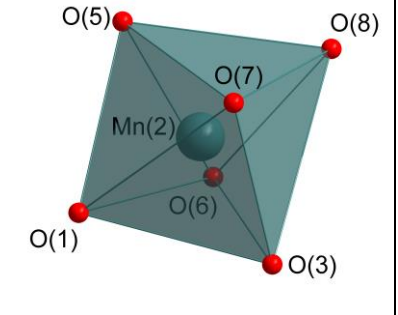
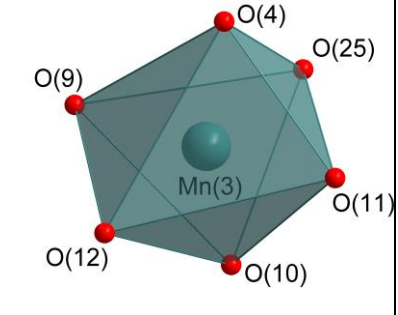
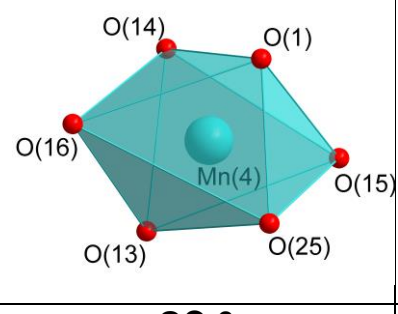
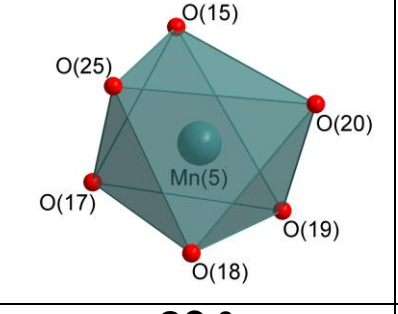
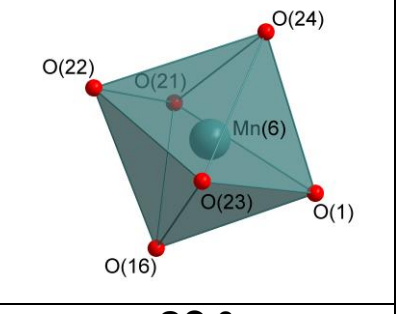
Mn ^{III}			
Mn(1)-O(3)	2.31(3)Å	Mn(4)-O(15)	2.28(3)Å
Mn(1)-O(4)	2.31(3)Å	Mn(4)-O(16)	2.27(3)Å
Mn(1)-Oeq	1.89(3)Å-1.93(2)Å	Mn(4)-Oeq	1.89(3)Å-1.94(3)Å
∠O(3)-Mn(1)-Oeq	89.5(1)°	∠O(15)-Mn(4)-Oeq	90.9(1)°
∠O(4)-Mn(1)-Oeq	90.5(1)°	∠O(16)-Mn(4)-Oeq	89.1(1)°
Mn ^{II}			
Mn(2)-O(1)	2.18(3)Å	Mn(5)-O(19)	2.26(3)Å
Mn(2)-O(8)	2.37(3)Å	Mn(5)-O(25)	2.10(3)Å
Mn(2)-Oeq	2.04(3)Å-2.28(3)Å	Mn(5)-Oeq	2.01(3)Å-2.39(3)Å
∠O(1)-Mn(2)-Oeq	91.2(1)°	∠O(19)-Mn(5)-Oeq	88.3(1)°
∠O(8)-Mn(2)-Oeq	88.8(1)°	∠O(25)-Mn(5)-Oeq	91.4(1)°
Mn(3)-O(12)	2.28(3)Å	Mn(6)-O(1)	2.16(3)Å
Mn(3)-O(25)	2.19(3)Å	Mn(6)-O(22)	2.28(4)Å
Mn(3)-Oeq	2.08(3)Å-2.39(2)Å	Mn(6)-Oeq	2.11(3)Å-2.28(3)Å
∠O(12)-Mn(3)- Oeq	90.5(1)°	∠O(1)-Mn(6)-Oeq	92.1(1)°
∠O(25)-Mn(3)- Oeq	89.8(1)°	∠O(22)-Mn(6)-Oeq	87.5(1)°

The octahedral coordination geometry for the Mn^{II} is notably distorted as evidenced by the SHAPE analysis and octahedral cis angles (see **Table 3-11**) This is not unexpected for a high-spin d⁵ ion.

Since this first publication there have been many variations on this cluster type. Most of them are isostructural to the compound discussed above, but vary in terms of the nature of the carboxylic acid, terminal ligand and in some cases even the incorporated metals.^[98] Some selected examples are variants of the $[\text{Mn}_6\text{O}_2(\text{piv})_{10}\text{L}_4]$, where the terminal ligands L are pyridine,^[99-100] pyrazol derivatives,^[101] or mixtures of solvent molecules like water^[102] or THF^[103] with other aromatic N-heterocycles.

Furthermore, derivatives where the carboxylic acid is acetate^[104-105] or benzoate^[98, 106-109] as well as some examples of aggregates of multiple Mn₆ units connected via multidentate ligands^[110-112] have been reported.

Table 3-11 SHAPE analysis of the Mn coordination environment in [Mn₆O₂(piv)₁₀(pivH)₄], deviation factor from optimal octahedral coordination geometry (OC-6) and sum of the absolute values of the deviation from the 90° octahedral cis angles (Σ).

		
OC-6 1.65	OC-6 1.18	OC-6 1.72
Σ 71.5	Σ 68.9	Σ 92.3
		
OC-6 1.37	OC-6 1.14	OC-6 1.20
Σ 64.2	Σ 78.8	Σ 77.9

Interestingly, some of the reported syntheses describe the formation of a Mn₆ cluster from the reaction of the previously discussed triangular [Mn₃O(O₂C-R)₆(L)₃]X clusters^[106] or else [Mn₁₂O₁₂(O₂CCH₃)₁₆(H₂O)₄]^[109] to access the {Mn₆O₂} derivatives, highlighting the way in which these clusters seem to be interconnected and could potentially represent local thermodynamic minima along the same reaction coordinate.

Figure 3.2-4 shows a proposed way of how the triangular compound could react to form the hexanuclear complex. Some of the bridging carboxylates as well as at least two of the terminal ligands on the triangular compound detach. Two of these fragments then recombine, the $\mu_3\text{-O}$ coordinates to a vacant site on one of the Mn^{III} ions to form the $\mu_4\text{-O}$ bridge in the hexanuclear complex. The carboxylates form new bridges between the triangular fragments. Terminal ligands, which can be excess carboxylate or solvent molecules, complete the coordination spheres.

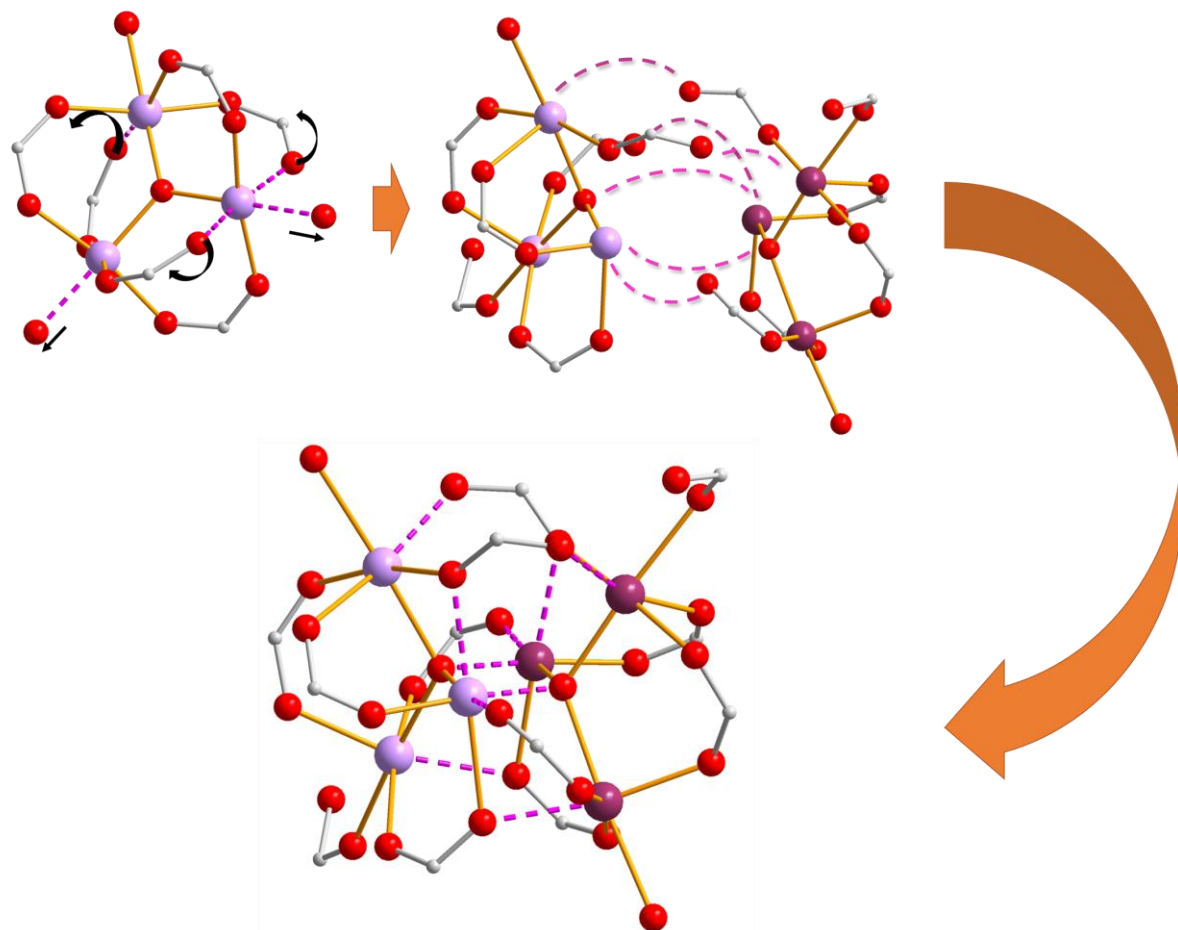


Figure 3.2-4 Suggested route for the recombination of two triangular Mn_3O units into the Mn_6O_2 core.

3.2.3 $[\text{Mn}_6\text{O}_2(\text{piv})_{10}(\text{pivH})_2(4\text{-Me-py})_2]$

The reaction of the three solids $\text{Mn}(\text{O}_2\text{C-CH}_3)_2 \cdot 4\text{H}_2\text{O}$ and KMnO_4 and pivalic acid (pivH) at 200°C for 2h yields a clear red solution, indicating the reduction of the permanganate. To the clear solution is then MeCN is then added along with 4-Me-

pyridine. Single crystals of $[\text{Mn}_6\text{O}_2(\text{piv})_{10}(\text{pivH})_2(4\text{-Me-py})_2]$ (**11**) suitable for X-Ray diffraction are obtained after one day.

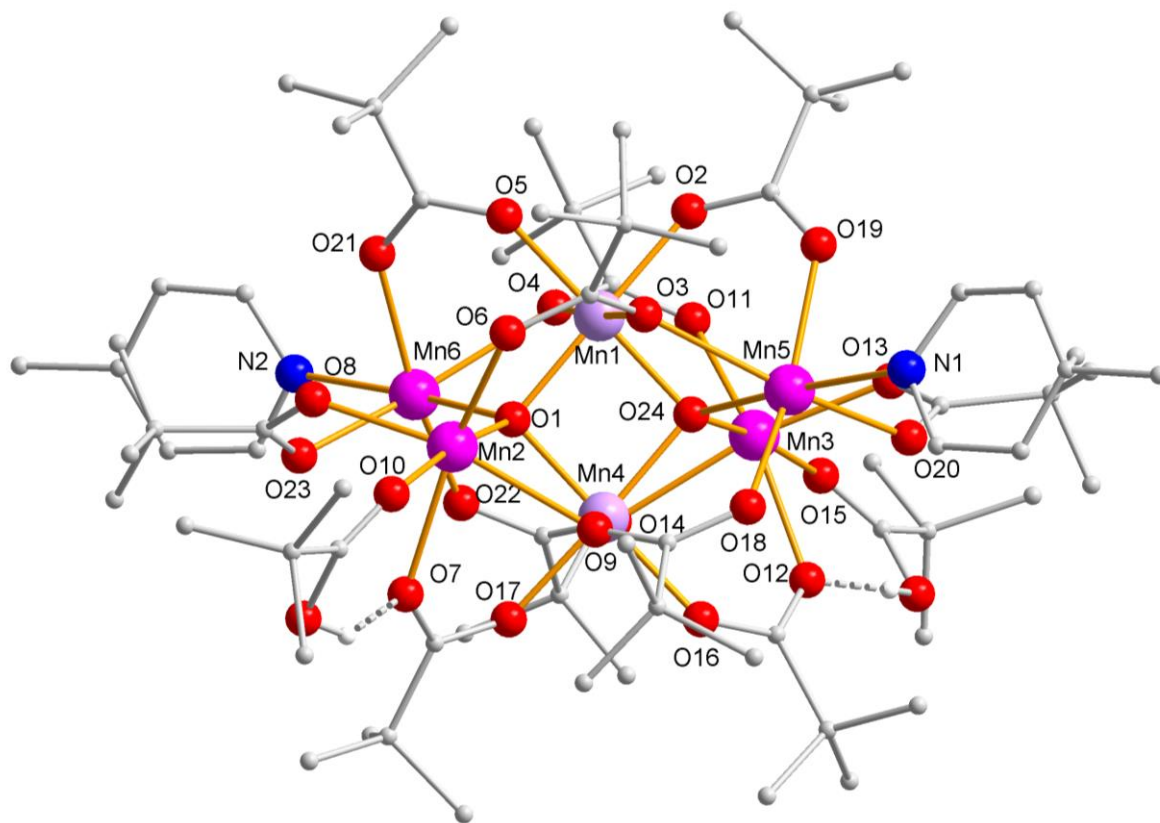


Figure 3.2-5 The molecular structure of $[\text{Mn}_6\text{O}_2(\text{piv})_{10}(\text{pivH})_2(4\text{-Me-py})_2]$ (**11**), organic H-atoms are omitted for clarity.

The molecular structure of (**11**) is similar to the one discussed earlier. The terminal ligands L are two 4-Me-py molecules and two pivalic acid molecules forming a hydrogen bridge to one of the bridging pivalates.

Compound (**11**) crystallises in the triclinic space group $P\bar{1}$ with a unit cell volume of 4666.6\AA^3 . The significantly reduced unit cell compared to the reference compound is due to the different crystal system (triclinic) with the only symmetry element of an inversion centre. This change is also reflected within the crystal packing as shown in **Figure 3.2-6**.

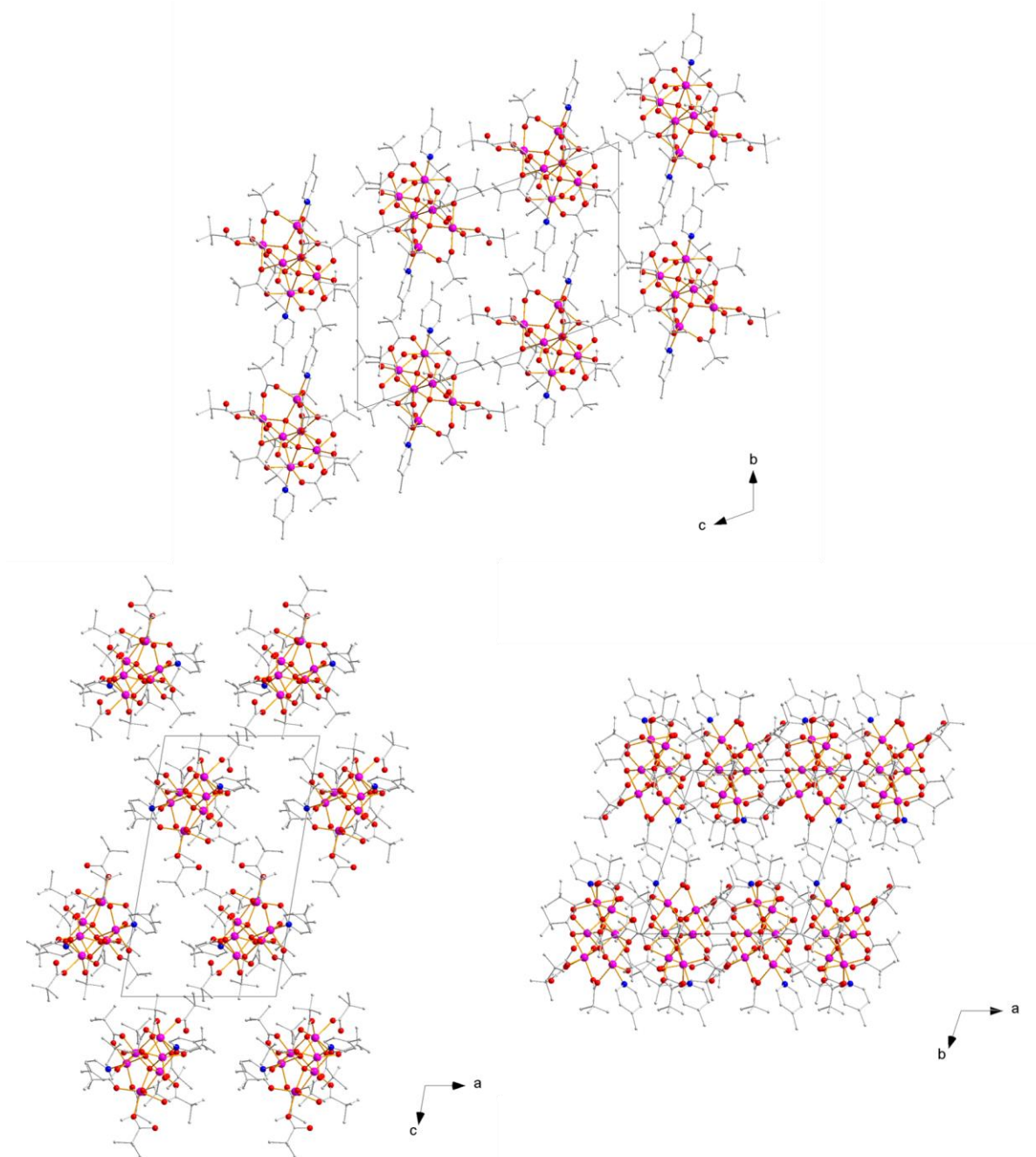


Figure 3.2-6 Unit cell of $[\text{Mn}_6\text{O}_2(\text{piv})_{10}(\text{pivH})_2(4\text{-Me-py})_2]$ (**11**) viewed along the crystallographic a-, b- and c-axis.

Similarly to the reference compound the six Mn ions are all octahedrally coordinated, the two Mn^{III} ions (Mn(1) and Mn(4)) show the same Jahn-Teller elongation comparing the four longer Mn-O bond lengths (Mn(1)-O(3) = 2.199(4)Å, Mn(1)-O(4) = 2.255(4)Å, Mn(4)-O(9) = 2.240(5)Å, Mn(4)-O(14) = 2.266(4)Å) to that in the central plane of the octahedron (Mn(1)-O_{eq} = 1.885(4)Å-1.956(4)Å, Mn(4)-O_{eq} = 1.877(4)Å-1.945(4)Å). The octahedral coordination of the Mn^{II} is distorted, as reflected in the octahedral

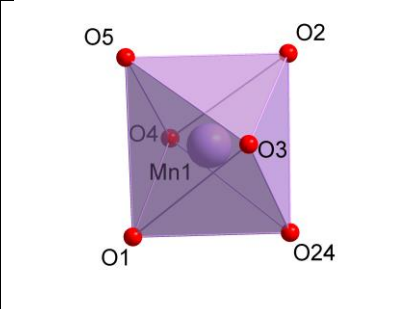
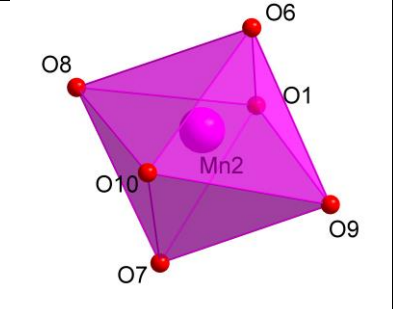
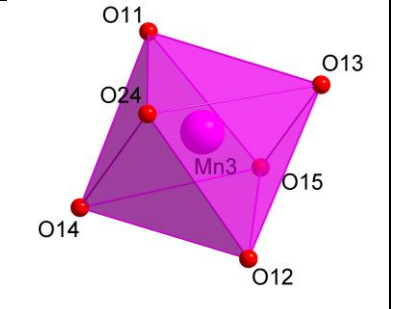
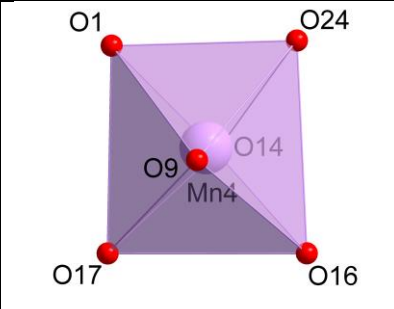
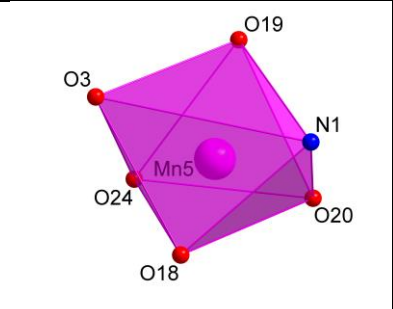
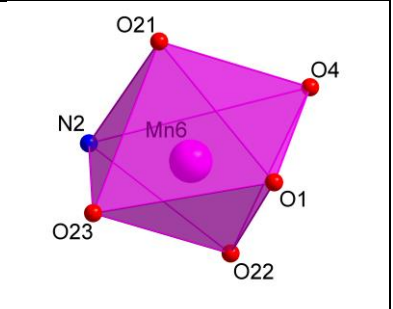
angles, as was the case for the reference compound. Selected bond lengths and angles are listed in **Table 3-12**.

Table 3-12 Selected bond lengths and angles of $[\text{Mn}_6\text{O}_2(\text{piv})_{10}(\text{pivH})_2(4\text{-Me-py})_2]$ (**11**).

Mn ^{II}			
Mn(1)-O(3)	2.199(4)Å	Mn(4)-O(9)	2.240(5)Å
Mn(1)-O(4)	2.255(4)Å	Mn(4)-O(14)	2.266(4)Å
Mn(1)-O _{eq}	1.885(4)Å- 1.956(4)Å	Mn(4)-O _{eq}	1.877(4)Å- 1.945(4)Å
∠O(3)-Mn(1)-O _{eq}	90.5(2)°	∠O(9)-Mn(4)-O _{eq}	90.1(2)°
∠O(4)-Mn(1)-O _{eq}	89.5(2)°	∠O(14)-Mn(4)-O _{eq}	89.9(2)°
Mn ^{III}			
Mn(2)-O(6)	2.091(6)Å	Mn(5)-O(19)	2.141(5)Å
Mn(2)-O(7)	2.255(6)Å	Mn(5)-O(18)	2.100(6)Å
Mn(2)-O _{eq}	2.104(4)Å- 2.299(5)Å	Mn(5)-O _{eq}	2.108(4)Å- 2.378(5)Å
∠O(6)-Mn(2)-O _{eq}	95.1(2)°	∠O(19)-Mn(5)-O _{eq}	87.6(2)°
∠O(7)-Mn(2)-O _{eq}	85.0(2)°	∠O(18)-Mn(5)-O _{eq}	93.5(2)°
Mn(3)-O(11)	2.116(6)Å	Mn(6)-O(21)	2.153(5)Å
Mn(3)-O(12)	2.221(5)Å	Mn(6)-O(22)	2.108(4)Å
Mn(3)-O _{eq}	2.094(5)Å- 2.308(5)Å	Mn(6)-O _{eq}	2.127(3)Å- 2.382(3)Å
∠O(11)-Mn(3)-O _{eq}	94.6(2)°	∠O(21)-Mn(6)-O _{eq}	87.1(2)°
∠O(12)-Mn(3)-O _{eq}	85.5(2)°	∠O(22)-Mn(6)-O _{eq}	94.2(2)°

A SHAPE analysis and investigation of the octahedral cis angles was carried out, the results are listed in **Table 3-13**. The results are very similar to that of the reference compound and indeed, due to the better quality of the crystallographic data, it can be observed that changing the terminal ligand from a carboxylate to an N-donor has no impact on the distortion of the octahedra of the Mn^{II}. This is probably the result of the constraints of the edge sharing of the coordination polyhedra between the Mn^{III} and Mn^{II}. (see **Figure 3.2-7**)

Table 3-13 SHAPE analysis of the Mn coordination environment in $[\text{Mn}_6\text{O}_2(\text{piv})_{10}(\text{pivH})_2(4\text{-Me-py})_2]$ (**11**), deviation factor from optimal octahedral coordination geometry (OC-6) and sum of the absolute values of the deviation from the 90° octahedral cis angles (Σ).

		
OC-6	OC-6	OC-6
0.939	1.15	1.09
Σ	Σ	Σ
50.0	86.1	82.2
		
OC-6	OC-6	OC-6
1.12	2.47	2.57
Σ	Σ	Σ
57.1	96.5	95.8

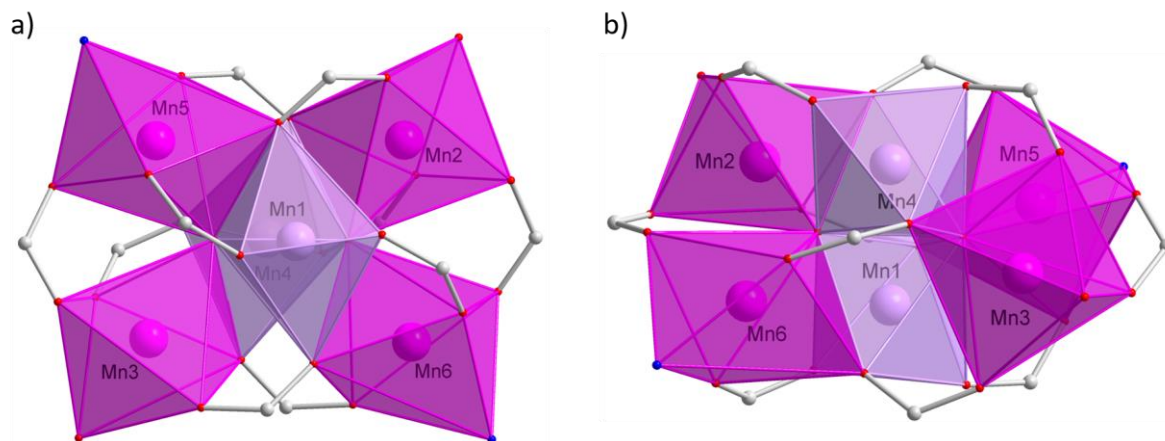


Figure 3.2-7 Visualisation of the edge sharing connection between the six Mn ions in $[\text{Mn}_6\text{O}_2(\text{piv})_{10}(\text{pivH})_2(4\text{-Me-py})_2]$ (**11**), front view (a) and top down view (b), 'Butyl groups and H-atoms omitted for clarity.

The relationship between the Mn_6O_2 compounds and the triangular Mn_3O complexes discussed in section 3.1 makes these ideal for use in the same way as using the Mn_3O triangles as starting materials to target larger structures. Furthermore, due to the fact that $[Mn_6O_2(piv)_{10}(pivH)_2(4-Me-py)_2]$ (**11**) consists of two different types of Mn ions with different valences adds another layer of customisation to the assisted self-assembly process.

3.2.4 Summary of Hexanuclear mixed valence $[Mn_6O_2]^{10+}$ core complexes

In this section the importance of manganese-based compounds for molecular magnetism and their important role in biological processes has been described. Using these preformed hexanuclear clusters as starting materials is a useful means to introduce mixed valence states of Mn into larger compounds via the assisted self-assembly approach.

A suggestion as to how the recombination of two triangular Mn_3O clusters could yield a Mn_6O_2 compound was put forward. This was inspired by various publications that suggest a common reaction coordinate for the various Mn-based clusters discussed in the literature from Mn_3O through Mn_6O_2 up to $Mn_{12}O_{12}$ and potentially even bigger Mn clusters. The Mn_3O and Mn_6O_2 clusters may represent local minima along this reaction coordinate.

4 Mn-based coordination clusters

4.1 Introduction

The importance of Mn-based materials in regards to their magnetic and biochemical relevance has been discussed in section 3.2. Nevertheless, some key aspects are repeated here.

The role of manganese in the research area of single-molecule magnetism is dominated by the historical aspect of $[\text{Mn}_{12}\text{O}_{12}(\text{O}_2\text{CCH}_3)_{16}(\text{H}_2\text{O})_4]$ being the first molecule to have been identified as possessing magnetic bistability.^[1-3]

Since then, Mn-based single-molecule magnets have been shown to possess some of the most impressive properties in terms of their magnetic behaviour. To this date, Mn_{12}OAc remains the most investigated SMM, a simple search for “Mn12” in the database at the Cambridge Crystallographic Data Centre (CCDC) reveals over 250 unique structures, the latest one being from an article in 2019.^[113]

The interest in Mn^{III} -based materials is due to the fact that this d^4 ion in a high spin octahedral configuration shows Jahn-Teller distortion, making it naturally uniaxial and thus Ising in nature. In addition, manganese can be justifiably described as the 3d transition metal ion with the largest number of stabilisable oxidation states. This fact makes manganese one of the most important metals in energy conversion research including battery technology.

Biology uses this versatility in many enzyme systems as well in the water oxidising centre found in Photosystem II^[114] and there is a great amount of interesting research published in the literature about this process, some of it by our working group^[95-96, 115] with the prospect of this fundamental research leading the way to artificial photosynthesis or even environmentally friendlier methods of hydrogen generation via water splitting.

In the scope of this thesis, a synthetic approach using the preformed Mn_6 cluster described in section 3.2 is presented. This assisted self-assembly process leads to a variety of Mn-Ln clusters with different nuclearities and magnetic properties.

4.2 Decanuclear Mn₇Ln₃ complexes

The results of this section have recently been published in an article^[116] and are summarised here.

The synthesis of the [Mn^{III}₇Ln₃(O)₄(OH)₄(mdea)₃(piv)₉(NO₃)₃] series of compounds uses the assisted self-assembly approach, utilising the preformed Mn₆ cluster discussed in section 3.2 and the *N*-methyldiethanolamine (mdea) ligand as starting material.

The reaction of solid Ln(NO₃)₃·6H₂O with a slurry of [Mn₆O₂(piv)₁₀(pivH)₂(4-Me-py)₂] and *N*-methyldiethanolamine in MeCN at 70°C gives a dark-brown solution. The solution was stirred for 35 minutes, cooled down, filtered, and left to evaporate slowly at room temperature. Dark brown crystals of [Mn^{III}₇Ln₃(O)₄(OH)₄(mdea)₃(piv)₉(NO₃)₃] (Ln = Nd (**12**), Sm (**13**) and Eu (**14**)) suitable for X-Ray structure determination were obtained after one week. For the Gd analogue (**15**) small changes to the crystallisation method are necessary. Once the reaction solution is set up for crystallisation, it has to be filtered again after one day in order to remove any traces of recrystallised starting material. Dark colour crystals of (**15**) are then obtained after one week.

The complexes (**12**)-(15) are isostructural, however (**12**) and (**15**) crystallise in the triclinic space group $P\bar{1}$ while compounds (**13**) and (**14**) crystallise in the monoclinic space group $P2_1/n$. The crystal structure of (**12**) is described here. (**Figure 4.2-1**)

The core of (**12**) can be rationalised as a homometallic Mn₄^{III}(O)(OH)₃ cubane at the top connected to a second Mn^{III}Nd₃(O)₃(OH) cubane on the bottom of the molecule, connected via the middle Mn^{III}. (**Figure 4.2-2**)

The central Mn^{III} is bridged via three μ_4 -O²⁻ to the remaining three Mn^{III} arranged in a triangle on the outside of the cluster. As a result, the coordination environment for the central Mn^{III} only consists only of oxygens from the O²⁻ bridges, three in the cubane at the top and the other three inside the cubane on the bottom and bridging to the three Mn^{III} on the outside.

The outer Mn^{III} of the molecule are each chelated by a deprotonated mdea²⁻ ligand, with the deprotonated alcohol arms forming μ_2 -bridges to an Mn^{III} at the top and a

Nd^{III} on the bottom. The octahedral coordination sphere for the outer Mn^{III} is completed by two bridging pivalates. One of the pivalates is connected in a $\mu_2\text{-}\eta^1\text{:}\eta^1$ -bridging mode to the Nd^{III}, while the second one forms a $\mu_3\text{-}\eta^2\text{:}\eta^1$ -bridge between the Mn^{III} and two Nd^{III}. In addition to the bridging alcohol arm of the mdea²⁻ ligands and the O²⁻ bridge, the octahedral coordination environment for the three Mn^{III} on the top is completed via a bridging $\mu_3\text{-OH}^-$ and three bridging pivalates.

Similarly, the three Nd^{III} are also bridged by a $\mu_3\text{-OH}^-$ on the bottom. The Nd^{III} are all nine-coordinate with a coordination polyhedron that can be described as a distorted tricapped trigonal prism. In addition to the two $\mu_4\text{-O}^{2-}$, the $\mu_3\text{-OH}^-$, one deprotonated alcohol arm of the mdea²⁻ ligand and the three bridging pivalates, the coordination sphere of the Nd^{III} is completed by a chelating nitrate ion.

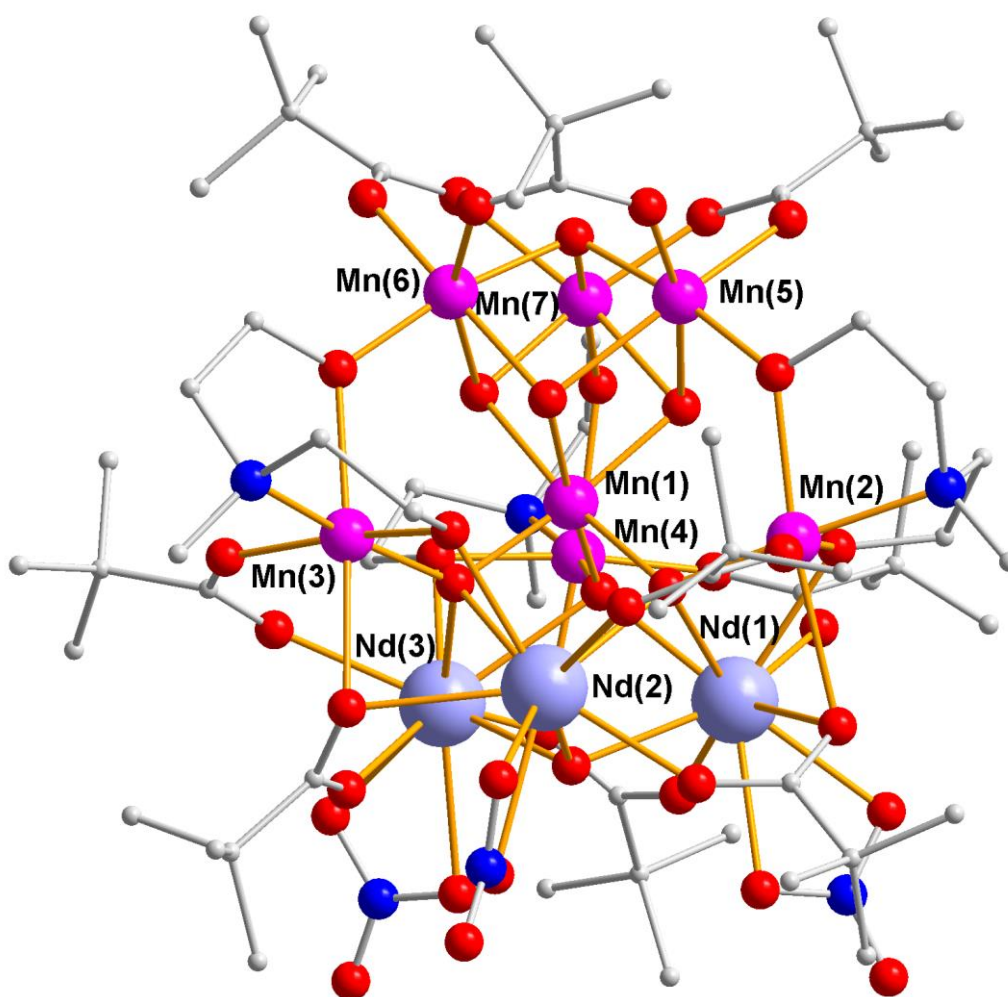


Figure 4.2-1 The molecular structure of $[\text{Mn}^{\text{III}}_7\text{Nd}_3(\text{O})_4(\text{OH})_4(\text{mdea})_3(\text{piv})_9(\text{NO}_3)_3]$ (**12**), H-atoms have been omitted for clarity.

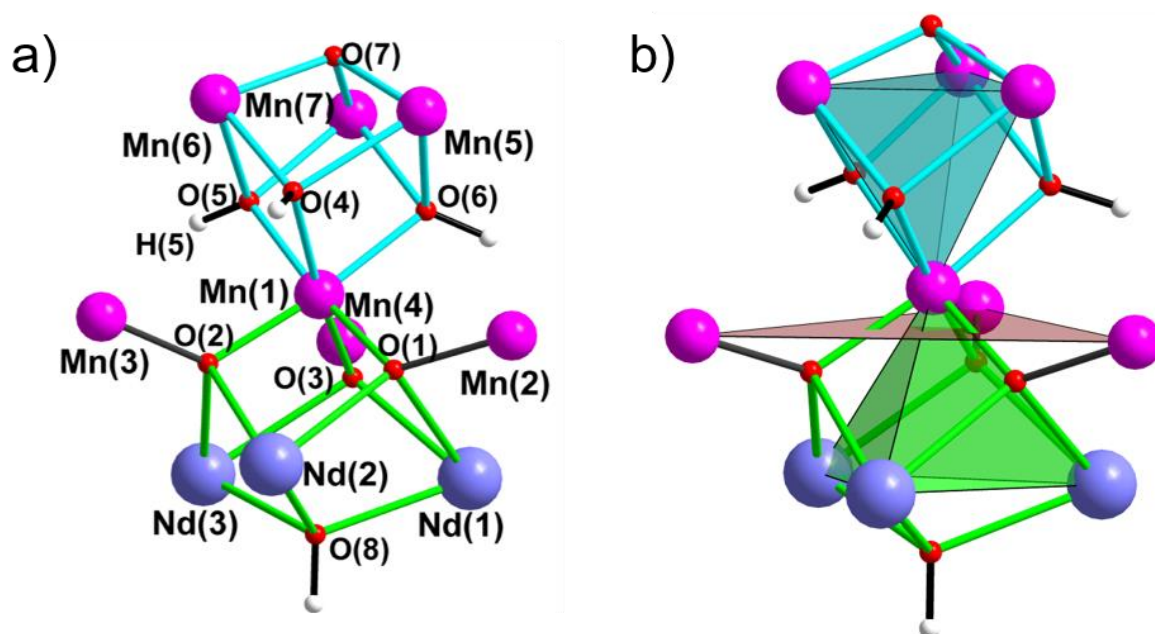


Figure 4.2-2 Visualisation of the core composition of $[\text{Mn}^{\text{III}}_7\text{Nd}_3(\text{O})_4(\text{OH})_4(\text{mdea})_3(\text{piv})_9(\text{NO}_3)_3]$ (**12**), two cubanes connected via the middle Mn^{III} are highlighted with green and light blue bonds respectively (a) and the resulting corner sharing tetrahedra (b).

There are no obvious interactions between two neighbouring clusters in the crystal structure, however they are aligned nicely with the parallel triangular plans of the top and bottom tetrahedra shown in **Figure 4.2-2 (b)** being oriented parallel to each other throughout the crystal packing. (**Figure 4.2-3**)

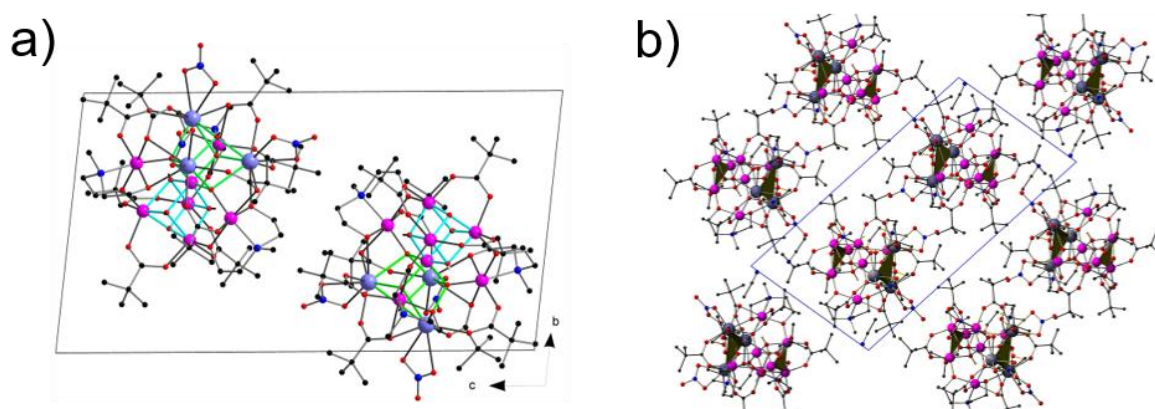


Figure 4.2-3 The unit cell of (**12**) shown along the crystallographic a-axis (a) showing no obvious interaction between two neighbouring complexes and the crystal packing of (**12**) along the crystallographic b-axis (b) highlighting the parallel arrangement of the triangular planes of the top and bottom tetrahedron shown in brown.

The magnetic properties of compounds (12)-(15) were investigated using SQUID magnetometry. The values for the temperature dependence of the magnetic susceptibility at room temperature are in relatively good agreement with the theoretical values, $23.42 \text{ cm}^3\cdot\text{K}\cdot\text{mol}^{-1}$ ($25.92 \text{ cm}^3\cdot\text{K}\cdot\text{mol}^{-1}$) for (12), $19.20 \text{ cm}^3\cdot\text{K}\cdot\text{mol}^{-1}$ ($20.50 \text{ cm}^3\cdot\text{K}\cdot\text{mol}^{-1}$) for (13), $24.07 \text{ cm}^3\cdot\text{K}\cdot\text{mol}^{-1}$ ($21.00 \text{ cm}^3\cdot\text{K}\cdot\text{mol}^{-1}$) for (14) and $45.00 \text{ cm}^3\cdot\text{K}\cdot\text{mol}^{-1}$ ($44.60 \text{ cm}^3\cdot\text{K}\cdot\text{mol}^{-1}$) for (15). Furthermore, the χT vs T curves for the Nd (12), Sm (13) and Eu(14) analogue show similar trends.

The χT values are essentially constant on lowering the temperature from 300K down to 150K after which they decrease to reach values of $6.13 \text{ cm}^3\cdot\text{K}\cdot\text{mol}^{-1}$ for (12), $3.72 \text{ cm}^3\cdot\text{K}\cdot\text{mol}^{-1}$ for (13) and $2.25 \text{ cm}^3\cdot\text{K}\cdot\text{mol}^{-1}$ for (14) respectively. The profiles of the χT curves suggest mostly antiferromagnetic interactions between the Mn^{III} centres. The fact that the low temperature χT values seem to reach a minimum value below 10K suggests that the spin ground states at low temperatures are well-defined.

Given that Eu^{III} is diamagnetic at low temperature and Sm^{III} is close to non-magnetic ($C = 0.09 \text{ cm}^3\cdot\text{K}\cdot\text{mol}^{-1}$) suggests a spin ground-state of $S = 2$ for the Mn^{III}_7 , a possible spin arrangement sees the spins in the cubane aligned ferromagnetically with those of the three outer Mn^{III} coupled antiferromagnetically, leaving one Mn^{III} spin uncompensated.

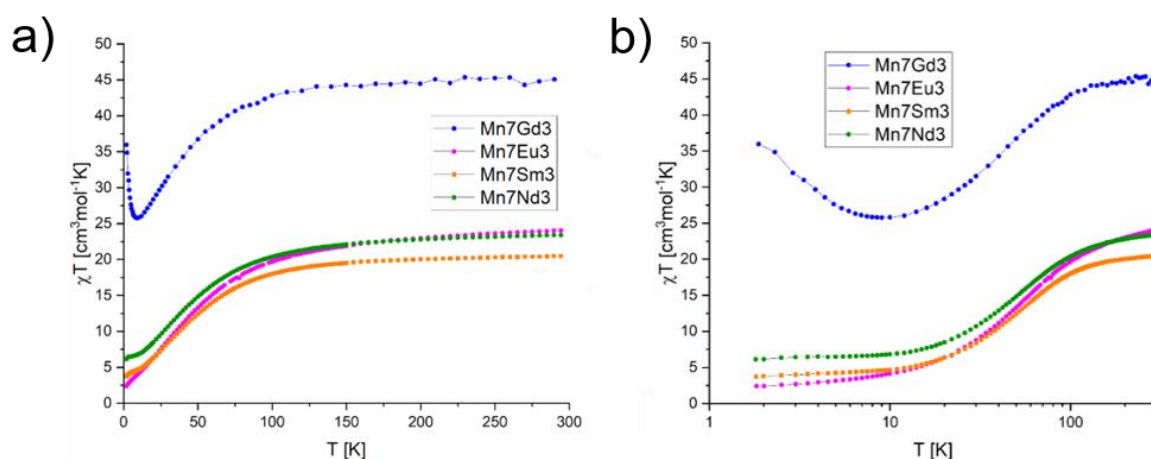


Figure 4.2-4 The temperature dependent dc susceptibility for the compounds (12)-(15) measured at 1000Oe in the 1.8-300K range (a) and a zoomed in logarithmic graph for the low temperature region (b).

For the Gd analogue (15) the χT value follows a similar trend with decreasing temperature between 300K to circa 15K, but unlike the previously described

measurements the χT value rises sharply from 15K down to 1.8K, reaching a value of $35.96 \text{ cm}^3 \cdot \text{K} \cdot \text{mol}^{-1}$. The χT value at 1.8K roughly corresponds to a spin ground-state of $S = 17/2$, which can be rationalized in a similar spin arrangement as for (13) and (14), but with a ferromagnetically coupled Gd^{III}_3 triangle (with $S = 21/2$), to which the residual $S = 4/2$ spin from the Mn_7 unit is coupled antiferromagnetically.

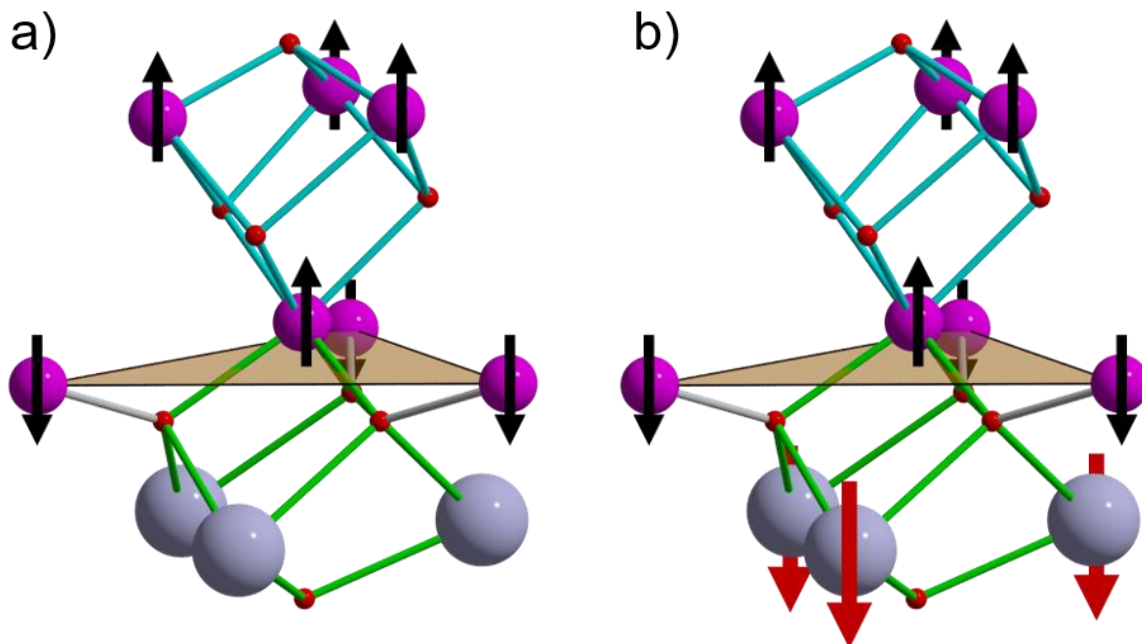


Figure 4.2-5 Rationalisation of the spin arrangement based on the results of the temperature dependent dc susceptibility for (13) (a) and (15) (b). In both cases the seven Mn^{III} are coupled in a way that results in an $S = 2$ residual spin, for (13) this is equal to the corresponding spin ground-state, while for (15) the residual spin is antiferromagnetically coupled to the three ferromagnetically coupled Gd^{III} amounting to a total spin ground-state of $S = 17/2$.

The magnetisation curve for the Gd^{III} analogue (15) shows no saturation even at higher fields. (**Figure 4.2-6**) In addition, there is an inflection point at an applied field of around 3.5 with $\mu_B = 18 \mu_B$ above which the magnetisation begins to rise again. This suggests that at higher fields and as a result of the population of higher lying states at higher fields, the residual spin of the Mn_7 is flipped to be parallel to that of the three Gd^{III} . This would result in an $S = 25/2$ state.

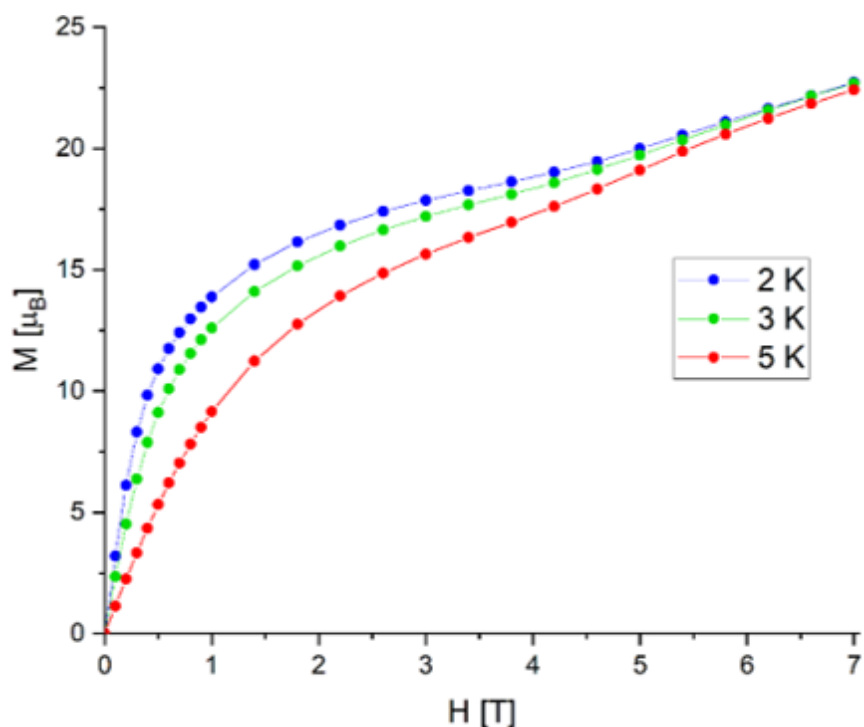


Figure 4.2-6 The magnetisation curve for $[\text{Mn}^{\text{III}}_7\text{Gd}_3(\text{O})_4(\text{OH})_4(\text{mdea})_3(\text{piv})_9(\text{NO}_3)_3]$ (**15**) at 2, 3 and 5K measured for applied dc fields from 0 to 7T.

Variable temperature ac susceptibility measurements under zero applied dc field were carried out on all four Mn_7Ln_3 complexes to probe the slow relaxation of magnetisation. The corresponding graphs are shown in **Figure 4.2-7**.

For the Eu^{III} analogue (**14**) no out-of-phase ac signal could be observed, while (**12**), (**13**) and (**15**) all show clear frequency dependent signals, both in-phase (χ') and out-of-phase (χ''), indicating slow relaxation of magnetisation characteristic of single-molecule magnets.

The Gd^{III} analogue (**15**) shows out-of-phase (χ'') signals below 3 K, but without visible maxima above 1.8 K. A possible rationalisation for the dynamic magnetic behaviour is that the Mn^{III}_7 moiety within the cluster shows small uniaxial anisotropy D , combined with the residual spin ground-state of $S = 2$ this does not result in a barrier U_{eff} sufficient enough to give observable slow relaxation at 1.8 K for the Eu^{III} analogue (**14**).

However, replacing the three Eu^{III} with three ferromagnetically coupled Gd^{III} in (**15**) increases spin ground state to $17/2$. Assuming that the anisotropy D is unchanged,

this would result in an increase of U_{eff} by a factor of ca. 18, resulting in observable slow relaxation, but without maxima at zero dc field.

The Nd (**12**) and Sm (**13**) analogues each display out-of-phase χ'' signals with maxima above 2.0 K. The corresponding Arrhenius-plots derived from the ac susceptibilities are shown in **Figure 4.2-8**. From these, energy barriers for the reversal of magnetisation could be calculated, resulting in $U_{\text{eff}} = 27.4\text{K}$ for (**12**) and 13.4K for (**13**), with pre-exponential factors of $\tau_0 = 3.6 \cdot 10^{-9}\text{s}$ and $2.1 \cdot 10^{-7}\text{s}$, respectively.

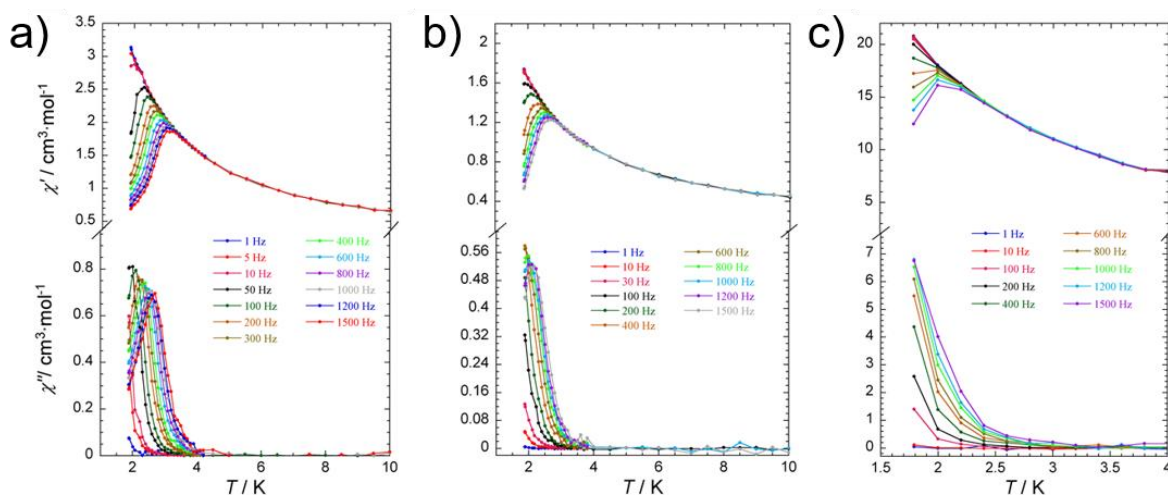


Figure 4.2-7 The temperature dependence of the in-phase (χ') and out-of-phase (χ'') ac susceptibility measured at varying frequencies with zero applied dc field for (**12**) (a), (**13**) (b) and (**15**) (c).

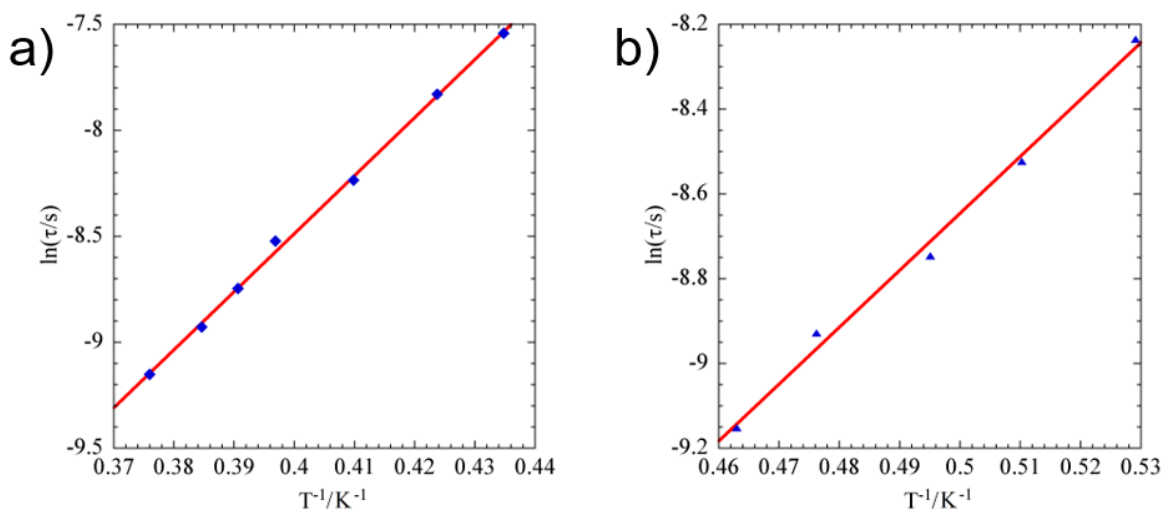


Figure 4.2-8 The Arrhenius plots derived from the ac susceptibility data for (**12**) (a) and (**13**) (b).

There is only a small number of Mn-4f SMMs incorporating the lighter lanthanides so far reported in the literature. It is reasonable to assume that a large part of the SMM behaviour arises from the anisotropy within the Nd₃ and Sm₃ triangles when comparing the out-of-phase data for (12) and (13) with those of (15)

It is worth noting that the anisotropy ellipsoids for Nd (oblate) and Sm (prolate) are inversely related to those of Er (prolate) and Dy (oblate). (**Figure 1.2-3**) Considering that most 3d-4f based SMMs incorporate Dy^{III} this is a valuable finding for the fundamental understanding of SMM behaviour for the lighter lanthanides.

4.3 Nonanuclear Mn₅Ln₄ complexes

This type of structure was previously reported^[43] for Ln = Tb, Dy, Ho, Er and Y with L = H₂O. For this thesis it was of interest to investigate whether it might be possible to expand the series across the whole lanthanide series.

The synthetic method is essentially the same as for the decanuclear compounds described above. Solid Ln(NO₃)₃·xH₂O is added to a suspension of N-methyldiethanolamine and [Mn₆O₂(piv)₁₀(pivH)₂(4-Me-py)₂] in MeCN. The reaction mixture is stirred under reflux for 40min, left to cool down, filtered and set aside for crystallisation. Brown crystals of [Mn₅Ln₄O₆(mdea)₂(mdeaH)₂(piv)₆(NO₃)₄(MeCN)₂] suitable for single crystal X-Ray diffraction are obtained after two weeks.

The Tb analogue (16) could be successfully resynthesised and compounds with an isostructural core for Ln = Er (17) and Tm (18) with L = H₂O were obtained. Additionally, structural variations of [Mn₅Ln₄O₆(mdea)₂(mdeaH)₂(piv)₆(NO₃)₄L₂] for Ln = Gd, where the water molecule in the structure is replaced by MeOH or iPrOH.

Furthermore, some crystals for Ln = Pr were obtained that showed the same unit cell, however the full structure could not be measured and no bulk measurements were done.

Given that the compounds are isostructural, the Er analogue (17) will be described here.

[Mn₅Er₄O₄(OH)₂(mdea)₄(piv)₆(NO₃)₄(H₂O)₂]·MeCN (17) crystallises in the triclinic space group $P\bar{1}$ with Z = 1, the unit cell volume is 2106.3Å³. Only half of a molecule

is within the asymmetric unit. The inversion centre is between two molecules and the central Mn^{III} in the centre of the molecule is situated on the unit cell edge. The core structure is essentially identical to that reported in the literature, however for (17) one of the bridging $\mu_3\text{-O}^{2-}$ is actually a $\mu_3\text{-OH}^-$, in turn both H₂mdea ligands are fully deprotonated, as opposed to two ligands being singly and the two being doubly deprotonated. (see **Figure 4.3-2**)

The core of (17) can be rationalised as two distorted Mn₂Er₂ cubanes, sharing the middle Mn^{IV}. (see **Figure 4.3-1**) The central Mn^{IV} in the centre of the molecular structure is coordinated by two $\mu_3\text{-O}^{2-}$ and $\mu_3\text{-OH}^-$ bridging to the two cubanes and two $\mu_4\text{-O}^{2-}$ bridging to the remaining Mn on the outside of the molecule. One of the Er^{III} ions is eight-coordinate, its coordination environment is made up of the two O²⁻ linking it to the central Mn^{IV} as well as a deprotonated alcohol arm of the mdea²⁻ ligand. Two pivalates are coordinated to this Er^{III}, one is bridging to a Mn^{III} inside the cubane, the other one is bridging to one of the Mn^{III} outside the cubane. The coordination environment of the Er^{III} is completed by a chelating nitrate anion and the coordinated water molecule.

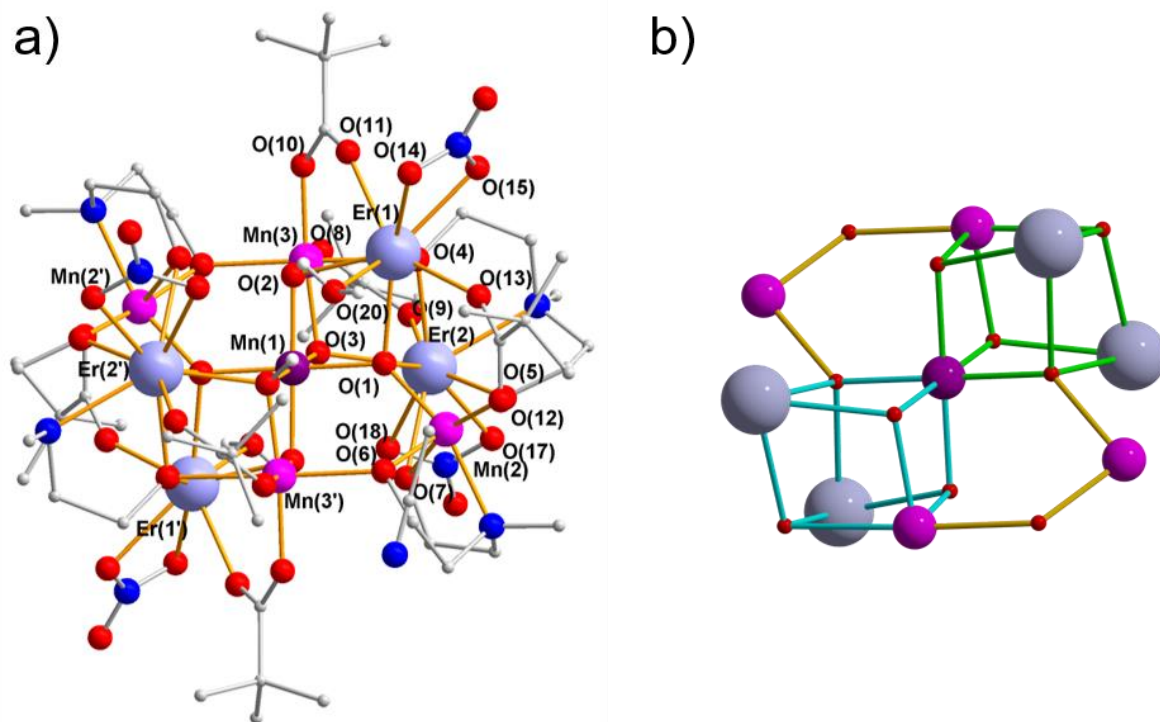


Figure 4.3-1 Molecular structure of $[\text{Mn}_5\text{Er}_4\text{O}_4(\text{OH})_2(\text{mdea})_4(\text{piv})_6(\text{NO}_3)_4(\text{H}_2\text{O})_2]\cdot\text{MeCN}$ (17) (a), the organic H-atoms and solvent MeCN have been omitted for clarity and scheme of the two distorted cubanes sharing the middle Mn^{IV} vertex (b).

The second Er^{III} is nine-coordinate, it is chelated by one of the mdea²⁻ ligands which is engaged in a $\mu_4\text{-}\eta^3\text{:}\eta^2\text{:}\eta^1$ -coordination mode, one of the deprotonated alcohol arms is bridging the three ions at the top of the cubane, while the second one is bridging to one of the outside Mn^{III}. Further chelation happens by a nitrate anion in addition to a bridging pivalate. Furthermore, the Er^{III} is coordinated by an O²⁻ and a OH⁻ the OH⁻ is μ_3 -bridging to the central Mn^{IV} and one of the Mn^{III} inside the cubane, the O²⁻ is engaged in a μ_4 -bridge connecting the two Er^{III} in the cubane, the central Mn^{IV} and one Mn^{III} on the outside. The coordination sphere on the Er^{III} is completed by the second deprotonated alcohol arm of one of the mdea²⁻ ligands which bridging to the Mn^{III} on the outside.

Finally, the Mn^{III} that are not part of the cubane unit are chelated by a deprotonated mdea²⁻ ligand engaged in a $\mu_3\text{-}\eta^2\text{:}\eta^2\text{:}\eta^1$ -coordination mode, bridging to an Er^{III} in one cubane and a Mn^{III} in the other cubane unit. The aforementioned deprotonated alcohol arm bridging to the Er^{III}, the $\mu_4\text{-O}^{2-}$ and a bridging pivalate complete the octahedral coordination sphere of the Mn^{III} on the outside of the cubane units.

The intermolecular Er-Er distance between two molecules is 7.92 Å.

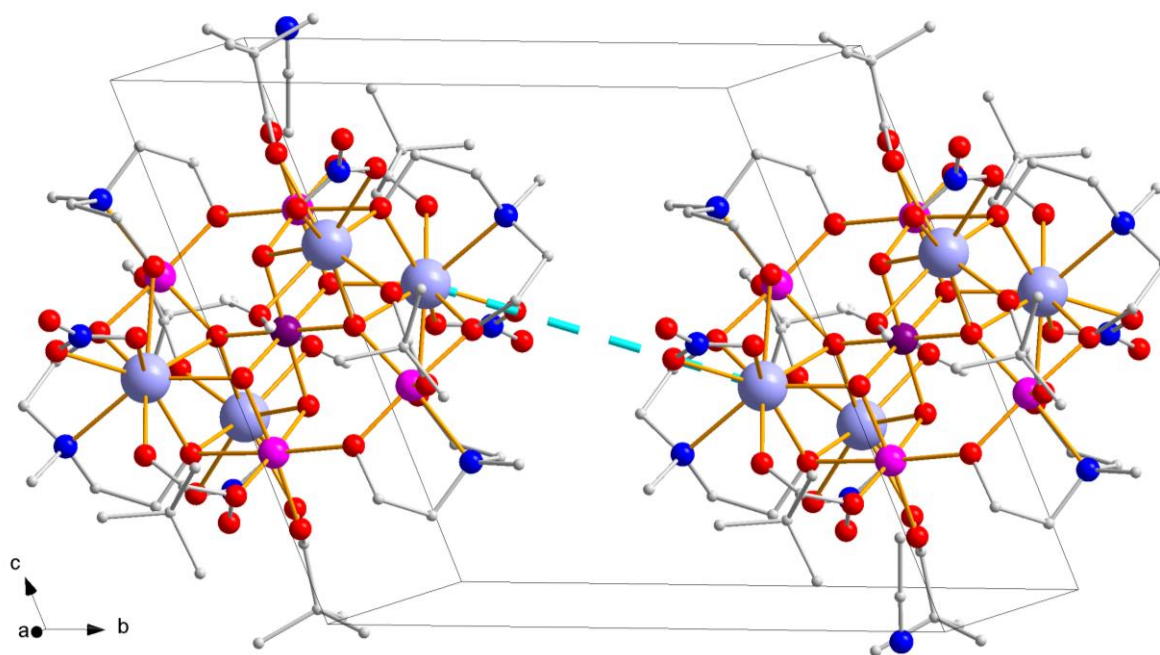


Figure 4.3-2 Unit cell of $[\text{Mn}_5\text{Er}_4\text{O}_4(\text{OH})_2(\text{mdea})_4(\text{piv})_6(\text{NO}_3)_4(\text{H}_2\text{O})_2]\cdot\text{MeCN}$ (**17**), highlighted in turquoise is the intermolecular Er-Er distance, organic H-atoms have been omitted for clarity.

In order to isolate compounds of the same composition with further lanthanides, attempts were made to modify the synthetic method. It was found that the synthesis for the lanthanides left of Tb is not pure, especially the Gd analogue showed various products.

By manipulating the reaction conditions and changing the solvent some progress could be made, although a synthetic method to get a pure product is still not realised.

Using the same reaction conditions but changing the solvent to methanol and iso-propanol, respectively.

$[\text{Mn}_5\text{Gd}_4\text{O}_6(\text{mdea})_2(\text{mdeaH})_2(\text{piv})_6(\text{NO}_3)_4(\text{iPrOH})]$ (**19**) crystallises in the triclinic space group $P\bar{1}$ with $Z = 1$. The unit cell volume is similar to that of (**17**) with 2149.9\AA^3 .

The core structure is essentially identical to that described for (**17**), but the Mn^{IV} is now situated in the middle of the unit cell. Leading to the centrosymmetry of the space group now being translated inside the molecule, rather than between two half molecules inside the space group. (**Figure 4.3-3**)

Furthermore, an isopropanol molecule has taken the position of the water molecule on Gd(1).

The intermolecular Gd-Gd distance of 9.18\AA in (**19**) is now significantly longer than that in (**17**). (see **Figure 4.3-4**)

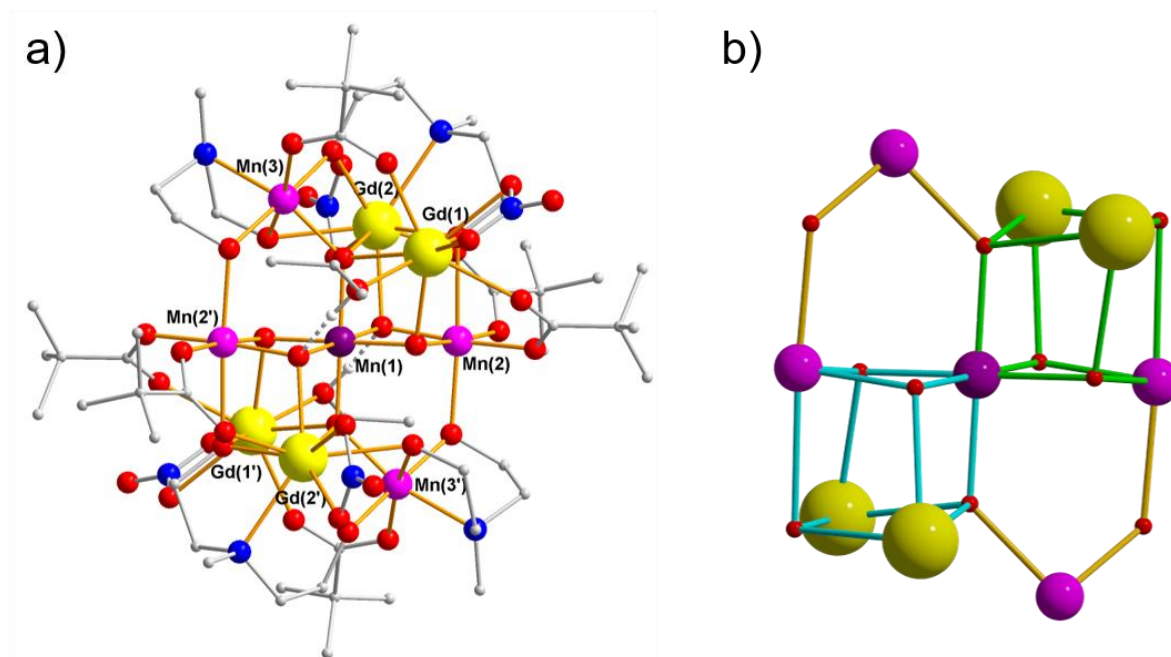


Figure 4.3-3 Molecular structure of $[\text{Mn}_5\text{Gd}_4\text{O}_6(\text{mdea})_2(\text{mdeaH})_2(\text{piv})_6(\text{NO}_3)_4(\text{iPrOH})_2]$ (19) (a), the organic H-atoms have been omitted for clarity and scheme of the two distorted cubanes sharing the middle Mn^{IV} vertex (b).

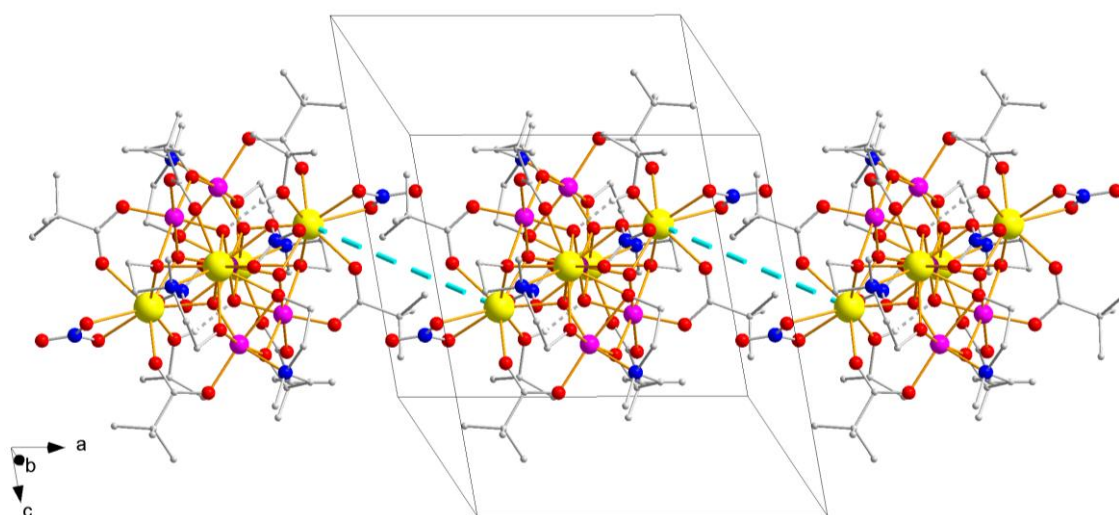


Figure 4.3-4 The Unit cell of $[\text{Mn}_5\text{Gd}_4\text{O}_6(\text{mdea})_2(\text{mdeaH})_2(\text{piv})_6(\text{NO}_3)_4(\text{iPrOH})_2]$ (19) with two adjacent molecules, highlighted in turquoise is the intermolecular Gd-Gd distance, organic H-atoms have been omitted for clarity.

For the reaction using methanol as solvent the resulting core structure also very similar to the two structures described above. However, there are a few key differences.

Firstly, all four of the H₂mdea ligands are now doubly deprotonated, to account for the charge balance, there are only two nitrate counterions present in the molecular structure. Secondly, for Gd^{III} are now both nine-coordinate, with the coordinating solvent molecule on Gd(1) now replaced by two MeOH molecules.

Finally, [Mn₅Gd₄O₆(mdea)₄(piv)₆(NO₃)₂(MeOH)₄] (**20**) crystallises in the triclinic space group $P\bar{1}$ with $Z = 2$ and a unit cell volume of 4583.8 Å³, resulting in a different crystal packing.

While the molecule itself still appears to be centrosymmetric, the unit cell is comprised of four quarters of one molecule on the cell edge along the crystallographic c-axis, while two halves of a molecule are located in the plane spanned by the b- and a-axes, the two molecules situated in the a-b-plane are oriented at a 65° angle compared to the four on the c-axes, caused by the γ angle of the unit cell.

This change in the orientation of the molecules is shown in **Figure 4.3-6** showing the unit cell of [Mn₅Gd₄O₆(mdea)₄(piv)₆(NO₃)₂(MeOH)₄] and is also visible in the crystal packing shown in **Figure 4.3-7**.

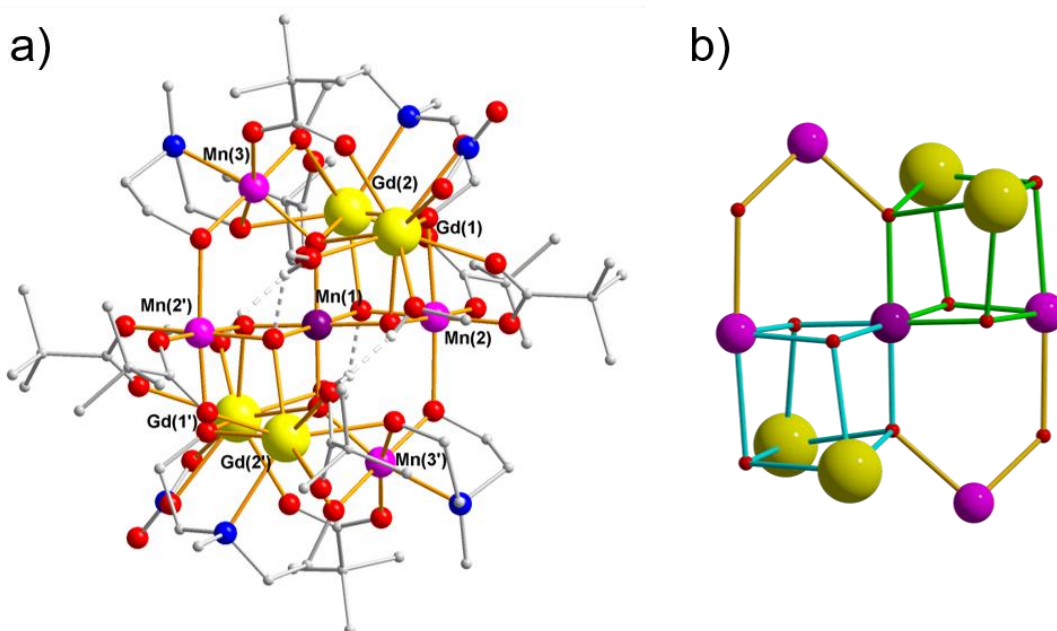


Figure 4.3-5 Molecular structure of [Mn₅Gd₄O₆(mdea)₄(piv)₆(NO₃)₂(MeOH)₄] (**20**) (a) with the organic H-atoms omitted for clarity and scheme of the two distorted cubanes sharing the middle Mn^{IV} vertex (b).

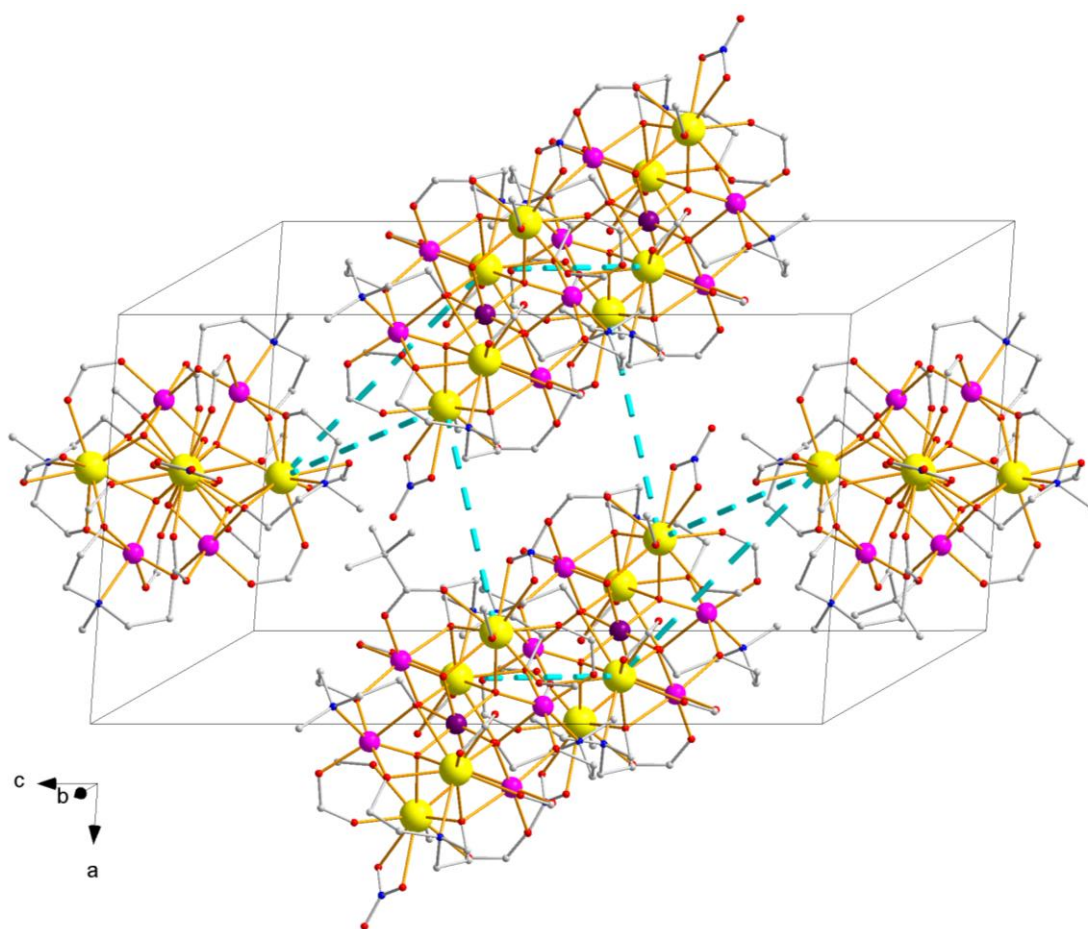


Figure 4.3-6 The Unit cell of $[\text{Mn}_5\text{Gd}_4\text{O}_6(\text{mdea})_4(\text{piv})_6(\text{NO}_3)_2(\text{MeOH})_4]$ (**20**), highlighted in turquoise are the closest intermolecular Gd-Gd distances, the 'Butyl-groups and organic H-atoms have been omitted for clarity.

The shortest intermolecular Gd-Gd distance in (**20**) is 8.80\AA located between the molecule in the a-b-plane and those on the c-axes, while the distance between two molecules situated on the c-axes is marginally shorter with 8.83

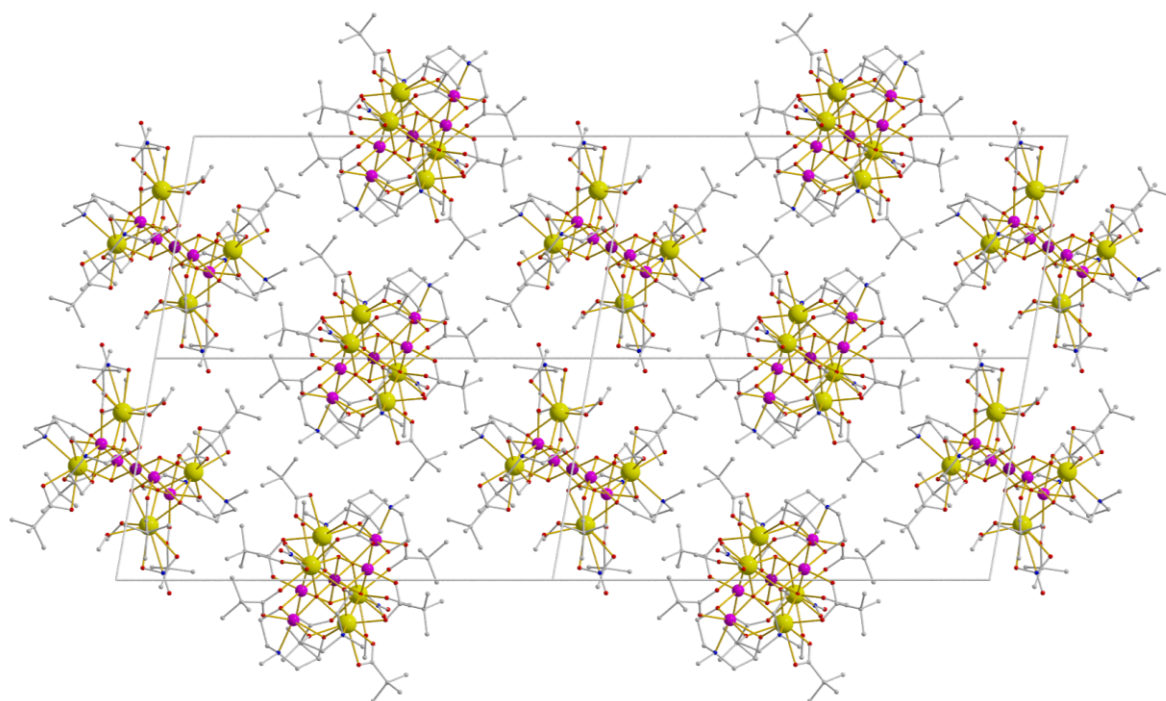


Figure 4.3-7 Crystal packing of **(20)** along the crystallographic a-axis highlighting the orientation of the two types of molecules caused by their position on the crystallographic axes.

It is very interesting to see, how changing the solvent used from MeCN to more protic solvents like iPrOH and MeOH changes the molecular structure of the compounds.

While the coordination of the alcohol solvents to the Gd^{III} is not completely surprising, since the original structure has a water molecule coordinated to the lanthanide, the effect this change has on the molecular structure, especially for **(20)** is remarkable.

The coordination of methanol leads to a change in the coordination number of one of the Gd^{III} from eight- to nine-coordinate. Furthermore, this leads to the H₂mdea ligands both being doubly deprotonated, as opposed to having two singly deprotonated Hmdea⁻ for the Er^{III} analogue **(17)**. The deprotonated alcohol arms of the ligands are heavily involved in hydrogen bonding with the hydrogen of the coordinated methanol molecules.

Due to the H₂mdea ligands in **(20)** being doubly deprotonated, the charge is only compensated by two coordinated nitrate counteranions, giving the complex a new composition.

4.4 Tetranuclear Mn_2Ln_2 complexes

The complex of the composition $[Mn_2Gd_2(OH)_2(mdeaH)_2(piv)_6(NO_3)_2] \cdot MeCN$ has been reported in the same article presenting the decanuclear compounds discussed in section 4.2.^[116]

It was noted, that for the synthesis of the decanuclear compounds showed a noticeable amount of by-product for the Gd^{III} analogue. Naturally, the goal was to isolate these by-products to purify the synthesis of the decanuclear complexes as well as investigate the composition of the by-products.

The compound $[Mn_2Gd_2(OH)_2(mdeaH)_2(piv)_6(NO_3)_2] \cdot MeCN$ (**21**) can be obtained in a mixture of the deca- and nonanuclear analogues presented in the previous sections.

The synthesis method was varied in terms of stoichiometry, reaction time and temperature, resulting in a new crystal structure being obtained for the Pr analogue. (**22**). Additionally, a third analogue of the compound with Nd was identified by a unit cell measurement.

Since the Pr analogue (**22**) represents a new addition to this family of compounds, its crystal structure is described here.

$[Mn_2Pr_2(OH)_2(mdeaH)_2(piv)_6(NO_3)_2] \cdot 2MeCN$ (**22**) crystallises in the triclinic space group $P\bar{1}$ with $Z = 2$, the inversion centre of the centrosymmetric space group lies in the middle of the molecule.

Compound (**22**) represents a type II butterfly according to the classifications explained in section 1.4. This means that the Pr^{III} ions are situated in the body positions of the butterfly, while the Mn^{III} occupy the positions in the wing-tips. (**Figure 4.4-1**)

Two μ_3 -OH⁻-groups bridge between the two Pr^{III} and one Mn^{III} . The Pr^{III} are bridged to one Mn^{III} by two pivalates, the bridging to the second Mn^{III} occurs via the deprotonated alcohol arm of one of the ligands. The coordination sphere of the Pr^{III} is completed by a chelating pivalate and nitrate ion.

The octahedral coordination environment of the Mn^{III} is completed by the chelating $Hmdea^-$ ligand, bridging to the Pr^{III} via the deprotonated alcohol arm, while the protonated alcohol arm is chelating the Mn^{III} .

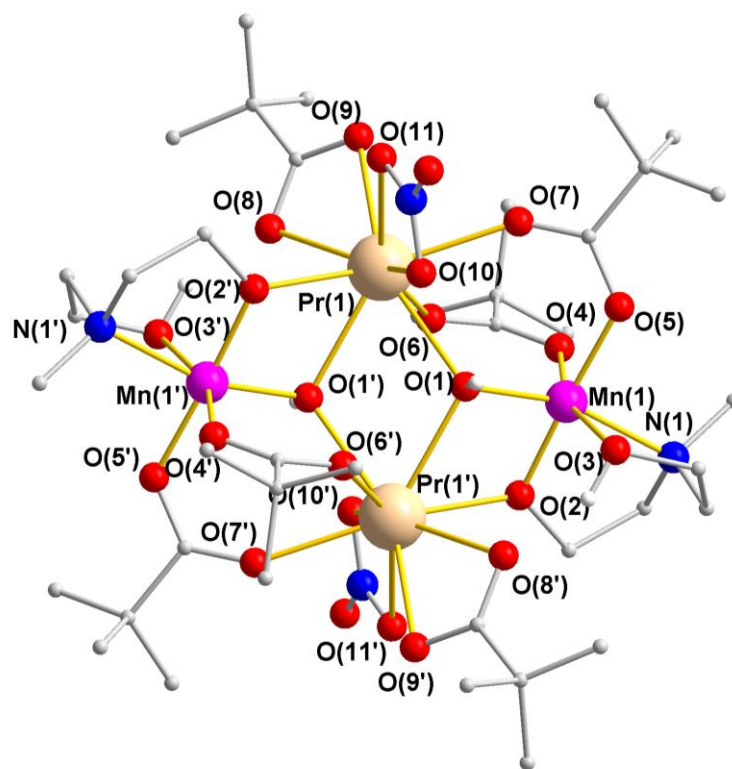


Figure 4.4-1 Molecular structure of $[\text{Mn}_2\text{Pr}_2(\text{OH})_2(\text{mdeaH})_2(\text{piv})_6(\text{NO}_3)_2] \cdot 2\text{MeCN}$ (**22**) with the organic H-atoms and solvent MeCN omitted for clarity.

There are no obvious intermolecular interactions observed, the shortest Mn-Mn distance is 8.58Å. (see **Figure 4.4-2**)

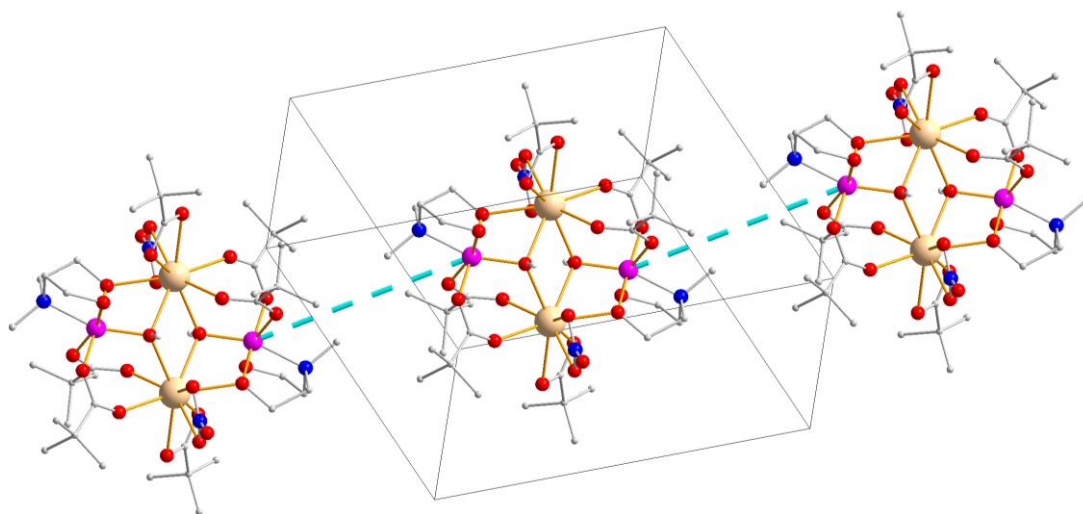


Figure 4.4-2 The Unit cell of $[\text{Mn}_2\text{Pr}_2(\text{OH})_2(\text{mdeaH})_2(\text{piv})_6(\text{NO}_3)_2] \cdot 2\text{MeCN}$ (**22**) with two adjacent molecules, highlighted in turquoise is the intermolecular Mn-Mn distance, organic H-atoms have been omitted for clarity.

The Compound $[\text{Mn}_2\text{Pr}_2(\text{OH})_2(\text{mdeaH})_2(\text{piv})_6(\text{NO}_3)_2]\cdot 2\text{MeCN}$ (**22**) represents a new addition to the already vast family of tetranuclear butterfly compounds. Additionally, it represents one of the rarer Type II butterflies, where the Ln^{III} ion is situated in the body positions, while the transition metal occupies the wingtip positions.

Furthermore, the introduction of Pr^{III} could potentially make this compound an interesting candidate for further magnetic studies. This is especially true given the anisotropy ellipsoid of Pr^{III} as was highlighted in section 1.1. Pr^{III} shows the same oblate anisotropy ellipsoid as is the case for Dy^{III} , which is very popular in molecular magnetism.

4.5 Summary of Mn-based coordination clusters

In this section the synthesis and magnetic characterisation of a series of Mn/4f coordination clusters was presented. The recipe follows previously published work by our group.^[43]

The synthesis uses the preformed $[\text{Mn}_6\text{O}_2(\text{piv})_{10}(\text{pivH})_2(4\text{-Me-py})_2]$ building block and N-methyldiethanolamine in an assisted self-assembly approach.

It was possible to expand the synthesis across the lanthanide series. It was previously believed that the nature of the lanthanide was the main factor to prompt a structure change from the Mn_5Ln_4 motif to the Mn_7Ln_3 motif, for $\text{Ln} < \text{Gd}$. For Gd we saw the synthesis resulting in a mixture of both of these structure types as well as a third tetranuclear Mn_2Gd_2 butterfly. The belief was that this is a result of the difference in ionic radius or element specific.

However, in the scope of this thesis it was possible to also produce the Mn_5Ln_4 structure type for Pr^{III} (identified via the unit cell parameters) as well as the Mn_2Ln_2 butterfly type for Pr^{III} and Nd^{III} (the latter one was also identified via the unit cell parameters), a more graphical overview can be found in **Table 4-1**, previously synthesised compounds that were analysed in the scope of this thesis are marked by a yellow checkmark, compounds found and analysed in this thesis are marked by a green checkmark.

Table 4-1 Overview of the various structure types discussed in this section over the course of the lanthanide series, yellow checkmarks highlight previously synthesised compounds, green checkmarks highlight compounds synthesised in the scope of this thesis.

	La	Ce	Pr	Nd	Sm	Eu	Gd	Tb	Dy	Ho	Er	Tm	Yb	Lu	Y	
Mn ₇ Ln ₃				✓	✓	✓	✓									✓
Mn ₅ Ln ₄			✓				✓	✓	✓	✓	✓	✓				
Mn ₂ Ln ₂			✓	✓			✓									

These findings suggest that it should be possible to obtain all three structure types over the whole lanthanide series by changing the reaction conditions accordingly.

It is also worth highlighting that for the Nd^{III} and Sm^{III} analogues of the Mn₇Ln₃ series discussed in section 4.2 slow relaxation of magnetisation was observed. These analogues represent new additions to the small number of Nd^{III} and Sm^{III} SMMs, this is especially remarkable as the shape of their anisotropy ellipsoids is the opposite shape than that of their respective counterparts Er^{III} and Dy^{III}.

Potential future work would involve further tweaking of the reaction conditions to isolate more structural analogues across the lanthanide series, as well as the magnetic characterisation of potentially interesting candidates found so far.

5 Fe-based coordination clusters

5.1 Tetranuclear M_2Ln_2 complexes

5.1.1 Introduction

As was shown in recent reviews,^[45, 117] and briefly discussed in section 1.4, the M_2Ln_2 “butterfly” cluster type can be used as a very useful “test-bed” to investigate the influence of various parameters on the magnetic and electronic properties within mixed transition metal lanthanide complexes. (see **Figure 5.1-1**)

Thus these robust systems, that can be subtly manipulated by the use of different ligands, co-ligands, solvents and metals are of huge importance for the fundamental understanding of molecular magnetism.

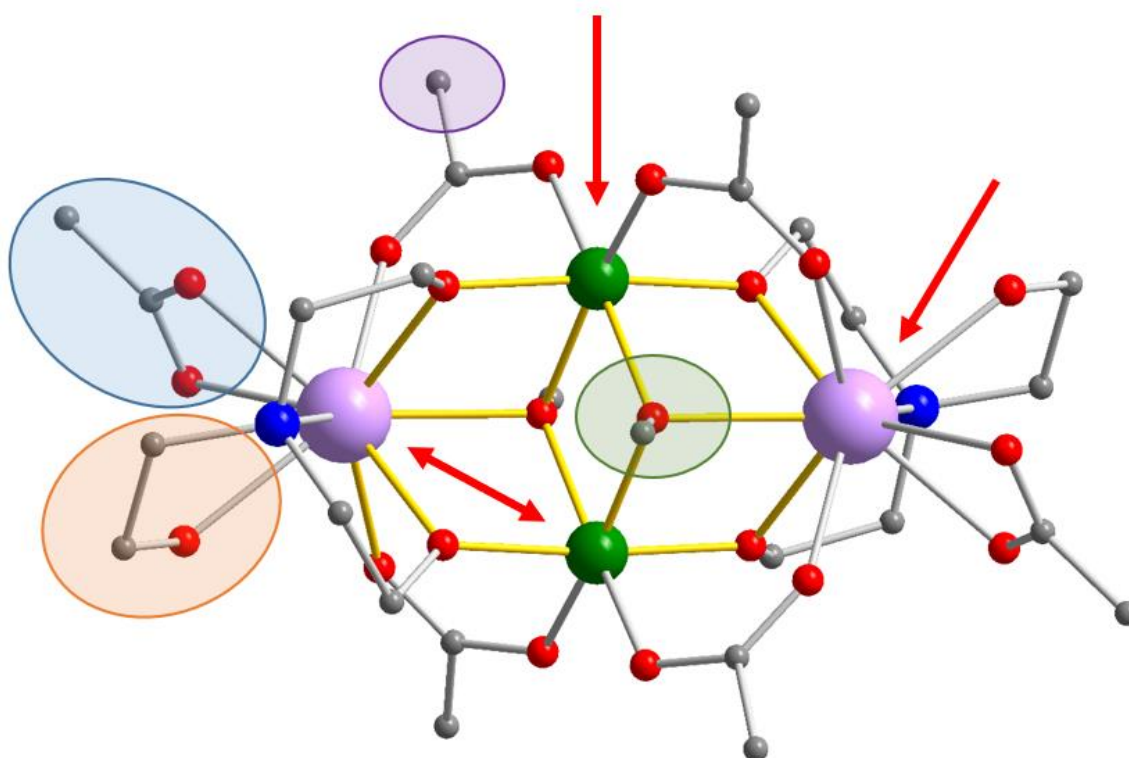


Figure 5.1-1 Scheme highlighting the possible variations in the M_2Ln_2 butterflies using the triethanolamine ligand. Coloured circles represent the nature of the bridging carboxylate (violet), μ_3 -bridging ligand (green), chelating co-ligand (blue) and substitution of the ligand (orange). Red arrows refer to the possibility of replacing the metal ions used and changing from type I to type II butterflies by changing the position of the transition metal and rare earth ions.

In the scope of this chapter a few selected examples of this structure type resulting from the reaction of trinuclear starting materials such as those discussed in section 3.1 are presented. The different reaction routes starting from transition metal triangles was highlighted in a recent publication,^[27] and a modified scheme illustrating how these compounds can be formed is shown in **Figure 5.1-2**. Here the new routes to chiral and other butterfly compounds are highlighted with the red arrows.

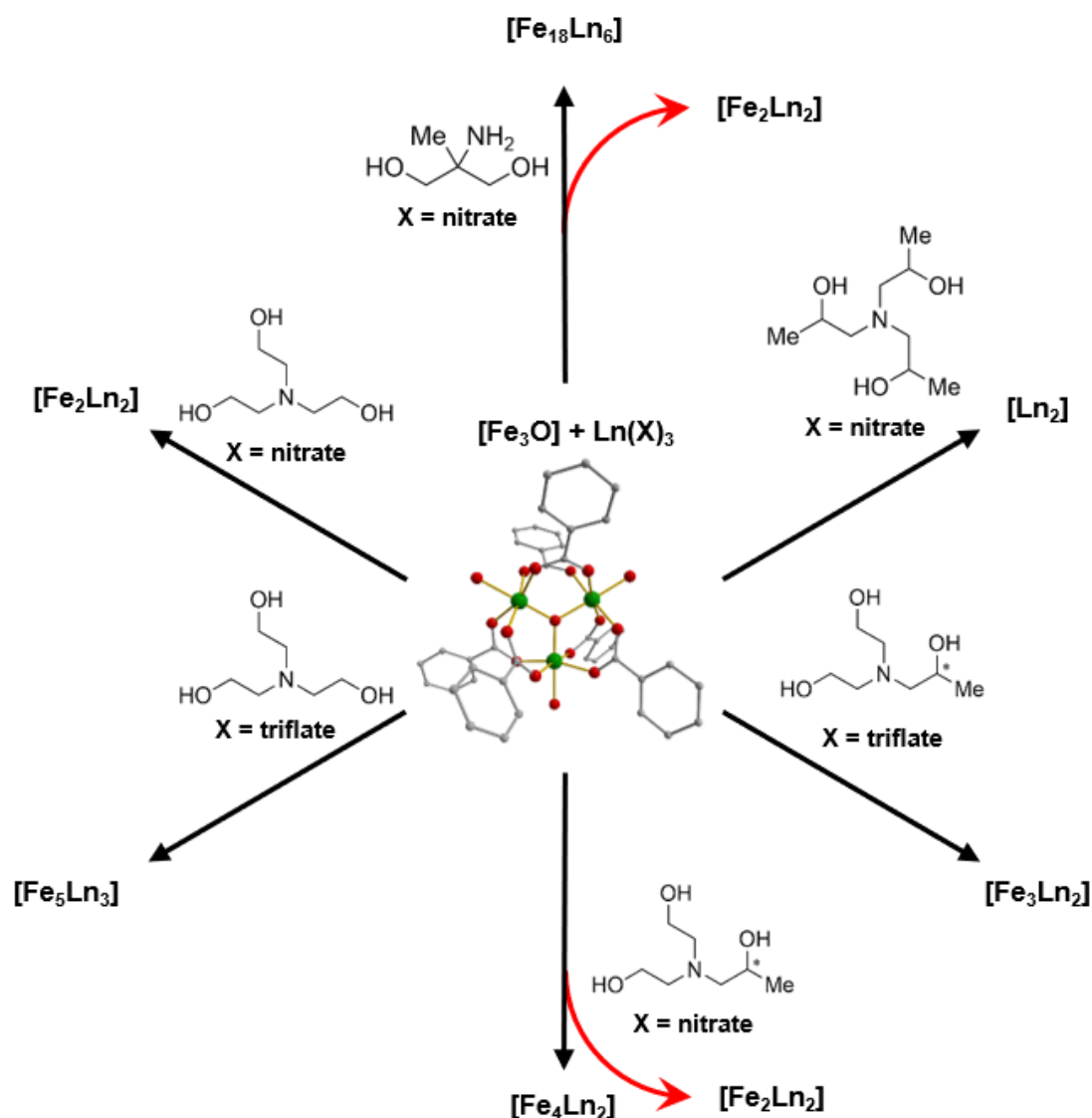


Figure 5.1-2 Synthetic strategy for obtaining Fe-Ln based coordination clusters, based on reference ^[27], the additional red arrows highlight the modified strategies discussed in sections 5.1.2 and 5.1.3.

5.1.2 $[M_2Ln_2(ampd)_4(O_2C-Ph)_6]$ synthesised with 2-amino-2-methyl-1,3-propanediol

In this synthetic approach the method to obtain the Fe_2Ln_2 butterfly core motif using the tripodal triethanolamine ligand is modified. The ligand used in this procedure is 2-amino-2-methyl-1,3-propanediol (H_2ampd), which is similar to the $teaH_3$ ligand and its derivatives used in many literature compounds^[40, 118-120] in that it can also adopt an O-N-O coordination pattern, but due to the structural composition it should be harder for the nitrogen atom to adopt a chelating position, since the tertiary carbon carrying the amino- and alcohol groups is essentially fixed in a tetrahedral angle. This effectively gives H_2ampd a similar tripodal type, but it should be more rigid compared to $teaH_3$. (Figure 5.1-3)



Figure 5.1-3 Skeletal formula of 2-amino-2-methyl-1,3-propanediol (H_2ampd).

$[M_3O(O_2C-Ph)_6(H_2O)_3]NO_3$ is dissolved in MeCN and 2-amino-2-methyl-1,3-propanediol and $Ln(NO_3)_3 \cdot 6H_2O$ are also dissolved separately in MeCN. Both solutions are stirred for 15 minutes. Afterwards the homogeneous suspension containing the Ln salt and ligand are dropwise added to the solution of the transition metal triangle. The reaction mixture is heated to $80^\circ C$ for 1h, cooled down and filtered, single crystals of $[M_2Ln_2(\mu_3-ampd)_4(O_2C-Ph)_6]$ suitable for single crystal X-Ray diffraction are obtained after 3 days. This reaction adds yet another reaction pathway to the scheme shown in Figure 5.1-2.

$[Fe_2Gd_2(ampd)_4(O_2C-Ph)_6]$ (**23**) was synthesised using the $[Fe_3O(O_2C-Ph)_6(H_2O)_3]NO_3$ starting material and $Gd(NO_3)_3 \cdot 6H_2O$. Compound (**23**) crystallises in the triclinic space group $P\bar{1}$ with $Z = 1$, the inversion centre of the centrosymmetric space group lies in the middle of the molecule, putting half of the molecule in the asymmetric unit.

[Fe₂Gd₂(ampd)₄(O₂C-Ph)₆] represents a type I butterfly, meaning that the Fe^{III} ions are situated in the body position, whilst the Gd^{III} ions occupy the wing-tip positions. The position of the bridging μ₃-OR groups in the middle of the cluster is occupied by two deprotonated ampd²⁻ ligands bridging the body and wing-tip positions.

The Gd^{III} ions are chelated by one benzoate, another μ₂-η¹:η¹-benzoate bridges between the Gd^{III} and Fe^{III}. Two different types of coordination modes are observed for the ampd²⁻ ligands. The first ampd²⁻ ligand is chelates to the Gd^{III} with one of the deprotonated alcohol arms and the amino group, whilst the second deprotonated alcohol arm forms a μ₂-bridge to the Fe^{III}. The second ampd²⁻ ligand chelates to the Fe^{III} with one of the deprotonated alcohol arms forming a μ₃-bridge between the Gd^{III} and the two Fe^{III} centres whilst the second alcohol arm is involved in another μ₂-bridging mode between the Fe^{III} and the other Gd^{III}. The amino-group is also coordinated to the Fe^{III}. Thus, the coordination sphere of the Fe centres is O₅N. The O₈N coordination sphere of the Gd^{III} is completed by a monodentate benzoate. The second oxygen of the carboxylate group of this benzoate is hydrogen bonded to both amino groups of the two ampd²⁻ ligands.

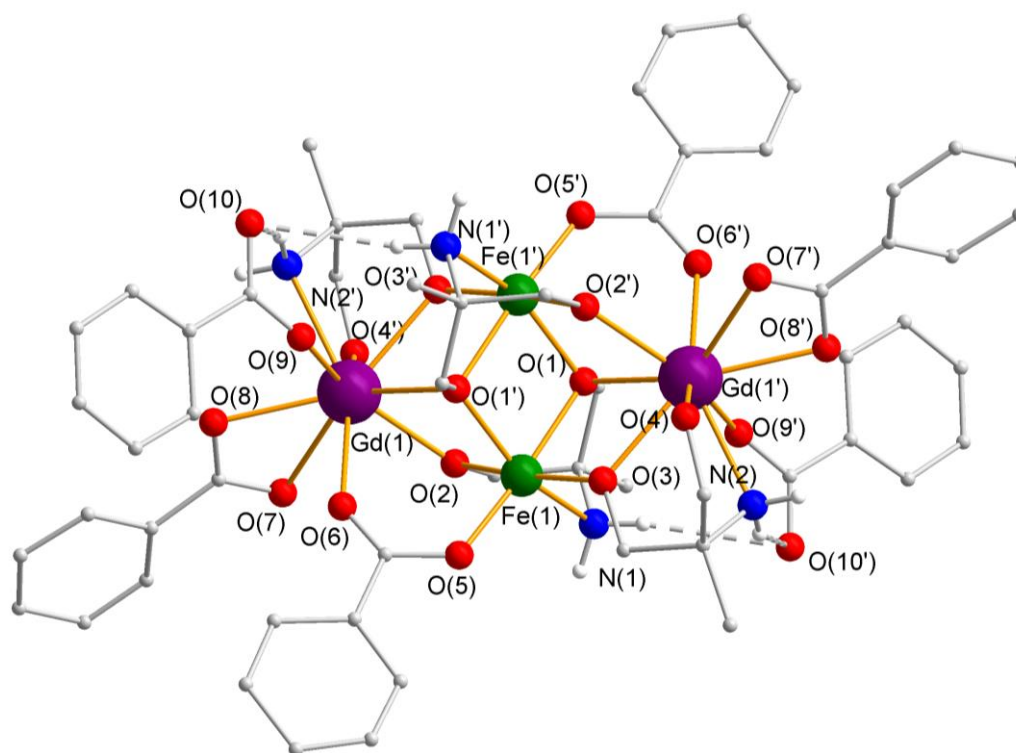


Figure 5.1-4 The molecular structure of [Fe₂Gd₂(ampd)₄(O₂C-Ph)₆] (**23**), dashed lines symbolise the hydrogen bonds between the amino group and monodentate benzoate, organic H-atoms omitted for clarity.

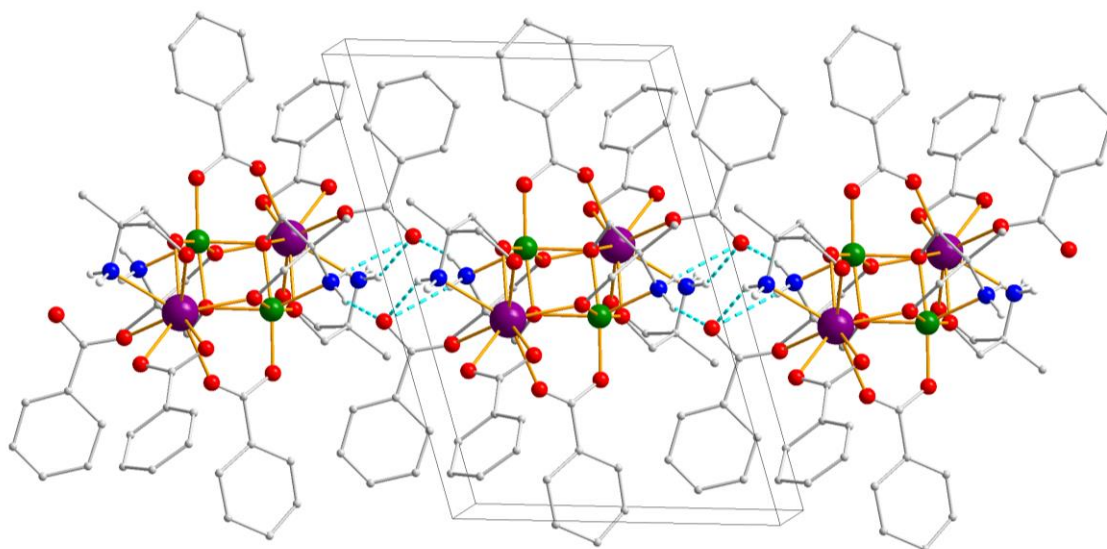


Figure 5.1-5 Unit cell of $[\text{Fe}_2\text{Gd}_2(\text{ampd})_4(\text{O}_2\text{C-Ph})_6]$ (**23**) with two adjacent molecules of the crystal structure, highlighted in turquoise are the hydrogen bonds between the amino groups and monodentate benzoates, interconnecting the molecules.

There is significant hydrogen bonding present, both intra- and also intermolecularly, as is shown in **Figure 5.1-5**. The hydrogen bonding leads to a nicely packed arrangement of (**23**), arranging the molecules into 1D chains along the crystallographic axis. (see **Figure 5.1-6**)

It was not possible to investigate the magnetic properties of (**23**) at this time, but given the composition of the compound, having replaced the bridging $\mu_3\text{-OR}$ with one of the alcohol arms of the ligand compound (**23**) is definitely an interesting candidate for further magnetic studies. The coordination mode of the ligand could provide additional exchange pathways, potentially impacting magnetic behaviour.

Furthermore, there are potential subtle changes that can be made to the ligand and the nature of the trinuclear starting material, as the core structure seems to be rather rigid, as is usually the case with the butterfly motif.

One such modification could be to introduce chirality, modifying only one of the alcohol arms of H_2ampd could introduce a chirality centre at the tertiary carbon in the middle.

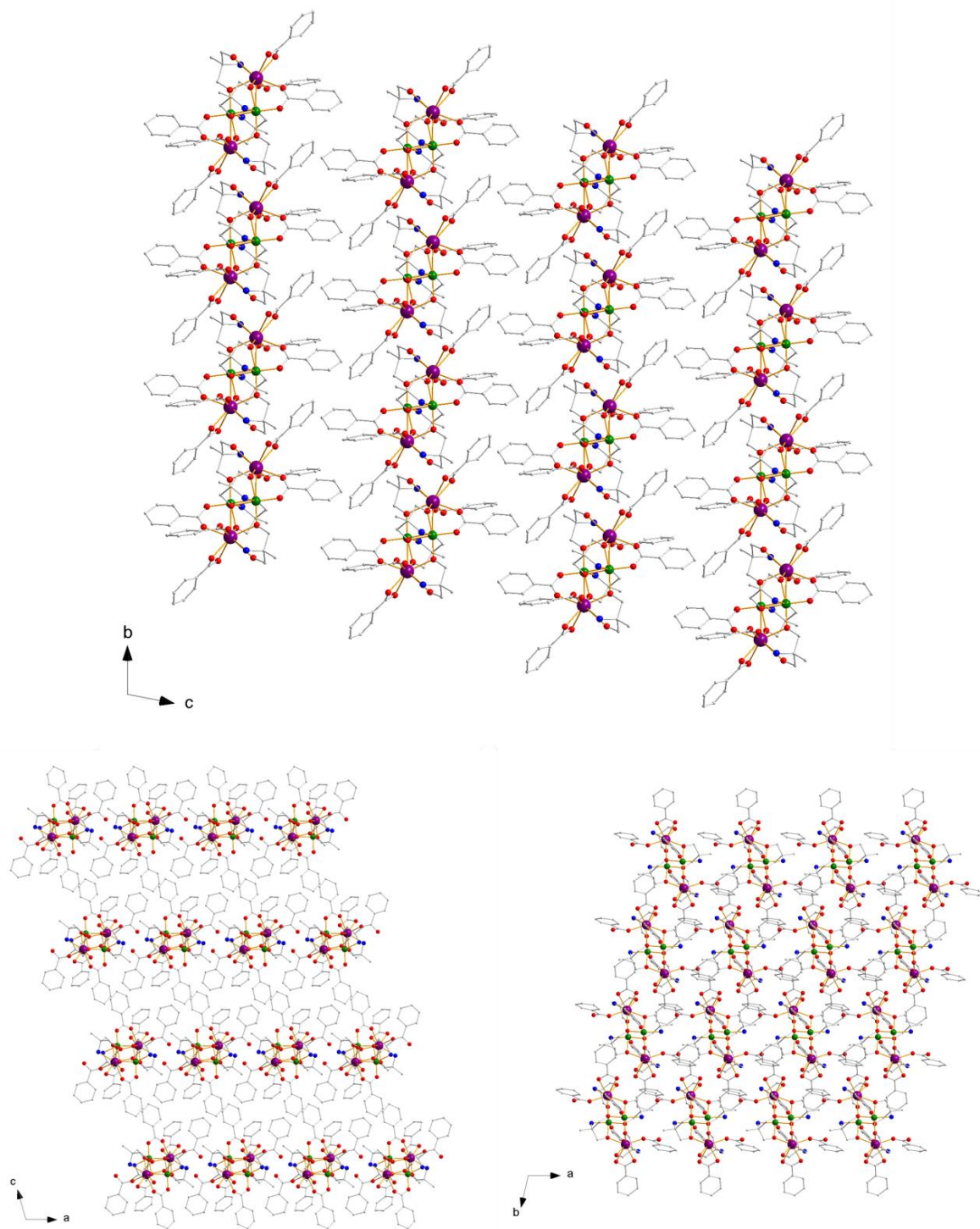


Figure 5.1-6 The crystal packing of $[\text{Fe}_2\text{Gd}_2(\text{ampd})_4(\text{O}_2\text{C-Ph})_6]$ (**23**) along its crystallographic a-, b- and c-axis, the view along the a- and b-axis highlights the chain-like arrangement caused by the hydrogen bonding.

After the successful synthesis of a new tetranuclear complex using the H₂ampd ligand the synthesis was changed using a different triangular starting material to incorporate different transition metals into the system.

Compounds **(24)** and **(25)** are obtained by the same reaction as compound **(23)** but using the trinuclear [Cr₃O(O₂C-Ph)₆(H₂O)₃]NO₃ starting material and Y(NO₃)₃·6H₂O (**(24)**) or Dy(NO₃)₃·6H₂O respectively. The compounds are isomorphous, the Y^{III} analogue will be described here.

[Cr₂Y₂(ampd)₄(O₂C-Ph)₆]·MeCN (**(24)**) crystallises in the triclinic space group $P\bar{1}$ with $Z = 2$. Contrary to **(23)** the inversion centre is not inside the molecule but there are two separate halves of the molecule inside the asymmetric unit. The core structure is similar to that of **(23)** with two doubly deprotonated ampd²⁻ ligands and two benzoates bridging the inner Cr^{III} ions and the outer Y^{III} ions, however instead of having a chelating and a monodentate benzoate completing the coordination sphere of the Y^{III}, it is now eight coordinate with both benzoates being monodentate. (see **Figure 5.1-7**)

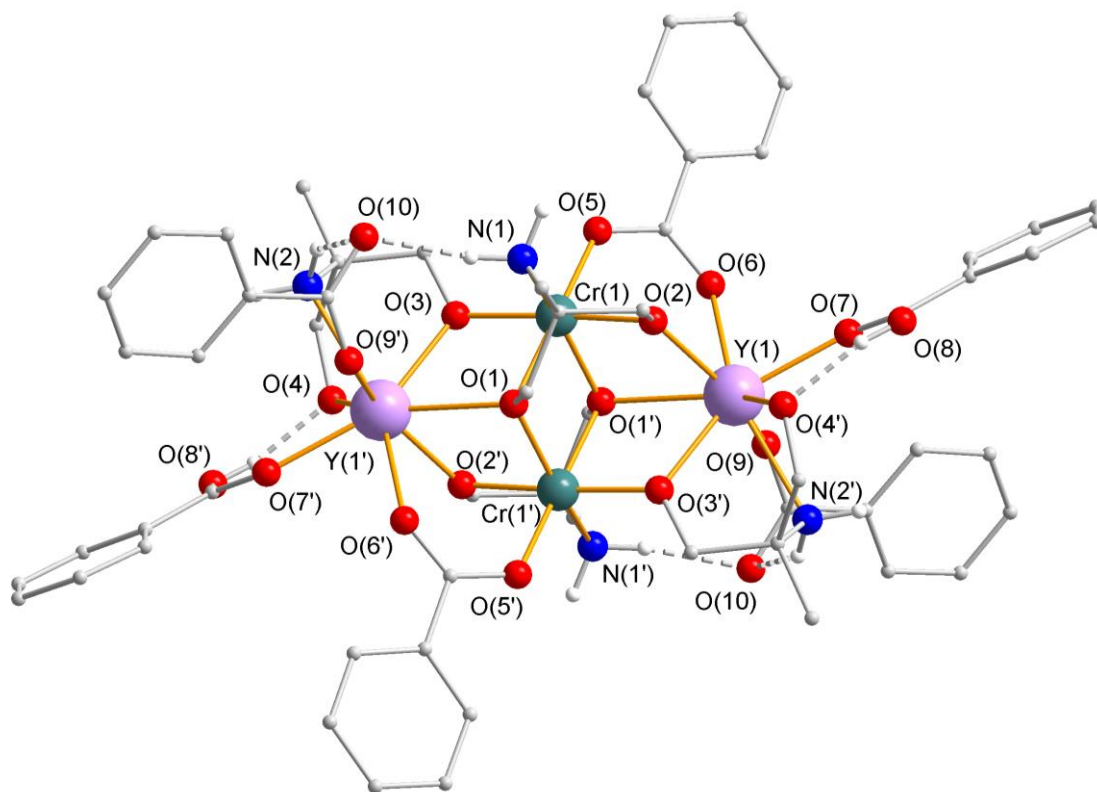


Figure 5.1-7 The molecular structure of [Cr₂Y₂(ampd)₄(O₂C-Ph)₆]·MeCN (**(24)**), dashed lines show the hydrogen bonding between the deprotonated monodentate benzoates. Organic H-atoms have been omitted for clarity.

The deprotonated benzoates form hydrogen bonds to both amino groups of the ampd^{2-} ligands.

It is worth noting that in contrast to **(23)** there is no obvious intermolecular hydrogen bond interaction taking place. There seems to be however an interaction taking place with the solvent MeCN molecule. The lack of strong hydrogen bond interaction as was the case for **(23)** leads to a less densely packed structure, as evidenced by the packing diagrams shown in **Figure 5.1-8**.

Despite the differences in terms of the crystal structure resulting from the chelating benzoate being monodentate for **(24)** and **(25)**, the synthetic success of introducing a different transition metal into the complex by using the corresponding trinuclear starting material is proof of the adaptability of the synthesis.

Subsequent synthesis with other trivalent triangles were so far unsuccessful. However, the ability of the ligand system to adopt nearly identical core structures for different transition metals used highlights the robustness of the butterfly test-bed and prompts further investigations of possible variations of the synthetic strategy using the H_2ampd ligand.

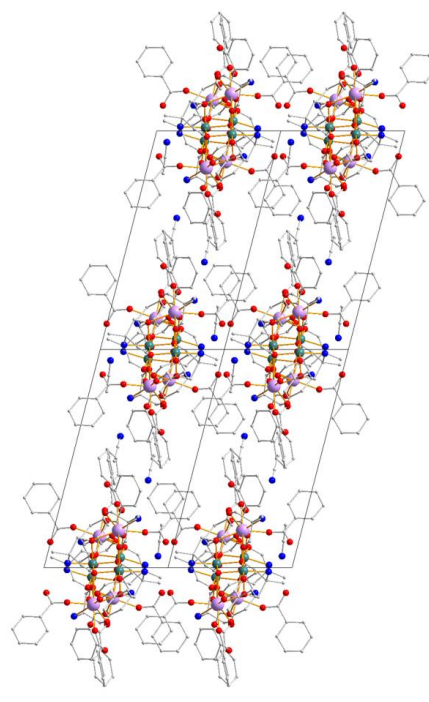
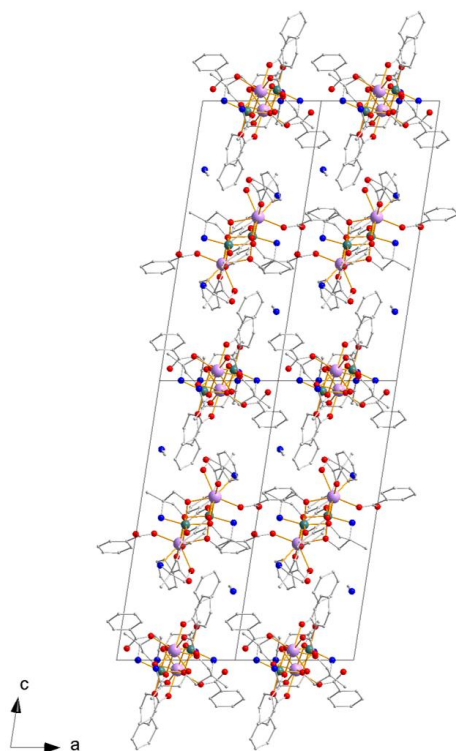
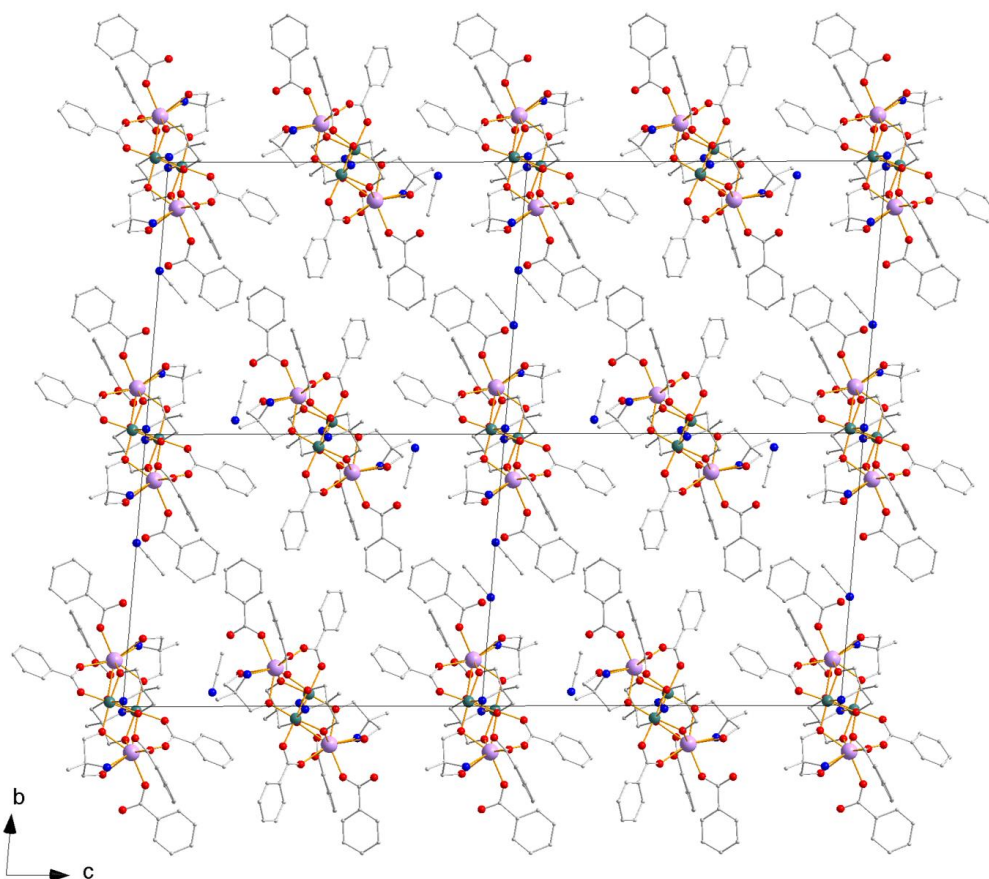


Figure 5.1-8 The crystal packing of $[\text{Cr}_2\text{Y}_2(\text{ampd})_4(\text{O}_2\text{C-Ph})_6]$ (**24**) along its crystallographic a-, b- and c-axis.

5.1.3 $[\text{Fe}_2\text{Dy}_2(\mu_3\text{-OH})_2(\text{Me-teaH})_2(\text{O}_2\text{C-Ph})_6]$ synthesised with the chiral Me-teaH₃ ligand

The principle of using a “test-bed” like the M_2Ln_2 butterfly system is to make subtle changes to an established system and observe the influence these changes have on the reaction as well as the magnetic and electronic behaviour of the final product. One such attempt was the functionalisation of the tripodal triethanolamine ligand by substituting a hydrogen atom on one of the ethanol arms with a methyl group, causing a chiral centre at the substituted carbon. (see **Figure 5.1-9**) The results of this synthetic approach are published in a recent article^[121] and are summarised here.

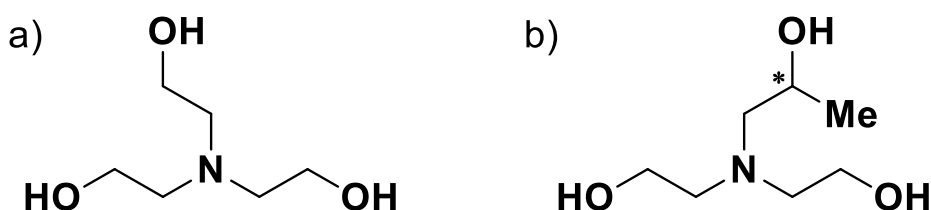


Figure 5.1-9 Skeletal formulas of the tripodal ligands Triethanolamine (teaH₃) (a) and the chiral [N,N-bis-(2-hydroxyethyl)-amino]-2-propanol (Me-teaH₃) (b) with the chiral carbon marked with a star.

It was found that the reaction of $[\text{Fe}_3\text{O}(\text{O}_2\text{C-Ph})_6(\text{H}_2\text{O})_3]\text{NO}_3$ with *rac*-Me-teaH₃ and $\text{Dy}(\text{NO}_3)_3 \cdot 6\text{H}_2\text{O}$ in a mixture of MeCN and MeOH at 50°C for 35min yields crystals of $[\text{Fe}_2\text{Dy}_2(\mu_3\text{-OH})_2(\text{Me-teaH})_2(\text{O}_2\text{C-Ph})_6]$ (**26**) after 12h.

Compound (**26**) crystallises in the triclinic space group $P\bar{1}$ with one molecule in the unit cell and thus the asymmetric unit corresponds to half of the molecule. The inversion centre naturally relates the R- and S-versions of the racemic ligand. Usually this leads to a 50:50 disorder of R- and S-enantiomers within the asymmetric unit of the unit cell and thus crystal structure, at least in most known cases for 3d ions, but here the 4f ion seems to enable the perfect chiral separation of the two enantiomers within the molecule and thus crystal structure. (**Figure 5.1-10 a**)

One alcohol arm chelating the Dy^{III} remains protonated and for the racemic Me-teaH₃ this is the substituted alcohol arm which is probably the result of the induced weaker acidity of the alcohol function. The two other deprotonated alcohol arms form η^2 -bridges between the Dy^{III} and Fe^{III}. Furthermore, two $\mu_2\text{-}\eta^1\text{:}\eta^1$ -benzoates bridge the Dy^{III} and Fe^{III}. The coordination sphere of the Dy^{III} is completed by a chelating benzoate and a $\mu_3\text{-OH}$ which connects a wingtip Dy^{III} to both body Fe^{III} ions. The

octahedral coordination sphere of the Fe^{III} is thus constituted by O atoms from the four bridging carboxylates and the two $\mu_3\text{-OH}$.

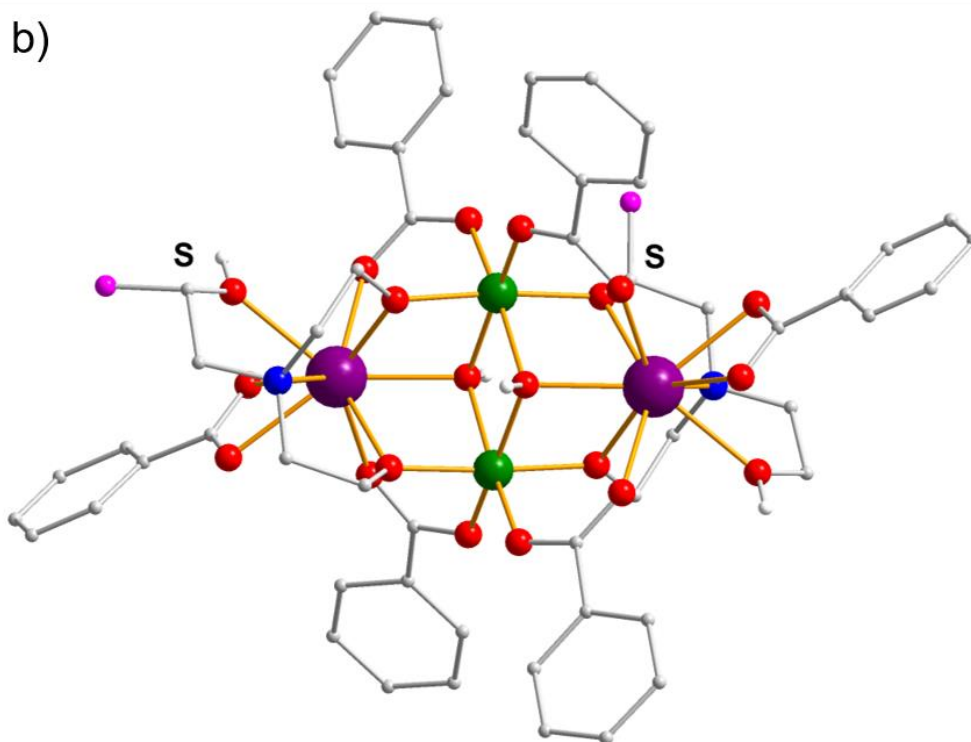
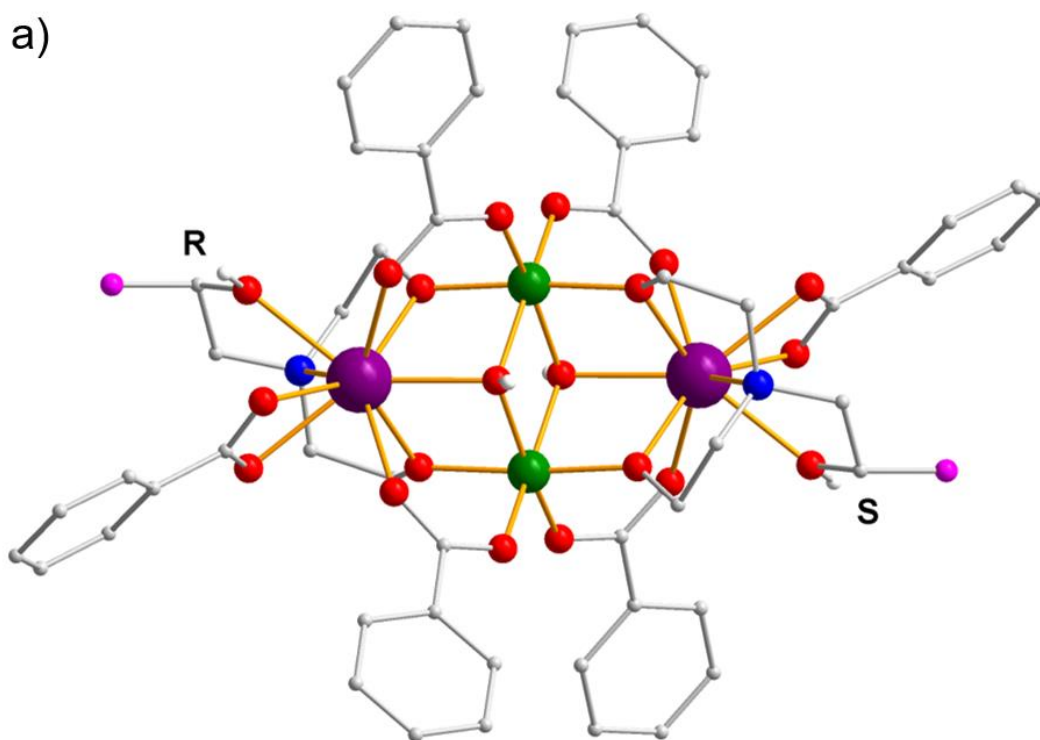


Figure 5.1-10 The molecular structures of $[\text{Fe}_2\text{Dy}_2(\mu_3\text{-OH})(R,S\text{-Me-teaH})_2(\text{O}_2\text{C-Ph})_6]$ (**26**) (a) and $[\text{Fe}_2\text{Dy}_2(\mu_3\text{-OH})(S,S\text{-Me-teaH})_2(\text{O}_2\text{C-Ph})_6]$ (**27**) (b) highlighted in pink are the chiral methyl-groups of the Me-teaH₃ ligand, organic H-atoms are omitted for clarity.

When using the enantiomerically pure *R*- or *S*-Me-teaH₃ the same overall molecular structure is obtained, however due to the fact that the ligand is enantiomerically pure the structure is no longer centrosymmetric.

The unit cell parameters are very close to those found for the centrosymmetric structure, despite the change in space group to *P1*, as evidenced by the packing diagram shown in **Figure 5.1-11**. There is still one molecule in the unit cell, but there are a few key differences in the structural details compared with the centrosymmetric structure.

Compound (**27**) crystallises in the triclinic space group *P1* with *Z* = 1, which results in the removal of the centrosymmetry compared to (**26**). The composition of the core structure is nearly identical with that of (**26**) with the only difference being that the substituted alcohol arm of the ligand on Dy(1) is no longer protonated and chelating but instead deprotonated and bridging to Fe(2). (**Figure 5.1-10 b**)

This conformation is probably caused by steric constraints highlighted by the space filling representation of (**26**) and (**27**) shown in **Figure 5.1-12**. In this figure highlighted in green are the possible hydrogen atoms that could be replaced by the methyl group, while for the hydrogen atoms highlighted in orange the substitution with the methyl group would result in very close contact to the bridging benzoates, excluding them from possible substitution.

The synthesis with the *R*-Me-teaH₃ leads to a slightly different outcome, whilst one side of the molecule adopts the expected conformation comparable to (**26**), the second *R*-Me-teaH₃ ligand undergoes noticeable racemisation. Furthermore, the yield of the reaction with the enantiomerically pure *R*-Me-teaH₃ was rather low, precluding further experiments.

Due to the racemisation of the compound using the *R*-Me-teaH ligand, the structural comparison with (**26**) is only carried out using the structure for [Fe₂Dy₂(μ₃-OH)(*S,S*-Me-teaH)₂(O₂C-Ph)₆] (**27**).

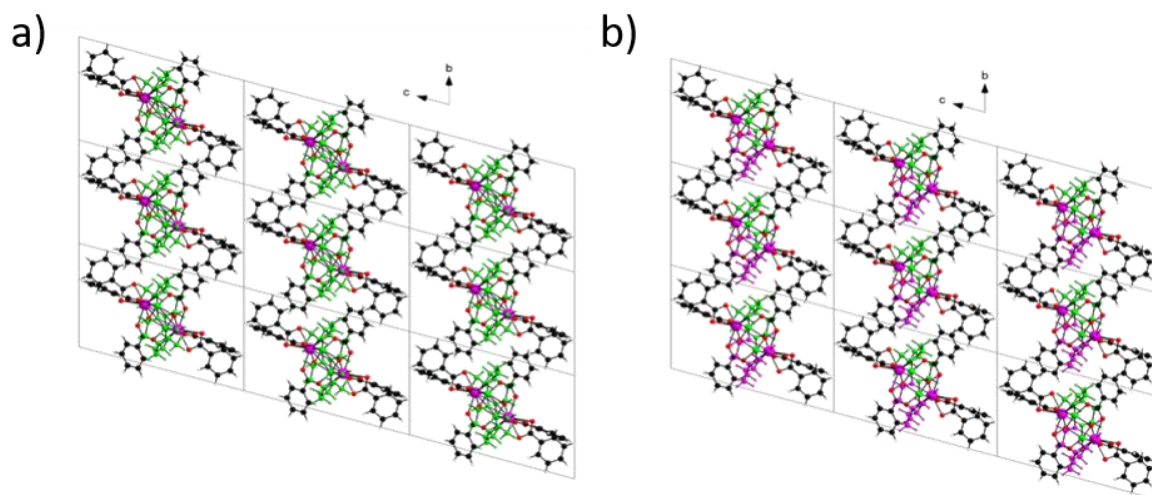


Figure 5.1-11 The packing diagrams of $[\text{Fe}_2\text{Dy}_2(\mu_3\text{-OH})(R,S\text{-Me-teaH})_2(\text{O}_2\text{C-Ph})_6]$ (**26**) (a) and $[\text{Fe}_2\text{Dy}_2(\mu_3\text{-OH})(S,S\text{-Me-teaH})_2(\text{O}_2\text{C-Ph})_6]$ (**27**) (b) highlighting the similarities in the crystal structure despite the change in space group.

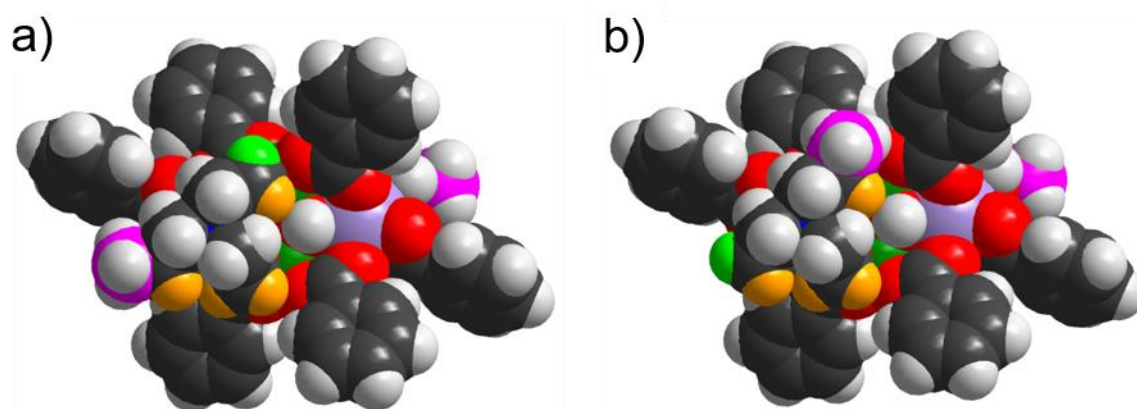


Figure 5.1-12 Space-filling models of (**26**) (a) and (**27**) (b). The methyl carbons of the substituted Me-teaH₃ ligands are highlighted in pink. Highlighted in orange are the four hydrogen atoms that cannot be replaced by the methyl group, leaving the hydrogen highlighted in green as the only possible substitution site.

In order to probe the influence of introducing chirality into the molecule, the magnetic properties of (**26**) and (**27**) were investigated.

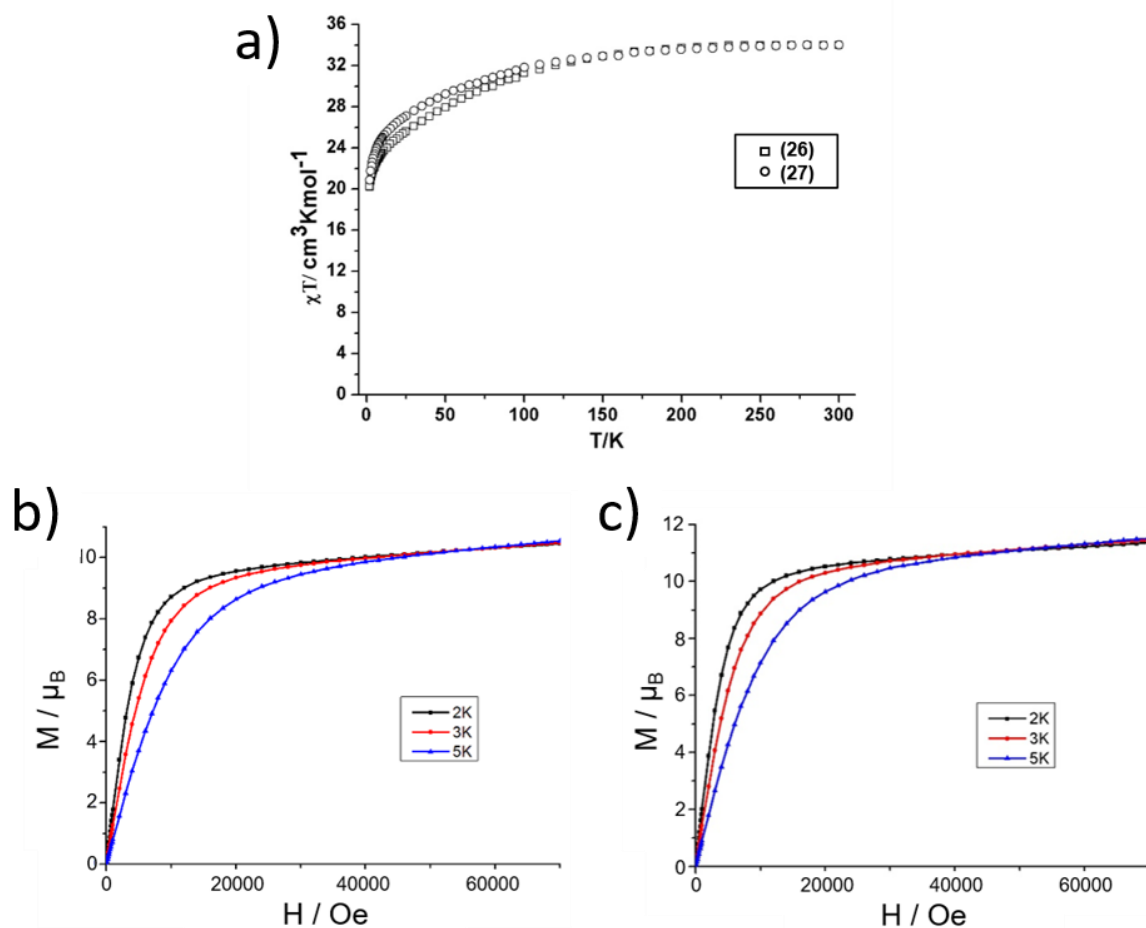


Figure 5.1-13 Magnetic data of $[\text{Fe}_2\text{Dy}_2(\mu_3\text{-OH})_2(\text{Me-teaH})_2(\text{O}_2\text{C-Ph})_6]$, χT vs T plot of (26) and (27) (a), M vs H plot for (26) (b) and M vs H plot for (27) (c).

The temperature dependant susceptibility measurements for (26) and (27) are very similar, both compounds show a steady decrease of the χT product on decreasing the temperature from 300K to 1.8K (Figure 5.1-13 a), which suggests dominant antiferromagnetic interactions in line with previously reported results for the analogues using the unsubstituted teaH₃ ligand.^[40, 44, 118]

The magnetisation curves for both compounds (Figure 5.1-13 b and c) are also very similar, showing a steady increase upon application of an external field, there is no saturation visible even at higher fields.

Whilst the static magnetic properties for (26) and (27) are very similar the dynamic properties show significant differences. To investigate the relaxation of the compounds ac magnetic susceptibility experiments were conducted.

A comparison of the experimental data with those of the previously reported unsubstituted analogue^[118] is shown in **Figure 5.1-14**. Similarly to the unsubstituted literature compound (**26**) shows virtually no frequency-dependence without any maxima, whilst (**27**) shows a strong frequency-dependence of the in-phase signal with a maximum at around 4K. The out-of-phase signal shows a strong increase for (**27**) compared to (**26**), suggesting a significantly increased SMM behaviour for (**27**). This can be underlined by the χ'/χ'' ratio listed in **Table 5-1**.

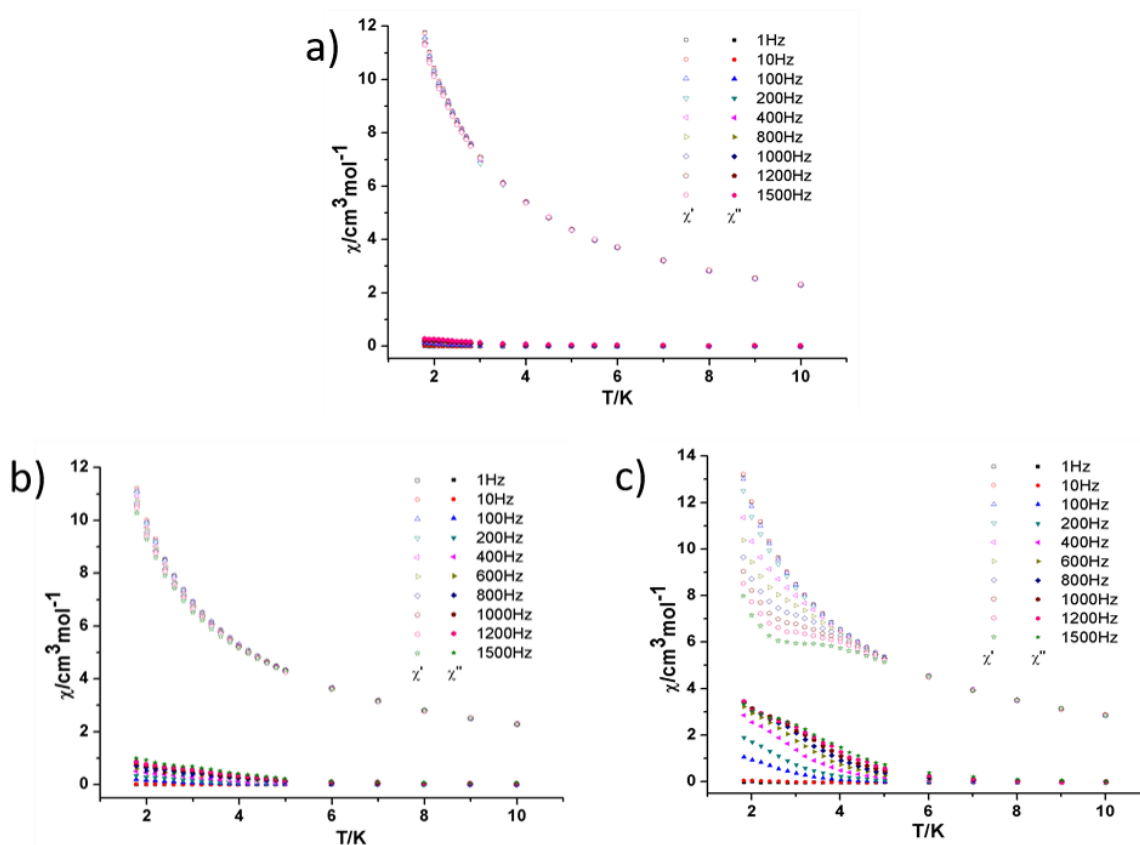


Figure 5.1-14 Dynamic temperature dependant ac susceptibility measurements under zero applied dc field of the previously reported $[\text{Fe}_2\text{Dy}_2(\mu_3\text{-OH})_2(\text{teaH})_2(\text{O}_2\text{C-Ph})_6]$ with the unsubstituted teaH₃ ligand (a), $[\text{Fe}_2\text{Dy}_2(\mu_3\text{-OH})_2(R,S\text{-Me-teaH})_2(\text{O}_2\text{C-Ph})_6]$ (**26**) (b) and $[\text{Fe}_2\text{Dy}_2(\mu_3\text{-OH})_2(S,S\text{-Me-teaH})_2(\text{O}_2\text{C-Ph})_6]$ (**27**) (c), filled circles show the out-of-phase data, while open circles show the in-phase.

Figure 5.1-15 shows the frequency-dependences for (**26**) and (**27**) under their optimal applied dc-fields of 2000Oe for (**26**) and 1500Oe for (**27**) respectively. The corresponding Arrhenius-plots derived from these data are shown in **Figure 5.1-16**.

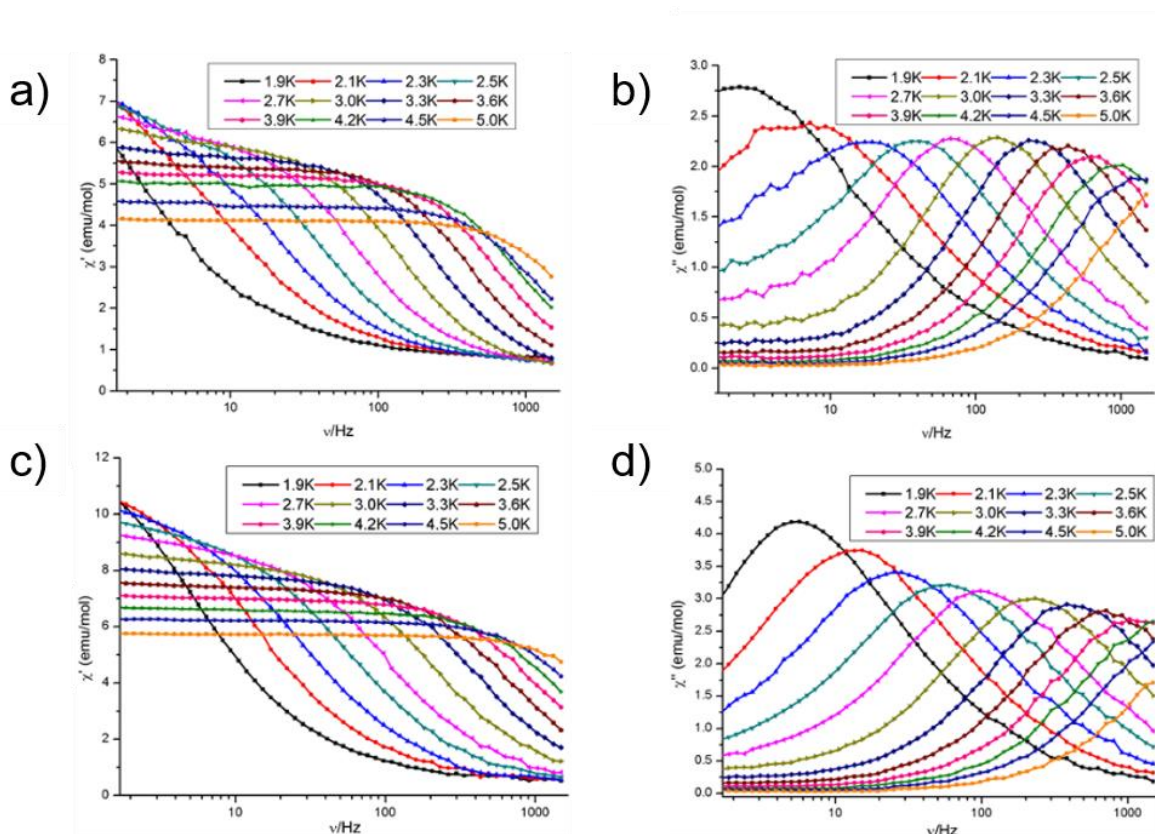


Figure 5.1-15 Frequency-dependences of the components of the ac magnetic susceptibility for the (26) and (27), in-phase (a) and out-of-phase (b) for (26) under 2000Oe, in-phase (c) and out-of-phase (d) under 1500Oe for (27).

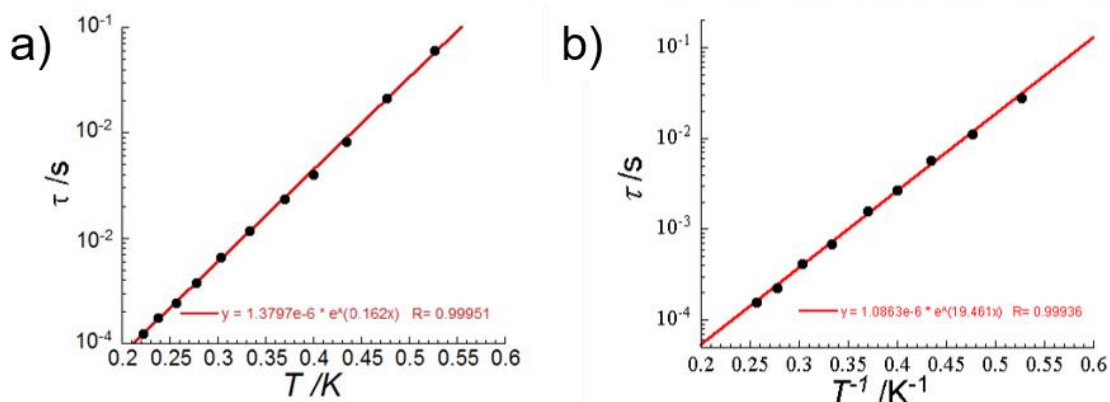


Figure 5.1-16 Arrhenius-plots derived from the frequency-dependences of (26) (a) and (27) (b).

The comparison of the energy barriers and pre-exponential factors for (26) and (27) with the ones of the literature compound (see **Table 5-1**) shows that substituting on of the hydrogens by a methyl-group enhances U_{eff} by about 20%. Furthermore, the significantly enhanced zero-field relaxation for (27) shows that introducing chirality

into the molecule and therefore breaking symmetry greatly enhances the SMM behaviour.

Table 5-1 The Energy barriers for reversal of magnetisation and pre-exponential factors derived from the Arrhenius plots for $[\text{Fe}_2\text{Dy}_2(\mu_3\text{-OH})_2(\text{teaH})_2(\text{O}_2\text{C-Ph})_6]$, **(26)**, **(27)** and **(30)**.

	$\text{Fe}_2\text{Dy}_2(\text{teaH})_2$	26	27	30
U_{eff}	16.2 K	20.2 K	19.5 K	16.8 K
τ_0	1.9×10^{-6} s	1.4×10^{-6} s	1.1×10^{-6} s	3.2×10^{-8} s
χ''/χ'	0.025	0.043	0.667	*

To prove the assumption that breaking the symmetry has the potential to greatly increase the SMM behaviour another similar system was investigated.

Similarly to the synthesis of **(26)** and **(27)**, compound **(28)** is the product of the reaction of $\text{Dy}(\text{NO}_3)_3 \cdot 6\text{H}_2\text{O}$ and Me-teaH₃ with $[\text{Fe}_3\text{O}(\text{O}_2\text{C-Ph})_6(\text{H}_2\text{O})_3]\text{NO}_3$ in a mixture of MeCN and MeOH, in contrast to the synthesis of **(26)** and **(27)**, there are different molar ratios of the ingredients used and the reaction takes place at room temperature.

This reaction yields crystals of good quality for all variants of the methylated ligand used, with no racemisation observed.

$[\text{Fe}_2\text{Dy}_2(\mu_3\text{-OH})_2(\text{Me-teaH})_2(\text{O}_2\text{C-Ph})_4(\text{NO}_3)_2]$ **(28)** using the racemic Me-teaH₃ ligand, and its analogues using the enantiomerically pure R-ligand **(29)** and S-ligand **(30)** respectively, are isomorphous to their respective counterparts described above.

Compound **(28)** crystallises in the triclinic space group $P\bar{1}$ with $Z = 1$, while **(29)** and **(30)** adopt the $P1$ space group, due to the removal of the centrosymmetry. The core of the compounds is basically identical to that of **(26)**, with the chelating benzoate being replaced by a chelating nitrate ion. (see **Figure 5.1-17**)

Due to the fact that all three variants of the compound were obtained this compound type lends itself to investigate their magnetic properties along the same lines as was done for **(26)** and **(27)**.

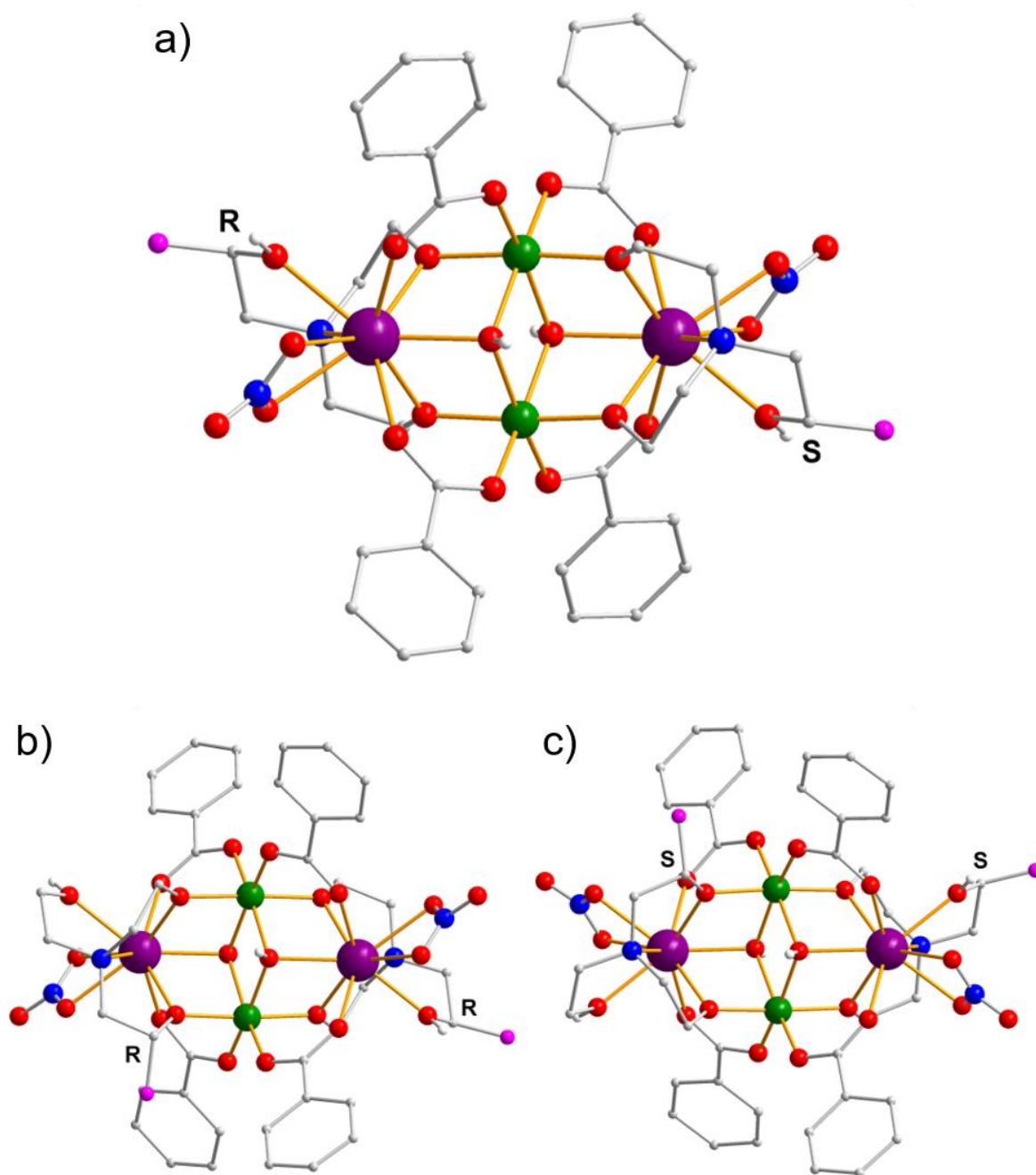


Figure 5.1-17 Molecular structures of $[\text{Fe}_2\text{Dy}_2(\mu_3\text{-OH})_2(\text{Me-teaH})_2(\text{O}_2\text{C-Ph})_4(\text{NO}_3)_2]$ (**28**) (a) using the racemic Me-teaH₃ ligand, as well as (**29**) (b) and (**30**) (c) using the enantiomerically pure *R*- and *S*-Me-teaH₃ ligand respectively. Highlighted in pink are the chiral methyl-groups of the Me-teaH₃ ligand, organic H-atoms are omitted for clarity.

As expected, the temperature dependant susceptibility measurements for (**28**), (**29**) and (**30**) are very similar, all compounds show a steady decrease of the χT product on decreasing the temperature from 300K to 1.8K (**Figure 5.1-18 a**), suggesting similar interactions as explained for (**26**) and (**27**).

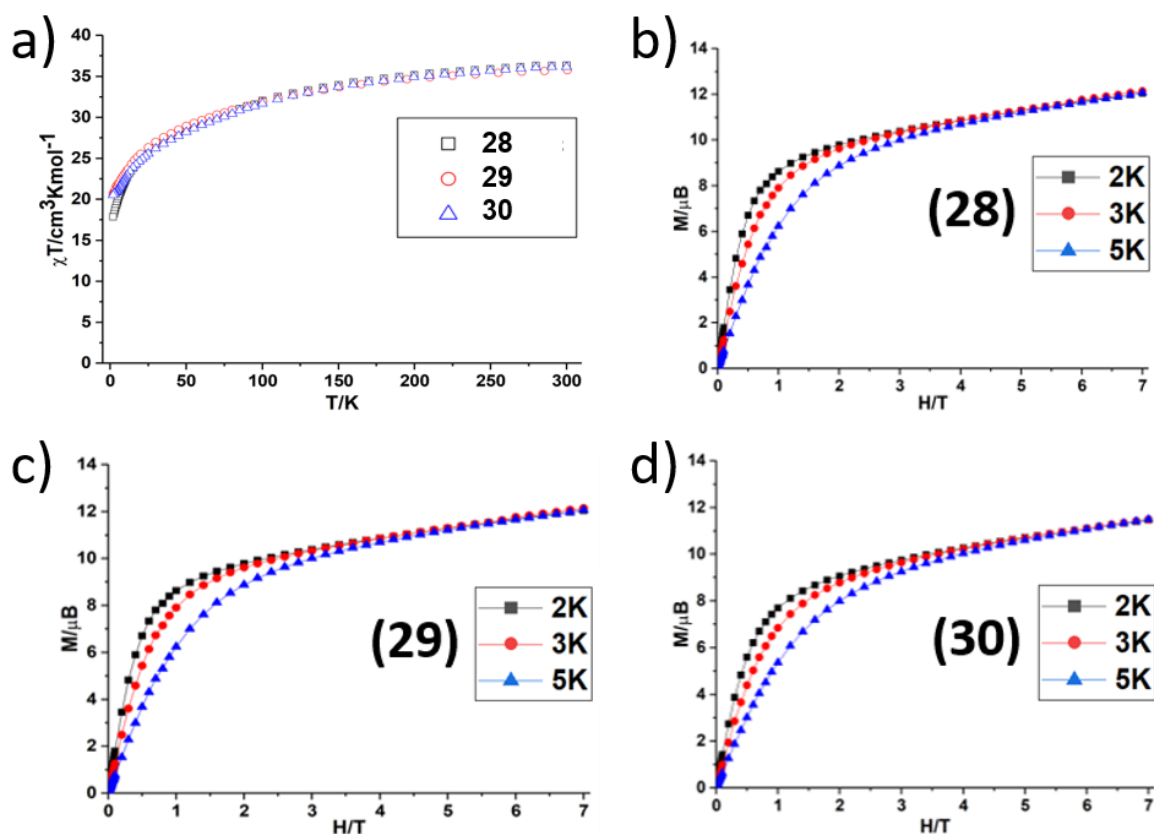


Figure 5.1-18 Magnetic data of $[\text{Fe}_2\text{Dy}_2(\mu_3\text{-OH})_2(\text{Me-teaH})_2(\text{O}_2\text{C-Ph})_4(\text{NO}_3)_2]$ (**28**), combined χT vs T plot (a), M vs H plot for (**28**) (b), (**29**) (c) and (**30**) (d).

The magnetisation curves for the compounds (**Figure 5.1-18** b, c and d) are also very similar, showing a steady increase upon application of an external field, similarly to (**26**) and (**27**) there is no saturation visible even at higher fields.

To probe the relaxation of the compounds *ac* magnetic susceptibility experiments were conducted. Compound (**28**) does not show any in the 500-3000Oe range, however both (**29**) and (**30**) show a maximum for an applied field of 1000Oe. (see **Figure 5.1-19** b and c) Furthermore for an applied field of 3000Oe the (**30**) shows an additional maximum at 3000Oe. To better compare the results the maxima at 1000Oe were investigated for (**29**) and (**30**), with the result being that the graphs are virtually superimposable. (see **Figure 5.1-20**)

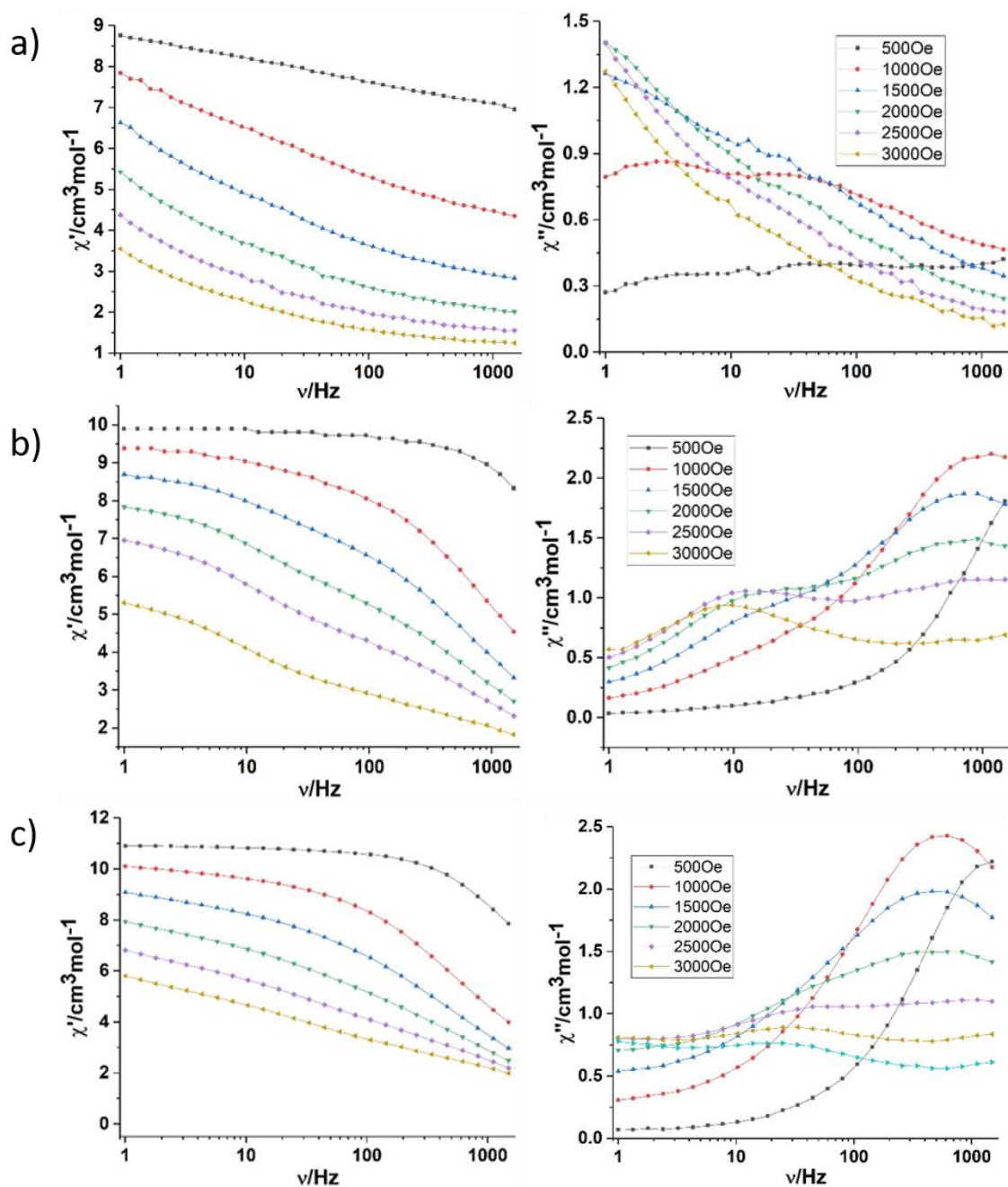


Figure 5.1-19 The in-phase (left) and out-of-phase (right) components of the ac susceptibility under various applied dc fields for **(28)** (a), **(29)** (b) and **(30)** (c).

The behaviour of **(30)** for an applied field of 3000Oe leads to the observation of two relaxation processes up to 3.6 K. (**Figure 5.1-21**) One is at the lower frequency around 100 Hz, the other at high frequency (over 1500 Hz). The Cole-Cole plots can be fitted using a two relaxation pathway Debye model,^[122-123] with $\alpha = 0.13-0.42$ and $\alpha = 0.46-0.70$ for the different frequencies in which the relaxation is observed. The Arrhenius plots derived from these data are shown in **Figure 5.1-22**, showing an

energy barrier of 16.8 K and pre-exponential factor of $3.2 \cdot 10^{-8}$ s. This is below the value that was found for (26) and (27), additionally it was not possible to extract an energy barrier for (29). However, it is worth noting that the most important aspect of this analysis is the very large enhancement of the zero-field relaxation behaviour for (29) and (30) compared to (28). (see Table 5-1)

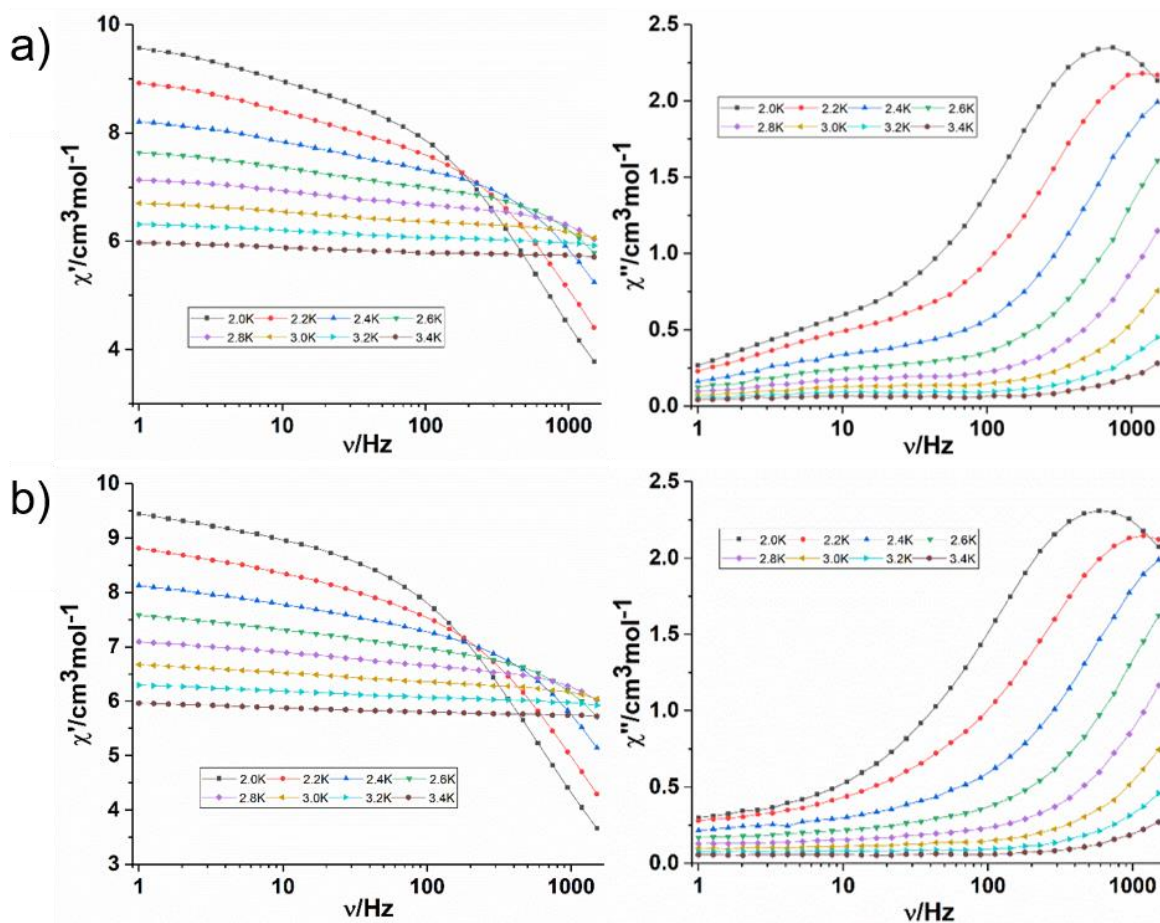


Figure 5.1-20 The in-phase (left) and out-of-phase (right) susceptibility for (29) (a) and (30) (b) for varying temperatures under an applied dc field of 1000Oe, the graphs are virtually superimposable.

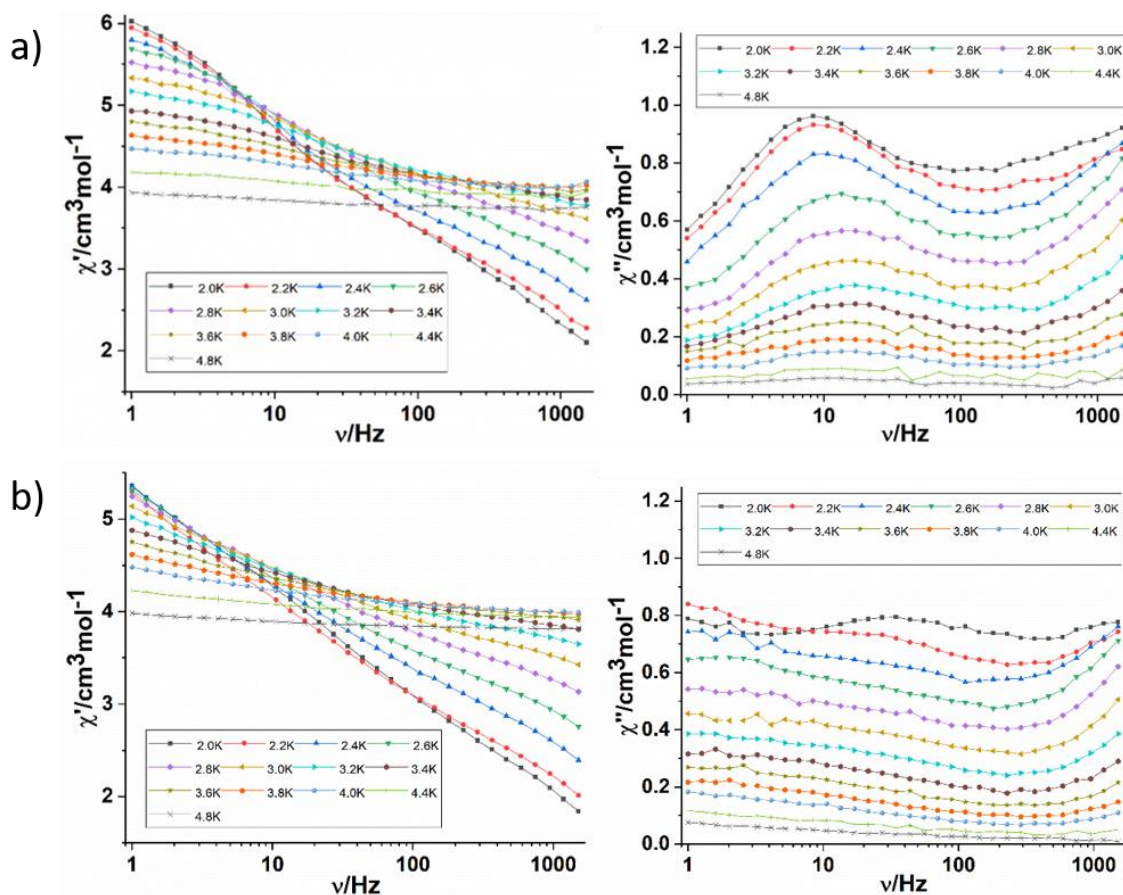


Figure 5.1-21 The in-phase (left) and out-of-phase (right) susceptibility for (29) (a) and (30) (b) for varying temperatures under an applied dc field of 3000Oe.

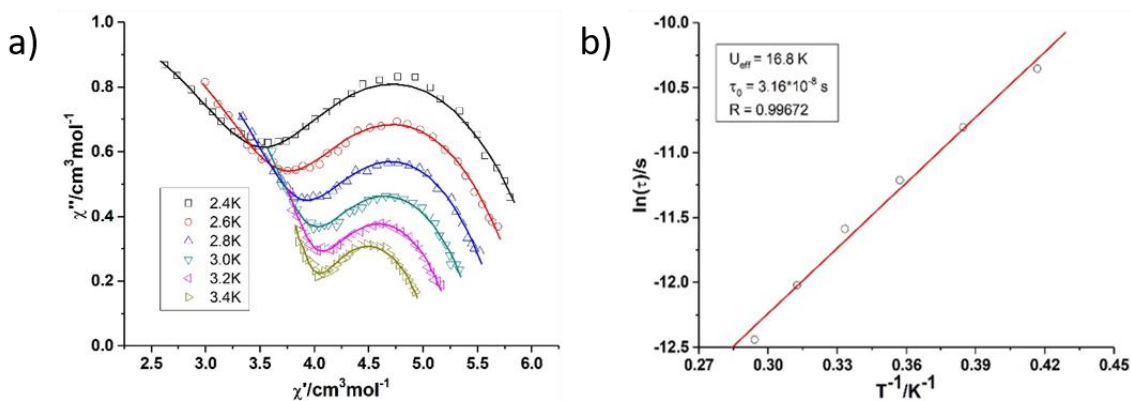


Figure 5.1-22 The Cole-Cole plots (a) and Arrhenius plot (b) for (30), derived from the relaxation data at an applied dc field of 3000Oe shown in Figure 5.1-21.

The conclusions that can be drawn from the investigation of the magnetic data for (26)-(30) are quite remarkable. It could be shown that breaking the symmetry within the crystal structure has an immediate effect on the magnetic relaxation behaviour.

This means that for (27) the SMM behaviour was greatly enhanced by introducing the chiral Me-teaH₃ ligand.

For (29) and (30) the effect is arguably even more impactful as the removal of the centrosymmetry potentially enables the slow relaxation of magnetisation in the first place. Presumably the removal of symmetry by introduction of a chiral ligand suppresses the quantum tunnelling of magnetisation, therefore enabling the slow relaxation of magnetisation in (30) at zero dc field.

5.1.4 Summary of tetranuclear M₂Ln₂ complexes

To summarise the previous section, it is important to stress how versatile and at the same time very robust the butterfly “test-bed” is. It is very important for the fundamental understanding of relaxation processes taking place to be able to make subtle changes and investigate their effect on the system.

The introduction of a chiral centre on the ligand for compounds (26)-(30) led to the breaking of the centrosymmetry for the enantiomerically pure ligands and in turn drastically changed the magnetic behaviour.

In the case of the [Fe₂Dy₂(μ₃-OH)₂(Me-teaH)₂(O₂C-Ph)₆] this led to the improvement of the SMM properties while for [Fe₂Dy₂(μ₃-OH)₂(Me-teaH)₂(O₂C-Ph)₄(NO₃)₂] breaking the symmetry within the molecule enabled the slow relaxation of magnetisation in the first place. In both cases it can be suggested that the removal of symmetry actually limits certain relaxation pathways and therefore essentially quenching the quantum tunnelling of magnetisation.

Furthermore, section 5.1.2 shows that it was possible to expand the library of possible reactions using tripodal ligands with a similar O-N-O coordination mode. A first version of the reaction scheme shown at the beginning of the chapter was originally established by Baniodeh et al.^[42] and has been built upon since then.

In line with the reaction scheme this section further highlights how the use of different trinuclear transition metal complexes opens up the possibility to introduce other metals into established compounds via the assisted self-assembly approach.

5.2 Giant cyclic coordination clusters synthesised with 2-amino-2-methyl-1,3-propanediol

The nature of cyclic coordination clusters (CCCs) provides fascinating candidates for studies on magnetic behaviour within a bounded, molecular system which also possesses an infinite chain character. Thus, the cyclic nature of such compounds provides valuable opportunities to study exotic magnetic phenomena, arising from the interplay of the magnetic coupling within the molecule, the periodic boundary conditions established by the cyclised nature, as well as their mesoscopic size.

Possibly a useful analogy here is to the quantum confinement seen for the (in)famous “particle in a box” and the possible expansion of this idea to multidimensional levels.

Although very few examples of CCCs have been reported and thoroughly investigated to date^[39, 42, 124-133] a small number of these actually turn out to be SMMs.^[39, 130-133] This prompts more research into this area.

In addition to the intriguing magnetic interactions within the cyclised chain the macroscopic size of these cyclic coordination clusters gives rise to another interesting aspect: the nanoscopic sizes which can result means that they represent a bridge between molecular properties and effects arising from their nanoscale dimensions.

In this section the $[\text{Fe}_{18}\text{Ln}_6(\mu\text{-OH})_6(\text{ampd})_{12}(\text{Hampd})_{12}(\text{O}_2\text{C-Ph})_{24}](\text{NO}_3)_6 \cdot 38\text{MeCN}$ CCC is presented. This compound was originally discovered in our group by Baniodeh^[134] and previously briefly described by the author.^[135] Since it was clear that this could be a fascinating molecule to explore, this system was revisited in the scope of the current thesis and the results obtained so far have recently been published in an article in the Journal of the American Chemical Society.^[27]

5.2.1 $[\text{Fe}_{18}\text{Ln}_6(\mu\text{-OH})_6(\text{ampd})_{12}(\text{Hampd})_{12}(\text{O}_2\text{C-Ph})_{24}](\text{NO}_3)_6 \cdot 38\text{MeCN}$

The reaction of $[\text{Fe}_3\text{O}(\text{O}_2\text{C-Ph})_6(\text{H}_2\text{O})_3]\text{NO}_3$ in MeCN with a mixture of $\text{Ln}(\text{NO}_3)_3 \cdot x\text{H}_2\text{O}$ (Ln = Pr-Lu) and 2-amino-2-methyl-1,3-propanediol suspended in MeCN at room temperature results in a clear solution after 1 hour. After filtering and sealing the solution pale yellow crystals suitable for X-Ray diffraction are obtained after 3 days.

The synthesis yields isostructural compounds over almost the whole lanthanide series (Pr-Lu). However, for the earlier lanthanides left of Tb, there are impurities

present. As has been shown in section 5.1.2, an analogous reaction for Gd resulted in the formation of a tetranuclear $\{\text{Fe}_2\text{Gd}_2\}$ compound, it is therefore not unreasonable to assume that the by-product formed for $\text{Ln} < \text{Tb}$ is indeed of the same tetranuclear composition.

The crystal structures for $\text{Ln} = \text{Gd}$, **Tb(31)**, **Dy(32)**, **Ho(33)**, **Er(34)**, **Lu(35)** and **Y(36)** have been obtained, although the data for the Gd analogue are not of good quality. For $\text{Ln} = \text{Pr}$, **Nd**, **Sm** and **Eu** the unit cell parameters as well as the shape and colour of the crystals suggest isostructural compounds, however they have not been fully characterised.

The crystal and molecular structure of the Dy^{III} analogue (**32**) will be described here as exemplary for the isostructural series.

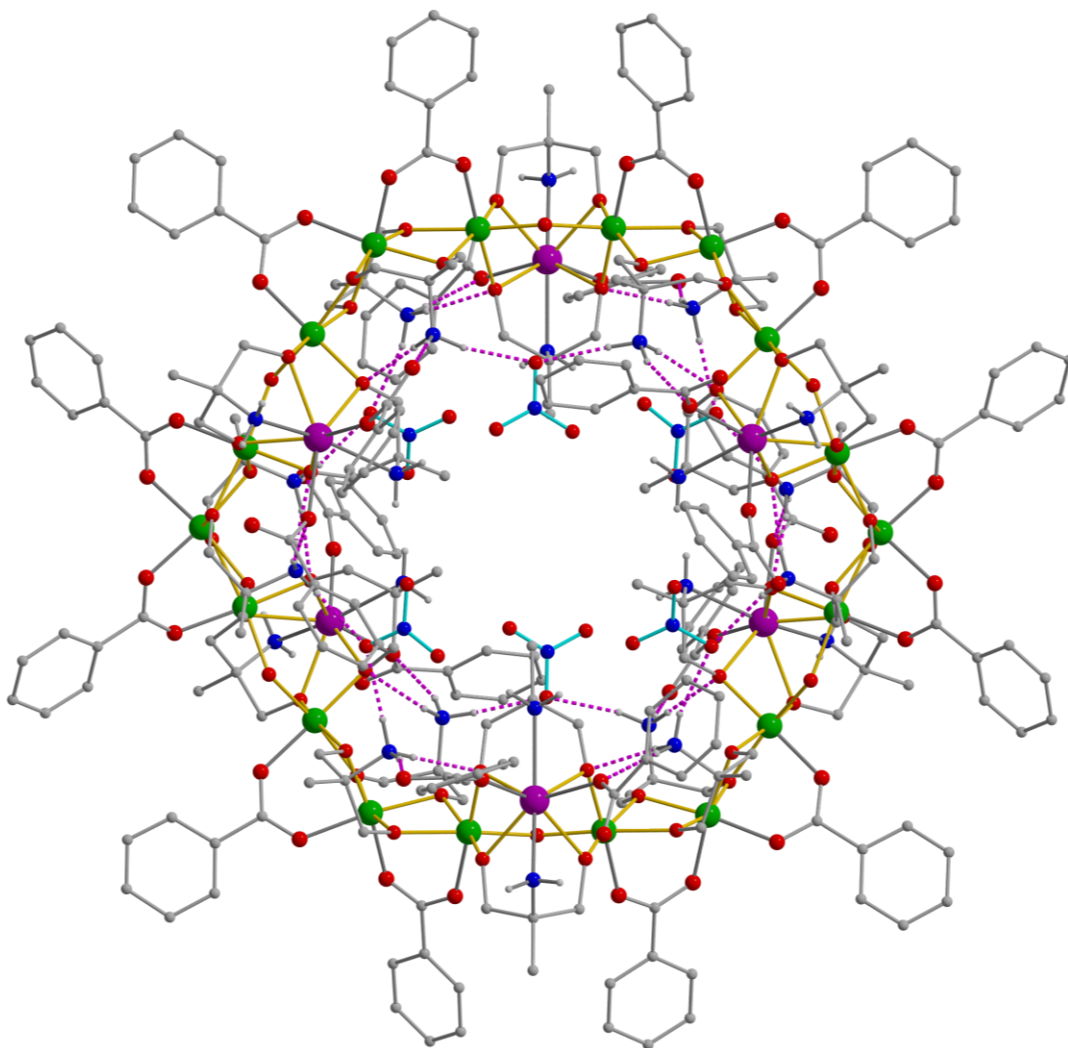


Figure 5.2-1 The molecular structure of the giant cyclic coordination cluster $[\text{Fe}_{18}\text{Dy}_6(\mu\text{-OH})_6(\text{ampd})_{12}(\text{Hampd})_{12}(\text{O}_2\text{C-Ph})_{24}](\text{NO}_3)_6 \cdot 38\text{MeCN}$ (**32**), top down view, the solvent MeCN molecules and organic H-atoms have been omitted for clarity.

Compound **(32)** crystallises in the orthorhombic space group *Pccn* with $Z = 4$ with an inversion centre situated in the middle of the molecule, leading to an aesthetically pleasing cyclic arrangement within the molecule. (**Figure 5.2-1**)

The structure can be broken down into small repeating units: six triangular $\{\text{Fe}_2\text{Dy}(\mu\text{-OH})(\text{ampd})_2(\text{O}_2\text{C-Ph})_2\}$ moieties are linked via mononuclear $\{\text{Fe}(\text{Hampd})_2(\text{O}_2\text{C-Ph})_2\}$ units and form the cyclic system. If a plane is constructed through the linking Fe units, the triangular building blocks are arranged in a modified delta chain motif alternating in their orientation above and below the Fe_6 plane constructed by the linking Fe^{III} . (**Figure 5.2-3**)

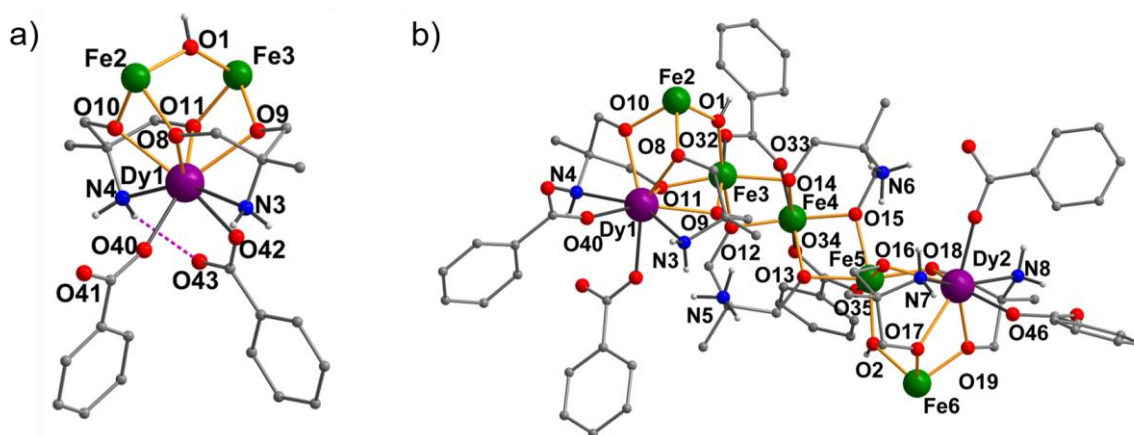


Figure 5.2-2 The triangular $\{\text{Fe}_2\text{Dy}(\mu\text{-OH})(\text{ampd})_2(\text{O}_2\text{C-Ph})_2\}$ building block of **(32)** (a) and connection of two of these building blocks via a mononuclear $\{\text{Fe}(\text{Hampd})_2(\text{O}_2\text{C-Ph})_2\}$ unit (b).

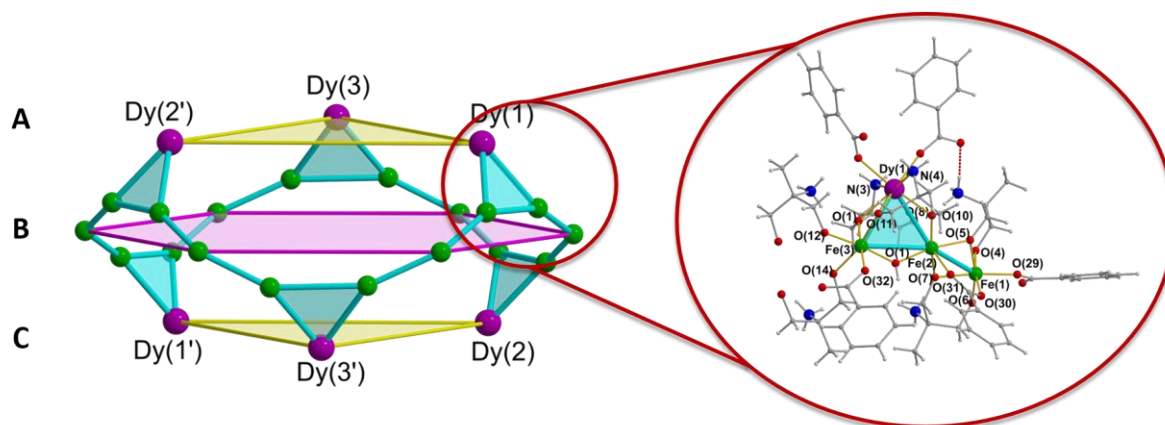


Figure 5.2-3 Scheme of the hexagonal plane spanned by the bridging mononuclear Fe units and alternating triangular Fe_2Dy moieties above and below the plane.

Within the Fe₂Dy triangle, the Dy^{III} ions are chelated by the O and N atoms of two doubly deprotonated ampd²⁻ ligands, with the two deprotonated alcohol arms forming μ₂-bridges to the two Fe^{III}. The coordination sphere of the Dy^{III} is completed by two monodentate benzoates. A μ₂-OH⁻ bridges the two Fe^{III} in the base of the triangle, the linkage to the mononuclear Fe^{III} unit is via a bridging benzoate with the deprotonated alcohol arm of two Hampd⁻ ligands completing the octahedral coordination sphere of the Fe^{III} in the base of the triangle.

Within the linking {Fe(Hampd)₂(O₂C-Ph)₂} unit, the two Hampd⁻ ligands have their alcohol arms deprotonated, as was the case for the ligands in the triangular unit. However, the amino group is now protonated, with the resulting primary ammonium groups forming hydrogen bonds to the monodentate benzoates coordinating the Dy^{III}. The octahedral coordination of the Fe^{III} is completed by two benzoates, forming *syn,syn*-bridges to two Fe^{III} in the bases of two adjacent triangular units. (**Figure 5.2-2** b)

There is a significant amount of hydrogen bonding observed within the molecule, the two protonated amino groups are effectively responsible for the macroscopic shape of the complex. The hydrogen bonds formed between these ammonium groups and the monodentate benzoates on the Dy^{III} tilt the Fe₂Dy triangle by roughly 60° towards the centre of the molecule. Furthermore, the six nitrate counterions are situated in the cavity in the middle of the cluster and are held in place via hydrogen bonds to the second primary ammonium groups. (**Figure 5.2-1**)

The tilting of the Fe₂Dy triangle leads to the plane spanned by the three Dy^{III} being inside the hexagonal plane constructed by the bridging mononuclear Fe units (see **Figure 5.2-1**), due to the symmetry inside the molecule with the Fe₂Dy triangles alternating above and below the Fe₆ plane this leads to an arrangement loosely resembling a pseudo cubic close packing (ccp) arrangement with the sequence A (Dy₃ triangle above the Fe₆ plane), B (Fe₆ plane) and C (Dy₃ triangle below the Fe₆ plane rotated by 60°), as shown in **Figure 5.2-3**.

This triangular arrangement of the Dy^{III} has previously been shown to potentially lead to show a toroidal arrangement. Similar examples have been reported in the literature with two Dy₃ sandwiching a single ion^[24] or trimesate in a giant sandwich.^[136]

Due to the relatively long Dy₃-Dy₃ distances, there are no interactions expected between the two Dy₃ triangles.

As was touched on in the introduction, nanoscale clusters offer unique insights into magnetic properties, as their size can potentially lead to magnetic properties reminiscent of bulk materials rather than discrete clusters.

The space-filling representation shown in **Figure 5.2-4** shows the nanoscale dimensions of [Fe₁₈Dy₆(μ-OH)₆(ampd)₁₂(Hampd)₁₂(O₂C-Ph)₂₄](NO₃)₆·38MeCN (**32**).

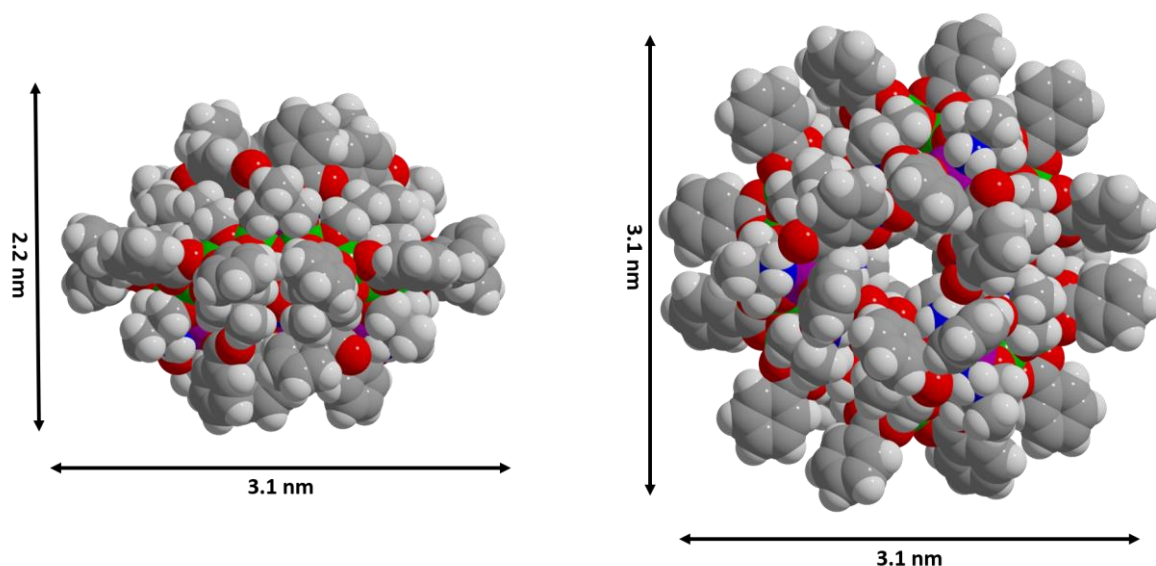


Figure 5.2-4 [Fe₁₈Dy₆(μ-OH)₆(ampd)₁₂(Hampd)₁₂(O₂C-Ph)₂₄](NO₃)₆·38MeCN (**32**) in the space-filling representation, highlighting the nanoscale dimensions of the cluster.

The crystal packing in (**32**) (see **Figure 5.2-5**) is heavily influence by the aromatic ligand shell established by the benzoates on the outside of the cluster. The clusters are aligned orthogonally to each other, which can be visualised in the crystal packing along the crystallographic a-axis. Only looking at the structural representation shown in **Figure 5.2-1** and **Figure 5.2-4** one could fall for the illusion that compound (**32**) is planar, indeed the complex is far from planar, as can be seen from the side on view in the space-filling representation and the crystal packing.

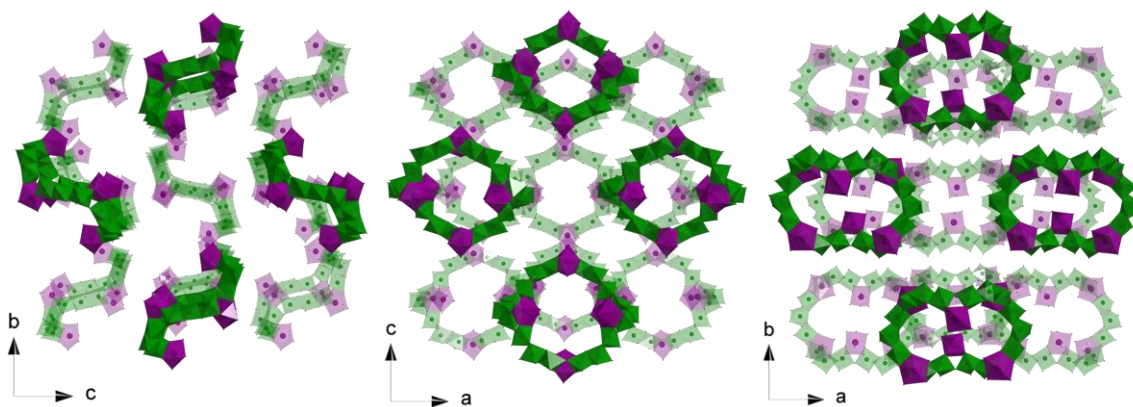


Figure 5.2-5 The crystal packing along the crystallographic a-, b-, and c-axis in $[\text{Fe}_{18}\text{Dy}_6(\mu\text{-OH})_6(\text{ampd})_{12}(\text{Hampd})_{12}(\text{O}_2\text{C-Ph})_{24}](\text{NO}_3)_6 \cdot 38\text{MeCN}$ (**32**).

The nanoscale dimensions and the potential setup of the Dy^{III} to show a toroidal arrangement prompted the magnetic investigation of compound (**32**). The magnetic data were calculated based on the molecular weights obtained from the elemental analysis. Because the Lu analogue was also available the commonly used procedure of diamagnetic substitution of the lanthanide was investigated for both the diamagnetic Y^{III} (without any f electrons) as well as Lu^{III} (with a filled shell of f-electrons) to probe if the presence of f-electrons has an impact on the residual magnetic behaviour after replacing the paramagnetic Dy^{III} with the diamagnetic Y^{III} or Lu^{III} .

The dc magnetic susceptibility data were measured from 2-300K with an applied field of 1000Oe. In the case of the Lu^{III} analogue (**35**) the χT product at 300K is $50.23 \text{ cm}^3 \cdot \text{K} \cdot \text{mol}^{-1}$, while for the Y^{III} analogue (**36**) it is $48.30 \text{ cm}^3 \cdot \text{K} \cdot \text{mol}^{-1}$, both of these values are much lower than the expected values for eighteen Fe^{III} ions ($78.8 \text{ cm}^3 \cdot \text{K} \cdot \text{mol}^{-1}$ with $S = 5/2$, $g = 2$, $C = 4.375 \text{ cm}^3 \cdot \text{K} \cdot \text{mol}^{-1}$) and six diamagnetic Y^{III} or Lu^{III} ions.

Upon decreasing the temperature, the χT value decreases to $1.60 \text{ cm}^3 \cdot \text{K} \cdot \text{mol}^{-1}$ for (**35**) and $1.10 \text{ cm}^3 \cdot \text{K} \cdot \text{mol}^{-1}$ for (**36**), suggesting that the interaction within the Fe_{18} ring are predominantly antiferromagnetic.

For the Dy^{III} analogue (**32**) the χT product at 300K is $145.0 \text{ cm}^3 \cdot \text{K} \cdot \text{mol}^{-1}$, which is lower than the theoretical value of $163.8 \text{ cm}^3 \text{ K mol}^{-1}$ for six Dy^{III} ions (${}^6\text{H}_{15/2}$, $g = 4/3$, $S = 5/2$, $L = 5$, $J = 15/2$ $C = 14.17 \text{ cm}^3 \text{ K mol}^{-1}$) and eighteen non-interacting Fe^{III} ($S = 5/2$, $g = 2$, $C = 4.375 \text{ cm}^3 \text{ K mol}^{-1}$) The χT product gradually decreases from 300K to 50K,

below 50K there is a sharp decrease of the χT product until it reaches $49.4 \text{ cm}^3 \cdot \text{K} \cdot \text{mol}^{-1}$ at 2K. This further validates the assumption of dominant antiferromagnetic interactions within this $\text{Fe}_{18}\text{Dy}_6$ cluster.

The magnetisation data was also measured for the three compounds at 2, 3 and 5K and fields of 0-7T, the combined data for 2K are shown in **Figure 5.2-6**. The magnetisation data for **(32)** does not saturate, which is not surprising given the strong antiferromagnetic interactions and the presence of six anisotropic Dy^{III} ions.

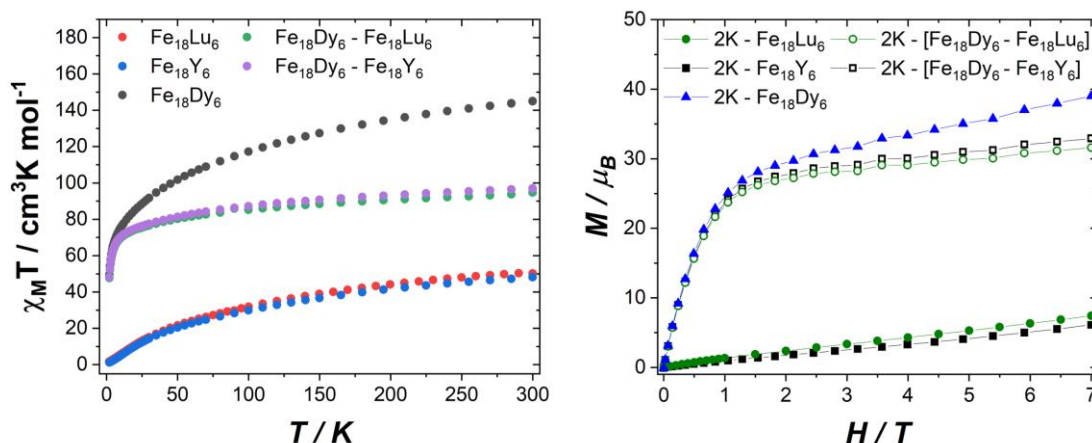


Figure 5.2-6 The temperature dependence of the χT value and the field dependence of the magnetisation at 2K for **(32)**, **(35)** and **(36)**.

The magnetic data suggest that there must be significant antiferromagnetic interactions within the system, since underlying Fe_{18} ring is fairly similar to an antiferromagnetically coupled ring reported by King et al.^[137] the magnetic data for the diamagnetically substituted analogues **(35)** and **(36)** was compared with that of the Fe_{18} ring.

For that reason, ALPS/QMC^[6-7] calculations conducted in collaboration with Prof. Jürgen Schnack at the University of Bielefeld and magnetostructural correlations (MSC) according to Cañada-Vilalta et al.^[4] were conducted, suggesting a weak-weak-strong coupling scheme for the underlying Fe_{18} ring with the corresponding coupling constants $J_1=J_2 = 8\text{K}$ and $J_3 = 28\text{K}$. The strong interaction takes place between the Fe^{III} in the base of the Fe_2Ln triangle. (**Figure 5.2-7 b**) Using the same technique on the Fe_{18} ring from the literature yields results that are consistent with the original

calculations for that compound, showing the same weak-weak-strong coupling pattern as was found for (35). (Figure 5.2-7 a)

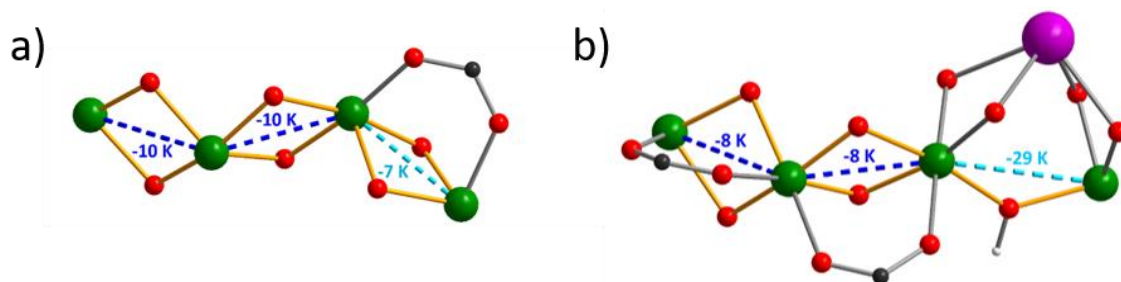


Figure 5.2-7 The repeating unit of the Fe₁₈ ring reported by King et al.^[137] (a) and compound (36), dashed lines highlight the coupling between the Fe^{III} with the corresponding J_{FeFe} values calculated using the magnetostructural correlations according to Cañada-Viltalta et al.^[4]

In order to explore potential SMM behaviour, ac magnetic susceptibility studies were carried out on the Dy^{III} analogue (32). Compound (32) shows clear signals in the out-of-phase susceptibility without the need to apply a static dc field. (Figure 5.2-8)

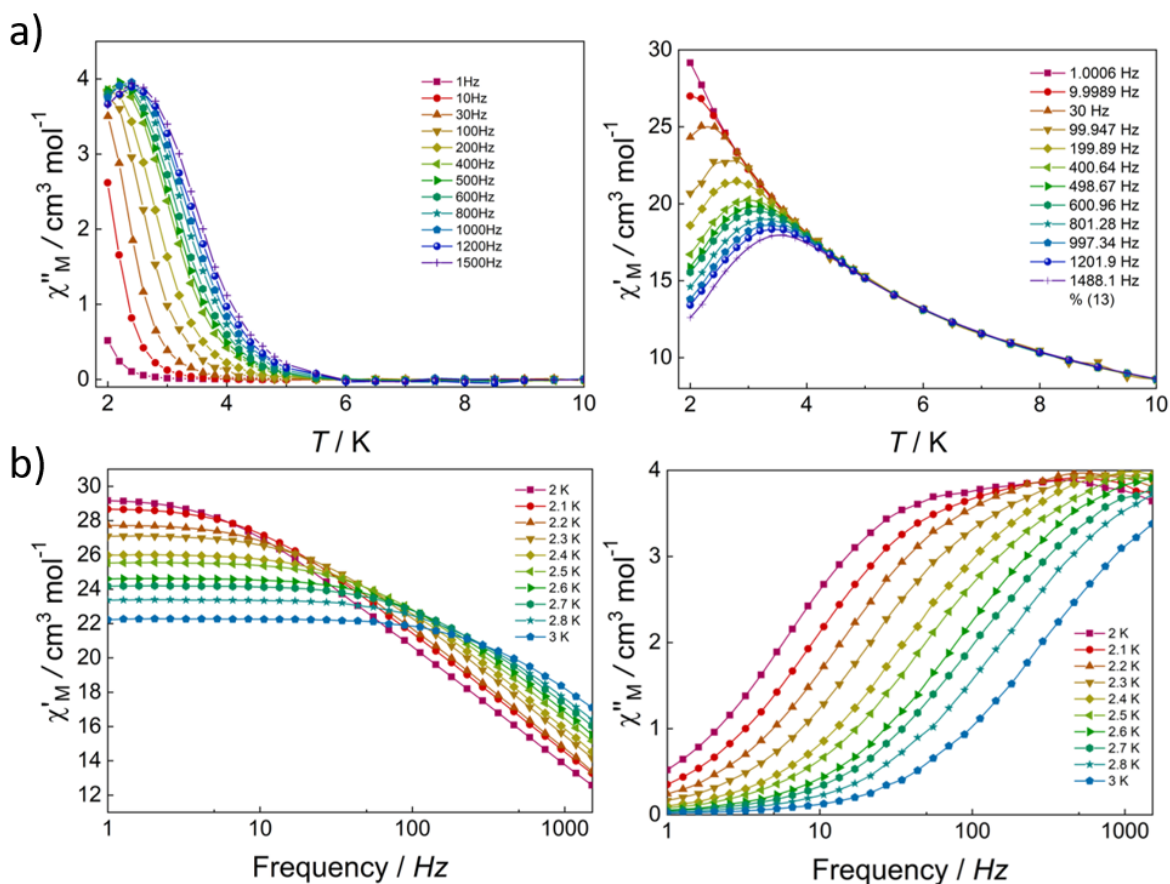


Figure 5.2-8 The temperature dependent (a) and frequency dependent (b) ac magnetic susceptibility measurements for Fe₁₈Dy₆(μ-OH)₆(ampd)₁₂(Hampd)₁₂(O₂C-Ph)₂₄[(NO₃)₆·38MeCN] (32).

The Cole-Cole plots derived from the ac susceptibility data show asymmetric semicircles at high temperature and two distorted semicircles at lower temperature, the Arrhenius-plot derived from the frequency-dependent ac susceptibility are plotted as a function of $1/T$ between 2.0 and 2.5K, revealing a thermally activated mechanism with an energy barrier of 14.7K and a pre-exponential factor τ_0 of 2.98×10^{-7} s. (**Figure 5.2-9**)

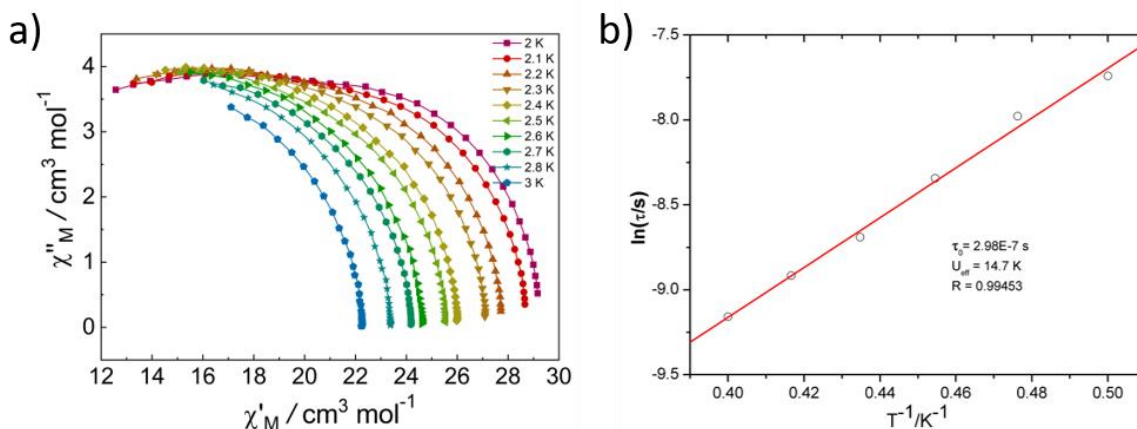


Figure 5.2-9 The Cole-Cole plots (a) and Arrhenius plot (b) for **(32)**.

The result of the ac susceptibility measurements show that $\text{Fe}_{18}\text{Dy}_6(\mu\text{-OH})_6(\text{ampd})_{12}(\text{Hampd})_{12}(\text{O}_2\text{C-Ph})_{24}[(\text{NO}_3)_6 \cdot 38\text{MeCN}]$ (**32**) is a single-molecule magnet, showing slow relaxation of magnetisation without the need to apply a static dc field. As of the time of writing, this makes compound **(32)** the biggest Fe-4f SMM reported in the literature.

To probe the possible toroidal arrangement suggested by the crystal structure an analysis using the MAGELLAN^[5] software was done. The software analyses the electrostatic environment of Dy ions rising from their coordination environment. The author of the software suggests only using it for pure Dy^{III} compounds, since an easy electrostatic model cannot reliably account for possible interactions with other metal ions.

Nonetheless, given the topology of the system, with the two Dy₃ triangles sandwiching a strongly antiferromagnetically coupled Fe₁₈ ring it was concluded that this could potentially exclude the Dy^{III} from any interaction with the Fe₁₈ ring. The result of the

analysis is presented in **Figure 5.2-10**, showing the propeller shaped orientation of the Dy^{III} anisotropy axes.

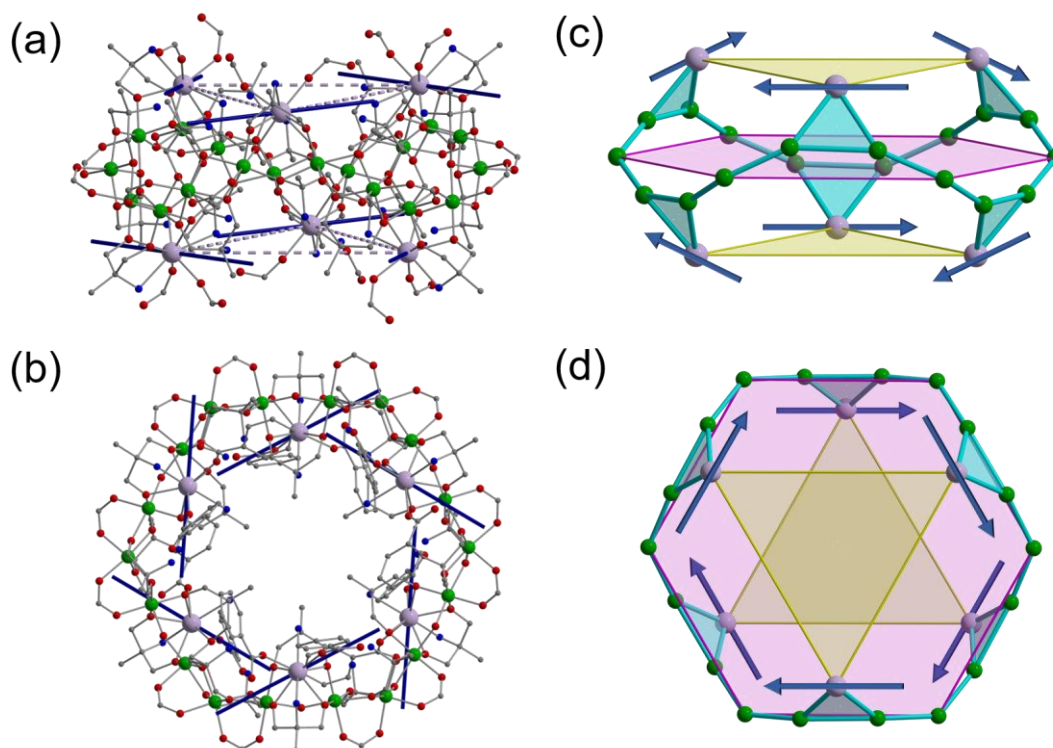


Figure 5.2-10 The arrangement of the anisotropy axes of the Dy^{III} ions (blue) as a result of the Magellan^[5] analysis $\text{Fe}_{18}\text{Dy}_6(\mu\text{-OH})_6(\text{ampd})_{12}(\text{Hampd})_{12}(\text{O}_2\text{C-Ph})_{24}(\text{NO}_3)_6 \cdot 38\text{MeCN}$ (**32**), side-on (a) and top-down (b) view of the crystal structure, the Phenyl-groups, nitrate counteranions and H-atoms are omitted for clarity. (c) and (d) show a proposed spin arrangement on a simplified scheme of the crystal structure.

The results of the MAGELLAN analysis in conjunction with the theoretical considerations discussed earlier prompted the analysis of (**32**) in a microSQUID experiment in a collaboration with the group of Prof. Wolfgang Wernsdorfer at KIT to investigate a possible hysteresis, the result of which can be seen in **Figure 5.2-11**.

The microSQUID measurements show a nice hysteresis loop of (**32**) with drastic changes of the spin orientation at around 0.5T, the magnetic behaviour is consistent with those shown by other toroidal arrangements.^[26]

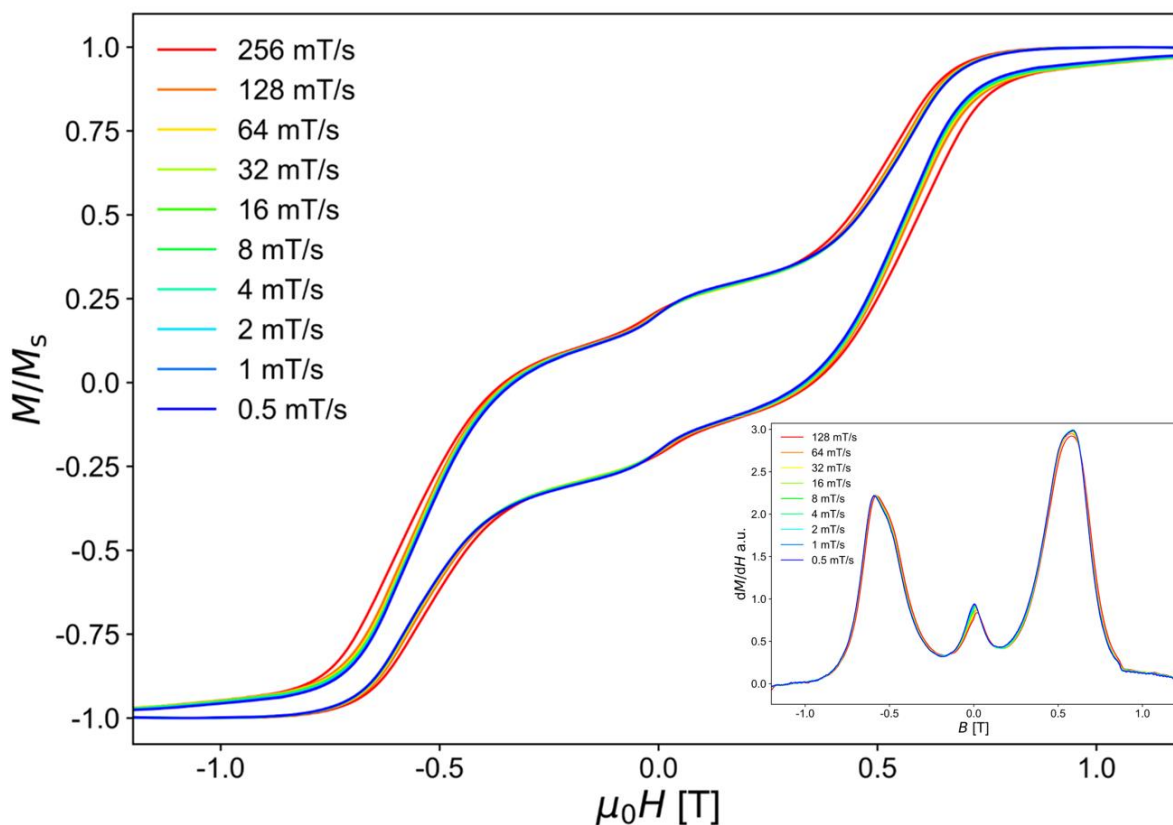


Figure 5.2-11 The microSQUID of $\text{Fe}_{18}\text{Dy}_6(\mu\text{-OH})_6(\text{ampd})_{12}(\text{Hampd})_{12}(\text{O}_2\text{C-Ph})_{24}(\text{NO}_3)_6 \cdot 38\text{MeCN}$ (**32**) measured at 30mK for varying field sweep rates, the inset shows the derivative of the plot.

In order to get fundamentally understand the magnetic processes happening for (**32**) all of the insights gained were combined to find a suitable model of the magnetic interactions within the molecule.

Due to the sheer size of the system with eighteen isotropic Fe^{III} with $S = 5/2$ and six anisotropic Dy^{III} with $S = 5/2$ it is virtually impossible to do any quantum calculations on (**32**). At the same time, the strong spin-orbit interaction of Dy^{III} means, that a spin-only model would be a poor approximation.

Therefore, reasonable assumptions have been made to come to a semi-quantitative solution of the magnetic interactions within (**32**)

Firstly, because the antiferromagnetic interaction between the two Fe^{III} in the base of the Fe_2Dy triangle is very strong as evidenced by the MSC, these are estimated as a singlet dimer that do not contribute to the magnetic behaviour at low temperatures. This approximation results in the rest of the system following a sawtooth chain of alternating Dy and Fe ions coupled by an effective exchange J_1^{eff} and an additional

next-nearest neighbor exchange J_2^{eff} between adjacent Fe ions, the corresponding scheme is shown in **Figure 5.2-12**.

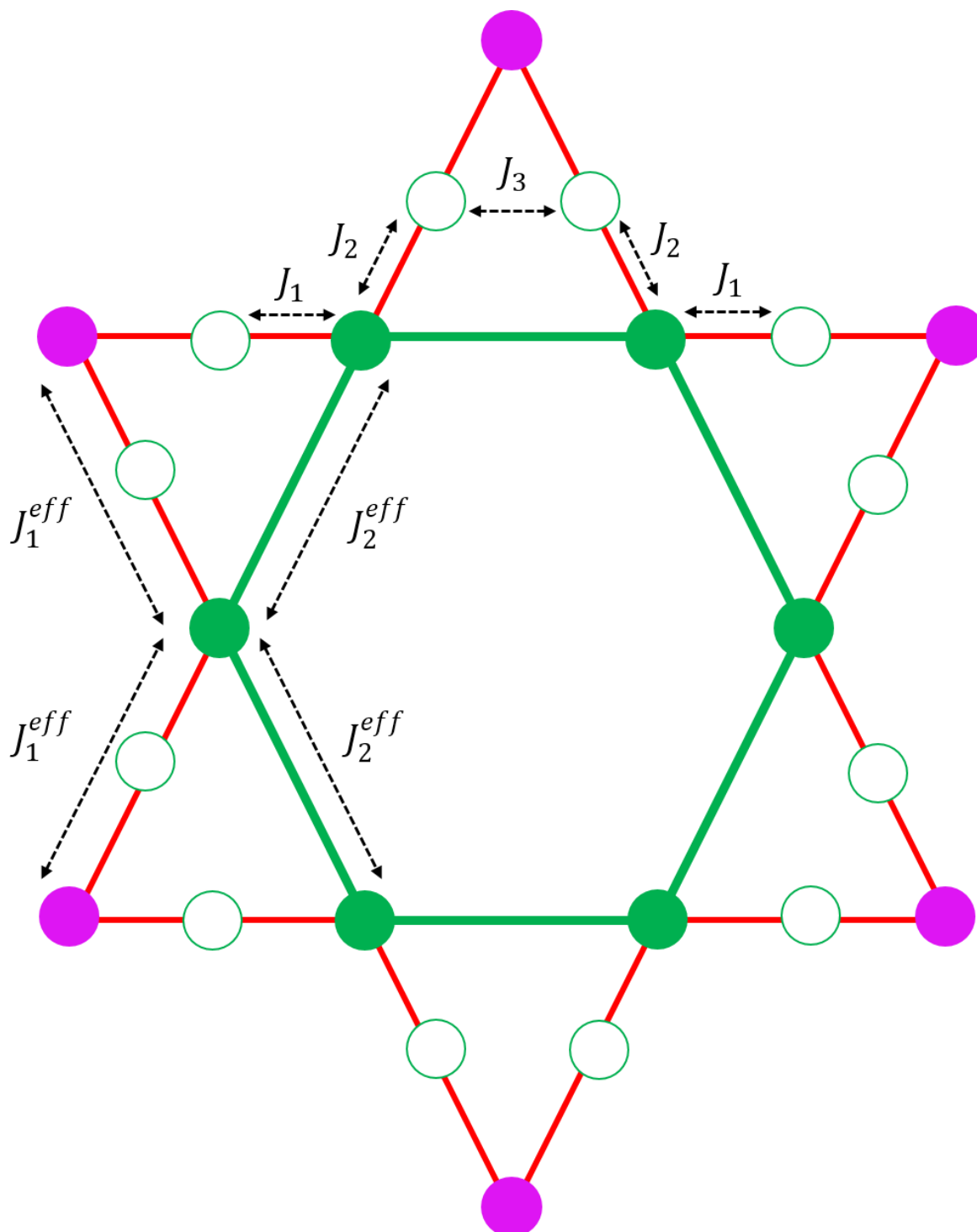


Figure 5.2-12 Sawtooth chain model highlighting the magnetic coupling in (32), open green circles show the locked Fe₂ dimer in the base of the Fe₂Dy triangle resulting from the strong antiferromagnetic interaction J_3 , filled green circles represent the connecting Fe^{III} in the hexagonal plane in the middle of the molecule, pink circles represent Dy^{III}. The scheme results in the two effective coupling constants J_1^{eff} between the Fe^{III} in the hexagon and Dy^{III}, while J_2^{eff} is the coupling constant for the interaction within the Fe₆ hexagon.

Lastly, to determine the character of the ground state of the molecule, the spin quantum numbers have been replaced by fictitious values of $s_{Dy}^{eff} = 1$ for Dy and $s_{Fe}^{eff} = \frac{1}{2}$ for Fe. These semi-quantitative calculations confirm, that the system is indeed toroidal, the energy diagrams derived from the calculations show a relatively large gap between the ground and excited states. (**Figure 5.2-13**)

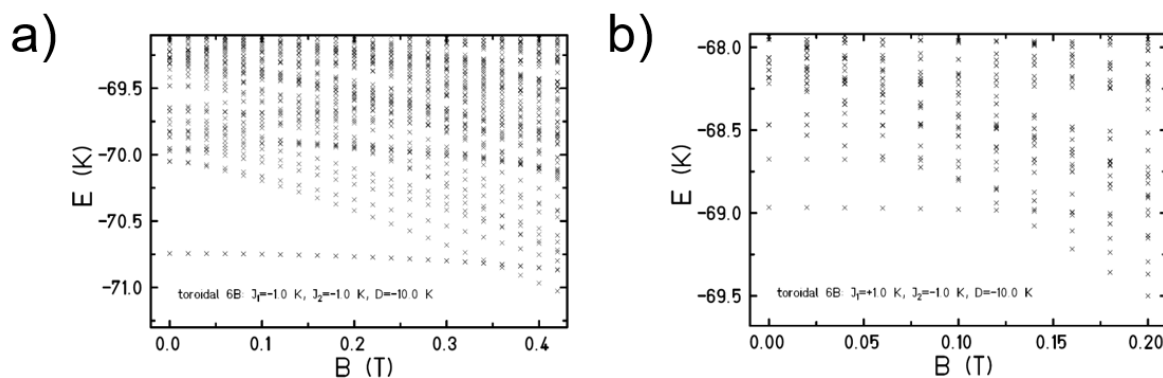


Figure 5.2-13 The energy diagram of **(32)** calculated from the model taking into account the assumptions stated in the text with antiferromagnetic interaction for J_1^{eff} (a) and ferromagnetic interaction for J_1^{eff} (b). In both cases the ground state is ferrotoroidal.

A ferrotoroidal arrangement of the anisotropy axes suggested by the calculated energy diagrams is consistent with toroidal system described in the literature, showing a similar shape of the hysteresis curve.^[24]

The magnetic data of $Fe_{18}Dy_6(\mu-OH)_6(ampd)_{12}(Hampd)_{12}(O_2C-Ph)_{24}[(NO_3)_6 \cdot 38MeCN]$ **(32)** are rather impressive. The results discussed show that not only is **(32)** the biggest Fe-4f single-molecule magnet, but at the same time it also shows the biggest toroidal arrangement of magnetic moments.

Seeing as the technological relevance of toroidal moments is heavily discussed in the scientific community in recent years,^[138] speaks to the importance of the results discussed.

5.2.2 Summary of giant cyclic coordination clusters

In conclusion it was possible to adapt the strategy used to obtain the tetranuclear compounds described in section 5.1.2 to synthesise giant cyclic coordination clusters

of the composition $\text{Fe}_{18}\text{Ln}_6(\mu\text{-OH})_6(\text{ampd})_{12}(\text{Hampd})_{12}(\text{O}_2\text{C-Ph})_{24}](\text{NO}_3)_6 \cdot 38\text{MeCN}$ for $\text{Ln} = \text{Tb}, \text{Dy}, \text{Ho}, \text{Er}, \text{Lu}$ and Y , and analyse their magnetic behaviour.

It could be shown, that the Dy^{III} variant (**32**) is the biggest Fe-4f containing single-molecule magnet at the time of its publication, showing slow relaxation of the magnetisation without the need to apply an external dc field.

Furthermore, the use of semi-quantitative quantum calculations in conjunction with microSQUID measurements concluded that the arrangement of the anisotropic axes for the Dy^{III} in (**32**) is toroidal, making compound (**32**) the biggest toroidal arrangement.

The nanoscale dimensions of these compounds could provide fundamental understanding of exotic magnetic behaviour such as those discussed here. In addition, these toroidal arrangements have been suggested to show properties of molecular Skyrmions.

Skyrmion-based devices, are anticipated to play a distinctive role in data storage and processing in the future due to their relatively small sizes and low energy consumption.^[139]

6 Overall summary and conclusion

In this thesis various pathways to obtain magnetically relevant compounds are presented. There is an increasing amount of research focussing on the future of modern electronic devices. The field of molecular magnetism is of significant relevance to this topic, given the role of rare earth metals in modern devices due to their exciting magnetic properties.

The concept of assisted self-assembly to target clusters incorporating transition metals and rare earth materials was introduced. This concept uses preformed clusters to introduce transition metals into these complexes while at the same time manipulating the kinetics of any given reaction by limiting the availability of the transition metal.

Furthermore, the important role of so-called butterfly complexes, due to their use as “test-bed” systems was highlighted. The key aspects of recent publications^[45, 117] highlighting the benefits of these butterfly complexes to the fundamental understanding of 3d-4f interactions have been presented, introducing their classification as Type I and Type II butterflies and further benchmarks to judge the quality of any given butterfly SMM.

The compounds presented in this thesis have been analysed using single-crystal X-Ray diffraction and their magnetic properties have been investigated using SQUID magnetometry. In addition to in-house methods, various collaborations have been established to gain access to more advanced analysis methods. These collaborations include ⁵⁷Fe Mößbauer experiments with the group of Prof. Schünemann and mass spectrometry experiments with the group of Prof. Niedner-Schatteburg at the University of Kaiserslautern (TUK), as well as theoretical calculations using ALPS and Quantum Monte Carlo methods with Prof. Schnack at the University of Bielefeld. Furthermore, collaborations at the Karlsruhe Institute of Technology (KIT) with the group of Prof. Bräse provided the opportunity to analyse the effect of chiral variants of some ligands used on the magnetic behaviour of single-molecule magnets.

In Chapter 3, the building blocks used were presented, highlighting their various tuning possibilities in regard to the transition metals and co-ligands used. One type of building blocks presented in this work is the well-known trinuclear oxo-centred

transition metal triangle, historically referred to as the basic carboxylate. In addition to their use as starting materials for 3d/4f synthesis these trinuclear complexes show interesting magnetic properties themselves. The composition of the basic carboxylate, with three transition metals coupled via a central $\mu_3\text{-O}^{2-}$, predisposes them to show exotic electronic properties such as spin frustration. One of the basic carboxylates investigated has an Fe_3O core, with one of the bridging carboxylates being replaced by a sulfate ion, giving the usually positively charged complex an overall neutral charge, as well as impacting the electronic structure. Magnetic measurements on this $[\text{Fe}_3\text{O}(\text{O}_2\text{C-Ph})_5\text{SO}_4]$ showed that the magnetic coupling within the compound is of complex nature below 50K, highlighting the frustrated nature of the triangle.

Further synthesis with different transition metals resulted in mixed valence and mixed transition metal analogues of the triangles, selected examples of which have been analysed via mass spectrometry.

Furthermore, a special example of the building blocks used, a hexanuclear Mn-based complex with a mixed valence $[\text{Mn}_6\text{O}_2]^{10+}$ core, was examined. It could be suggested that the hexanuclear compound is the result of the recombination of two Mn_3O trinuclear clusters and a possible process for this rearrangement was presented.

Chapter 4 explores the use of the hexanuclear starting material to access a series of Mn/4f coordination clusters. It was possible to expand the system across the series of the lanthanides, producing new analogues of structural motifs found in the literature. Previously a nonanuclear core of the composition Mn_5Ln_4 was reported in the literature for the heavier lanthanides on the right-hand side of $\text{Gd}^{[140]}$, while for the earlier lanthanides a decanuclear core of the composition Mn_7Ln_3 was found. These results were recently published^[116]. Over the course of the thesis, it was established, that a third structural type of a Mn_2Ln_2 Type II butterfly could not only be found for Gd, but was actually accessible for additional lanthanides and is potentially available over the whole series. This insight suggests that the butterfly compound represents a thermodynamic sink within this synthesis.

Chapter 5 explores the use of trinuclear starting material using tripodal ligands. In this chapter, two types of compounds were obtained: (I) new examples of Type I butterfly

systems for two different ligand systems and (II) a giant cyclic coordination cluster, showing fascinating magnetic properties.

For the butterfly systems presented in Chapter 5 it was shown that the use of a chiral ligand system dramatically changes the magnetic relaxation properties of the system.

By breaking the symmetry of the crystal structure, quantum tunnelling of magnetisation can potentially be quenched, enhancing slow relaxation as was shown for compound (27). A second example of the symmetry breaking effect of the chiral ligand is shown for the complexes (29) and (30), where the use of a chiral ligand enabled slow relaxation of magnetisation to be detected for the first time in this system. These systematic studies on butterfly compounds further substantiate the usefulness of this structure type as a “test-bed” system to investigate the effects of subtle changes on the magnetic properties.

Lastly, the cyclic coordination cluster presented in chapter 5, represents another example of exotic magnetic behaviour. Not only is the tetraicosanuclear compound $[\text{Fe}_{18}\text{Dy}_6(\mu\text{-OH})_6(\text{ampd})_{12}(\text{Hampd})_{12}(\text{O}_2\text{C-Ph})_{24}](\text{NO}_3)_6 \cdot 38\text{MeCN}$ (32) the biggest Fe/4f single-molecule magnet to date, but it also shows the biggest toroidal arrangement of Dy^{III} spins reported to date. The results of this chapter have recently been published in an article in the Journal of the American Chemical Society.^[27] These nanoscale structures provide valuable insights into magnetic processes. Furthermore, toroidal arrangements like that found for (32) are suggested to show properties of molecular Skyrmions, a type of quasi-particle that is predicted to have a potentially valuable role in the future of data storage and processing.

The research presented in this thesis provides new results in the field of molecular magnetism, as well as opening up possibilities for further investigation. Future experiments are possible using the systematic approach provided by assisted self-assembly processes, allowing the introduction of various transition metals and co-ligands into a given synthetic system. Furthermore, the results show how small changes to the molecular structure, for example by introducing a chiral centre into the ligand can have a huge impact on the crystal and therefore magnetic structure of single-molecule magnets.

7 Experimental section

7.1 General procedures

The coordination spheres and their deviations from the perfect geometries were calculated by the software SHAPE 2.1.^[78] Images of molecular structures were generated by the software Diamond 4.6.4.

FT-IR-spectroscopy. The infrared spectra were collected by a “Platinum Alpha ATR” from Bruker in a range from 400 cm⁻¹ to 4000 cm⁻¹ with a resolution of 1 cm⁻¹.

Elemental analysis. For the determination of the carbon-, hydrogen- and nitrogen proportion the CHNS-analysis device “Vario Micro Cube” from Perkin Elmer was used.

Single crystal x-ray diffraction measurements. The crystal structures were measured with different types of diffractometers:

Agilent “SuperNova” (dual source: MoK_α, λ = 0.71073; CuK_α, λ = 1.54184; detector: EosS2 (detector type: CCD)).

Stoe “StadiVari” (single source: MoK_α, λ = 0.71073; detector: Dectris Pilatus (300K) (detector type: CMOS).

Stoe “StadiVari” (single source: GaK_α, λ = 1.34143; detector: Dectris Eiger2 R 4M (detector type: HPC).

Bruker SMART Apex CCD diffractometer using a MoK_α, λ = 0.71073 rotating anode source

The crystals were attached to the goniometer head with perfluoro ether oil. In order to determine the unit cell, first some frames were recorded at different angles of rotation.

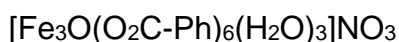
The data were corrected semi-empirically for absorption.^[141] The structure determination and refinement were performed using SHELXT^[142] and SHELXL,^[141] using the program OLEX2.^[143]

SQUID measurements. The investigation of magnetic properties of a polycrystalline sample was carried out with a QuantumDesign MPMS-XL7 (Magnetisation, χT and AC measurements) in the 1.8-300K temperature range and applied fields from -7-7Tesla. AC-susceptibility measurements were carried out under a frequency between 1-1500 Hz with an oscillating magnetic field of 3·10⁻⁴ T.

MicroSQUID measurements. Single crystal measurements were carried out on a micro-SQUID by the group of Prof. Wernsdorfer (KIT) for different temperatures and different sweep rates.

7.2 Synthesis

All commercial reagents have been used without further purification.



This compound has been prepared by a modified literature^[134, 144-145] procedure.

A solution of $\text{Fe}(\text{NO}_3)_3 \cdot 9\text{H}_2\text{O}$ (6.06g, 15 mmol) in absolute ethanol (30 ml) was added to a second solution of sodium benzoate/ benzoic acid (7.2 g, 50 mmol)/ (4.6 g, 40 mmol) in dist. Water (50 ml). The resulting orange suspension was stirred at 60°C for 2h and further 2h at ambient temperature. The orange-brown product was washed with water/EtOH/Et₂O (5/5/5ml). The product was then collected and dried under vacuum.

Generic “M₃O”

$\text{MCl}_3 \cdot x\text{H}_2\text{O}$ (M= Cr, Fe), $\text{M}(\text{NO}_3)_3 \cdot x\text{H}_2\text{O}$ (M= Cr, Fe), $\text{MCl}_2 \cdot x\text{H}_2\text{O}$ (M= Mn, Co, Ni), $\text{M}(\text{NO}_3)_2 \cdot x\text{H}_2\text{O}$ (M= Mn, Co, Ni) (15 mmol) and sodium benzoate (50mmol) are mixed in water, the resulting precipitate is washed and dried at room temperature.

(1) A solution of $\text{FeCl}_3 \cdot 6\text{H}_2\text{O}$ (1.00eq) in water (3.33eq) was added slowly to a solution of $\text{Na}(\text{O}_2\text{C-Ph})$ (1.46eq) in water (20.0eq). The flesh-colored precipitate of iron benzoate formed was washed with water and dried at room temperature.

A portion (1.00 eq) was mixed with 96% ethanol (145 eq) to give a milky orange suspension. 20% perchloric acid (3.47 eq) was slowly added until the solution cleared. It was then gently warmed on a steam bath for 10 minutes and filtered hot. Boiling water (481 eq) was added to the filtrate and orange solid formed immediately. It was left to cool, filtered off in air, and washed with 60:40 water-acetone. The resulting orange powder was dried on air. Crystalline material suitable for X-Ray diffraction can be obtained by recrystallisation from ethanol.

(2) The compound was prepared with the same procedure as (1) but NaBPh_4 (4 eq) was added instead of perchloric acid, the reaction mixture was then kept under reflux

for 1h, filtered hot and left to crystallise. Orange crystals formed after 3 days. Anal., calc. (%): C, 63.5 (62.3); H, 4.1 (4.5)

(3) The compound was prepared with the same procedure as (1) but adding HCl (4 eq) instead of perchloric acid, the reaction mixture was then kept under reflux for 1h, filtered hot and left to crystallise. Orange/red crystals formed after 3 days.

(4) The compound was prepared with the same procedure as (1) but adding H₂SO₄ (4eq) instead of perchloric acid. Anal., calc. (%): C, 43.5 (46.9); H, 3.5 (4.6); S, 2.6 (2.9).

(5) [Fe₃O(O₂C-Ph)₆(H₂O)₃]NO₃ (0.331g, 30mmol) and N-(p-aminobenzenesulfonate)-1,8-naphthalimide (0.043g, 0.100mmol) are dissolved in a mixture of 20ml MeOH and 5ml DMF, the reaction mixture is stirred at 90°C for 2h, left to cool down, filtered and left in air for crystallisation. Yellow crystals can be obtained after 2 weeks.

(6) "Fe₃O" (0.20g, 2eq) and "Ni₃O" (0.10g, 1eq) are dissolved in 35ml pyridine. The mixture is heated to 90°C for 2h, filtered and left to crystallise. Dark crystals of [Fe^{III}₂Fe^{II}O(O₂C-Ph)₆(py)₃] are obtained after 1 week. Anal. calc. (%): C, 55.9 (59.5); H, 3.7 (3.9); N, 4.3 (3.7)

(7) "Cr₃O" (0.20g, 2eq) and "Mn₃O" (0.10g, 1eq) are dissolved in 35ml pyridine. The mixture is heated to 90°C for 2h, filtered and left to crystallise. Dark green crystals of [Cr₃O(O₂C-Ph)₆(py)₃]·py are obtained after 1 week. Anal. calc. (%): C, 56.3 (59.8); H, 3.9 (4.1); N, 5.3 (5.5)

(8) "Fe₃O" (0.20g, 2eq) and "Co₃O" (0.10g, 1eq) are dissolved in 35ml pyridine. The mixture is heated to 90°C for 2h, filtered and left to crystallise. A dark brown microcrystalline powder precipitates within 2 days.

(9) "Fe₃O" (0.20g, 2eq) and "Mn₃O" (0.10g, 1eq) are dissolved in 35ml pyridine. The mixture is heated to 90°C for 2h, filtered and left to crystallise. A dark brown microcrystalline powder precipitates within 2 days.

(10) A solution of Cr(NO₃)₃·9H₂O (3.57g, 15 mmol) in absolute ethanol (30 ml) was added to a second solution of sodium acetate (7.4 g, 90 mmol) in dest. Water (50 ml). The resulting green suspension was stirred at 60°C for 2 h and further 2 h at ambient temperature. The greenish grey product was washed with water/EtOH/Et₂O

(5/5/5mL). 100mg of the intermediate product were dissolved in 35ml pyridine, heated to 60°C over 1h and left to crystallise. Green crystals of $[\text{Cr}_3\text{O}(\text{OAc})_6(\text{py})_3]\text{NO}_3$ are obtained after 1 week.

(11) $\text{Mn}(\text{OAc})_2 \cdot 4\text{H}_2\text{O}$ (3.00 g, 12.00 mmol) was mixed with KMnO_4 (1.90 g, 12.00 mmol) and pivalic acid (18.36 g, 180.00 mmol). The solids were heated to 60°C until the pivalic acid became liquid and then was stirred and heated to ca. 200°C. The solution was stirred for 2h at 200°C until it turned beige flesh pink. After cooling the mixture to 100°C, MeCN (10ml) and 4-Me-py (0.6ml) were added. The temperature is again increased to ca. 200°C, after 5 min the heater was then turned off and MeCN (30ml) was given to the mixture. Red brown crystals form immediately upon cooling the reaction mixture. The microcrystalline intermediate is recrystallised from 1:1 MeCN/ CH_2Cl_2 , washed with ca. 20ml MeCN and dried in air. Anal., calc. (%): C, 44.2 (49.0); H, 6.5 (7.1); N, 0.85 (1.6) ; IR: $\nu = 2960$ (s), 2927 (m), 1693 (m), 1611 (m), 1570 (vs), 1482 (vs), 1459 (w), 1414 (vs), 1373 (s), 1359 (s), 1319 (w), 1225 (s), 1207 (m), 1030 (w), 1014 (w), 976 (w), 936 (w), 894 (w), 804 (w), 788 (w), 724 (w), 601 (s), 550 (m), 535 (w), 488 (w), 435 cm^{-1} (w).

(12) $\text{Nd}(\text{NO}_3)_3 \cdot 6\text{H}_2\text{O}$ (0.29 g, 0.66 mmol) was added to a stirred slurry of (11) (0.20 g, 0.11 mmol) and *N*-methyldiethanolamine (0.140 g, 1.17 mmol) in MeCN (15 ml). After stirring for 5 minutes at room temperature, the mixture was heated at 70°C for 35 minutes to give a dark-brown solution. The solution was allowed to cool, filtered, and left to evaporate slowly at room temperature in a 25 ml glass covered with parafilm. Dark brown crystals were obtained after one week, collected by filtration, washed with 5 ml cold MeCN, and dried in air. Yield: 65 mg (27.0 % based on Mn). Anal., calc. (%): C, 29.93 (30.06); H, 5.07 (4.96); N, 3.34 (3.50); IR (KBr): $\nu/\text{cm}^{-1} = 3419$ (b, m), 2962 (s), 2929 (s), 2871 (s), 1608 (vs), 1564 (s), 1548 (s), 1484 (vs), 1463 (s), 1408 (vs), 1372 (s), 1358 (s), 1282 (s), 1223 (s), 1068 (s), 1027 (w), 996 (m), 903 (w), 816 (w), 794 (w), 758 (w), 736 (w), 682 (w), 632 (s), 614 (s), 549 (m), 460 (w).

(13) The compound was obtained by the same procedure using $\text{Sm}(\text{NO}_3)_3 \cdot 6\text{H}_2\text{O}$ in place of $\text{Nd}(\text{NO}_3)_3 \cdot 6\text{H}_2\text{O}$. Their IR spectra are similar. Yield: 60 mg (25.0 % based on Mn). Anal., calc. (%): C, 29.66 (29.84); H, 4.99 (4.92); N, 3.37 (3.48)

(14) The compound was obtained by the same procedure using $\text{Eu}(\text{NO}_3)_3 \cdot 6\text{H}_2\text{O}$ in place of $\text{Nd}(\text{NO}_3)_3 \cdot 6\text{H}_2\text{O}$. Their IR spectra are similar. Yield: 62 mg (25.8 % based on Mn). Anal., calc. (%): C, 29.57 (29.78); H, 5.03 (4.91); N, 3.34 (3.47)

(15) For this compound the same synthetic procedure as for (12) was used but using $\text{Gd}(\text{NO}_3)_3 \cdot 6\text{H}_2\text{O}$ instead of $\text{Nd}(\text{NO}_3)_3 \cdot 6\text{H}_2\text{O}$ and adding small changes: after the solution was left for the evaporation, after one day it was again filtered to remove any brown crystals of the starting material (11). The filtrate was covered again with parafilm and left for further crystallisation. After one week new, darker crystals of (15) were formed and filtered off. Yield: 25 mg (10.4 % based on Mn). Anal., calc. (%): C, 29.39 (29.58); H, 4.97 (4.88); N, 3.41 (3.45)

(16) N-methyldiethanolamine (0.147 g, 1.23 mmol) and (11) (0.20 g, 0.11 mmol) were mixed and stirred in MeCN (15 mL) for 15 min. $\text{Tb}(\text{NO}_3)_3 \cdot 6\text{H}_2\text{O}$ (0.365g, 0.66mmol) was added and stirred for another 10 min at room temperature. The dark-brown mixture was then heated and maintained under reflux for 40 min. After cooling to room temperature, the solution was filtered and covered with a lid with small holes in it to ensure slow evaporation of the solvent (at room temperature). After two to three weeks brown crystals were formed, filtered, washed with cold MeCN (5ml) and dried in air.

(17) The compound was obtained by the same procedure using $\text{Er}(\text{NO}_3)_3 \cdot 6\text{H}_2\text{O}$ in place of $\text{Tb}(\text{NO}_3)_3 \cdot 6\text{H}_2\text{O}$.

(18) The compound was obtained by the same procedure using $\text{Tm}(\text{NO}_3)_3 \cdot 6\text{H}_2\text{O}$ in place of $\text{Tb}(\text{NO}_3)_3 \cdot 6\text{H}_2\text{O}$.

(19) The compound was obtained by the same procedure using $\text{Gd}(\text{NO}_3)_3 \cdot 6\text{H}_2\text{O}$ in place of $\text{Tb}(\text{NO}_3)_3 \cdot 6\text{H}_2\text{O}$ as well as changing the solvent to iPrOH. Yield: 30 mg (14.4 % based on Mn). IR [cm^{-1}]: $\nu = 2962$ (br), 2871 (w), 1589 (m), 1560 (m), 1543 (m), 1482 (s), 1457 (m), 1406 (s), 1361 (s), 1281 (s), 1223 (s), 1112 (s), 1084 (m), 1059 (s), 1026 (s), 993 (s), 946 (s), 895 (s), 815 (m), 786 (m), 759 (m), 735 (m), 675 (m), 583 (s), 556 (s), 495 (s), 445 (w) cm^{-1} .

(20) The compound was obtained by the same procedure using $\text{Gd}(\text{NO}_3)_3 \cdot 6\text{H}_2\text{O}$ in place of $\text{Tb}(\text{NO}_3)_3 \cdot 6\text{H}_2\text{O}$ as well as changing the solvent to MeOH. Yield: 141 mg (49.1 % based on Mn). IR [cm^{-1}]: $\nu = 2957$ (br), 2820 (w), 1568 (m), 1562 (s), 1482 (s),

1457 (w), 1408 (s), 1361 (s), 1359 (s), 1295 (s), 1223 (s), 1082 (m), 1055 (m), 1030 (s), 1008 (s), 895 (s), 784 (m), 696 (s), 636 (m), 612 (m), 554 (m), 548 (m), 503 (s), 449 (m) cm^{-1}

(21) The compound was obtained by the same procedure using $\text{Gd}(\text{NO}_3)_3 \cdot 6\text{H}_2\text{O}$ in place of $\text{Tb}(\text{NO}_3)_3 \cdot 6\text{H}_2\text{O}$. The reaction mixture was filtered after 1 week to remove brown precipitate.

(22) The compound was obtained by the same procedure using $\text{Pr}(\text{NO}_3)_3 \cdot 6\text{H}_2\text{O}$ in place of $\text{Tb}(\text{NO}_3)_3 \cdot 6\text{H}_2\text{O}$. The reaction mixture was filtered after 1 week to remove brown precipitate.

(23) $\text{Gd}(\text{NO}_3)_3 \cdot 6\text{H}_2\text{O}$ (0.158 g, 0.350 mmol) and 2-amino-2-methyl-1,3-propanediol (H_2ampd) (0.210 g, 1.998 mmol) were dissolved in 40 ml MeCN, simultaneously a second solution of the second of $[\text{Fe}_3\text{O}(\text{O}_2\text{C-Ph})_6(\text{H}_2\text{O})_3]\text{NO}_3$ (0.250 g, 0.230 mmol) in 5 ml MeCN was prepared. Both solutions were stirred separately at room temperature for 15 min. Afterwards the white milky suspension of the lanthanide salt and the ligand was slowly added to the solution of $[\text{Fe}_3\text{O}(\text{O}_2\text{C-Ph})_6(\text{H}_2\text{O})_3]\text{NO}_3$. The combined reaction mixture was sealed and stirred further for 60 min at 80°C . The solution was then filtered warm and sealed. After 2 weeks, yellow crystals of (23) are obtained.

(24) The compound is obtained by the same procedure as (23) but using $\text{Y}(\text{NO}_3)_3 \cdot 6\text{H}_2\text{O}$ and "Cr3O" instead in place of $\text{Gd}(\text{NO}_3)_3 \cdot 6\text{H}_2\text{O}$ and $[\text{Fe}_3\text{O}(\text{O}_2\text{C-Ph})_6(\text{H}_2\text{O})_3]\text{NO}_3$.

(25) The compound is obtained by the same procedure as (23) but using $\text{Dy}(\text{NO}_3)_3 \cdot 6\text{H}_2\text{O}$ and "Cr3O" instead in place of $\text{Gd}(\text{NO}_3)_3 \cdot 6\text{H}_2\text{O}$ and $[\text{Fe}_3\text{O}(\text{O}_2\text{C-Ph})_6(\text{H}_2\text{O})_3]\text{NO}_3$.

(26) $\text{Fe}_3\text{O}(\text{O}_2\text{CPh})_6(\text{H}_2\text{O})_3](\text{O}_2\text{CPh})$ (0.25 g, 0.242 mmol), Me-teaH_3 (0.326 g, 2 mmol) and $\text{Dy}(\text{NO}_3)_3 \cdot 6\text{H}_2\text{O}$ (0.116 g, 0.25 mmol) were dissolved in MeCN/MeOH (25/10 ml). The orange-brown solution was stirred with heating at 50°C for 35 min and then left to cool in a closed vial. Crystallisation began after 12 h and the crystals were collected after two days Yield: 84% (based on Dy). Anal., calc.(%): C, 47.80 (47.26); H, 4.46 (4.45); N, 4.46 (4.99) IR [cm^{-1}]: $\nu = 3361$ (br), 3064 (w), 2970 (w), 2853 (br), 2502 (w), 2251 (w), 1687 (m), 1596 (s), 1549 (s), 1491 (w), 1450 (m), 1389 (s), 1315 (m), 1267

(m), 1175 (m), 1123 (m), 1090 (m), 1037 (w), 1024 (w), 897 (m), 864 (w), 790 (w), 718 (s), 687 (m), 674 (m), 588 (m), 521 (w), 452 (w), 431 (w).

(27) $[\text{Fe}_3\text{O}(\text{O}_2\text{CPh})_6(\text{H}_2\text{O})_3](\text{O}_2\text{CPh})$ (0.25 g, 0.242 mmol) and $\text{Dy}(\text{NO}_3)_3 \cdot 6\text{H}_2\text{O}$ (0.116 g, 0.25 mmol) were dissolved in 10 ml of MeCN. To this was added a solution of S-Me-teaH₃ (0.326 g, 2 mmol) dissolved in 5 ml MeCN. The solution was stirred and MeCN (10 ml) was subsequently added followed by the addition of MeOH (10 ml). The orange-brown solution was stirred with heating at 50°C for 35 min and then left to cool in a closed vial. Crystallisation began after 5-7 days and the crystals were collected after one week Yield: 26% (based on Dy). Anal., Calc.(%): C, 47.80 (47.26); H, 4.46 (4.41); N, 4.88 (4.99) IR [cm^{-1}]: $\nu = 3361$ (br), 3064 (w), 2970 (w), 2853 (br), 2502 (w), 2251 (w), 1687 (m), 1596 (s), 1549 (s), 1491 (w), 1450 (m), 1389 (s), 1315 (m), 1267 (m), 1175 (m), 1123 (m), 1090 (m), 1037 (w), 1024 (w), 897 (m), 864 (w), 790 (w), 718 (s), 687 (m), 674 (m), 588 (m), 521 (w), 452 (w), 431 (w).

(28) . A mixture of Me-teaH₃ (0.163 g, 1 mmol) and $\text{Dy}(\text{NO}_3)_3 \cdot 6\text{H}_2\text{O}$ (0.116 g, 0.25 mmol) in MeCN/MeOH (10/2.5 ml) was added to a solution of $[\text{Fe}_3\text{O}(\text{O}_2\text{CPh})_6(\text{H}_2\text{O})_3](\text{O}_2\text{CPh})$ (0.125 g, 0.121 mmol) in MeCN (10 ml) under stirring. The orange-brown solution was stirred for 20 min and then left to a closed vial. Crystallisation began after one day and the crystals were collected after two days Yield: 72% (based on Dy). Anal., calc.(%): C, 38.16 (38.32); H, 4.34 (4.45); N, 6.95 (6.88)

(29) The compound was obtained by the same procedure as (28) but using enantiomerically-pure R-Me-teaH₃ instead in place of the racemic Me-teaH₃. Anal., calc.(%): C, 38.95 (38.87); H, 4.10 (4.20); N, 7.74 (7.85)

(30) The compound was obtained by the same procedure as (28) but using enantiomerically-pure S-Me-teaH₃ instead in place of the racemic Me-teaH₃. Anal., calc.(%): C, 38.77 (38.87); H, 4.17 (4.20); N, 7.88 (7.85)

(31) $\text{Tb}(\text{NO}_3)_3 \cdot 6\text{H}_2\text{O}$ (0.159 g, 0.350 mmol) and 2-amino-2-methyl-1,3-propanediol (H₂ampd) (0.210 g, 1.998 mmol) were dissolved in 40 ml MeCN, simultaneously a second solution of the second of $[\text{Fe}_3\text{O}(\text{O}_2\text{C-Ph})_6(\text{H}_2\text{O})_3]\text{NO}_3$ (0.250 g, 0.230 mmol) in 5 ml MeCN was prepared. Both solutions were stirred separately at room temperature for 15 min. Afterwards the white milky suspension of the lanthanide salt

and the ligand was slowly added to the solution of $[\text{Fe}_3\text{O}(\text{O}_2\text{C-Ph})_6(\text{H}_2\text{O})_3]\text{NO}_3$. The combined reaction mixture was sealed and stirred further for 60 min at room temperature. The solution was then filtered, sealed and left for crystallisation. After 3 days, pale green crystals of **(31)** are collected. Anal., calc.(%): C, 38.91 (36.43); H, 4.39 (4.92); N, 5.99 (6.07) for the dried sample.

(32) The compound was obtained by the same procedure using $\text{Dy}(\text{NO}_3)_3 \cdot 6\text{H}_2\text{O}$ in place of $\text{Tb}(\text{NO}_3)_3 \cdot 6\text{H}_2\text{O}$. Yield: 15% based on Dy., Anal., Calc. (%): C, 39.49 (39.50); H, 4.79 (4.70); N, 5.18 (5.23) for **(32)**·10H₂O; IR [cm^{-1}]: $\nu = 2897$ (w), 1594 (m), 1518 (s), 1391 (s), 1300 (w), 1175 (w), 1065 (s), 1021 (m), 900 (m), 800 (m), 716 (s)

(33) The compound was obtained by the same procedure using $\text{Ho}(\text{NO}_3)_3 \cdot 6\text{H}_2\text{O}$ in place of $\text{Tb}(\text{NO}_3)_3 \cdot 6\text{H}_2\text{O}$, Anal., Calc. (%): C, 39.25 (39.50); H, 4.41 (4.70); N, 5.65 (5.23) for **(33)**·10H₂O; the IR spectrum looks identical to that of **(32)**

(34) The compound was obtained by the same procedure using $\text{Er}(\text{NO}_3)_3 \cdot 6\text{H}_2\text{O}$ in place of $\text{Tb}(\text{NO}_3)_3 \cdot 6\text{H}_2\text{O}$, Anal., Calc. (%): C, 38.35 (39.50); H, 4.35 (4.70); N, 5.78 (5.23) for **(34)**·10H₂O; the IR spectrum looks identical to that of **(32)**

(35) The compound was obtained by the same procedure using $\text{Lu}(\text{NO}_3)_3 \cdot 6\text{H}_2\text{O}$ in place of $\text{Tb}(\text{NO}_3)_3 \cdot 6\text{H}_2\text{O}$, Anal., Calc. (%): C, 38.77 (38.95); H, 4.38 (4.80); N, 5.53 (5.42) for **(35)**·2MeCN·20H₂O; the IR spectrum looks identical to that of **(32)**

(36) The compound was obtained by the same procedure using $\text{Y}(\text{NO}_3)_3 \cdot 6\text{H}_2\text{O}$ in place of $\text{Tb}(\text{NO}_3)_3 \cdot 6\text{H}_2\text{O}$, Anal., Calc. (%): C, 40.54 (40.83); H, 4.91 (5.11); N, 5.41 (5.71) for **(36)**·20H₂O; the IR spectrum looks identical to that of **(32)**

8 Crystallographic data

Table 8-1 Crystallographic data for compound (1) and (2).

Compound	(1)	(2)
Empirical formula	C ₆₀ H ₆₀ O ₂₀ ClFe ₃	C ₄₅ H ₄₀ BO ₁₅ Fe ₃
Formula weight/ gmol ⁻¹	1304.08	999.13
Temperature/K	199.99(10)	200.00(10)
Crystal system	monoclinic	monoclinic
Space group	P2 ₁ /c	P2 ₁ /c
a/Å	14.7314(2)	11.8656(5)
b/Å	18.6789(2)	29.6749(18)
c/Å	21.6553(2)	20.6174(14)
α/°	90	90
β/°	91.3550(10)	94.135(5)
γ/°	90	90
Volume/Å ³	5957.14(12)	7240.7(7)
Z	4	8
ρ _{calc} /g/cm ³	1.454	1.833
μ/mm ⁻¹	6.832	10.239
F(000)	2700	4104.0
Diffraction type	Agilent SuperNova	Agilent SuperNova
Radiation	CuKα (λ = 1.54184)	CuKα (λ = 1.54184)
2θ range for data collection/°	6.002 to 142.1	5.228 to 144.338
Index ranges	-17 ≤ h ≤ 18, -22 ≤ k ≤ 16, -26 ≤ l ≤ 26	-14 ≤ h ≤ 14, -29 ≤ k ≤ 36, -25 ≤ l ≤ 24
Reflections collected	33822	50506
Independent reflections	11299 [R _{int} = 0.0289, R _{sigma} = 0.0361]	13855 [R _{int} = 0.2230, R _{sigma} = 0.1443]
Data/restraints/parameters	11299/3/643	13855/4/725
Goodness-of-fit on F ²	1.042	1.349
Final R indexes [I ≥ 2σ (I)]	R ₁ = 0.0711, wR ₂ = 0.2176	R ₁ = 0.2198, wR ₂ = 0.4806
Final R indexes [all data]	R ₁ = 0.0924, wR ₂ = 0.2373	R ₁ = 0.3315, wR ₂ = 0.5679
Largest diff. peak/hole / e Å ⁻³	1.28/-0.98	1.80/-0.61

Table 8-2 Crystallographic data for compound (3) and (4).

Compound	(3)	(4)
Empirical formula	C ₇₆ H ₈₈ ClFe ₃ N ₂ O ₁₃	C ₄₃ H ₅₃ Fe ₃ O ₂₁ S
Formula weight/ gmol ⁻¹	1440.48	1105.46
Temperature/K	180.15	180.15
Crystal system	tetragonal	monoclinic
Space group	P41	P21/c
a/Å	25.5415(3)	16.8646(6)
b/Å	25.5415(3)	18.4331(5)
c/Å	12.9709(2)	16.2427(6)
α/°	90	90
β/°	90	106.143(3)
γ/°	90	90
Volume/Å ³	8461.8(2)	4850.2(3)
Z	4	4
ρ _{calc} /cm ³	1.131	1.514
μ/mm ⁻¹	3.214	1.007
F(000)	3028.0	2292.0
Diffraction type	Stoe StadiVari	Stoe StadiVari
Radiation	GaKα (λ = 1.34143)	MoKα (λ = 0.71073)
2θ range for data collection/°	6.022 to 123.966	4.656 to 66.46
Index ranges	-33 ≤ h ≤ 12, -33 ≤ k ≤ 33, -17 ≤ l ≤ 17	-25 ≤ h ≤ 21, -17 ≤ k ≤ 28, -24 ≤ l ≤ 24
Reflections collected	56332	36637
Independent reflections	19816 [Rint = 0.0260, Rsigma = 0.0327]	16536 [Rint = 0.0381, Rsigma = 0.0417]
Data/restraints/parameters	19816/6/912	16536/8/623
Goodness-of-fit on F ²	1.072	1.065
Final R indexes [I ≥ 2σ (I)]	R1 = 0.0671, wR2 = 0.1932	R1 = 0.0628, wR2 = 0.1636
Final R indexes [all data]	R1 = 0.0820, wR2 = 0.2070	R1 = 0.0958, wR2 = 0.1956
Largest diff. peak/hole / e Å ⁻³	1.35/-0.74	1.21/-1.20

Table 8-3 Crystallographic data for compound (5) and (6).

Compound	(5)	(6)
Empirical formula	$C_{48}H_{34.67}Fe_{0.67}N_{2.67}O_{17.33}S_{2.67}$	$C_{57}H_{45}Fe_3N_3O_{13}$
Formula weight/ gmol ⁻¹	1048.84	1147.51
Temperature/K	293(2)	200.00(10)
Crystal system	monoclinic	triclinic
Space group	P21/n	P-1
a/Å	17.0833(13)	20.3973(4)
b/Å	6.9827(11)	20.6696(5)
c/Å	35.728(5)	20.8625(4)
α/°	90	60.512(2)
β/°	102.699(9)	73.159(2)
γ/°	90	60.753(2)
Volume/Å ³	4157.7(9)	6666.3(3)
Z	3	4
ρ _{calc} /cm ³	1.257	1.143
μ/mm ⁻¹	3.030	5.618
F(000)	1620.0	2360.0
Diffractometer type	Agilent SuperNova	Agilent SuperNova
Radiation	CuKα (λ = 1.54184)	CuKα (λ = 1.54184)
2θ range for data collection/°	5.352 to 143.864	4.876 to 142.14
Index ranges	-10 ≤ h ≤ 20, -6 ≤ k ≤ 8, -44 ≤ l ≤ 43	-18 ≤ h ≤ 25, -25 ≤ k ≤ 25, -25 ≤ l ≤ 24
Reflections collected	16606	68073
Independent reflections	7748 [Rint = 0.1010, Rsigma = 0.1088]	25312 [Rint = 0.0322, Rsigma = 0.0388]
Data/restraints/parameters	7748/0/485	25312/2/1362
Goodness-of-fit on F ²	1.375	1.063
Final R indexes [I ≥ 2σ (I)]	R1 = 0.2252, wR2 = 0.5187	R1 = 0.0421, wR2 = 0.1068
Final R indexes [all data]	R1 = 0.3262, wR2 = 0.6040	R1 = 0.0604, wR2 = 0.1156
Largest diff. peak/hole / e Å ⁻³	1.25/-0.95	0.39/-0.43

Table 8-4 Crystallographic data for compound (7) and (11).

Compound	(7)	(11)
Empirical formula	C ₆₃ H ₅₁ Cr ₃ N ₄ O ₁₉	C ₇₂ H ₁₂₄ Mn ₆ N ₂ O ₂₆
Formula weight/ gmol ⁻¹	1324.05	1763.36
Temperature/K	180.15	150.0
Crystal system	hexagonal	triclinic
Space group	P63/m	P-1
a/Å	13.1619(3)	13.8565(7)
b/Å	13.1619(3)	15.5894(7)
c/Å	19.2754(5)	23.9663(9)
α/°	90	107.941(3)
β/°	90	93.742(4)
γ/°	120	106.128(4)
Volume/Å ³	2891.82(15)	4666.6(4)
Z	2.00004	2
ρ _{calc} /cm ³	1.521	1.255
μ/mm ⁻¹	3.605	4.559
F(000)	1362.0	1856.0
Diffraction type	Stoe StadiVari	Stoe StadiVari
Radiation	GaKα (λ = 1.34143)	GaKα (λ = 1.34143)
2θ range for data collection/°	7.84 to 131.122	5.366 to 119.994
Index ranges	-17 ≤ h ≤ 17, -17 ≤ k ≤ 16, -25 ≤ l ≤ 9	-17 ≤ h ≤ 17, -20 ≤ k ≤ 18, -18 ≤ l ≤ 30
Reflections collected	29438	53545
Independent reflections	2567 [Rint = 0.0282, Rsigma = 0.0154]	20511 [Rint = 0.0371, Rsigma = 0.0378]
Data/restraints/parameters	2567/0/143	20511/1/983
Goodness-of-fit on F ²	1.121	1.430
Final R indexes [I ≥ 2σ (I)]	R1 = 0.0527, wR2 = 0.1539	R1 = 0.1384, wR2 = 0.3402
Final R indexes [all data]	R1 = 0.0616, wR2 = 0.1627	R1 = 0.1656, wR2 = 0.3618
Largest diff. peak/hole / e Å ⁻³	0.32/-0.75	6.19/-1.01

Table 8-5 Crystallographic data for compound (12) and (13).

Compound	(12)	(13)
Empirical formula	C ₆₈ H ₁₃₀ Mn ₇ N ₁₀ Nd ₃ O ₄₁	C ₆₆ H ₁₂₇ Mn ₇ N ₉ O ₄₁ Sm ₃
Formula weight/ gmol ⁻¹	2561.11	2538.39
Temperature/K	100(2)	100(2)
Crystal system	triclinic	monoclinic
Space group	P-1	P21/n
a/Å	14.3814(11)	22.0593(10)
b/Å	15.0511(11)	18.4408(8)
c/Å	25.8828(19)	24.1213(11)
α/°	91.889(1)	90
β/°	100.900(1)	95.685(1)
γ/°	111.755(1)	90
Volume/Å ³	5076.9(7)	9764.1(8)
Z	2	4
ρ _{calc} /cm ³	1.675	1.727
μ/mm ⁻¹	2.428	2.732
F(000)	2582.0	5100.0
Diffraction type	Bruker SMART Apex	Bruker SMART Apex
Radiation	MoKα (λ = 0.71073)	MoKα (λ = 0.71073)
2θ range for data collection/°	2.932 to 52.2	2.884 to 56.044
Index ranges	-17 ≤ h ≤ 17, -14 ≤ k ≤ 18, -32 ≤ l ≤ 29	-29 ≤ h ≤ 18, -24 ≤ k ≤ 24, -30 ≤ l ≤ 31
Reflections collected	26251	54229
Independent reflections	19657 [Rint = 0.0536, Rsigma = 0.1147]	21971 [Rint = 0.0520, Rsigma = 0.0749]
Data/restraints/parameters	19657/5/1135	21971/76/1198
Goodness-of-fit on F ²	1.062	0.948
Final R indexes [I ≥ 2σ (I)]	R1 = 0.0854, wR2 = 0.1824	R1 = 0.0400, wR2 = 0.0665
Final R indexes [all data]	R1 = 0.1365, wR2 = 0.2042	R1 = 0.0618, wR2 = 0.0715
Largest diff. peak/hole / e Å ⁻³	3.61/-1.82	1.67/-0.63

Table 8-6 Crystallographic data for compound (14), for (15) a unit cell measurement confirmed the identity of the compound.

Compound	(14)	(15)
Empirical formula	C ₆₆ H ₁₂₇ Eu ₃ Mn ₇ N ₉ O ₄₁	C ₆₆ H ₁₂₇ Mn ₇ N ₉ Gd ₃ O ₄₁
Formula weight/ gmol ⁻¹	2543.22	2559.08
Temperature/K	100(2)	
Crystal system	monoclinic	triclinic
Space group	P21/n	P-1
a/Å	22.2719(13)	14.320(2)
b/Å	18.6189(10)	14.958(2)
c/Å	24.3325(14)	25.736(3)
α/°	90	91.692(2)
β/°	95.658(1)	101.228(2)
γ/°	90	111.819(2)
Volume/Å ³	10041.0(10)	4988(2)
Z	4	2
ρ _{calc} /cm ³	1.682	-
μ/mm ⁻¹	2.776	-
F(000)	5112.0	-
Diffraction type	Bruker SMART Apex	-
Radiation	MoKα (λ = 0.71073)	-
2θ range for data collection/°	3.364 to 55.946	-
Index ranges	-25 ≤ h ≤ 27, -24 ≤ k ≤ 22, -30 ≤ l ≤ 30	-
Reflections collected	48877	-
Independent reflections	21988 [R _{int} = 0.0757, R _{sigma} = 0.0769]	-
Data/restraints/parameters	21988/85/1239	-
Goodness-of-fit on F ²	0.979	-
Final R indexes [I ≥ 2σ (I)]	R1 = 0.0516, wR2 = 0.1258	-
Final R indexes [all data]	R1 = 0.0709, wR2 = 0.1362	-
Largest diff. peak/hole / e Å ⁻³	3.86/-2.21	-

Table 8-7 Crystallographic data for compound (16) and (17).

Compound	(16)	(17)
Empirical formula	C ₅₄ H ₁₁₂ Mn ₅ N ₁₀ O ₄₀ Tb ₄	C ₅₄ H ₁₁₂ Er ₄ Mn ₅ N ₁₀ O ₄₀
Formula weight/ gmol ⁻¹	2451.91	2485.27
Temperature/K	293(2)	293(2)
Crystal system	triclinic	triclinic
Space group	P-1	P-1
a/Å	13.7880(7)	13.7240(4)
b/Å	14.0682(8)	13.9128(4)
c/Å	13.9313(8)	14.0191(4)
α/°	107.985(4)	108.501(2)
β/°	108.996(4)	109.074(2)
γ/°	109.873(4)	108.988(2)
Volume/Å ³	2118.9(2)	2106.30(11)
Z	1	1
ρ _{calc} /cm ³	1.922	1.959
μ/mm ⁻¹	21.428	17.201
F(000)	1211.0	1223.0
Diffraction type	Stoe StadiVari	Stoe StadiVari
Radiation	GaKα (λ = 1.34143)	GaKα (λ = 1.34143)
2θ range for data collection/°	6.592 to 120.152	6.592 to 125.05
Index ranges	-17 ≤ h ≤ 17, -6 ≤ k ≤ 18, -17 ≤ l ≤ 16	-18 ≤ h ≤ 18, -15 ≤ k ≤ 18, -18 ≤ l ≤ 8
Reflections collected	22300	27254
Independent reflections	9342 [R _{int} = 0.0373, R _{sigma} = 0.0305]	9992 [R _{int} = 0.0217, R _{sigma} = 0.0200]
Data/restraints/parameters	9342/0/524	9992/0/524
Goodness-of-fit on F ²	1.026	1.050
Final R indexes [I ≥ 2σ (I)]	R1 = 0.0498, wR2 = 0.1322	R1 = 0.0338, wR2 = 0.0943
Final R indexes [all data]	R1 = 0.0516, wR2 = 0.1343	R1 = 0.0371, wR2 = 0.0969
Largest diff. peak/hole / e Å ⁻³	4.33/-1.71	1.56/-1.62

Table 8-8 Crystallographic data for compound (18) and (19).

Compound	(18)	(19)
Empirical formula	C ₅₄ H ₁₀₈ Mn ₅ N ₁₀ O ₄₀ Tm ₄	C ₅₆ H ₁₁₈ Gd ₄ Mn ₅ N ₈ O ₄₀
Formula weight/ gmol ⁻¹	621.98	2447.28
Temperature/K	150.0	150.0
Crystal system	triclinic	triclinic
Space group	P-1	P-1
a/Å	13.7279(4)	13.2859(4)
b/Å	13.9014(4)	14.0277(4)
c/Å	14.0175(4)	14.1432(4)
α/°	108.472(2)	66.192(2)
β/°	109.047(2)	79.307(2)
γ/°	108.935(2)	63.011(2)
Volume/Å ³	2107.54(11)	2148.93(12)
Z	4	1
ρ _{calc} /cm ³	1.960	1.891
μ/mm ⁻¹	18.003	20.599
F(000)	1223.0	1211.0
Diffraction type	Stoe StadiVari	Stoe StadiVari
Radiation	GaKα (λ = 1.34143)	GaKα (λ = 1.34143)
2θ range for data collection/°	6.586 to 128.316	5.942 to 128.576
Index ranges	-15 ≤ h ≤ 18, -17 ≤ k ≤ 18, -18 ≤ l ≤ 9	-17 ≤ h ≤ 17, -18 ≤ k ≤ 18, -18 ≤ l ≤ 9
Reflections collected	28585	26491
Independent reflections	10271 [R _{int} = 0.0223, R _{sigma} = 0.0203]	10398 [R _{int} = 0.0387, R _{sigma} = 0.0331]
Data/restraints/parameters	10271/0/524	10398/4/527
Goodness-of-fit on F ²	1.062	1.046
Final R indexes [I ≥ 2σ (I)]	R1 = 0.0303, wR2 = 0.0820	R1 = 0.0541, wR2 = 0.1510
Final R indexes [all data]	R1 = 0.0349, wR2 = 0.0845	R1 = 0.0588, wR2 = 0.1574
Largest diff. peak/hole / e Å ⁻³	1.09/-0.54	2.79/-3.65

Table 8-9 Crystallographic data for compound **(20)** and **(21)**.

Compound	(20)	(21)
Empirical formula	C ₆₄ H ₁₃₆ Gd ₄ Mn ₅ N ₆ O ₄₀	C ₄₀ H ₈₀ Gd ₂ Mn ₂ N ₄ O ₂₄
Formula weight/ gmol ⁻¹	2533.48	1425.46
Temperature/K	293(2)	293(2)
Crystal system	triclinic	triclinic
Space group	P-1	P-1
a/Å	14.0920(5)	10.9783(3)
b/Å	14.3664(6)	13.9773(4)
c/Å	25.3113(9)	21.8074(5)
α/°	80.389(3)	78.517(2)
β/°	88.751(3)	79.273(2)
γ/°	65.306(3)	68.500(2)
Volume/Å ³	4583.8(3)	3027.53(15)
Z	2	2
ρ _{calc} /cm ³	1.836	1.564
μ/mm ⁻¹	19.325	14.186
F(000)	2526.0	1436.0
Diffraction type	Stoe StadiVari	Stoe StadiVari
Radiation	GaKα (λ = 1.34143)	GaKα (λ = 1.34143)
2θ range for data collection/°	5.982 to 125.064	3.626 to 124.998
Index ranges	-18 ≤ h ≤ 17, -18 ≤ k ≤ 18, -33 ≤ l ≤ 21	-14 ≤ h ≤ 4, -18 ≤ k ≤ 16, -28 ≤ l ≤ 28
Reflections collected	50495	33709
Independent reflections	21503 [Rint = 0.0658, Rsigma = 0.0594]	14168 [Rint = 0.0472, Rsigma = 0.0390]
Data/restraints/parameters	21503/12/1098	14168/6/662
Goodness-of-fit on F ²	1.055	1.051
Final R indexes [I ≥ 2σ (I)]	R1 = 0.0818, wR2 = 0.2215	R1 = 0.0757, wR2 = 0.2240
Final R indexes [all data]	R1 = 0.1042, wR2 = 0.2482	R1 = 0.0876, wR2 = 0.2359
Largest diff. peak/hole / e Å ⁻³	2.83/-2.17	2.83/-1.69

Table 8-10 Crystallographic data for compound **(22)** and **(23)**.

Compound	(22)	(23)
Empirical formula	C ₄₄ H ₈₆ Mn ₂ N ₆ O ₂₄ Pr ₂	C ₅₈ H ₆₈ Fe ₂ Gd ₂ N ₄ O ₂₀
Formula weight/ gmol ⁻¹	737.44	1567.36
Temperature/K	293(2)	150
Crystal system	triclinic	triclinic
Space group	P-1	P-1
a/Å	10.9078(4)	10.3596(6)
b/Å	13.3251(5)	10.6845(7)
c/Å	13.7408(5)	14.9927(9)
α/°	100.104(3)	97.980(6)
β/°	112.766(3)	103.802(6)
γ/°	111.712(3)	100.387(5)
Volume/Å ³	1588.23(11)	1556.18(17)
Z	2	1
ρ _{calc} /cm ³	1.542	1.672
μ/mm ⁻¹	10.195	17.866
F(000)	752.0	784.0
Diffraction type	Stoe StadiVari	Agilent SuperNova
Radiation	GaKα (λ = 1.34143)	CuKα (λ = 1.54184)
2θ range for data collection/°	6.538 to 124.992	6.184 to 141.72
Index ranges	-12 ≤ h ≤ 14, -17 ≤ k ≤ 14, -18 ≤ l ≤ 13	-11 ≤ h ≤ 12, -11 ≤ k ≤ 13, -18 ≤ l ≤ 17
Reflections collected	17638	11451
Independent reflections	7489 [Rint = 0.0390, Rsigma = 0.0325]	5869 [Rint = 0.0684, Rsigma = 0.0860]
Data/restraints/parameters	7489/0/367	5869/0/354
Goodness-of-fit on F ²	1.067	1.025
Final R indexes [I ≥ 2σ (I)]	R1 = 0.0501, wR2 = 0.1360	R1 = 0.0644, wR2 = 0.1574
Final R indexes [all data]	R1 = 0.0524, wR2 = 0.1448	R1 = 0.0928, wR2 = 0.1785
Largest diff. peak/hole / e Å ⁻³	1.97/-4.14	2.63/-1.72

Table 8-11 Crystallographic data for compound (24) and (25).

Compound	(24)	(25)
Empirical formula	C ₆₄ H ₆₀ Cr ₂ N ₈ O ₂₀ Y ₂	C ₆₆ H ₇₃ Cr ₂ Dy ₂ N ₈ O ₂₂
Formula weight/ gmol ⁻¹	1543.02	1759.32
Temperature/K	180.0	180.0
Crystal system	triclinic	triclinic
Space group	P-1	P-1
a/Å	9.9834(3)	9.9672(3)
b/Å	18.0050(7)	20.3385(5)
c/Å	23.1749(8)	21.8025(5)
α/°	82.580(3)	111.210(2)
β/°	79.636(3)	98.652(2)
γ/°	74.518(3)	98.252(2)
Volume/Å ³	3934.6(2)	3978.41(19)
Z	2	2
ρ _{calc} /cm ³	1.302	1.469
μ/mm ⁻¹	3.186	11.651
F(000)	1572.0	1762.0
Diffraction type	Stoe StadiVari	Stoe StadiVari
Radiation	GaKα (λ = 1.34143)	GaKα (λ = 1.34143)
2θ range for data collection/°	5.816 to 123.99	3.876 to 123.996
Index ranges	-11 ≤ h ≤ 13, -23 ≤ k ≤ 23, -30 ≤ l ≤ 27	-10 ≤ h ≤ 13, -26 ≤ k ≤ 22, -25 ≤ l ≤ 28
Reflections collected	44136	47873
Independent reflections	18303 [R _{int} = 0.0728, R _{sigma} = 0.0583]	18593 [R _{int} = 0.0422, R _{sigma} = 0.0448]
Data/restraints/parameters	18303/0/787	18593/6/834
Goodness-of-fit on F ²	1.218	1.048
Final R indexes [I ≥ 2σ (I)]	R1 = 0.0905, wR2 = 0.2701	R1 = 0.0766, wR2 = 0.2037
Final R indexes [all data]	R1 = 0.0953, wR2 = 0.2776	R1 = 0.0929, wR2 = 0.2166
Largest diff. peak/hole / e Å ⁻³	2.55/-1.51	6.86/-1.51

Table 8-12 Crystallographic data for compound **(26)** and **(27)**.

Compound	(26)	(27)
Empirical formula	C ₇₈ H ₈₆ Dy ₂ Fe ₂ N ₆ O ₂₄	C ₇₈ H ₈₆ Dy ₂ Fe ₂ N ₆ O ₂₄
Formula weight/ gmol ⁻¹	1928.22	1928.22
Temperature/K	180(2)	150(2)
Crystal system	triclinic	triclinic
Space group	P-1	P1
a/Å	11.5295(12)	11.5041(19)
b/Å	12.0665(11)	12.171(2)
c/Å	16.9409(18)	16.960(3)
α/°	70.010(8)	69.789(2)
β/°	77.329(8)	77.125(2)
γ/°	65.111(8)	65.389(2)
Volume/Å ³	2001.2(4)	2017.3(6)
Z	1	1
ρ _{calc} /cm ³	1.600	1.587
μ/mm ⁻¹	2.280	3.109
F(000)	972.0	972.0
Diffraction type	Bruker SMART Apex	Bruker SMART Apex
Radiation	MoKα (λ = 0.71073)	synchrotron (λ = 0.80000)
2θ range for data collection/°	2.568 to 53.53	5.488 to 59.178
Index ranges	-14 ≤ h ≤ 14, -15 ≤ k ≤ 15, -21 ≤ l ≤ 21	-14 ≤ h ≤ 14, -15 ≤ k ≤ 15, -20 ≤ l ≤ 20
Reflections collected	15518	24522
Independent reflections	8473 [Rint = 0.0477, Rsigma = 0.0724]	15458 [Rint = 0.0733, Rsigma = 0.0548]
Data/restraints/parameters	8473/12/515	15458/152/1005
Goodness-of-fit on F ²	0.958	1.080
Final R indexes [I ≥ 2σ (I)]	R1 = 0.0328, wR2 = 0.0552	R1 = 0.0496, wR2 = 0.1363
Final R indexes [all data]	R1 = 0.0501, wR2 = 0.0571	R1 = 0.0527, wR2 = 0.1396
Largest diff. peak/hole / e Å ⁻³	0.69/-0.86	2.01/-2.43
Flack parameter	-	0.002(19)

Table 8-13 Crystallographic data for compound (28) and (29).

Compound	(28)	(29)
Empirical formula	C52H72Dy2Fe2N8O24	C52H67Dy2Fe2N9O22
Formula weight/ gmol ⁻¹	1629.87	1606.84
Temperature/K	150.15	100(2)
Crystal system	triclinic	triclinic
Space group	P-1	P1
a/Å	11.6266(7)	11.5919(3)
b/Å	11.6907(6)	11.5984(2)
c/Å	12.9347(6)	13.2585(2)
α /°	95.404(4)	94.6150(10)
β /°	115.454(5)	114.698(2)
γ /°	91.188(4)	100.051(2)
Volume/Å ³	1576.74(16)	1571.04(6)
Z	1	1
ρ_{calc} /cm ³	1.716	1.698
μ /mm ⁻¹	16.794	2.884
F(000)	816.0	802.0
Diffraction type	Stoe IPDS II	Bruker SMART Apex
Radiation	CuK α (λ = 1.54184)	Mo-K α (λ = 0.71073)
2 θ range for data collection/°	7.614 to 141.754	3.432 to 67.506
Index ranges	-14 \leq h \leq 13, -14 \leq k \leq 11, -15 \leq l \leq 15	-18 \leq h \leq 18, -17 \leq k \leq 16, -19 \leq l \leq 19
Reflections collected	11970	48401
Independent reflections	5959 [Rint = 0.0291, Rsigma = 0.0426]	19581 [Rint = 0.0395, Rsigma = 0.0420]
Data/restraints/parameters	5959/2/414	19581/7/803
Goodness-of-fit on F ²	1.045	1.094
Final R indexes [$I \geq 2\sigma(I)$]	R1 = 0.0292, wR2 = 0.0718	R1 = 0.0238, wR2 = 0.0596
Final R indexes [all data]	R1 = 0.0349, wR2 = 0.0765	R1 = 0.0302, wR2 = 0.0615
Largest diff. peak/hole / e Å ⁻³	0.59/-0.86	1.63/-0.88
Flack parameter	-	0.014(8)

Table 8-14 Crystallographic data for compound **(30)** and **(31)**.

Compound	(30)	(31)
Empirical formula	C ₅₂ H ₆₇ Dy ₂ Fe ₂ N ₉ O ₂₂	C ₃₄₀ H ₄₆₈ Fe ₁₈ N ₆₈ O ₁₂₀ Tb ₆
Formula weight/ gmol ⁻¹	1606.84	9386.62
Temperature/K	150(2)	150(2)
Crystal system	triclinic	orthorhombic
Space group	P1	Pccn
a/Å	11.6765(13)	31.042(2)
b/Å	11.7139(13)	35.196(3)
c/Å	13.3408(15)	36.629(3)
α/°	114.696(2)	90
β/°	94.758(2)	90
γ/°	100.073(2)	90
Volume/Å ³	1607.3(3)	40020(5)
Z	1	4
ρ _{calc} /cm ³	1.660	1.558
μ/mm ⁻¹	3.878	2.412
F(000)	802.0	19208.0
Diffractometer type	Bruker SMART Apex	Bruker SMART Apex
Radiation	synchrotron (λ = 0.79945)	synchrotron (λ = 0.79945)
2θ range for data collection/°	5.07 to 61.654	3.46 to 59.954
Index ranges	-14 ≤ h ≤ 14, -15 ≤ k ≤ 15, -17 ≤ l ≤ 17	-35 ≤ h ≤ 38, -43 ≤ k ≤ 43, -42 ≤ l ≤ 45
Reflections collected	23351	322321
Independent reflections	13540 [R _{int} = 0.0202, R _{sigma} = 0.0332]	40873 [R _{int} = 0.0839, R _{sigma} = 0.0502]
Data/restraints/parameters	13540/26/800	40873/151/1998
Goodness-of-fit on F ²	1.064	1.106
Final R indexes [I ≥ 2σ (I)]	R ₁ = 0.0182, wR ₂ = 0.0459	R ₁ = 0.0701, wR ₂ = 0.1722
Final R indexes [all data]	R ₁ = 0.0197, wR ₂ = 0.0466	R ₁ = 0.1073, wR ₂ = 0.2079
Largest diff. peak/hole / e Å ⁻³	1.05/-0.89	3.15/-0.84
Flack parameter	0.064(6)	hk-tb1b_sq

Table 8-15 Crystallographic data for compound **(32)** and **(33)**.

Compound	(32)	(33)
Empirical formula	C ₃₄₀ H ₄₆₈ Dy ₆ Fe ₁₈ N ₆ O ₁₂₀	C ₃₈₄ H ₅₃₄ Fe ₁₈ Ho ₆ N ₉₀ O ₁₂₀
Formula weight/ gmol ⁻¹	9408.10	10325.86
Temperature/K	150(2)	100(2)
Crystal system	orthorhombic	triclinic
Space group	Pccn	P-1
a/Å	30.998(3)	21.497(3)
b/Å	35.263(4)	21.602(3)
c/Å	36.545(5)	24.858(4)
α/°	90	78.866(2)
β/°	90	72.105(2)
γ/°	90	78.555(2)
Volume/Å ³	39947(8)	10659(3)
Z	4	1
ρ _{calc} /cm ³	1.564	1.609
μ/mm ⁻¹	2.498	1.785
F(000)	19232.0	5298.0
Diffractometer type	Bruker SMART Apex	Bruker SMART Apex
Radiation	synchrotron (λ = 0.79947)	MoKα (λ = 0.71073)
2θ range for data collection/°	3.61 to 61.238	2.786 to 35.998
Index ranges	-39 ≤ h ≤ 39, -44 ≤ k ≤ 44, -46 ≤ l ≤ 46	-18 ≤ h ≤ 18, -18 ≤ k ≤ 18, -21 ≤ l ≤ 21
Reflections collected	331540	63686
Independent reflections	42967 [Rint = 0.0695, Rsigma = 0.0417]	14651 [Rint = 0.0935, Rsigma = 0.0801]
Data/restraints/parameters	42967/225/2215	14651/0/832
Goodness-of-fit on F ²	1.083	1.020
Final R indexes [I ≥ 2σ (I)]	R1 = 0.0503, wR2 = 0.1322	R1 = 0.1167, wR2 = 0.2898
Final R indexes [all data]	R1 = 0.0775, wR2 = 0.1606	R1 = 0.1645, wR2 = 0.3396
Largest diff. peak/hole / e Å ⁻³	2.19/-1.23	2.26/-0.89

Table 8-16 Crystallographic data for compound **(34)** and **(35)**.

Compound	(34)	(35)
Empirical formula	C ₃₄₀ H ₄₆₈ Er ₆ Fe ₁₈ N ₆ O ₁₂₀	C ₂₉₄ H ₄₆₈ Fe ₁₈ Lu ₆ N ₆₆ O ₁₀₈
Formula weight/ gmol ⁻¹	9436.66	8710.44
Temperature/K	150(2)	150(2)
Crystal system	orthorhombic	orthorhombic
Space group	Pccn	Pccn
a/Å	30.960(3)	30.964(2)
b/Å	35.298(3)	35.270(3)
c/Å	36.550(3)	36.627(3)
α/°	90	90
β/°	90	90
γ/°	90	90
Volume/Å ³	39943(6)	40001(5)
Z	4	4
ρ _{calc} /cm ³	1.569	1.446
μ/mm ⁻¹	2.704	2.950
F(000)	19280.0	17808.0
Diffractometer type	Bruker SMART Apex	Bruker SMART Apex
Radiation	synchrotron (λ = 0.79947)	? (λ = 0.79947)
2θ range for data collection/°	3.878 to 58.35	3.874 to 49.766
Index ranges	-36 ≤ h ≤ 37, -37 ≤ k ≤ 43, -43 ≤ l ≤ 43	-14 ≤ h ≤ 32, -31 ≤ k ≤ 35, -37 ≤ l ≤ 38
Reflections collected	201393	69896
Independent reflections	37719 [R _{int} = 0.0666, R _{sigma} = 0.0522]	23934 [R _{int} = 0.0593, R _{sigma} = 0.0704]
Data/restraints/parameters	37719/233/2112	23934/373/1950
Goodness-of-fit on F ²	1.118	1.719
Final R indexes [I ≥ 2σ (I)]	R ₁ = 0.0712, wR ₂ = 0.1794	R ₁ = 0.0876, wR ₂ = 0.2331
Final R indexes [all data]	R ₁ = 0.1262, wR ₂ = 0.2408	R ₁ = 0.1559, wR ₂ = 0.2808
Largest diff. peak/hole / e Å ⁻³	3.20/-1.45	2.93/-2.56

Table 8-17 c Crystallographic data for compound (36).

Compound	(36)
Empirical formula	C ₃₄₀ H ₄₆₈ Fe ₁₈ N ₆₈ O ₁₂₀ Y ₆
Formula weight/ gmol ⁻¹	8966.56
Temperature/K	150(2)
Crystal system	orthorhombic
Space group	Pccn
a/Å	31.0085(19)
b/Å	35.2926(18)
c/Å	36.613(2)
α/°	90
β/°	90
γ/°	90
Volume/Å ³	40068(4)
Z	4
ρ _{calc} /cm ³	1.486
μ/mm ⁻¹	1.149
F(000)	18584.0
Diffractometer type	Bruker SMART Apex
Radiation	synchrotron (λ = 0.79947)
2θ range for data collection/°	3.462 to 49.764
Index ranges	-30 ≤ h ≤ 32, -35 ≤ k ≤ 37, -34 ≤ l ≤ 38
Reflections collected	162568
Independent reflections	24443 [R _{int} = 0.0857, R _{sigma} = 0.0605]
Data/restraints/parameters	24443/172/2000
Goodness-of-fit on F ²	1.088
Final R indexes [I ≥ 2σ (I)]	R ₁ = 0.0936, wR ₂ = 0.2369
Final R indexes [all data]	R ₁ = 0.1636, wR ₂ = 0.3252
Largest diff. peak/hole / e Å ⁻³	1.53/-0.58

9 Literature

- [1] A. Caneschi, D. Gatteschi, R. Sessoli, A. L. Barra, L. C. Brunel, M. Guillot, *J. Am. Chem. Soc.* **1991**, *113*, 5873-5874.
- [2] R. Sessoli, D. Gatteschi, A. Caneschi, M. A. Novak, *Nature* **1993**, *365*, 141-143.
- [3] R. Sessoli, H. L. Tsai, A. R. Schake, S. Wang, J. B. Vincent, K. Folting, D. Gatteschi, G. Christou, D. N. Hendrickson, *J. Am. Chem. Soc.* **1993**, *115*, 1804-1816.
- [4] C. Cañada-Vilalta, T. A. O'Brien, E. K. Brechin, M. Pink, E. R. Davidson, G. Christou, *Inorg. Chem.* **2004**, *43*, 5505-5521.
- [5] N. F. Chilton, D. Collison, E. J. L. McInnes, R. E. P. Winpenny, A. Soncini, *Nat. Commun.* **2013**, *4*, 2551.
- [6] A. F. Albuquerque, F. Alet, P. Corboz, P. Dayal, A. Feiguin, S. Fuchs, L. Gamper, E. Gull, S. Gürtler, A. Honecker, R. Igarashi, M. Körner, A. Kozhevnikov, A. Läuchli, S. R. Manmana, M. Matsumoto, I. P. McCulloch, F. Michel, R. M. Noack, G. Pawłowski, L. Pollet, T. Pruschke, U. Schollwöck, S. Todo, S. Trebst, M. Troyer, P. Werner, S. Wessel, *J. Magn. Magn. Mater.* **2007**, *310*, 1187-1193.
- [7] B. Bauer, L. D. Carr, H. G. Evertz, A. Feiguin, J. Freire, S. Fuchs, L. Gamper, J. Gukelberger, E. Gull, S. Guertler, A. Hehn, R. Igarashi, S. V. Isakov, D. Koop, P. N. Ma, P. Mates, H. Matsuo, O. Parcollet, G. Pawłowski, J. D. Picon, L. Pollet, E. Santos, V. W. Scarola, U. Schollwöck, C. Silva, B. Surer, S. Todo, S. Trebst, M. Troyer, M. L. Wall, P. Werner, S. Wessel, *J.- Stat. Mech.:Theory Exp.* **2011**, *2011*, P05001.
- [8] L. H. Gade, *Koordinationschemie*, Wiley-VCH, Weinheim, **2012**.
- [9] J. R. Gispert, *Coordination Chemistry*, Wiley-VCH, Weinheim, **2008**.
- [10] O. Kahn, *Molecular Magnetism*, Wiley-VCH, Weinheim, **1993**.
- [11] H. Q. L. H. Lueken, *Magnetochemie*, Teubner, Stuttgart, **1999**.
- [12] A. F. Orchard, *Magnetochemistry*, Oxford University Press, Oxford, **2003**.
- [13] J.-P. Launay, M. Verdaguer, *Electrons in Molecules: From Basic Principles to Molecular Electronics*, Oxford University Press, Oxford, **2014**.
- [14] L. Ungur, L. F. Chibotaru, *Inorg. Chem.* **2016**, *55*, 10043-10056.
- [15] J. D. Rinehart, J. R. Long, *Chem. Sci.* **2011**, *2*.
- [16] H. T. Diep, *Frustrated Spin Systems*, University of Cergy-Pontoise, France, **2005**.
- [17] M. Mekata, *Physics Today* **2003**, *56*, 12-13.
- [18] W. Schweika, M. Valldor, P. Lemmens, *Phys. Rev. Lett.* **2007**, *98*, 067201.
- [19] J. Tang, I. Hewitt, N. T. Madhu, G. Chastanet, W. Wernsdorfer, C. E. Anson, C. Benelli, R. Sessoli, A. K. Powell, *Angew. Chem., Int. Ed.* **2006**, *45*, 1729-1733.
- [20] J. Luzon, K. Bernot, I. J. Hewitt, C. E. Anson, A. K. Powell, R. Sessoli, *Phys. Rev. Lett.* **2008**, *100*, 247205.
- [21] P. H. Guo, J. L. Liu, Z. M. Zhang, L. Ungur, L. F. Chibotaru, J. D. Leng, F. S. Guo, M. L. Tong, *Inorg Chem* **2012**, *51*, 1233-1235.
- [22] G. Novitchi, G. Pilet, L. Ungur, V. V. Moshchalkov, W. Wernsdorfer, L. F. Chibotaru, D. Luneau, A. K. Powell, *Chem. Sci.* **2012**, *3*, 1169-1176.
- [23] A. Baniodeh, N. Magnani, S. Brase, C. E. Anson, A. K. Powell, *Dalton Trans.* **2015**, *44*, 6343-6347.

- [24] K. R. Vignesh, A. Soncini, S. K. Langley, W. Wernsdorfer, K. S. Murray, G. Rajaraman, *Nat. Commun.* **2017**, *8*, 1023.
- [25] J. Wu, X.-L. Li, M. Guo, L. Zhao, Y.-Q. Zhang, J. Tang, *Chem. Commun.* **2018**, *54*, 1065-1068.
- [26] X.-L. Li, J. Tang, *Dalton Trans.* **2019**, *48*, 15358-15370.
- [27] H. Kaemmerer, A. Baniodeh, Y. Peng, E. Moreno-Pineda, M. Schulze, C. E. Anson, W. Wernsdorfer, J. Schnack, A. K. Powell, *J. Am. Chem. Soc.* **2020**, *142*, 14838-14842.
- [28] B. B. Van Aken, J. P. Rivera, H. Schmid, M. Fiebig, *Nature* **2007**, *449*, 702-705.
- [29] G. J. Long, W. T. Robinson, W. P. Tappmeyer, D. L. Bridges, *J. Chem. Soc., Dalton Trans.* **1973**, 573-579.
- [30] G. J. Long, *Mössbauer Spectroscopy Applied to Inorganic Chemistry*, Springer, Boston, **1984**.
- [31] N. N. Greenwood, *Mössbauer Spectroscopy*, Springer, Netherlands, **1971**.
- [32] L. Scherthan, S. F. M. Schmidt, H. Auerbach, T. Hochdorffer, J. A. Wolny, W. L. Bi, J. Y. Zhao, M. Y. Hu, T. Toellner, E. E. Alp, D. E. Brown, C. E. Anson, A. K. Powell, V. Schunemann, *Angew. Chem., Int. Ed.* **2019**, *58*, 3444-3449.
- [33] L. Scherthan, R. F. Pflieger, H. Auerbach, T. Hochdörffer, J. A. Wolny, W. Bi, J. Zhao, M. Y. Hu, E. E. Alp, C. E. Anson, R. Diller, A. K. Powell, V. Schünemann, *Angew. Chem., Int. Ed.* **2020**, *59*, 8818-8822.
- [34] R. E. P. Winpenny, *Dalton Trans.* **2002**, 1-10.
- [35] M. Varga, in *Fabrication and Self-Assembly of Nanobiomaterials* (Ed.: A. M. Grumezescu), William Andrew Publishing, **2016**, pp. 57-90.
- [36] W.-S. Hung, Q.-F. An, M. De Guzman, H.-Y. Lin, S.-H. Huang, W.-R. Liu, C.-C. Hu, K.-R. Lee, J.-Y. Lai, *Carbon* **2014**, *68*, 670-677.
- [37] Y. Zhang, X. Zhu, S. Yang, F. Zhai, F. Zhang, Z. Niu, Y. Feng, W. Feng, X. Zhang, L. Li, R. Li, W. Hu, *Nanoscale* **2019**, *11*, 12781-12787.
- [38] C. Hanske, E. H. Hill, D. Vila-Liarte, G. González-Rubio, C. Matricardi, A. Mihi, L. M. Liz-Marzán, *ACS Appl. Mater. Interfaces* **2019**, *11*, 11763-11771.
- [39] O. Botezat, J. van Leusen, V. C. Kravtsov, P. Kögerler, S. G. Baca, *Inorg. Chem.* **2017**, *56*, 1814-1822.
- [40] M. Murugesu, A. Mishra, W. Wernsdorfer, K. A. Abboud, G. Christou, *Polyhedron* **2006**, *25*, 613-625.
- [41] Y.-F. Zeng, G.-C. Xu, X. Hu, Z. Chen, X.-H. Bu, S. Gao, E. C. Sañudo, *Inorg. Chem.* **2010**, *49*, 9734-9736.
- [42] A. Baniodeh, C. E. Anson, A. K. Powell, *Chem. Sci.* **2013**, *4*, 4354-4361.
- [43] V. Mereacre, A. M. Ako, R. Clérac, W. Wernsdorfer, I. J. Hewitt, C. E. Anson, A. K. Powell, *Chem. Eur. J.* **2008**, *14*, 3577-3584.
- [44] V. Mereacre, A. Baniodeh, C. E. Anson, A. K. Powell, *J. Am. Chem. Soc.* **2011**, *133*, 15335-15337.
- [45] Y. Peng, A. K. Powell, *Coord. Chem. Rev.* **2021**, *426*, 213490.
- [46] Z. Zhang, Y. Zhang, Z. Zheng, in *Recent Development in Clusters of Rare Earths and Actinides: Chemistry and Materials* (Ed.: Z. Zheng), Springer Berlin Heidelberg, Berlin, Heidelberg, **2017**, pp. 1-49.
- [47] X.-Y. Zheng, X.-J. Kong, L.-S. Long, in *Recent Development in Clusters of Rare Earths and Actinides: Chemistry and Materials* (Ed.: Z. Zheng), Springer Berlin Heidelberg, Berlin, Heidelberg, **2017**, pp. 51-96.
- [48] X.-Y. Zheng, X.-J. Kong, Z. Zheng, L.-S. Long, L.-S. Zheng, *Acc. Chem. Res.* **2018**, *51*, 517-525.

- [49] F.-S. Guo, M. Day Benjamin, Y.-C. Chen, M.-L. Tong, A. Mansikkamäki, A. Layfield Richard, *Science* **2018**, 362, 1400-1403.
- [50] A. Werner, *Ber. Dtsch. Chem. Ges.* **1908**, 41, 3447-3465.
- [51] R. Weinland, P. Dinkelacker, *Ber. Dtsch. Chem. Ges.* **1909**, 42, 2997-3018.
- [52] R. Weinland, E. Gussmann, *Ber. Dtsch. Chem. Ges.* **1909**, 42, 3881-3894.
- [53] R. F. Weinland, E. Gussmann, *Z. Anorg. Chem.* **1910**, 67, 250-252.
- [54] L. A. Welo, *London Edinburgh Philos. Mag. J. Sci* **1928**, 6, 481-509.
- [55] L. A. Welo, *Phys. Rev.* **1928**
- 32, 320.
- [56] L. E. Orgel, *Nature* **1960**, 187, 504-505.
- [57] B. N. Figgis, G. B. Robertson, *Nature* **1965**, 205, 694-695.
- [58] F. E. Sowrey, C. Tilford, S. Wocadlo, C. E. Anson, A. K. Powell, S. M. Bennington, W. Montfrooij, U. A. Jayasooriya, R. D. Cannon, *J. Chem. Soc., Dalton Trans.* **2001**, 862-866.
- [59] A. N. Georgopoulou, Y. Sanakis, A. K. Boudalis, *Dalton Trans.* **2011**, 40, 6371-6374.
- [60] W.-S. Xia, J. Radosevich, A. Ellern, *Acta Crystallogr. E* **2006**, 62, 1213-1215.
- [61] L. W. Hessel, C. Romers, *Recl. Trav. Chim. Pays-Bas* **1969**, 88, 545-552.
- [62] A. R. E. Baikie, M. B. Hursthouse, L. New, P. Thornton, R. G. White, *J. Chem. Soc., Chem. Commun.* **1980**, 684-685.
- [63] R.-X. Gao, Y.-Y. Gao, R.-J. Xie, L.-M. Han, *Chem. Pap.* **2020**, 74, 895-901.
- [64] Y. Sun, L.-L. Zhu, H.-H. Zhang, *Acta Crystallogr. E* **2009**, 65, m1402-m1403.
- [65] H. Hatop, M. Ferbinteanu, H. W. Roesky, F. Cimpoesu, M. Schiefer, H.-G. Schmidt, M. Noltemeyer, *Inorg. Chem.* **2002**, 41, 1022-1025.
- [66] K. O. Abdulwahab, M. A. Malik, P. O'Brien, I. J. Vitorica-Yrezabal, G. A. Timco, F. Tuna, R. E. P. Winpenny, *Dalton Trans.* **2018**, 47, 376-381.
- [67] V. I. Ponomarev, O. S. Filipenko, L. O. Atovmyan, S. A. Bobkova, K. I. Turte, *Dokl. Akad. Nauk. SSSR* **1982**, 262, 346-350.
- [68] F. A. Cotton, W. Wang, *Inorg. Chem.* **1982**, 21, 2675-2678.
- [69] P. Poganiuch, S. Liu, G. C. Papaefthymiou, S. J. Lippard, *J. Am. Chem. Soc.* **1991**, 113, 4645-4651.
- [70] V. Gorinchoy, O. Cuzan-Munteanu, O. Petuhov, E. Melnic, V. C. Kravtsov, S. Shova, *J. Therm. Anal. Calorim.* **2019**, 138, 2623-2633.
- [71] M. M. Amini, M. Yadavi, S. W. Ng, *Acta Crystallogr. E* **2004**, 60, 492-494.
- [72] M. M. Amini, M. Yadavi, S. W. Ng, *Acta Crystallogr. E* **2004**, 60, 495-497.
- [73] S. Shova, D. Prodius, V. Mereacre, Y. A. Simonov, J. Lipkowski, C. Turta, *Inorg. Chem. Commun.* **2004**, 7, 292-295.
- [74] S. Melnic, D. Prodius, H. Stoeckli-Evans, S. Shova, C. Turta, *Eur. J. Med. Chem.* **2010**, 45, 1465-1469.
- [75] I. Shweky, L. E. Pence, G. C. Papaefthymiou, R. Sessoli, J. W. Yun, A. Bino, S. J. Lippard, *J. Am. Chem. Soc.* **1997**, 119, 1037-1042.
- [76] P. Alborés, E. Rentschler, *Inorg. Chem.* **2008**, 47, 7960-7962.
- [77] R. D. Cannon, R. P. White, in *Prog. Inorg. Chem.*, **1988**, pp. 195-298.
- [78] M. Llunell, D. Casanova, J. Cirera, P. Alemany, S. Alvarez, University of Barcelona, Barcelona, Spain, **2013**.
- [79] P. Guionneau, M. Marchivie, G. Bravic, J.-F. Létard, D. Chasseau, in *Spin Crossover in Transition Metal Compounds II* (Eds.: P. Gülich, H. A. Goodwin), Springer Berlin Heidelberg, Berlin, Heidelberg, **2004**, pp. 97-128.
- [80] J. Rogan, D. Poletti, L. Karanović, *Z. Anorg. Allg. Chem.* **2006**, 632, 133-139.

- [81] P. Das, C. K. Jain, S. K. Dey, R. Saha, A. D. Chowdhury, S. Roychoudhury, S. Kumar, H. K. Majumder, S. Das, *RSC Adv.* **2014**, *4*, 59344-59357.
- [82] C. Giacobozzo, F. Scordari, S. Menchetti, *Acta Crystallogr. B* **1975**, *31*, 2171-2173.
- [83] F. Scordari, *Mineral. Mag.* **1977**, *41*, 371-374.
- [84] N. F. Chilton, R. P. Anderson, L. D. Turner, A. Soncini, K. S. Murray, *J. Comput. Chem.* **2013**, *34*, 1164-1175.
- [85] D. P. DiVincenzo, *Fortschr. Physik* **2000**, *48*, 771-783.
- [86] J. F. Duncan, C. R. Kanekar, K. F. Mok, *J. Chem. Soc. A* **1969**, 480-482.
- [87] A. N. Georgopoulou, Y. Sanakis, V. Psycharis, C. P. Raptopoulou, A. K. Boudalis, *Hyperfine Interact.* **2010**, *198*, 229-241.
- [88] A. B. Carter, N. J. Zhang, I. A. Kuhne, T. D. Keene, A. K. Powell, J. A. Kitchen, *ChemistrySelect* **2019**, *4*, 1850-1856.
- [89] V. Alekseenko, A. Alekseenko, *J. Geochem. Explor.* **2014**, *147*, 245-249.
- [90] M. Tombers, J. Meyer, J. Meyer, A. Lawicki, V. Zamudio-Bayer, K. Hirsch, J. T. Lau, B. von Issendorff, A. Terasaki, T. A. Schlathölter, R. A. Hoekstra, S. Schmidt, A. K. Powell, E. Kessler, M. H. Prosenc, C. van Wüllen, G. Niedner-Schatteburg, *Chem. Eur. J.* **2022**, *28*, e202102592.
- [91] R. Bagai, G. Christou, *Chem. Soc. Rev.* **2009**, *38*, 1011-1026.
- [92] J. Liu, Y.-C. Chen, J.-L. Liu, V. Vieru, L. Ungur, J.-H. Jia, L. F. Chibotaru, Y. Lan, W. Wernsdorfer, S. Gao, X.-M. Chen, M.-L. Tong, *J. Am. Chem. Soc.* **2016**, *138*, 5441-5450.
- [93] O. Sozer, M. Kis, Z. Gombos, B. Ughy, *Front. Biosci.* **2011**, *16*, 619-643.
- [94] A. Mishra, W. Wernsdorfer, K. A. Abboud, G. Christou, *Chem. Commun.* **2005**, 54-56.
- [95] I. J. Hewitt, J.-K. Tang, N. T. Madhu, R. Clérac, G. Buth, C. E. Anson, A. K. Powell, *Chem. Commun.* **2006**, 2650-2652.
- [96] H. Fliegl, K. Fink, W. Klopffer, C. E. Anson, A. K. Powell, R. Clérac, *Phys. Chem. Chem. Phys.* **2009**, *11*, 3900-3909.
- [97] A. R. E. Baikie, A. J. Howes, M. B. Hursthouse, A. B. Quick, P. Thornton, *J. Chem. Soc., Chem. Commun.* **1986**, 1587-1587.
- [98] K. S. Gavrilenko, S. V. Punin, O. Cador, S. Golhen, L. Ouahab, V. V. Pavlishchuk, *Inorg. Chem.* **2005**, *44*, 5903-5910.
- [99] K. Köhler, H. W. Roesky, M. Noltemeyer, H.-G. Schmidt, C. Freire-Erdbrügger, G. M. Sheldrick, *Chem. Ber.* **1993**, *126*, 921-926.
- [100] A. S. Batsanov, Y. T. Struchkov, G. A. Timco, N. V. Gerbeleu, O. S. Manole, S. V. Grebenko, *Koord. Khim.* **1994**, *20*, 604.
- [101] M. A. Kiskin, A. A. Sidorov, I. G. Fomina, G. L. Rusinov, R. I. Ishmetova, G. G. Aleksandrov, Y. G. Shvedenkov, Z. V. Dobrokhotova, V. M. Novotortsev, O. N. Chupakhin, I. L. Eremenko, I. I. Moiseev, *Inorg. Chem. Commun.* **2005**, *8*, 524-528.
- [102] K. Nakata, H. Miyasaka, F. Iwahori, K.-i. Sugiura, M. Yamashita, *Polyhedron* **2005**, *24*, 2250-2256.
- [103] E. Fursova, V. Ovcharenko, K. Nosova, G. Romanenko, V. Ikorskii, *Polyhedron* **2005**, *24*, 2084-2093.
- [104] J. Kim, H. Cho, *Inorg. Chem. Commun.* **2004**, *7*, 122-124.
- [105] P. Karsten, J. Strahle, *Acta Crystallogr. C* **1998**, *54*, 1403-1406.
- [106] A. R. Schake, J. B. Vincent, Q. Li, P. D. W. Boyd, K. Folting, J. C. Huffman, D. N. Hendrickson, G. Christou, *Inorg. Chem.* **1989**, *28*, 1915-1923.

- [107] M. A. Halcrow, W. E. Streib, K. Folting, G. Christou, *Acta Crystallogr. C* **1995**, *51*, 1263-1267.
- [108] T. C. Stamatatos, D. Foguet-Albiol, S. P. Perlepes, C. P. Raptopoulou, A. Terzis, C. S. Patrickios, G. Christou, A. J. Tasiopoulos, *Polyhedron* **2006**, *25*, 1737-1746.
- [109] K. Nakata, H. Miyasaka, T. Ishii, M. Yamashita, K. Awaga, *Mol. Cryst. Liq. Cryst.* **2002**, *379*, 211-216.
- [110] K. Nakata, H. Miyasaka, K. Sugimoto, T. Ishii, K.-i. Sugiura, M. Yamashita, *Chem. Lett.* **2002**, *31*, 658-659.
- [111] V. Ovcharenko, E. Fursova, G. Romanenko, V. Ikorskii, *Inorg. Chem.* **2004**, *43*, 3332-3334.
- [112] C.-B. Ma, M.-Q. Hu, H. Chen, C.-N. Chen, Q.-T. Liu, *Eur. J. Inorg. Chem.* **2008**, *2008*, 5274-5280.
- [113] E.-C. Yang, S.-Y. Huang, W. Wernsdorfer, L.-X. Hong, M. Damjanovic, L. Niekamp, G.-H. Lee, *RSC Advances* **2019**, *9*, 37740-37746.
- [114] D. J. Vinyard, G. M. Ananyev, G. C. Dismukes, *Annu. Rev. Biochem.* **2013**, *82*, 577-606.
- [115] G. E. Kostakis, S. P. Perlepes, V. A. Blatov, D. M. Proserpio, A. K. Powell, *Coord. Chem. Rev.* **2012**, *256*, 1246-1278.
- [116] H. Kaemmerer, V. Mereacre, A. M. Ako, S. Mameri, C. E. Anson, R. Clérac, A. K. Powell, *Chem. Eur. J.* **2021**, *27*, 15096-15102.
- [117] Y. Peng, H. Kaemmerer, A. K. Powell, *Chem. Eur. J.* **2021**, *27*, 15044-15066.
- [118] A. Baniodeh, Y. Lan, G. Novitchi, V. Mereacre, A. Sukhanov, M. Ferbinteanu, V. Voronkova, C. E. Anson, A. K. Powell, *Dalton Trans.* **2013**, *42*, 8926-8938.
- [119] A. Baniodeh, V. Mereacre, N. Magnani, Y. H. Lan, J. A. Wolny, V. Schunemann, C. E. Anson, A. K. Powell, *Chem. Commun.* **2013**, *49*, 9666-9668.
- [120] S. K. Langley, L. Ungur, N. F. Chilton, B. Moubaraki, L. F. Chibotaru, K. S. Murray, *Inorg. Chem.* **2014**, *53*, 4303-4315.
- [121] A. Baniodeh, D. Wagner, Y. Peng, H. Kaemmerer, N. Leblanc, S. Bräse, J.-V. Naubron, C. E. Anson, A. Powell, *Chem. Eur. J.* **2021**, *27*, 15103-15109.
- [122] K. S. Cole, R. H. Cole, *J. Chem. Phys.* **1941**, *9*, 341-351.
- [123] D. Reta, N. F. Chilton, *Phys. Chem. Chem. Phys.* **2019**, *21*, 23567-23575.
- [124] K. Petukhov, M. S. Alam, H. Rupp, S. Strömsdörfer, P. Müller, A. Scheurer, R. W. Saalfrank, J. Kortus, A. Postnikov, M. Ruben, *Coord. Chem. Rev.* **2009**, *253*, 2387-2398.
- [125] O. Waldmann, R. Koch, S. Schromm, P. Müller, I. Bernt, R. W. Saalfrank, *Phys. Rev. Lett.* **2002**, *89*, 246401.
- [126] A. Baniodeh, I. J. Hewitt, V. Mereacre, Y. Lan, G. Novitchi, C. E. Anson, A. K. Powell, *Dalton Trans.* **2011**, *40*, 4080-4086.
- [127] K. R. Vignesh, S. K. Langley, B. Moubaraki, K. S. Murray, G. Rajaraman, *Chem. Eur. J.* **2015**, *21*, 16364-16369.
- [128] L. Qin, J. Singleton, W.-P. Chen, H. Nojiri, L. Engelhardt, R. E. P. Winpenny, Y.-Z. Zheng, *Angew. Chem., Int. Ed.* **2017**, *56*, 16571-16574.
- [129] A. Baniodeh, N. Magnani, Y. H. Lan, G. Buth, C. E. Anson, J. Richter, M. Affronte, J. Schnack, A. K. Powell, *npj Quantum Mater.* **2018**, *3*.
- [130] S. F. M. Schmidt, C. Koo, V. Mereacre, J. Park, D. W. Heerrmann, V. Kataev, C. E. Anson, D. Prodius, G. Novitchi, R. Klingeler, A. K. Powell, *Inorg. Chem.* **2017**, *56*, 4796-4806.

- [131] D. Prodius, V. Mereacre, P. Singh, Y. Lan, S. Mameri, D. D. Johnson, W. Wernsdorfer, C. E. Anson, A. K. Powell, *J. Mater. Chem. C* **2018**, *6*, 2862-2872.
- [132] S. Schmidt, D. Prodius, G. Novitchi, V. Mereacre, G. E. Kostakis, A. K. Powell, *Chem. Commun.* **2012**, *48*, 9825-9827.
- [133] I. A. Kühne, V. Mereacre, C. E. Anson, A. K. Powell, *Chem. Commun.* **2016**, *52*, 1021-1024.
- [134] A. Baniodeh, *Cooperative Effects in Non-Cyclic and Cyclic Fe^{III}/4f Clusters*, Cuvillier, Göttingen, **2013**.
- [135] H. Kaemmerer, Karlsruhe Institute of Technology (KIT) (Karlsruhe), **2017**.
- [136] G. Novitchi, W. Wernsdorfer, L. F. Chibotaru, J.-P. Costes, C. E. Anson, A. K. Powell, *Angew. Chem., Int. Ed.* **2009**, *48*, 1614-1619.
- [137] P. King, T. C. Stamatatos, K. A. Abboud, G. Christou, *Angew. Chem., Int. Ed.* **2006**, *45*, 7379-7383.
- [138] N. Talebi, S. Guo, P. A. v. Aken, *Nanophotonics* **2018**, *7*, 93-110.
- [139] A. Boleiningger, T. Lake, S. Hami, C. Vallance, *Sensors* **2010**, *10*, 1765-1781.
- [140] V. Mereacre, A. M. Ako, R. Clérac, W. Wernsdorfer, I. J. Hewitt, C. E. Anson, A. K. Powell, *Chem. Eur. J.* **2008**, *14*, 3577-3584.
- [141] G. M. Sheldrick, *Acta Crystallogr C Struct Chem* **2015**, *71*, 3-8.
- [142] G. M. Sheldrick, Bruker AXS Inc., **2003**.
- [143] O. V. Dolomanov, L. J. Bourhis, R. J. Gildea, J. A. K. Howard, H. Puschmann, *J. Appl. Crystallogr.* **2009**, *42*, 339-341.
- [144] R. Weinland, H. Holtmeier, *Z. Anorg. Allg. Chem.* **1928**, *173*, 49-62.
- [145] A. B. Blake, A. Yavari, W. E. Hatfield, C. N. Sethulekshmi, *J. Chem. Soc., Dalton Trans.* **1985**, 2509-2520.

10 Acknowledgements

I dedicate this thesis to my grand-parents, Prof. Dr. Hans-Klaus Neske and Inge Neske. Both of them served me as great examples of how important education is.

Of course, I would like to thank Prof. Dr. Annie K. Powell for giving me the opportunity to pursue a PhD in chemistry. Her support helped me become a better chemist, as well as learning how to be a better person.

Furthermore, Dr. Chris Anson has always had an open ear whenever I could bring myself to ask for help and he did help in a very patient way and without judging, however basic any question might have been.

Dr. Olaf Fuhr, Dr. Andreas Eichhöfer and Dr. Dieter Fenske are acknowledged for sacrificing their time to help with much needed X-Ray measurements.

I would like to thank the other part of the original three musketeers (3METeers) Dr. Thomas Ruppert and Dr. Rouven Pflieger for their comradery over the course of the PhD.

Umaira Shuaib and Jonas Braun are very appreciated for their overall friendly nature as well as for the occasional transport of samples to Campus North.

I can't forget to thank the hard-working students I had the pleasure of supervising over the course of my PhD, some of which have moved on from chemistry but have helped me with synthetic studies as well as help me become a better teacher, others have gone on to do well in their studies and without a doubt will be great chemists.

In addition to the current group members I would also express my gratitude to former group members that have helped shape the way I have developed both as a chemist and a person.

Dr. Yan Peng, my supervisor and mentor over the course of my Diplomarbeit provided me with an immense amount of knowledge to build on. Dr. Sebastian Habermann (formerly known as Schmidt) and Dr. Nicolas Leblanc already helped me find my way in the group during my Diplomarbeit, I'd like to think that we formed a great and long-lasting friendship over the course of the years.

Dr. Anthony Blue Carter has quickly become one of the best friends I have ever had. Not only is he one of the smartest people I have ever met but his funny and open personality has made the time we spent in the group very enjoyable!

I would like to thank every group member of the Powell group, past and present, that have helped me and so many others and in turn made the group into this friendly community that could almost be described as an extended family.

On that note I would obviously like to thank my mother. You have always stood behind me, no matter the bad decisions I might have made or how my laziness stood in my way from time to time. I wish you only happiness in your life and hope this thesis proves to you that you did well in raising your children.

Finally, I'm looking forward to the future I have in place with my fiancée. There have been some bumps along the way, but your calm nature has always helped me become the best possible version of myself. I'm looking forward to what the future has in store for us.

11 Appendix

11.1 List of abbreviations

SMM	Single Molecule Magnet
Å	Angstrom
SQUID	Superconducting Quantum Interference Device
H	Magnetic field
M	Magnetisation
χ	Magnetic Susceptibility
C	Curie-constant
U_{eff}	Energy barrier
τ_0	preexponential factor
dc	Direct current
ac	Alternating current
CCC	cyclic coordination cluster
QTM	quantum tunnelling of magnetisation
CCDC	Cambridge crystallographic data centre
Ln	rare earth
py	pyridine
Hpiv	pivalic acid
Ph	phenyl
^t But	tert-butyl
naph ⁻	N-(p-aminobenzenesulfonate)-1,8-naphthalimide
H ₂ mdea	N-methyldiethanolamine
teaH ₃	triethanolamine
Me-teaH ₃	[N,N-bis-(2-hydroxyethyl)-amino]-2-propanol
H ₂ ampd	2-amino-2-methyl-1,3-propanediol
MSC	magnetostructural correlations
QMC	Quantum Monte Carlo

11.2 List of tables

Table 3-1	SHAPE analysis of the Fe ^{III} coordination environment in (1), polyhedra drawn as they are oriented in the crystal structure, deviation factor from optimal octahedral coordination geometry (OC-6) and sum of the absolute values of the deviation from the 90° octahedral cis angles (Σ).....	24
Table 3-2	Space groups and unit cell volume of compounds (1)-(4).....	26
Table 3-3	SHAPE analysis of the Fe ^{III} coordination environment in (2), polyhedra are drawn as they are oriented in the crystal structure, deviation factor from optimal octahedral coordination geometry (OC-6) and sum of the absolute values of the deviation from the 90° octahedral cis angles (Σ).....	27
Table 3-4	SHAPE analysis of the Fe ^{III} coordination environment in (3), polyhedra are drawn as they are oriented in the crystal structure, deviation factor from optimal octahedral coordination geometry (OC-6) and sum of the absolute values of the deviation from the 90° octahedral cis angles (Σ).....	30
Table 3-5	SHAPE analysis of the Fe ^{III} coordination environment in (4), polyhedra are drawn as they are oriented in the crystal structure, deviation factor from optimal octahedral coordination geometry (OC-6) and sum of the absolute values of the deviation from the 90° octahedral cis angles (Σ).....	34
Table 3-6	SHAPE analysis of the Fe ^{III} coordination environment in (5), polyhedra are drawn as they are oriented in the crystal structure, deviation factor from optimal octahedral coordination geometry (OC-6) and sum of the absolute values of the deviation from the 90° octahedral cis angles (Σ).....	42
Table 3-7	Selected bond lengths and angles for the triangles in (6) discussed in the text.	45
Table 3-8	SHAPE analysis of the Fe coordination environment in (6), polyhedra are drawn as they are oriented in the crystal structure, deviation factor from optimal octahedral coordination geometry (OC-6) and sum of the absolute values of the deviation from the 90° octahedral cis angles (Σ).....	48
Table 3-9	SHAPE analysis of the Cr coordination environment in (7), deviation factor from optimal octahedral coordination geometry (OC-6) and sum of the absolute values of the deviation from the 90° octahedral cis angles (Σ).	50
Table 3-10	Selected bond lengths and angles for [Mn ₆ O ₂ (piv) ₁₀ (pivH) ₄].....	61
Table 3-11	SHAPE analysis of the Mn coordination environment in [Mn ₆ O ₂ (piv) ₁₀ (pivH) ₄], deviation factor from optimal octahedral coordination geometry (OC-6) and sum of the absolute values of the deviation from the 90° octahedral cis angles (Σ).....	62
Table 3-12	Selected bond lengths and angles of [Mn ₆ O ₂ (piv) ₁₀ (pivH) ₂ (4-Me-py) ₂] (11).	66
Table 3-13	SHAPE analysis of the Mn coordination environment in [Mn ₆ O ₂ (piv) ₁₀ (pivH) ₂ (4-Me-py) ₂] (11), deviation factor from optimal	

	octahedral coordination geometry (OC-6) and sum of the absolute values of the deviation from the 90° octahedral cis angles (Σ).....	67
Table 4-1	Overview of the various structure types discussed in this section over the course of the lanthanide series, yellow checkmarks highlight previously synthesised compounds, green checkmarks highlight compounds synthesised in the scope of this thesis.	88
Table 5-1	The Energy barriers for reversal of magnetisation and pre-exponential factors derived from the Arrhenius plots for [Fe ₂ Dy ₂ (μ_3 -OH) ₂ (teaH) ₂ (O ₂ C-Ph) ₆], (26), (27) and (30).....	105
Table 8-1	Crystallographic data for compound (1) and (2).	137
Table 8-2	Crystallographic data for compound (3) and (4).	138
Table 8-3	Crystallographic data for compound (5) and (6).	139
Table 8-4	Crystallographic data for compound (7) and (11).	140
Table 8-5	Crystallographic data for compound (12) and (13).	141
Table 8-6	Crystallographic data for compound (14), for (15) a unit cell measurement confirmed the identity of the compound.	142
Table 8-7	Crystallographic data for compound (16) and (17).	143
Table 8-8	Crystallographic data for compound (18) and (19).	144
Table 8-9	Crystallographic data for compound (20) and (21).	145
Table 8-10	Crystallographic data for compound (22) and (23).	146
Table 8-11	Crystallographic data for compound (24) and (25).	147
Table 8-12	Crystallographic data for compound (26) and (27).	148
Table 8-13	Crystallographic data for compound (28) and (29).	149
Table 8-14	Crystallographic data for compound (30) and (31).	150
Table 8-15	Crystallographic data for compound (32) and (33).	151
Table 8-16	Crystallographic data for compound (34) and (35).	152
Table 8-17	c Crystallographic data for compound (36).....	153

11.3 List of figures

Figure 1.2-1	Schematic representation of the double-well potential in Mn ₁₂ O ₁₂ (CH ₃ CO ₂) ₁₂ , reimaged from reference [2]. Degenerate ms states (a) removing degeneracy through application of an external field (b) and relaxation over the energy barrier after removal of the external field (c)	5
Figure 1.2-2	Schematic representation of the different relaxation processes, reprinted from reference [14] with permission from the American Chemical Society.	6
Figure 1.2-3	Illustration highlighting the inverse relationship of the anisotropy ellipsoids for the lanthanide series, reimaged from reference [15] Ln ^{III} = Ce-Sm show the opposite shape of the ellipsoids compared to Ln ^{III} = Dy-Yb, Tb does not have a counterpart as Eu is expected to be diamagnetic at low temperatures.....	7
Figure 1.2-4	Rationalisation of possible spin arrangements leading to spin frustration, arising from competing antiferromagnetic interactions that cannot be satisfied.	7
Figure 1.2-5	Arrangement of frustrated spins in a Kagomé lattice, reproduced from reference [18].....	8

Figure 1.2-6	Possible arrangement of non-collinear spins in vortex like orientations resulting in a toroidal (a), ferrotoroidal (b) and antiferrotoroidal (c) system.....	8
Figure 1.2-7	Possible spin ground states for the archetypical Dy ₃ toroidal moment, reprinted from reference [20] with permission from the American Physical Society.....	9
Figure 1.2-8	Alternative description of the toroidal moment as the fourth ferroic order arising from a tail-to-head arrangement of spins. Reprinted from reference [28] with permission from Springer Nature Limited.....	9
Figure 1.2-9	Decay of the radioactive Mößbauer source ⁵⁷ Co via the I=5/2 excited state to the I=3/2, 14.41keV state of ⁵⁷ Fe, the resonance of the excited 14.41keV energy level with the sample leads to the detection of the Mößbauer effect.....	10
Figure 1.3-1	Scheme of the synthetic procedure to form thin graphene membranes via the pressure-assisted self-assembly described in the text. Reprinted from reference [36] with the permission of Elsevier.....	13
Figure 1.3-2	Schematic overview of the temperature-assisted self-assembly process discussed in the text, reprinted from reference [37] with permission from the Royal Society of Chemistry.....	14
Figure 1.3-3	Schematic representation of the synthetic procedure to produce arrays of gold nanorods (a), SEM images of the formation of gold nanorod arrays from H ₂ O (b) and a H ₂ O/EtOH mixture (c), reprinted from reference [38] with permission by the American Chemical Society.....	15
Figure 1.4-1	The definition of the possible positions the metal ions can occupy (a) and the ball-and-stick representations of a Type I (b) or Type II (c) butterfly structure. Reprinted from reference [45] with permission from Elsevier.....	17
Figure 3.1-1	The original sum formula for the basic carboxylates published by Werner. ^[50]	20
Figure 3.1-2	Generic scheme of the basic carboxylates used in this work, highlighting the various tweaking possibilities of M (transition metals), R (aromatic substituents) and L (terminal ligand). The core of the three transition metals bridged by a μ ₃ -oxide ion remains the same for all variations.....	21
Figure 3.1-3	Molecular structure of [Fe ₃ O(O ₂ C-Ph) ₆ (EtOH) ₂ (H ₂ O)]ClO ₄ (1), H-atoms are omitted for clarity.....	23
Figure 3.1-4	Unit cell of [Fe ₃ O(O ₂ C-Ph) ₆ (EtOH) ₂ (H ₂ O)]ClO ₄ (1), highlighted in turquoise is the distance between two benzoates (3.707Å) interacting via π-π stacking. H-atoms omitted for clarity.....	25
Figure 3.1-5	Molecular structure of [Fe ₃ O(O ₂ C-Ph) ₆ (EtOH) ₂ (H ₂ O)]BPh ₄ (2), organic H-atoms are omitted for clarity.....	26
Figure 3.1-6	Unit cell of [Fe ₃ O(O ₂ C-Ph) ₆ (EtOH) ₂ (H ₂ O)]BPh ₄ (2), highlighted in turquoise is the distance between two benzoates (4.173Å) interacting via π-π stacking. H-atoms omitted for clarity.....	28
Figure 3.1-7	Molecular structure of [Fe ₃ O(O ₂ C- <i>t</i> -But-Ph) ₆ (py) ₂ Cl] (3), organic H-atoms are omitted for clarity.....	29

Figure 3.1-8	Unit cell of $[\text{Fe}_3\text{O}(\text{O}_2\text{C-}^t\text{But-Ph})_6(\text{Py})_2\text{Cl}]$ (3) (visual representation and view along the c-axis highlighting the 4_1 symmetry). H-atoms omitted for clarity.....	31
Figure 3.1-9	The molecular structure of $[\text{Fe}_3\text{O}(\text{O}_2\text{C-Ph})_5(\text{EtOH})_3\text{SO}_4]$ (4), organic H-atoms are omitted for clarity.	33
Figure 3.1-10	The unit cell of $[\text{Fe}_3\text{O}(\text{O}_2\text{C-Ph})_5(\text{EtOH})_3\text{SO}_4]$ (4), shown in turquoise are the closest C-C distances between the complexes (4.116\AA - 4.490\AA) H-atoms omitted for clarity.....	35
Figure 3.1-11	Magnetic data of $[\text{Fe}_3\text{O}(\text{O}_2\text{C-Ph})_5(\text{EtOH})_3\text{SO}_4]$ (4): χ vs T plot (a), χ^{-1} vs T plot (b), χT vs T (c) measured at 1000Oe with the best fit for χT discussed in the text shown as a red line and M vs H measured at 2, 3 and 5K (d).	36
Figure 3.1-12	Mössbauer spectrum of $[\text{Fe}_3\text{O}(\text{O}_2\text{C-Ph})_5(\text{EtOH})_3\text{SO}_4]$ (4) measured at 77 K. The solid line is the result of a least square analysis with parameters isomer shift $\delta = 0.53 \text{ mms}^{-1}$, quadrupole splitting $\Delta E_Q = 0.42 \text{ mms}^{-1}$ and a line width of $\Gamma = 0.33 \text{ mms}^{-1}$. The experimental error of δ , ΔE_Q and Γ is $\pm 0.02 \text{ mms}^{-1}$	38
Figure 3.1-13	Visual representation (a) of the unit cell of $[\text{Fe}(\text{H}_2\text{O})_6](\text{naph})_3$ (5) and view along the b-axis (b) highlighting the π -stacking effect of the N-(p-aminobenzenesulfonate)-1,8-naphthalimide anions, organic H-atoms omitted for clarity.	40
Figure 3.1-14	Cutout of the structure of (5) highlighted in red is the angle between the stacked N-(p-aminobenzenesulfonate)-1,8-naphthalimide anions.	41
Figure 3.1-15	Cutout of one $[\text{Fe}(\text{H}_2\text{O})_6](\text{naph})_3$ moiety, π - π stacking highlighted in turquoise, the distances between π systems is well within the commonly accepted values (3.5 - 3.6\AA), organic H atoms omitted for clarity.	42
Figure 3.1-16	The molecular structure of $[\text{Fe}_3\text{O}(\text{O}_2\text{C-Ph})_6(\text{py})_3]_2$ (6), organic H-atoms and solvent pyridine molecules are omitted for clarity.	45
Figure 3.1-17	The unit cell of $[\text{Fe}^{\text{III}}_2\text{Fe}^{\text{II}}\text{O}(\text{O}_2\text{C-Ph})_6(\text{py})_3]$ (6), organic H-atoms omitted for clarity.....	47
Figure 3.1-18	The molecular structure of $[\text{Cr}_3\text{O}(\text{O}_2\text{C-Ph})_6(\text{py})_3]_2$ (7), organic H-atoms, solvent pyridine molecule and nitrate counter ion omitted for clarity.	50
Figure 3.1-19	Mass spectrum of $[\text{Fe}_2\text{CoO}(\text{O}_2\text{C-Ph})_6(\text{py})_3]^+$ (8), zoomed in graphs show the comparison between calculated spectra and experimental data.....	52
Figure 3.1-20	Cutout of the mass spectrum of (9) in the 906-913 m/z range, comparison between experimental data and calculated values for $[\text{Fe}_2\text{MnO}(\text{O}_2\text{C-Ph})_6(\text{py})_3]^+$ and $[\text{Fe}_3\text{O}(\text{O}_2\text{C-Ph})_6(\text{py})_3]^+$	53
Figure 3.1-21	Mass spectrum of (9), zoomed in graphs show the comparison between calculated spectra and experimental data.	54
Figure 3.1-22	Mass spectrum of (10), zoomed in graphs show the comparison between calculated spectra and experimental data.	55
Figure 3.2-1	The core structure of $[\text{Mn}_6\text{O}_2(\text{piv})_{10}(\text{pivH})_4]$ published by Baikie et al. ^[97] redrawn using the crystal data deposited with the cambridge crystallographic data centre (CCDC), the ^t Butyl groups on the carboxylates and organic H-atoms have been omitted for clarity...	58

Figure 3.2-2	Visualisation of the edge sharing connection between the six Mn ions in $[\text{Mn}_6\text{O}_2(\text{piv})_{10}(\text{pivH})_4]$, front view (a) and top down view (b), ^t Butyl groups and H-atoms omitted for clarity.	59
Figure 3.2-3	The unit cell of $[\text{Mn}_6\text{O}_2(\text{piv})_{10}(\text{pivH})_4]$ viewed along the crystallographic a-, b- and c-axis, highlighting the nice separation of the clusters by the aliphatic ligand shell.	60
Figure 3.2-4	Suggested route for the recombination of two triangular Mn_3O units into the Mn_6O_2 core.	63
Figure 3.2-5	The molecular structure of $[\text{Mn}_6\text{O}_2(\text{piv})_{10}(\text{pivH})_2(4\text{-Me-py})_2]$ (11), organic H-atoms are omitted for clarity.	64
Figure 3.2-6	Unit cell of $[\text{Mn}_6\text{O}_2(\text{piv})_{10}(\text{pivH})_2(4\text{-Me-py})_2]$ (11) viewed along the crystallographic a-, b- and c-axis.	65
Figure 3.2-7	Visualisation of the edge sharing connection between the six Mn ions in $[\text{Mn}_6\text{O}_2(\text{piv})_{10}(\text{pivH})_2(4\text{-Me-py})_2]$ (11), front view (a) and top down view (b), ^t Butyl groups and H-atoms omitted for clarity.	67
Figure 4.2-1	The molecular structure of $[\text{Mn}^{\text{III}}_7\text{Nd}_3(\text{O})_4(\text{OH})_4(\text{mdea})_3(\text{piv})_9(\text{NO}_3)_3]$ (12), H-atoms have been omitted for clarity.	71
Figure 4.2-2	Visualisation of the core composition of $[\text{Mn}^{\text{III}}_7\text{Nd}_3(\text{O})_4(\text{OH})_4(\text{mdea})_3(\text{piv})_9(\text{NO}_3)_3]$ (12), two cubanes connected via the middle Mn^{III} are highlighted with green and light blue bonds respectively (a) and the resulting corner sharing tetrahedra (b).	72
Figure 4.2-3	The unit cell of (12) shown along the crystallographic a-axis (a) showing no obvious interaction between two neighbouring complexes and the crystal packing of (12) along the crystallographic b-axis (b) highlighting the parallel arrangement of the triangular planes of the top and bottom tetrahedron shown in brown.	72
Figure 4.2-4	The temperature dependent dc susceptibility for the compounds (12)-(15) measured at 1000Oe in the 1.8-300K range (a) and a zoomed in logarithmic graph for the low temperature region (b). ...	73
Figure 4.2-5	Rationalisation of the spin arrangement based on the results of the temperature dependent dc susceptibility for (13) (a) and (15) (b). In both cases the seven Mn^{III} are coupled in a way that results in an $S = 2$ residual spin, for (13) this is equal to the corresponding spin ground-state, while for (15) the residual spin is antiferromagnetically coupled to the three ferromagnetically coupled Gd^{III} amounting to a total spin ground-state of $S = 17/2$	74
Figure 4.2-6	The magnetisation curve for $[\text{Mn}^{\text{III}}_7\text{Gd}_3(\text{O})_4(\text{OH})_4(\text{mdea})_3(\text{piv})_9(\text{NO}_3)_3]$ (15) at 2, 3 and 5K measured for applied dc fields from 0 to 7T.	75
Figure 4.2-7	The temperature dependence of the in-phase (χ') and out-of-phase (χ'') ac susceptibility measured at varying frequencies with zero applied dc field for (12) (a), (13) (b) and (15) (c).	76
Figure 4.2-8	The Arrhenius plots derived from the ac susceptibility data for (12) (a) and (13) (b).	76
Figure 4.3-1	Molecular structure of $[\text{Mn}_5\text{Er}_4\text{O}_4(\text{OH})_2(\text{mdea})_4(\text{piv})_6(\text{NO}_3)_4(\text{H}_2\text{O})_2] \cdot \text{MeCN}$ (17) (a), the organic H-atoms and solvent MeCN have been omitted for clarity and scheme of the two distorted cubanes sharing the middle Mn^{IV} vertex (b).	78

Figure 4.3-2	Unit cell of $[\text{Mn}_5\text{Er}_4\text{O}_4(\text{OH})_2(\text{mdea})_4(\text{piv})_6(\text{NO}_3)_4(\text{H}_2\text{O})_2]\cdot\text{MeCN}$ (17), highlighted in turquoise is the intermolecular Er-Er distance, organic H-atoms have been omitted for clarity.	79
Figure 4.3-3	Molecular structure of $[\text{Mn}_5\text{Gd}_4\text{O}_6(\text{mdea})_2(\text{mdeaH})_2(\text{piv})_6(\text{NO}_3)_4(\text{iPrOH})_2]$ (19) (a), the organic H-atoms have been omitted for clarity and scheme of the two distorted cubanes sharing the middle Mn^{IV} vertex (b).	81
Figure 4.3-4	The Unit cell of $[\text{Mn}_5\text{Gd}_4\text{O}_6(\text{mdea})_2(\text{mdeaH})_2(\text{piv})_6(\text{NO}_3)_4(\text{iPrOH})_2]$ (19) with two adjacent molecules, highlighted in turquoise is the intermolecular Gd-Gd distance, organic H-atoms have been omitted for clarity.	81
Figure 4.3-5	Molecular structure of $[\text{Mn}_5\text{Gd}_4\text{O}_6(\text{mdea})_4(\text{piv})_6(\text{NO}_3)_2(\text{MeOH})_4]$ (20) (a) with the organic H-atoms omitted for clarity and scheme of the two distorted cubanes sharing the middle Mn^{IV} vertex (b).	82
Figure 4.3-6	The Unit cell of $[\text{Mn}_5\text{Gd}_4\text{O}_6(\text{mdea})_4(\text{piv})_6(\text{NO}_3)_2(\text{MeOH})_4]$ (20), highlighted in turquoise are the closest intermolecular Gd-Gd distances, the ^t Butyl-groups and organic H-atoms have been omitted for clarity.	83
Figure 4.3-7	Crystal packing of (20) along the crystallographic a-axis highlighting the orientation of the two types of molecules caused by their position on the crystallographic axes.	84
Figure 4.4-1	Molecular structure of $[\text{Mn}_2\text{Pr}_2(\text{OH})_2(\text{mdeaH})_2(\text{piv})_6(\text{NO}_3)_2]\cdot 2\text{MeCN}$ (22) with the organic H-atoms and solvent MeCN omitted for clarity.	86
Figure 4.4-2	The Unit cell of $[\text{Mn}_2\text{Pr}_2(\text{OH})_2(\text{mdeaH})_2(\text{piv})_6(\text{NO}_3)_2]\cdot 2\text{MeCN}$ (22) with two adjacent molecules, highlighted in turquoise is the intermolecular Mn-Mn distance, organic H-atoms have been omitted for clarity.	86
Figure 5.1-1	Scheme highlighting the possible variations in the M_2Ln_2 butterflies using the triethanolamine ligand. Coloured circles represent the nature of the bridging carboxylate (violet), μ_3 -bridging ligand (green), chelating co-ligand (blue) and substitution of the ligand (orange). Red arrows refer to the possibility of replacing the metal ions used and changing from type I to type II butterflies by changing the position of the transition metal and rare earth ions.	89
Figure 5.1-2	Synthetic strategy for obtaining Fe-Ln based coordination clusters, based on reference ^[27] , the additional red arrows highlight the modified strategies discussed in sections 5.1.2 and 5.1.3.	90
Figure 5.1-3	Skeletal formula of 2-amino-2-methyl-1,3-propanediol (H_2ampd). .	91
Figure 5.1-4	The molecular structure of $[\text{Fe}_2\text{Gd}_2(\text{ampd})_4(\text{O}_2\text{C-Ph})_6]$ (23), dashed lines symbolise the hydrogen bonds between the amino group and monodentate benzoate, organic H-atoms omitted for clarity.	92
Figure 5.1-5	Unit cell of $[\text{Fe}_2\text{Gd}_2(\text{ampd})_4(\text{O}_2\text{C-Ph})_6]$ (23) with two adjacent molecules of the crystal structure, highlighted in turquoise are the hydrogen bonds between the amino groups and monodentate benzoates, interconnecting the molecules.	93
Figure 5.1-6	The crystal packing of $[\text{Fe}_2\text{Gd}_2(\text{ampd})_4(\text{O}_2\text{C-Ph})_6]$ (23) along its crystallographic a-, b- and c-axis, the view along the a- and b-axis highlights the chain-like arrangement caused by the hydrogen bonding.	94

Figure 5.1-7	The molecular structure of $[\text{Cr}_2\text{Y}_2(\text{ampd})_4(\text{O}_2\text{C-Ph})_6]\cdot\text{MeCN}$ (24), dashed lines show the hydrogen bonding between the deprotonated monodentate benzoates. Organic H-atoms have been omitted for clarity.	95
Figure 5.1-8	The crystal packing of $[\text{Cr}_2\text{Y}_2(\text{ampd})_4(\text{O}_2\text{C-Ph})_6]$ (24) along its crystallographic a-, b- and c-axis.	97
Figure 5.1-9	Skeletal formulas of the tripodal ligands Triethanolamine (teaH ₃) (a) and the chiral [N,N-bis-(2-hydroxyethyl)-amino]-2-propanol (Me-teaH ₃) (b) with the chiral carbon marked with a star.	98
Figure 5.1-10	The molecular structures of $[\text{Fe}_2\text{Dy}_2(\mu_3\text{-OH})(R,S\text{-Me-teaH})_2(\text{O}_2\text{C-Ph})_6]$ (26) (a) and $[\text{Fe}_2\text{Dy}_2(\mu_3\text{-OH})(S,S\text{-Me-teaH})_2(\text{O}_2\text{C-Ph})_6]$ (27) (b) highlighted in pink are the chiral methyl-groups of the Me-teaH ₃ ligand, organic H-atoms are omitted for clarity.	99
Figure 5.1-11	The packing diagrams of $[\text{Fe}_2\text{Dy}_2(\mu_3\text{-OH})(R,S\text{-Me-teaH})_2(\text{O}_2\text{C-Ph})_6]$ (26) (a) and $[\text{Fe}_2\text{Dy}_2(\mu_3\text{-OH})(S,S\text{-Me-teaH})_2(\text{O}_2\text{C-Ph})_6]$ (27) (b) highlighting the similarities in the crystal structure despite the change in space group.	101
Figure 5.1-12	Space-filling models of (26) (a) and (27) (b). The methyl carbons of the substituted Me-teaH ₃ ligands are highlighted in pink. Highlighted in orange are the four hydrogen atoms that cannot be replaced by the methyl group, leaving the hydrogen highlighted in green as the only possible substitution site.	101
Figure 5.1-13	Magnetic data of $[\text{Fe}_2\text{Dy}_2(\mu_3\text{-OH})_2(\text{Me-teaH})_2(\text{O}_2\text{C-Ph})_6]$, χT vs T plot of (26) and (27) (a), M vs H plot for (26) (b) and M vs H plot for (27) (c).	102
Figure 5.1-14	Dynamic temperature dependant ac susceptibility measurements under zero applied dc field of the previously reported $[\text{Fe}_2\text{Dy}_2(\mu_3\text{-OH})_2(\text{teaH})_2(\text{O}_2\text{C-Ph})_6]$ with the unsubstituted teaH ₃ ligand (a), $[\text{Fe}_2\text{Dy}_2(\mu_3\text{-OH})_2(R,S\text{-Me-teaH})_2(\text{O}_2\text{C-Ph})_6]$ (26) (b) and $[\text{Fe}_2\text{Dy}_2(\mu_3\text{-OH})_2(S,S\text{-Me-teaH})_2(\text{O}_2\text{C-Ph})_6]$ (27) (c), filled circles show the out-of-phase data, while open circles show the in-phase.	103
Figure 5.1-15	Frequency-dependences of the components of the ac magnetic susceptibility for the (26) and (27), in-phase (a) and out-of-phase (b) for (26) under 2000Oe, in-phase (c) and out-of-phase (d) under 1500Oe for (27).....	104
Figure 5.1-16	Arrhenius-plots derived from the frequency-dependences of (26) (a) and (27) (b).	104
Figure 5.1-17	Molecular structures of $[\text{Fe}_2\text{Dy}_2(\mu_3\text{-OH})_2(\text{Me-teaH})_2(\text{O}_2\text{C-Ph})_4(\text{NO}_3)_2]$ (28) (a) using the racemic Me-teaH ₃ ligand, as well as (29) (b) and (30) (c) using the enantiomerically pure R- and S-Me-teaH ₃ ligand respectively. Highlighted in pink are the chiral methyl-groups of the Me-teaH ₃ ligand, organic H-atoms are omitted for clarity.....	106
Figure 5.1-18	Magnetic data of $[\text{Fe}_2\text{Dy}_2(\mu_3\text{-OH})_2(\text{Me-teaH})_2(\text{O}_2\text{C-Ph})_4(\text{NO}_3)_2]$ (28), combined χT vs T plot (a), M vs H plot for (28) (b), (29) (c) and (30) (d).	107
Figure 5.1-19	The in-phase (left) and out-of-phase (right) components of the ac susceptibility under various applied dc fields for (28) (a), (29) (b) and (30) (c).	108

Figure 5.1-20	The in-phase (left) and out-of-phase (right) susceptibility for (29) (a) and (30) (b) for varying temperatures under an applied dc field of 1000Oe, the graphs are virtually superimposable.	109
Figure 5.1-21	The in-phase (left) and out-of-phase (right) susceptibility for (29) (a) and (30) (b) for varying temperatures under an applied dc field of 3000Oe.	110
Figure 5.1-22	The Cole-Cole plots (a) and Arrhenius plot (b) for (30) , derived from the relaxation data at an applied dc field of 3000Oe shown in Figure 5.1-21	110
Figure 5.2-1	The molecular structure of the giant cyclic coordination cluster $[\text{Fe}_{18}\text{Dy}_6(\mu\text{-OH})_6(\text{ampd})_{12}(\text{Hampd})_{12}(\text{O}_2\text{C-Ph})_{24}](\text{NO}_3)_6 \cdot 38\text{MeCN}$ (32), top down view, the solvent MeCN molecules and organic H-atoms have been omitted for clarity.	113
Figure 5.2-2	The triangular $\{\text{Fe}_2\text{Dy}(\mu\text{-OH})(\text{ampd})_2(\text{O}_2\text{C-Ph})_2\}$ building block of (32) (a) and connection of two of these building blocks via a mononuclear $\{\text{Fe}(\text{Hampd})_2(\text{O}_2\text{C-Ph})_2\}$ unit (b).	114
Figure 5.2-3	Scheme of the hexagonal plane spanned by the bridging mononuclear Fe units and alternating triangular Fe_2Dy moieties above and below the plane.	114
Figure 5.2-4	$[\text{Fe}_{18}\text{Dy}_6(\mu\text{-OH})_6(\text{ampd})_{12}(\text{Hampd})_{12}(\text{O}_2\text{C-Ph})_{24}](\text{NO}_3)_6 \cdot 38\text{MeCN}$ (32) in the space-filling representation, highlighting the nanoscale dimensions of the cluster.	116
Figure 5.2-5	The crystal packing along the crystallographic a-, b-, and c-axis in $[\text{Fe}_{18}\text{Dy}_6(\mu\text{-OH})_6(\text{ampd})_{12}(\text{Hampd})_{12}(\text{O}_2\text{C-Ph})_{24}](\text{NO}_3)_6 \cdot 38\text{MeCN}$ (32).	117
Figure 5.2-6	The temperature dependence of the χT value and the field dependence of the magnetisation at 2K for (32) , (35) and (36) . ..	118
Figure 5.2-7	The repeating unit of the Fe_{18} ring reported by King et al. ^[137] (a) and compound (36) , dashed lines highlight the coupling between the Fe^{III} with the corresponding J_{FeFe} values calculated using the magnetostructural correlations according to Cañada-Viltalta et al. ^[4]	119
Figure 5.2-8	The temperature dependent (a) and frequency dependent (b) ac magnetic susceptibility measurements for $\text{Fe}_{18}\text{Dy}_6(\mu\text{-OH})_6(\text{ampd})_{12}(\text{Hampd})_{12}(\text{O}_2\text{C-Ph})_{24}(\text{NO}_3)_6 \cdot 38\text{MeCN}$ (32).	119
Figure 5.2-9	The Cole-Cole plots (a) and Arrhenius plot (b) for (32)	120
Figure 5.2-10	The arrangement of the anisotropy axes of the Dy^{III} ions (blue) as a result of the Magellan ^[5] analysis $\text{Fe}_{18}\text{Dy}_6(\mu\text{-OH})_6(\text{ampd})_{12}(\text{Hampd})_{12}(\text{O}_2\text{C-Ph})_{24}(\text{NO}_3)_6 \cdot 38\text{MeCN}$ (32), side-on (a) and top-down (b) view of the crystal structure, the Phenyl-groups, nitrate counteranions and H-atoms are omitted for clarity. (c) and (d) show a proposed spin arrangement on a simplified scheme of the crystal structure.	121
Figure 5.2-11	The microSQUID of $\text{Fe}_{18}\text{Dy}_6(\mu\text{-OH})_6(\text{ampd})_{12}(\text{Hampd})_{12}(\text{O}_2\text{C-Ph})_{24}(\text{NO}_3)_6 \cdot 38\text{MeCN}$ (32) measured at 30mK for varying field sweep rates, the inset shows the derivative of the plot.	122
Figure 5.2-12	Sawtooth chain model highlighting the magnetic coupling in (32) , open green circles show the locked Fe_2 dimer in the base of the	

Fe₂Dy triangle resulting from the strong antiferromagnetic interaction J₃, filled green circles represent the connecting Fe^{III} in the hexagonal plane in the middle of the molecule, pink circles represent Dy^{III}. The scheme results in the two effective coupling constants J_{1eff} between the Fe^{III} in the hexagon and Dy^{III}, while J_{2eff} is the coupling constant for the interaction within the Fe₆ hexagon.

..... 123

Figure 5.2-13 The energy diagram of (32) calculated from the model taking into account the assumptions stated in the text with antiferromagnetic interaction for J_{1eff} (a) and ferromagnetic interaction for J_{1eff} (b). In both cases the ground state is ferrotoroidal..... 124